Mitigation of cross wind effects on road vehicles by porous screens

Dissertation

submitted to and approved by the

Department of Architecture, Civil Engineering and Environmental Sciences
University of Braunschweig – Institute of Technology

and the

Faculty of Engineering
University of Florence

in candidacy for the degree of a
Doktor-Ingenieur (Dr.-Ing.) /
Dottore di Ricerca in Mitigation of Risk due to Natural Hazard on Structures and Infrastructures[*)]

by
Davide Allori
Born 30.10.1982
from Prato (PO), Italy

Submitted on	16 March 2012
Oral examination on	08 May 2012
Professorial advisors	Prof. G. Bartoli Prof. U. Peil

2012

*) Either the German or the Italian form of the title may be used.

To my family and Azzurra,
for their support and love

Abstract

This dissertation deals with the strategies of mitigation of high cross-winds on road infrastructures in order to minimize the risk of vehicle overturning through the introduction of porous windbreaks. This aspect assumes special interest for large commercial vehicles (trucks, lorries, vans) since they are involved in a significant number of accidents and fatalities on EU roads every year.

A simple method to quantify the risk associated with the overturning problem of large vehicles for 23 different types of barriers is proposed. The developed risk procedure consists of three main phases: the hazard analysis, the vulnerability analysis and the risk analysis, in accordance with the risk framework developed by IGC 802.

The hazard part has the aim to evaluate the probability of wind speed and direction by a statistical analysis of historical anemometric data. A distribution probability function innovative for wind engineering applications (Burr type XII) and a procedure for the estimation of parameters are proposed. Two consolidated methods are followed for the analysis of wind data.

The vulnerability analysis consists in the analytical quantification of the cross-wind actions on a model of van (Luton van) positioned on a windy infrastructure, downstream of different porous barriers. To obtain these actions some tests were carried out in the CRIACIV wind tunnel on a model of Luton van at scale 1:20.

In order to perform extrapolations from the wind tunnel model to the prototype a scaling criterion for the porous element in the wind tunnel is necessary. In fact it is almost impossible to realize a proper geometric reproduction of porous elements due to their reduced dimensions at the usual wind tunnel scales. In order to find a general scaling criterion for porous elements several wind tunnel tests were performed on samples in confined and unconfined flow conditions. Considering that in the literature there is no scaling criterion that can be used in case of wind tunnel simulations of porous elements, a criterion is proposed herein. The correct scaling from the prototype to the model can be achieved by maintaining the same porosity level, obtained with any shape and arrangement of the holes, the same thickness to hydraulic diameter ratio and ensuring that Reynolds number effects are not present. The scaling procedure defined consists in applying the classical geometric scaling process to the general dimensions of the structures (in this case the dimensions of the windbreak) and using the criterion found only to the parts that can be schematized as porous media.

Combining this criterion and the results on the model of van it is possible to have a good correspondence between model and prototype and to provide the correct estimations for the wind actions on the van. With the aim to establish if the overturning phenomenon may occur, after a literature review a critical overturning

cross-wind speed threshold has been fixed, as a function of the vehicle speed.

In the risk analysis using the data provided by the hazard and the vulnerability steps, the risk is quantified in terms of probability of failure, i.e. overturning, for all different conditions of sheltering. In this way it is possible to choose a barrier rather than another depending on the accepted level of risk and the speed limit for the vehicle in the road infrastructure considered.

A possible future development of this research may consider not only the wind-induced actions on the infrastructure users but also the wind effects on the structure. It should be noticed that bridges without windbreaks present a better aerodynamic behaviour, although they are less comfortable for the users. Therefore one should define the best configuration of shields to be introduced on bridges in order to optimize the trade-off between safety users and structural response to wind excitation.

Sommario

Il presente lavoro analizza le strategie di mitigazione del rischio di ribaltamento dei veicoli causato da forti venti trasversali, attraverso l'introduzione di opportune barriere frangivento porose sulle principali infrastrutture stradali. Questo aspetto asssume particolare rilevanza per i veicoli commerciali (autotreni, autocarri telonati, furgoni) i quali a causa della loro scarsa aerodinamicità, risultano essere più suscettibili a fenomeni di ribaltamento, e sono spesso coinvolti ogni anno in un numero significativo di incidenti sulle strade europee.

Una semplice metodologia per la quantificazione del rischio associato al ribaltamento dei veicoli in corrispondenza di vari livelli di schermatura (23 differenti barriere porose) è stata proposta ed applicata ad un caso studio. La procedura di rischio sviluppata si inquadra all'interno del risk framework proposto dall' IGC 802. Più in particolare l'iter è composto da 3 fasi principali: l'analisi dell'hazard (pericolosità), la valutazione della vulnerabilità e l'analisi di rischio vera e propria.

L'analisi di pericolosità consiste nella valutazione della probabilità dell'hazard stesso (inteso come velocità e direzione del vento) attraverso un' accurata analisi statistica di dati anemometrici storici. In questa sezione per l'analisi di dati eolici sono state impiegate una innovativa funzione di distribuzione di probabilità (Burr type XII) e la relativa procedura per la stima dei parametri. I dati di vento sono stati elaborati seguendo due consolidate metodologie di analisi: il modello classico e quello ibrido, con lo scopo di operare dei confronti.

La seconda parte del lavoro è l'analisi della vulnerabilità del sistema. L'analisi consiste nella quantificazione delle azioni trasversali indotte dal vento su un modello di furgone posizionato a valle di differenti barriere porose. Per ottenere queste azioni alcuni test sono stati svolti nella galleria del vento a strato limite del CRIACIV su un modello di furgone in scala 1:20.

Al fine di operare estrapolazioni tra modello di galleria e prototipo è necessario conoscere la regola di scalatura da dover osservare qualora siano richiesti test aerodinamici su oggetti porosi. Infatti in caso di elementi porosi è quasi impossibile realizzare una vera e propria scalatura geometrica degli oggetti a causa delle loro ridotte dimensioni alle comuni scale operative di galleria. Con lo scopo di trovare un criterio generale di scalatura numerosi test in galleria del vento sono stati condotti su campioni porosi in due diverse condizioni di flusso: confinato e non confinato. Considerando inoltre che in letteratura non sono presenti criteri di similitudine o leggi di scala da impiegarsi, in questo lavoro è stato trovato e proposto un semplice criterio di scala. La corretta scalatura tra modello e prototipo può essere raggiunta mantenendo lo stesso livello di porosità, ottenuto con qualsiasi forma e disposizione dei fori, lo stesso rapporto tra spessore e diametro idraulico e assicurando inoltre che

gli effetti del numero di Reynolds non siano presenti. Il criterio di scalatura globale consiste nell'andare ad applicare il classico processo di scalatura geometrica alle dimensioni generali dell'opera (in questo caso le dimensioni esterne della barriera) e utilizzare le prescrizioni precedentemente esposte solo per la porzione di un oggetto che può essere schematizzato come mezzo poroso.

Utilizzando la regola di scalatura e i risultati dei test in galleria del vento sul modello del furgone è possibile avere una perfetta corrispondenza tra modello e prototipo, e operare così corrette estrapolazioni per le azioni aerodinamiche indotte dal vento sul furgone. Con lo scopo di stabilire se il fenomeno del ribaltamento avviene oppure no, una soglia critica di ribaltamento per la velocità del vento, in funzione della velocità del veicolo, è stata fissata a seguito di un'accurata analisi della letteratura esistente.

Infine nell'ultima fase di analisi, utilizzando i dati forniti in output dai due precedenti steps, il rischio è quantificato ed espresso in termini di probabilità di fallimento, cioè di ribaltamento del veicolo, in corrispondenza di diverse condizioni di riparo. In questo modo fissando l'infrastruttura di riferimento e la relativa tipologia di veicolo in analisi è possibile scegliere una barriera piuttosto che un'altra in funzione del livello di rischio che si intende accettare.

Un possibile sviluppo futuro di questa ricerca potrebbe consistere nell'includere all'interno del lavoro non solo le azioni indotte dal vento sugli utilizzatori dell'infrastruttura ma anche gli effetti del vento sulla struttura stessa. Infatti è da notare che un generico ponte senza barriere presenta un migliore comportamento aerodinamico nei confronti dell'azione del vento ma risulta essere meno confortevole per i suoi fruitori. Perciò dovrebbe essere definita la miglior configurazione di barriere da adottatare su un ponte che sia in grado di ottimizzare entrambi gli aspetti, sia quello relativo alla sicurezza degli utenti che quello puramente aerodinamico e strutturale dell'opera.

Zusammenfassung

Diese Arbeit hat zum Ziel, das Überschlagrisiko der Fahrzeuge auf den Hauptverkehrswegen, welches durch Seitenwinde verursacht wird, durch geeignete poröse Windschutzbarrieren zu verringern. Dieses Phänomen ist sehr relevant für Transportmittel, wie es zum Beispiel Lastkraftfahrzeuge, Lastwägen und Kleintransporter darstellen. Diese sind charakterisiert durch eine geringe Aerodynamik, welche das Überschlagen erleichtert, und sind deshalb jährlich in viele Unfälle auf Europas Straßen verwickelt.

Eine einfache Methode zur Quantifizierung des Überschlagrisikos der Fahrzeuge bezüglich diverser Schutzlevels (dreiundzwanzig unterschiedliche poröse Barrieren) ist vorgeschlagen worden und für eine Fallstudie angewandt worden. Diese entwickelte Risikobewertung, in Konkordanz mit dem *risk framework* des IGC 802, besteht aus drei Hauptfasen: Gefahrenanalyse, Vulnerabilitätsbewertung und Risikoanalyse.

Die Gefahrenanalyse hat das Ziel die Gefahrenwahrscheinlichkeit (Windrichtung und Windgeschwindigkeit) mittels einer akkuraten statistischen Analyse gegebener Windmessdaten zu kalkulieren. Hier ist eine innovative Wahrscheinlichkeitsverteilungsfunktion (Burr type XII) verwendet worden und die diesbezügliche Prozedur zur Kalkulation der Parameter für die Analyse der äolischen Daten ist vorgeschlagen worden. Die Winddaten sind mittels zweier fundierter Analysemethoden ausgewertet und verglichen worden: Dabei handelt es sich um das klassische und das hybride Modell.

Der zweite Teil dieser Arbeit ist eine Vulnerabilitätsanalyse, welche aus der analytischen Quantifizierung der Seiteneinwirkungen, induziert durch den Wind auf ein Kleintransporter Modell, positioniert hinter verschiedenen porösen Barrieren, besteht. Um diese Windeinwirkungen (*wind actions*) zu erhalten sind einige Tests in einem Grenzschichtwindkanal des CRIACIV mit einem Lieferwagen (Maßstab 1:20), durchgeführt worden.

Um eine Extrapolation vom Windkanal-Modell zum Prototypen erhalten zu können, benötigt man ein Skalierungskriterium für poröse Objekte im Windkanal. Im Falle von porösen Objekten ist es, aufgrund ihrer geringen Dimensionen, fast unmöglich eine geeignete geometrische Skalierung zu realisieren. Mit dem Ziel ein generelles Kriterium für die Skalierung zu finden, sind zahlreiche Tests im Windkanal mit porösen Samples unter zwei verschiedenen Strömungsbedingungen ausgeführt worden. Wenn man betrachtet, dass in der gegenwärtigen Literatur keine Skalierungskriterien oder Gesetze zu finden sind, so wird hier Eines vorgeschlagen. Die korrekte Skalierung zwischen Modell und Prototyp kann erreicht werden, indem man das gleiche Level der Porosität, unabhängig der Formen und Anordnungen

der Löcher, und das gleiche Verhältnis zwischen Abstand und hydraulischem Durchmesser beibehält und indem man die Effekte der Reynold's Nummer ausschließt. Das globale Skalierungskriterium besteht darin, den klassischen geometrischen Skalierungsprozess an die allgemeinen Dimensionen des Prototypen (in diesem Fall die äußeren Dimensionen der Barriere) anzuwenden und die vorher beschriebenen Bedingungen nur für die Portion eines Objekts zu benutzen, das als poröses Medium schematisiert werden kann.

Indem man die Skalierungsregel und die Testergebnisse, die man im Windkanal mit dem Modell des Kleintransporters erreicht hat, benutzt, ist es möglich eine perfekte Korrespondenz zwischen Modell und Prototyp zu bekommen. Eine korrekte Extrapolation für die aerodynamischen Aktionen, durch den Wind auf den Kleintransporter induziert, ist so möglich. Um herauszufinden, ob das Überschlagphänomen sich ereignet oder nicht, ist eine kritische Schwelle für die Windgeschwindigkeit, in Funktion der Geschwindigkeit des Transportmittels, nach einer akkuraten Literatursuche bestimmt worden.

In der Risikoanalyse, in der man die Daten des Outputs der zwei vorherigen Phasen verwendet, wurde das Risiko (Überschlagwahrscheinlichkeit) für alle diversen Schutzbedingungen berechnet. Auf diese Weise, in Funktion des akzeptierten Risikolevels, ist es möglich einen bestimmten Windschutz zu wählen und eine Geschwindigkeitsbegrenzung für eine gegebene Straße zu bestimmen.

Eine mögliche Entwicklung dieser Forschung in Zukunft besteht darin, nicht nur die Windaktionen an den Transportmitteln einzubeziehen, sondern auch die Aktionen einzuschließen, die durch den Wind auf die gesamte Infrastruktur induziert werden. Es ist hervorzuheben, dass eine Brücke ohne Schutzwall eine bessere aerodynamische Reaktion in Hinblick auf die Windaktion aufweist, aber unbequemer für die Benutzer ist. Deshalb müsste man die beste Schutzkonfiguration definieren, die man auf einer Brücke benutzen kann, um beide Aspekte zu optimieren: nicht nur in Bezug auf die Sicherheit der Benutzer sondern auch auf den aerodynamischen und strukturellen Aspekt der Brücke.

Acknowledgements

The first acknowledgement goes to my official tutors, Prof. Gianni Bartoli and Prof. Udo Peil, for their helpfulness and support. I am very indebted to Prof. Gianni Bartoli for his continuous supervision on the progress of my thesis and for being a constant example of dedication to research and teaching. I also reserve another grateful acknowledgement to my unofficial tutor Dr. Claudio Mannini for his passion for scientific research, his clarifying tutoring activity and his continuous support in the manuscript corrections. I would like to offer heartfelt thanks to Prof. Claudio Borri for the strong efforts made for this doctoral course and to Serena Cartei for her friendly support in the intricacy of administrative matters. A special acknowledgement is dedicated to Lorenzo Procino and Alessandra Borsani for their indispensable assistance during all the experimental campaign in CRIACIV wind tunnel. Further thanks go to the staff of the Institute of Steel Structures of Braunschweig for their warm hospitality during the winter nine months spent in Germany and for many fruitful scientific discussions and suggestions. Finally I would like to express deep gratitude to Prof. Antonio Miguel from University of Évora, for his useful remarks, encouragement and exchange of ideas especially in the fields of porous media and fluid mechanics. Last but not least, I am grateful to MEVACO Srl (Italia) and in particular to Mr. Walter Cembran, for providing porous materials without whom this work would not have been possible.

List of Figures

List of Tables

Contents

Chapter 1

Introduction

1.1 Natural hazard and disasters

Natural hazard events such as earthquakes, volcanic eruptions, hurricanes, landslides, floods, droughts and wildfires are commonly known as natural disasters. They refer specifically to those events in which impacts exceed local or national capacity to resist to them, thus requiring outside emergency assistance.

Since the 1960s, natural disasters worldwide have more than tripled and economic losses have increased more than eight times (Munich Re, 2001). Factors that explain the dramatic increase in disaster events and economic losses include: rapid and poorly controlled urbanization; widespread rural and urban poverty; ineffective public policy; increasing construction of infrastructures in hazard-prone areas. At the same time, the death toll has been halved owing to decades of international technical assistance giving priority to disaster rescue, relief, and more recently, preparedness.

Until the 1970s, the international community has considered disasters as exceptional circumstances, and the term *disaster management* typically referred to the remedial actions as response to their occurrence. Disasters were almost the exclusive domain of civil defence institutions, the Red Cross and Red Crescent Societies, and private voluntary organizations. However, in the 1970s and 1980s, the preparedness need and the relationship between development and disasters became more clearly defined. By the time the Declaration of Yokohama at the United Nations World Conference on Disaster Reduction was launched in 1994, it was widely recognized in the Americas that disaster impacts were mostly due to failed development approaches. The United Nations raised the profile of natural disasters by declaring the 1990s to be the International Decade of Natural Disaster Reduction. However, for the most part, national policies for natural hazard risk mitigation were not in place and vulnerability reduction was limited. A number of catastrophic events affecting the poor nations of the world in quick succession served as stark reminders of the urgency of addressing to disaster risk. These events permanently changed the perception that emergency preparedness and post-disaster response (which addresses only to effects, not causes) constituted an adequate approach.

Today risk management consists of both a post-disaster phase (emergency response, rehabilitation and reconstruction) and a pre-event phase including: risk identification, risk reduction, risk transfer, and preparedness. Each step involves tools, like hazard, vulnerability, and risk assessments, which aid decision-makers in selecting suitable measures and solutions. Such measures contain insurance and pooled risk arrangements, strengthening of early warning systems, and incorporating natural hazard risk management into: zoning and land-use planning; national and sector policies; engineering standards and codes relating to prevalent natural hazards.

Some countries are modernizing national disaster institutions. Others are revising legal frameworks and organizing or joining regional institutions for coordination and prevention of disasters. Still others are beginning to address long-standing structural obstacles to improve risk management, including: the low use of appropriate risk information by decision-makers; the minimal involvement of private sector in prevention and risk management; political paralysis to integrate prevention and mitigation; and the weak overall technical and operational capacity of disaster risk management institutions (Clarke and Caroline, 2000). Such efforts are critical for protecting vulnerable populations, safeguarding infrastructure, bolstering national security and shielding valuable economic assets from devastation.

1.2 Risk definitions

Risk and uncertainty are fundamental elements of human life, affecting every aspect of society and world events. They must be managed effectively to protect people from injury and to let society develop and progress. Today risk and uncertainty are frequently magnified in large scale in various areas of application including medical science, finance and business, insurance industry, all sectors of engineering and natural disaster. Natural disasters such as floods, earthquakes, wind storms, fires are the disruptive catastrophes that occurred worldwide in the last years.

Risk is often defined as a measure of probability and severity of adverse effects (Lowrance, 1976). Although an increasing number of managers in industry, government and academia are devoting a larger portion of their time and resources to improve the risk definition, it is still not possible to have an unequivocal definition. Today a lot of risk definitions exist, with similar principles and connotations, used to evaluate and estimate the risk. The results are strange and incomparable because those definitions are not standardized and there is not a general language of communication. The most important cornerstones have been made by two international codes published by International Organization for Standardization (ISO). The first one is the ISO73 (2009) which gives a basic definition of risk management and vocabulary and the second one is the ISO31000 (2009) that explains the principles and guidelines of risk management. Pliefke *et al.* (2007) turned out the wide range of risk definitions existing in literature and summarized the six principal classes that can be used. Here below is provided a list of widespread definitions:

$$Risk = Probability \cdot Consequences \tag{1.1}$$

$$Risk = Probability \cdot Loss \tag{1.2}$$

$$Risk = Probability \cdot Damage \tag{1.3}$$

$$Risk = Hazard \cdot Vulnerability \cdot Exposure \cdot Consequences \tag{1.4}$$

$$Risk = Hazard \cdot Vulnerability \cdot Exposure \tag{1.5}$$

$$Risk = Hazard \cdot Vulnerability \tag{1.6}$$

Each of those terms contains many parameters and aspects of different nature. Many attempts have been made for their definition, and many others still have to be completed. The previous formulas are the most important risk definitions, but they differ a lot because of the various meanings of the terms hazard, vulnerability, exposure, consequences, loss and damage. In order to have a common vocabulary it is necessary to give a standardized definition for every kind of variables that are involved in the risk definition. Following the instructions given by the new ISO73 (2009) Guide, it is possible to define each term of the risk equation. *Risk* is defined as the effect of uncertainty on objectives. The change in definition shifts the emphasis from the event (*something happens*) to the effect and, in particular, the effect on objectives. In the past, risk has been seen only as a negative concept that organizations should try to avoid or transfer to others. However it is now recognized that risk is simply a fact of life and cannot be avoided or denied. If the general variables involved in the risk definition are known, it is possible to change and control risk (*risk treatment*); thanks to this evaluation the risk management can be very easily negotiated. The term *Hazard* defines the probability that a dangerous event occurs in a precise location. The *Vulnerability* is given by an ensemble of conditional probabilities that an event damages a certain element, and it measures the sensitivity of the element behaviour to that event. *Exposure* identifies the probability that the examined element is hit and damaged by external actions. Finally the so-called *Consequences* are related to the damage costs. As regards *Loss* and *Damage*, they are the results of risk analysis and can indicate the potential system vulnerability.

1.3 Risk management

A very important risk management framework is given by Pliefke *et al.* (2007) who built an innovative method of risk assessment based in compliance with AS/NZS-4360 (1999). The risk management framework is made up of three important phases: risk identification, risk assessment and risk treatment (Fig. 1.1). Risk identification involves the application of a systematic process to understand what could happen, how, when and why. Failure to employ a systematic process for risk identification can lead organizations to concentrate their attention on the *known* risks, and hence miss those that are *unknown* that may be treated inadequately. Risk identification should also identify the existing controls that aim to modify the consequences or their probability of occurrence. After having outlined the model domain and identified all possible hazards to the system, the risk assessment phase starts to operate, representing the first crucial step of the risk management framework.

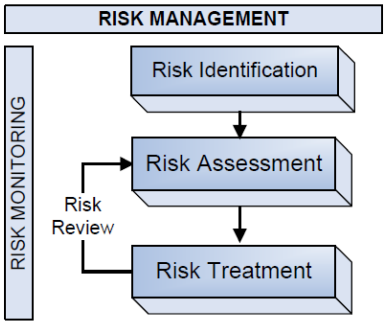

Fig. 1.1 The structure of risk management (Pliefke *et al.*, 2007).

The risk assessment itself consists of two sub-procedures, the risk analysis and the risk evaluation module, whose tasks are to be seen in quantifying the risk and comparing it to other competing risks (Fig. 1.2).

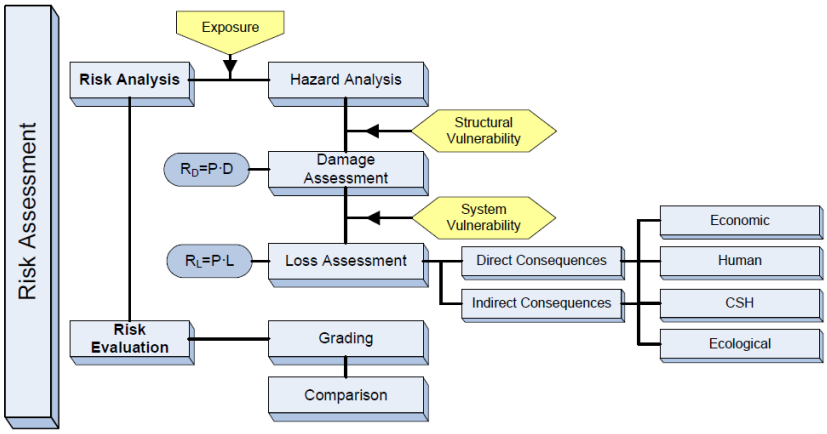

Fig. 1.2 The structure of risk assessment (Pliefke *et al.*, 2007).

The risk analysis represents the most complex and sophisticated part of risk management, because it is necessary to quantify the risk definition parameters and at the end the risk itself. If the exposure is known, the step forward is the development of hazard analysis, where it will be possible to identify the various risk parameters of the system in exam. After hazard evaluations, the hazard data are quantified and in relation with the system components which are exposed to the danger, it is possible to complete and calculate the damage and loss assessments. About the loss, it is necessary to distinguish between direct consequences, that occur at the same time of disaster, and the indirect consequences, that occur after the direct ones. In addition, each consequence class is further subdivided into tangible or economic consequences, that are directly measurable in monetary terms and intangible consequences, that are not directly appreciable such as injuries and fatalities, pollution of the environment and loss of cultural, social and historical values. Risk evaluation involves making a decision about the level or priority of each risk through the application of the criteria developed when the context was established. Risks are prioritized for attention and

cost benefit analysis is deployed to determine whether risk treatment is worthwhile.

Risk treatment is the process of selecting and implementing measures to modify the risk. It includes risk control-mitigation as its major element, but extends further to, for example, risk avoidance, risk transfer, risk financing, etc. Risk treatment normally involves activities that aim to change either the likelihood of the consequences or the type and magnitude of those consequences (Fig. 1.3).

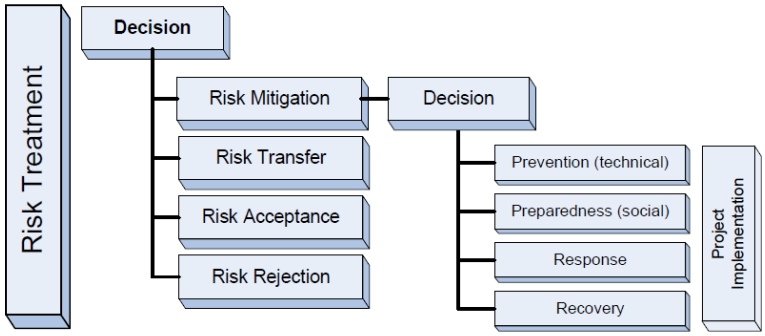

Fig. 1.3 The structure of risk treatment (Pliefke *et al.*, 2007).

1.4 Aeolian risk

The European global storm Kyrill in January 2007 was characterized by maximum measured wind speed over 225 km/h; it had as a consequence at least 44 direct casualties across Europe and 1000 million Euro total damage cost. This natural event confirmed the predictions according to which the warm winters in Europe are becoming more frequent, with a particularly high wind storm risk and associated economic losses and fatalities. In fact, Munich Re (2001), Augusti *et al.* (2001) and Gatzen *et al.* (2011) confirm the relevance of Aeolian risk and suggest the importance of new research in the field of wind engineering.

The closure of roads, bridges, viaducts and other wind-exposed structures for transportation of people and goods during high cross-winds has large and negative consequences, in terms of economic, human and social impacts. One example is the Croatian A1 highway between Zagreb and Split, with the most wind-sensitive location between the south entrance of Sveti Rok tunnel and Posedarje. In 2007 the A1 highway was closed for traffic of commercial vehicles, in order to safeguard the users, for 620 hours (25 days) in total (Juricko, 2008). Wind storms assume special interest for large commercial vehicles (trucks, lorries, vans) and passenger cars with trailers since they cause a significant number of accidents and fatalities on EU roads every year.

The occurrence of wind (speed and direction) depends on geographical conditions and cannot be generalized. In addition, the global and local climate changes are likely to increase both the strength and the frequency of wind storms in the most prone areas. It must be taken into consideration not only when road infrastructures are planned but also during the assessment of wind accidents.

In Germany westerly winds are predominant. According to Bitzel (1962), in the northern part of Germany, the duration of strong winds (6 to 7 Beaufort) is almost seven times higher than in the southern part, and stormy winds (min. 8 Beaufort) nine times higher (see Fig. 1.4a).

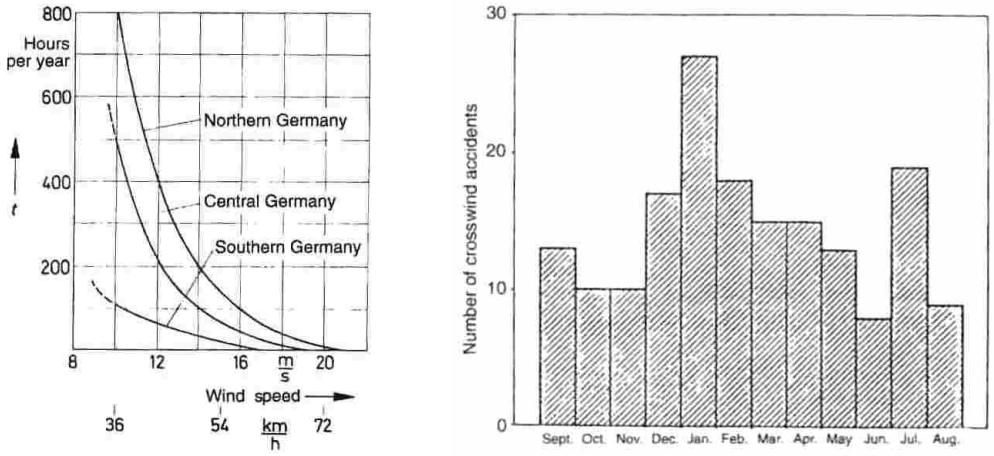

(a) Frequency of strong winds (b) Number of cross-wind accidents

Fig. 1.4 Strong wind data for Germany (1950-1959), by Bitzel (1962).

Especially during winter months, high winds stronger than 30 m/s can occur; in local storms and very gusty winds, speeds up to 50 m/s are often observed. Together with slippery road condition at this time of the year, the wind-caused accident rate increases, as shown by the statistics in Fig. 1.4b.

Regarding the risk framework introduced by Pliefke *et al.* (2007) and the problems induced by high cross-winds, it is useful to work in the part of risk framework called *Risk Treatment* (Fig. 1.3). In case of the overturning vehicles phenomenon it is fundamental to take *Decisions* and considering that the risk cannot be transferred nor rejected, it is necessary to work on the *Risk Mitigation* part.

(a) Preparedness (b) Prevention

Fig. 1.5 Risk mitigation measures.

Fig. 1.5 reports the most common measures of mitigation that are currently adopted to face the risk of cross-wind accidents. In particular it is possible to work on *Preparedness*, in order to make the user aware of the problem, by the use of luminous warning signs (Fig. 1.5a) or on *Prevention* through the introduction of suitable windbreak barriers (Fig. 1.5b).

The risk of overturning vehicles or closure of a given road infrastructure can be estimated using a risk relation as the equation (1.6). In this manner the *Risk* can be simply estimated by the product between the *Hazard* and the *Vulnerability*. In order to have a schematic view of the present research work Fig. 1.6 reports a conceptual map which briefly summarizes all the steps that will be used to quantify the risk.

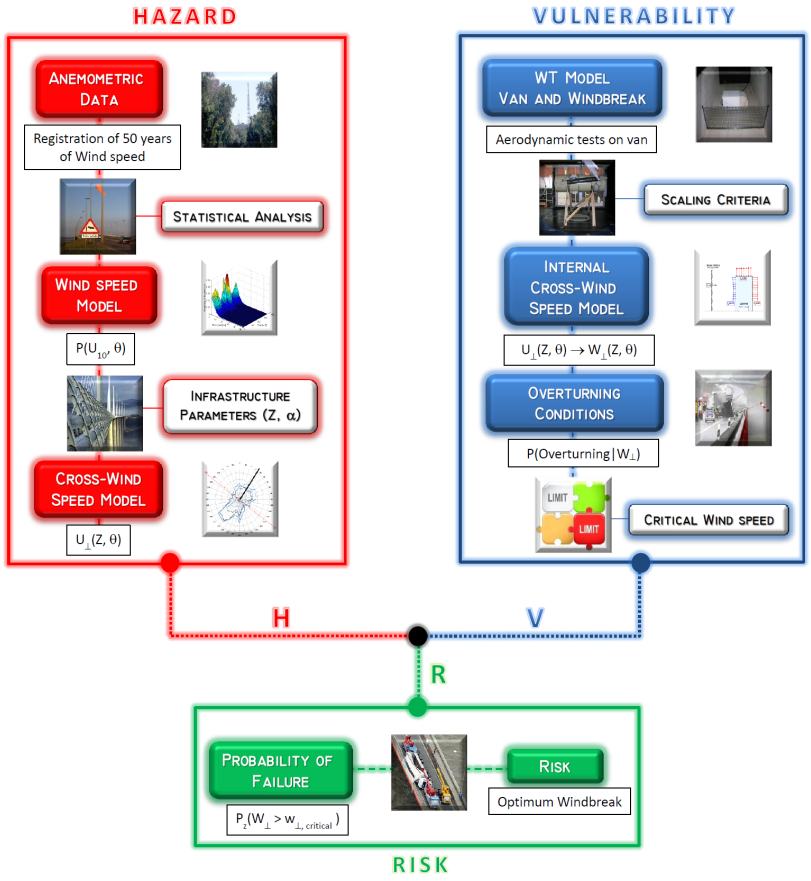

Fig. 1.6 Conceptual map of risk analysis.

In the hazard analysis a probabilistic model for external cross-wind speed is derived starting from historical records of wind speed and the definition of a reference infrastructure (road viaduct). Inside the vulnerability part several steps are collected, such as: wind tunnel model, scaling criteria, internal cross-wind speed model and overturning conditions for a given mean of transportation (Luton van). Knowing the scaling criteria for the wind tunnel simulation of porous elements, and respecting them on an appropriate wind tunnel model of the van positioned downstream of different porous barriers, it is possible to estimate an apparent internal cross-wind

speed. Using the internal cross-wind speed and the overturning conditions (*i.e. the critical overturning wind speed*), the probability of failure can be estimated, in function of different levels of shelter. The risk is expressed in terms of average number of hours in a year in which the reference infrastructure is expected to be closed in order to avoid roll-over phenomena.

1.5 Contributions and outline of the research work

This doctoral work deals with the strategies of mitigation of high cross-winds on road infrastructures in order to minimize the risk of overturning for large commercial vehicles through the introduction of porous wind fences. This aspect is nowadays recognized as a key issue in the design of several road infrastructures due to the high number of accidents and fatalities that happen on European routes every year. The contribution of this thesis is two-fold. Firstly, it aims to define a comprehensive scaling procedure that can be used when wind tunnel tests on porous structures are required. Secondly, it aims to quantify the risk associated with the overturning of high-sided vehicles for different levels of shelter.

The present dissertation is composed by nine chapters: two of them (Chapters 2 and 3) represent the literature review and the remaining chapters report the original contribute of the research. In this Chapter after a brief overview on natural hazard and risk management the reference Aeolian risk is introduced and discussed.

In Chapter 2, a short review of the principal wind actions on the users of civil engineering infrastructures is presented. More in detail the wind-effects on road and rail vehicles, as well as on pedestrians, are discussed.

In Chapter 3, an accurate review of the literature about the flow through porous screens and windbreak barriers is reported. In particular, the analysis of the state-of-the-art is conducted following two different methodologies: the flow through the porous media approach and the hydraulic resistance one.

In Chapter 4, the problems that are encountered in wind tunnel modelling of porous elements are shown. After a general outline of dimensional analysis, the failure of the geometric scaling procedure is shown.

In Chapters 5 and 6, the research of an innovative scaling procedure for porous elements is performed with the help of two experimental campaigns in the wind tunnel. Several tests on porous materials, represented by perforated plates, are carried out in two different flow configurations: confined and unconfined case.

In Chapter 7, wind tunnel tests were performed on a stationary high-sided commercial vehicle (Luton van) positioned downstream of several typologies of porous wind screens, in order to quantify the aerodynamic loads.

In Chapter 8, a simple risk procedure is developed. After an accurate identification of the hazard (cross-wind speed model) and the relative vulnerability of the system (van placed downstream of a windbreak in a windy site) the risk of overturning is quantified and minimized.

In Chapter 9, the final conclusions of the dissertation and its future outlook are summarized.

Chapter 2

Wind effects on the users of infrastructures

2.1 Introduction

Over the past twenty years considerable interest has been devoted to the provision of wind shielding on major bridges and footbridges. In order to protect their users from wind action, it is often necessary to use properly designed windbreak shields, both in case of bridges (where vehicles are intended to be safeguarded) and in case of footbridges (where pedestrians have to be protected). This interest is the consequence not only of economic losses due to the bridge closure in high wind condition but also of the risk of injury from overturning vehicles and from falling to the ground of pedestrians.

Whilst the effects of wind on a bridge structure have been extensively studied, this is not the case for the effects of the wind on the bridge users. No guidance is presently available on the optimum shape of barriers or fences to minimize wind effects. At present time, there are only few studies about wind comfort in urban and sport fields [Ratcliff and Peterka (1990) and Koss (2006)] but there are no contributions on pedestrian comfort on footbridges or vehicular comfort on bridges.

The sensitivity to these new issues has significantly increased in the last few years, so that many new interventions have been completed on existing structures. Clearly a 4 m high solid barrier would protect vehicles but would also be very expensive and have at the same time important consequences on the aerodynamics of the bridge. However to be balanced against its cost, there are considerable social, political, and financial benefits that can result from a crossing that can remain open in extreme weather conditions. Consequently the provision of full wind shielding on major bridges is becoming always more frequent. The Second Severn Crossing in United Kingdom has proved that such crossing can be successful. Alternatively enclosed bridges have been designed such as the Lantau Crossing in Honk Kong (*Kap Shui Mun bridge*) with a top open deck for traffic under normal conditions. In these cases, it is necessary to consider the increase of the wind action which bridge decks have to bear. The improvements have been made on structures already in service, therefore they had not been planned during the bridge design phase; consequently nor the loadings induced by these new works had been considered before.

The wind loading process on a bridge is determined by the topology of the flow around its cross-section, which includes several aspects (vortex shedding, separation and reattachment of the flow, characteristics of the wake downstream of the body). Long-span bridge cross-sectional geometry is typically outlined to optimize the aerodynamic performance of the overall structure, but a number of non-structural elements, such as railings, parapets, crash barriers and wind screens, are always necessary on a bridge deck, changing its initial aerodynamic shape [Jones *et al.* (1995); Ricciardelli *et al.* (2002); Ricciardelli (2003); Kleinhanss *et al.* (2007)]. This permanent alteration of the overall layout has a strong influence on the flow pattern around the bridge deck and consequently on the wind-induced loading process of the structure. It should be noticed that bridges without shields give a better aerodynamic response of the structure towards wind action, but they are also less comfortable for the users [Honda *et al.* (1992); Chen and Kareem (2003); Allori and Nuti (2008); Geyer (2008)]. Therefore it should be defined the best configuration of shields to be introduced on bridges in order to optimize both issues: the main one related to users comfort and the purely aerodynamic one. An additional criticism about crossings which have continuous barriers is that the pleasure of crossing is impaired because the view is obscured. However this topic carries little weight with regular road users who often witness accidents due to drivers who admire the view instead of watching the road.

The difficulties in cycling or driving in windy conditions are well known. Instinctively there is concern about driving on exposed roads or crossing high bridges and anyone who has driven on a highway in windy conditions will be aware of the difficulties that can occur when overtaking high-sided vehicles. There has been considerable research into the effect of wind loads on moving vehicles but in spite of this it is still claimed that 2 % of accidents could be due to windy conditions.

The effects of wind on ground vehicles, such as lorries or trains and cars, can be broadly considered to be of two types: low wind speed effects, such as drag coefficient increase in cross-winds and vehicle aerodynamic stability considerations and high wind speed effects. The overturning of road and rail vehicles due to high winds is very important. Every year in Europe there is a significant number of road accidents due to overturning vehicles, with consequent injury and traffic disruption (Fig. 2.1).

Fig. 2.1 Wind-induced accidents on road infrastructures.

Such accidents mainly happen in conditions of extreme wind velocities, but they also can occur at wind speeds with a sub-annual return period. For example in the January 25^{th} storm in 1990 in the United Kingdom, there were around 300 road vehicle accidents, in which death or injury occurred, that could be directly attributed to the moderate wind conditions (Baker and Reynolds, 1992). News reports of vehicles overturned by wind are numerous, however experience has now shown that a surprising number of seemingly minor accidents due to wind initiate traffic jams and can result in long delays at major crossing. Such accidents can therefore significantly increase the probability of high loading through conditions of heavy traffic coincident with wind.

Drivers in general and couriers in particular are becoming less tolerant towards delays and bridge closures. Moreover for a long time the good road handling and high level of insulation of a modern car have been changing the perception of what acceptable weather conditions for travelling are.

2.2 Wind effects on ground vehicles

The mechanical evolution of mean of transportation, that led to the attainment of high velocity, forces the road designers to pay attention to the problems related to the vehicle mechanics and in particular to the interaction between the vehicle and the road. An important issue to be analysed during the design phase is the evaluation of the possible actions due to wind. When the wind is blowing frontally with respect to the vehicle, it mainly causes resistance to the motion, that can be solved with an increase of the power of the engine; by contrast if the vehicle is subject to a system of transversal forces it can face it only in a passive manner, through its propulsion stability components. In case of high cross-winds, the vehicle can undergo lateral displacements (only road vehicles) and problems of overturning that can cause accidents (road and rail vehicles). The changes of trajectory depend on the wind velocity and the vehicle velocity. As velocity and direction of the wind are random variables, during the study stage of a road track, especially with particular track elements (exit from tunnels, high viaducts) it is necessary to forecast a deep investigation about the actions on vehicles and to identify the limitations due to the wind action.

A comprehensive review of all the aerodynamic force and moment coefficients for ground vehicles in cross-winds has been completed by Baker (1991a). He identified the three forces and moments: drag force, side force and lift force; pitching moment, yawing moment and rolling moment (Fig. 2.2), which were dependent upon:

- the yaw angle ψ or β: defined as the apparent angle between the direction of travel and the wind vector related to the vehicle; this is function of the vehicle speed, wind speed and wind direction;

- the wind angle: the angle between the direction of travel of the vehicle and the wind vector related to the ground;

- the Reynolds number, conventionally based upon the wind speed related to the vehicle and the vehicle height;

- the characteristics of the wind: velocity profile, turbulence intensity, turbulence intensity profile, turbulence length scale profile.

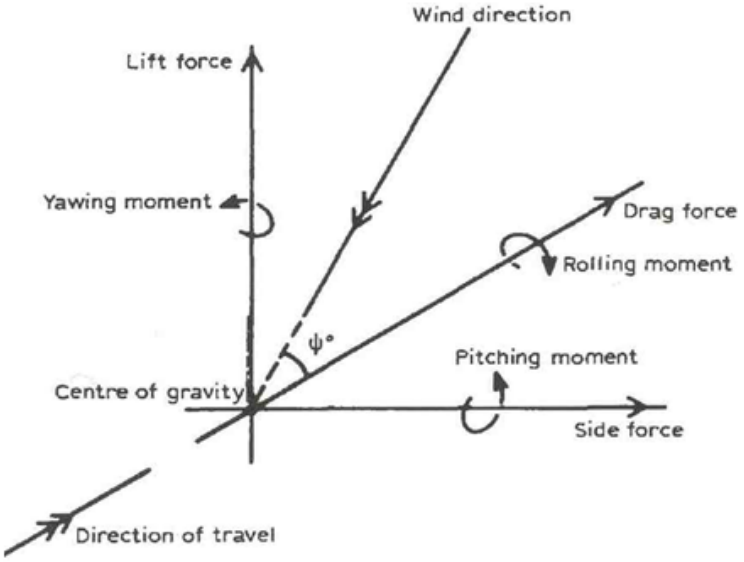

Fig. 2.2 Sign convention for forces and moments (Baker, 1991a).

Now there are two methods to obtain these aerodynamic data: the use of Computational Fluid Dynamics (CFD) and the use of wind tunnel tests (Sterling *et al.*, 2010). The paper by Matschke and Heine (2002) describes the results of a recent comparison between full scale, model scale and wind tunnel measurements to determine the cross-wind forces on a high speed train. This investigation shows that for the complex vehicle geometries and unsteady flow patterns, the uncertainty involved in the use of different grid generation techniques, turbulence models etc, together with excessively long run times for convergence, makes the use of CFD techniques unsuitable for routine calculations of the effects of cross-wind forces.

2.2.1 Rail vehicles

The nature of the flow around long, high-speed passenger trains in cross-winds has been investigated by a number of experimenters and it is well established for an idealized train shape [Mair and Stewart (1985); Copley (1987); Robinson (1987)] and for the British APT (Cooper, 1979). The typical flow field sketched in Fig. 2.3 exists for yaw angles less than about 40° or 50°. The wake flow consists of a system of inclined trailing vortices, similar to those found in missile wakes.

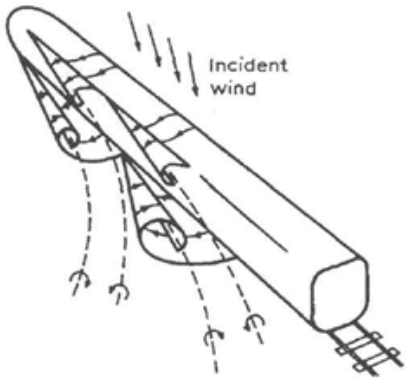

Fig. 2.3 Flow around high-speed trains in cross-wind (Cooper, 1979).

These vortices form themselves from the rolling up of the separated shear layers in the lee of the model to form ground-side and roof-side vortices which move away from the vehicle as the distance from the nose increases. The ground-side vortex moves away more rapidly, under the action of its relatively close image in the ground plane. These vortices eventually detach and are replaced by new vortices close to the train body.

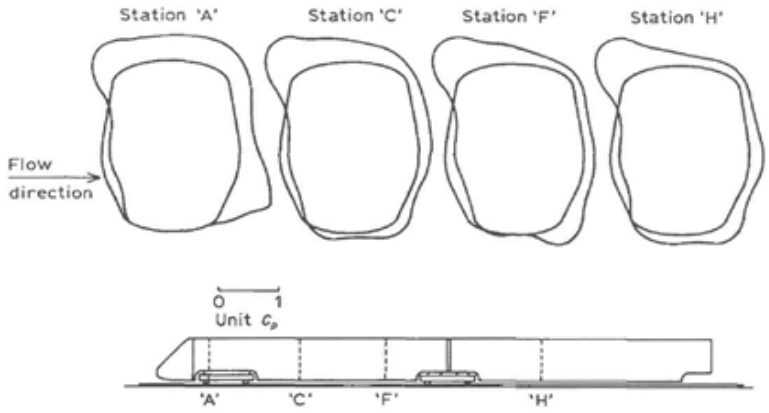

Fig. 2.4 The pressure distribution around a British APT train, with $\Psi = 20°$ (Cooper, 1979).

Fig. 2.4 shows the pressure contours around the body produced by such a flow pattern for the APT train. It can be seen that there is a substantial suction peak at the windward roof corner, caused by the speed-up of flow at that point, and a fairly uniform lee side pressure. Around the nose one would also expect a large suction peak due to flow acceleration in both horizontal and vertical directions.

In order to have a broad view of the problem, it is necessary to characterize the aerodynamic forces and moments on high-speed trains. For this kind of vehicles the most important parameters of practical interest are the side force coefficient (C_S), the lift force coefficient (C_L) and the rolling moment coefficient about the lee rail (C_{RL}). These aerodynamic coefficients can be defined as follows:

$$
\begin{aligned}
C_S &= \frac{F_S}{\frac{1}{2} \cdot \rho \cdot U^2 \cdot A_S} \\
C_L &= \frac{F_L}{\frac{1}{2} \cdot \rho \cdot U^2 \cdot A_L} \\
C_{RL} &= \frac{M_{RL}}{\frac{1}{2} \cdot \rho \cdot U^2 \cdot A_L \cdot H}
\end{aligned}
\tag{2.1}
$$

where: F_S is the side force, F_L is the lift force and M_{RL} is the overturning moment respect to the leeward rail due to the wind actions on the train; ρ is the mass density of air; U is the undisturbed flow velocity; A_S is the side area, A_L is the lift area and H the reference height of the train.

Fig. 2.5 shows these data for the leading car of the APT train obtained from static, low turbulence wind tunnel tests, for scales between $1/5^{th}$ and $1/50^{th}$ [Cooper (1978); Cooper (1982); Baker *et al.* (1985)]. In spite of the large variation in scale, these results agree with each other. Two different regimes can be distinguished, corresponding to the high and low yaw angle flows, with a steady increase in C_S, C_L and C_{RL} up to about $\Psi = 50°$, followed by a levelling off or decrease in the coefficients above this value.

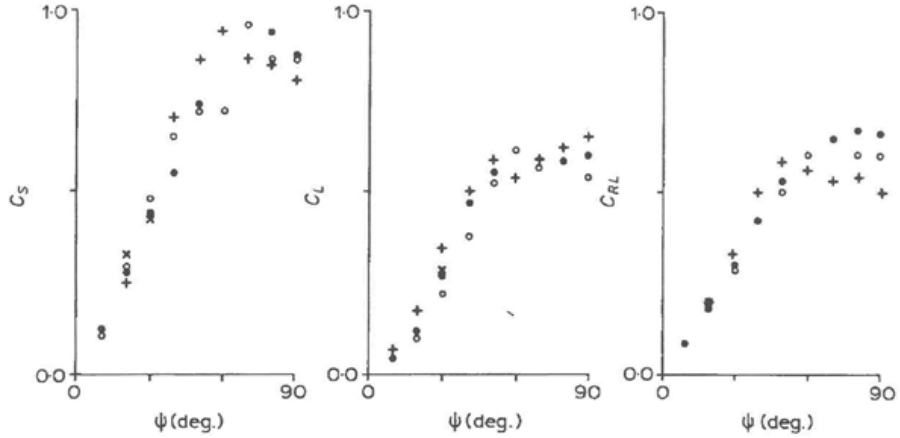

Fig. 2.5 Force and moment coefficient data on British APT (high speed train). + $1/5^{th}$ scale, • $1/35^{th}$ scale and ∘ $1/50^{th}$ scale (Baker, 1991a).

In general, there are two differences between high-speed and low-speed passenger trains, as the former are usually around 200 m long with a streamlined nose, while the latter are usually much shorter (40 ÷ 100 m) with rather blunt noses. Thus one might expect the flow patterns around such vehicles to be rather different from each other. The flow field around a short, blunt-ended passenger train has been investigated by Coleman and Baker (1990). In many ways the flow field is similar to the one for high-speed trains. At low yaw angles, surface flow visualization and wake velocity spectral measurements reveal a vortex shedding wake as it would be expected. The major difference from the high-speed train case seems to be around the vehicle nose, where the blunt end produces a large flow separation region in

the lee that, in mid-yaw angle range, can extend over a considerable length of the vehicle. The results for this kind of trains are shown in Fig. 2.6. It can be seen that for $\Psi < 40°$, the results are close to the corresponding high-speed trains force and moment coefficient data (Fig. 2.5).

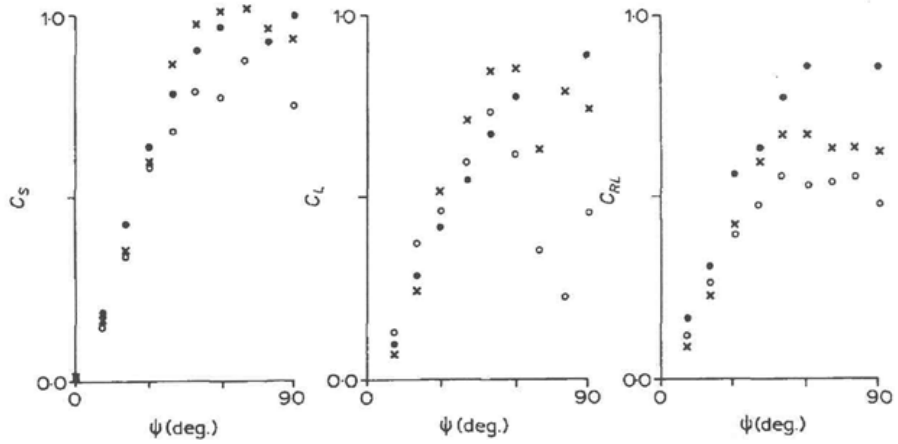

Fig. 2.6 Force and moment coefficient data on British Rail Class 141 (low speed train). + $1/5^{th}$ scale, • $1/35^{th}$ scale and ∘ $1/50^{th}$ scale (Baker, 1991a).

The basic criterion for rail overturning vehicle (Fig. 2.7) is very simple: the reaction at the windward wheels should fall to zero.

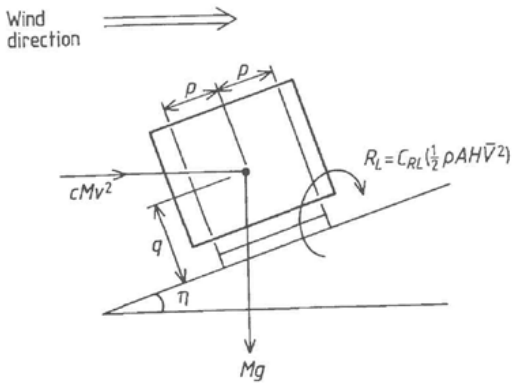

Fig. 2.7 The overturning train condition (Baker, 1991b).

From the Fig. 2.7, taking moments about the lee rail, it can be written:

$$C_{RL}(\frac{1}{2}\rho A\overline{V}^2 H) + cMv^2(q\cos\eta - p\sin\eta) = Mg(p\cos\eta + q\sin\eta) \qquad (2.2)$$

where: C_{RL} is the rolling moment coefficient that is function of yaw angle Ψ; A is the reference area; ρ is the mass density of the air; $\overline{V}$ is the wind speed related to moving vehicle; H is the vehicle height; c is the track curvature; v is the vehicle speed; q is the distance from the ground of the vehicle centre of gravity; η is the

cant of the railways track; p is the rail semi-axle length; M is the vehicle mass and g is the gravity acceleration.

Introducing in the previous equation the relationship between $\overline{V}$ and the wind direction (β) it is possible to evaluate the corresponding critical wind speed for each wind direction and to build a graph that relates it with the wind direction. It can be seen from Fig. 2.8 that the overturning wind speed, $U_A(\beta)$, reaches a minimum for $\beta \approx 70 \div 80°$ and steeply rises as β decreases or increases. For typical modern high-speed trains, $U_A(\beta)$ takes values around $45 \div 50$ m/s.

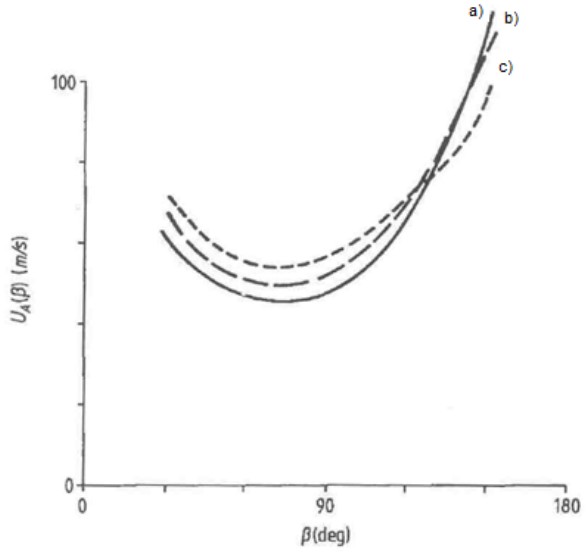

Fig. 2.8 Critical wind speeds for high-speed trains (η=0; c=∞)
a) v=65 m/s; b) v=50 m/s; c) v=35 m/s (Baker, 1991b).

2.2.2 Road vehicles

In order to assess wind-induced accident risk for road vehicles, rather more aerodynamic information is required than for rail vehicles, since the motion of these vehicles is not constrained by the running rails and aerodynamic yawing and pitching moments become important.

Coleman and Baker (1990) report detailed measurements of the flow field around an articulated lorry model with and without a turbulence simulation. Surface flow visualization showed that the most striking features of the flow, for low yaw angles, were corner vortices from the cab and trailer front windward corners, similar to those observed on building roofs. These vortices were very sensitive to parameters such as vehicle chamber and also to whether or not atmospheric turbulence was simulated. At high yaw angles again spectral measurements indicated the presence of a vortex-shedding wake.

A typical pressure distribution around a car is shown in Fig. 2.9 by Emmelmann (1987) for yaw angles (Ψ) of 0° and 15°. The pressure is represented by the pressure coefficient defined as $C_p = 2P/\rho U^2$, where P is the pressure. A large suction peak can be seen on the lee side of the vehicle for the cross-wind case, which can create vehicle stability problems.

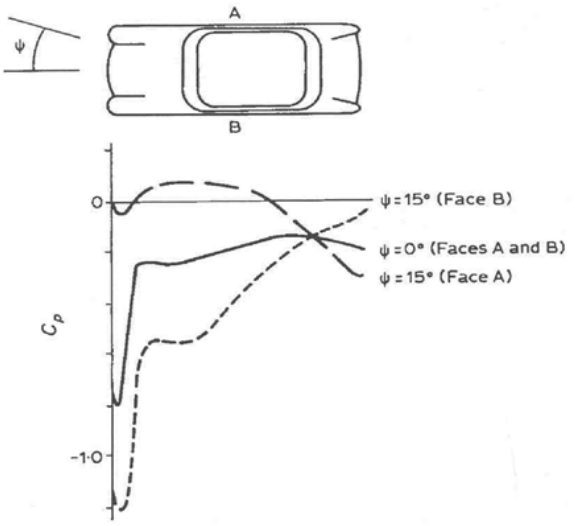

Fig. 2.9 Pressure distribution around a car at $\Psi = 0°$ and $15°$ (Emmelmann, 1987).

Force and moment coefficients[1] (Fig. 2.10) for a square-back car have been measured by many researchers with wind tunnel tests, but the pioneers of the work are Takanami *et al.* (1976) and Emmelmann (1987).

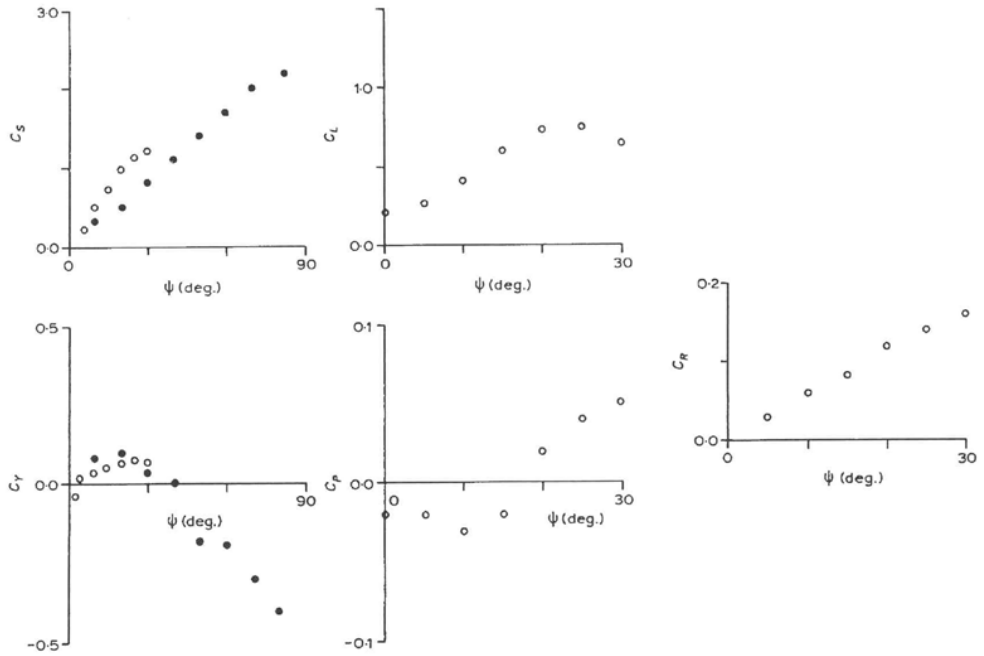

Fig. 2.10 Square-back car force and moment coefficients.
• Takanami *et al.* (1976) and ∘ Emmelmann (1987); (Baker, 1991a)

.

[1] C_S side force coefficient; C_L lift force coefficient; C_Y yawing moment coefficient; C_P pitching moment coefficient; C_R rolling moment coefficient.

If the yaw angle increases, the side force coefficient C_S steps up and the yawing moment coefficient C_Y seems to show a positive peak at $\Psi \approx 20 \div 30°$ and then falls to a negative value at higher values of Ψ.

The specification of aerodynamic forces and moments for vehicle overturning calculations is far from being straightforward. Firstly, it is necessary to evaluate the duration in time of a gust wind speed to blow a train over. For rail vehicles, both Cooper (1979) and Surrey *et al.* (1988) report dynamic calculations that suggest wind gust duration between 1.0 and 3.0 s and magnitudes just greater than the critical magnitude required for a vehicle overturning. For road vehicles, which are in general rather smaller and lighter than rail vehicles, gust duration is expected to be around 0.5 to 1.0 s. In fact, wind-induced road vehicles accidents occur at significantly lower wind speeds than for rail vehicles.

In reference to road vehicles, there are two principal types of accident: those related to course deviation of the vehicle (*side-slip*) and those due to actual overturning (Fig. 2.11). The calculation of the vehicle course deviation is very complex, because it is necessary to know the force time histories of the wind, the aerodynamic coefficients and the probabilistic model related to the driver response.

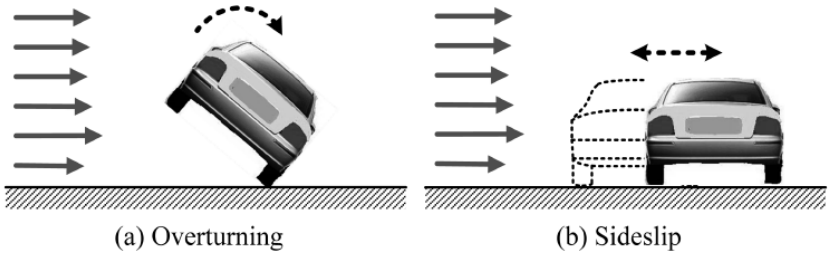

Fig. 2.11 Vehicle accidents in cross-wind (Kwon *et al.*, 2011).

The problem of vehicle overturning was studied more deeply by Baker *et al.* (1985) and Coleman and Baker (1990) who wrote the six equations of motion for a single mass, four wheel road vehicle under the action of the aerodynamic, tyre, body and motive forces, together with a compatibility condition for the displacements. In general the assessment of accident risk begins with some sort of mechanical model of the vehicle, which takes into account tyre and suspension dynamics, and with a model for the wind speed. Aerodynamic force and moment coefficients from wind tunnel tests are used in this approach, and sometimes a model of driver behaviour is also used. Then, it can be used to predict overturning wind speed for a variety of vehicle speeds and wind directions.

Studies of vehicle behaviour on bridges have shown that stability problems are relatively insensitive to the wind direction. This is illustrated by the results of some early static tests performed at Cranfield University on both stationary and moving bluff vehicles (Fig. 2.12). In fact, it can be seen that the overturning moment increases with wind speed and incidence as one might expect but that very significant lateral overturning could occur even when the wind blows at 15° with respect to the bridge deck axis.

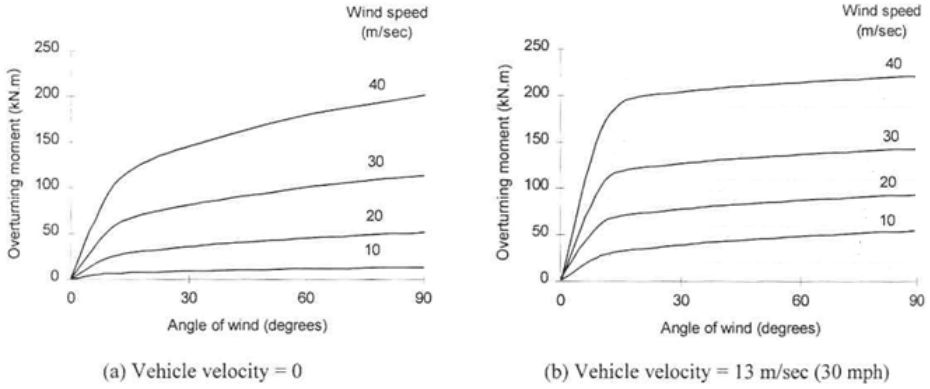

Fig. 2.12 Overturning moment on high-sided vehicles versus wind angle (Smith and Barker, 1998).

Fig. 2.12 shows that the overturning moment grows following two different linear trends. The first one is more pronounced and occurs for angles of wind in the range $0° \div 15°$, the second is less marked and takes place for wind directions from 15° to 90°. In addition, the diagrams highlight that both in case of stationary and moving vehicle the overturning moment is maximum for an angle of wind equal to 90°. This aspect confirms that when the wind blows perpendicularly to the longitudinal axis of the vehicle, the possibility to observe a roll-over is maximum.

The overturning cross-wind speed can be simply calculated from the following equation by Carr *et al.* (1993):

$$V_{over} = \sqrt{\frac{2Mg}{\rho A(C_L + 2C_{RM}l/t)}} \tag{2.3}$$

where: l is the wheel base, t is the mean wheel tread, ρ is air density, A is the vehicle frontal projected area, M is vehicle mass, g is gravity acceleration, C_L is the lift coefficient, C_{RM} is the rolling moment coefficient.

Carr *et al.* (1993) have carried out studies to identify vehicles which are particularly subject to overturning risk in cross-winds. Their results were obtained combining the aerodynamic effects of the high-sided vehicles, evaluated by wind tunnel tests, with the mechanical model of the vehicle dynamics (tyres, suspension, etc.). Fig. 2.13 shows the relationship between the vehicle speed and the critical cross-wind speed[2] for different high-sided vehicles, which are relatively more sensitive to overturning compared with small passenger cars. The graph also confirms that the overturning wind speeds for high-sided vehicles, except for the Luton van, are over 25 m/s at vehicle speed of 90 km/h, which is the speed limit of trucks on European highways.

[2]The critical cross-wind speed reported by Carr *et al.* (1993) in Fig. 2.13 is the orthogonal component of the wind speed with respect to the longitudinal axis of the vehicle.

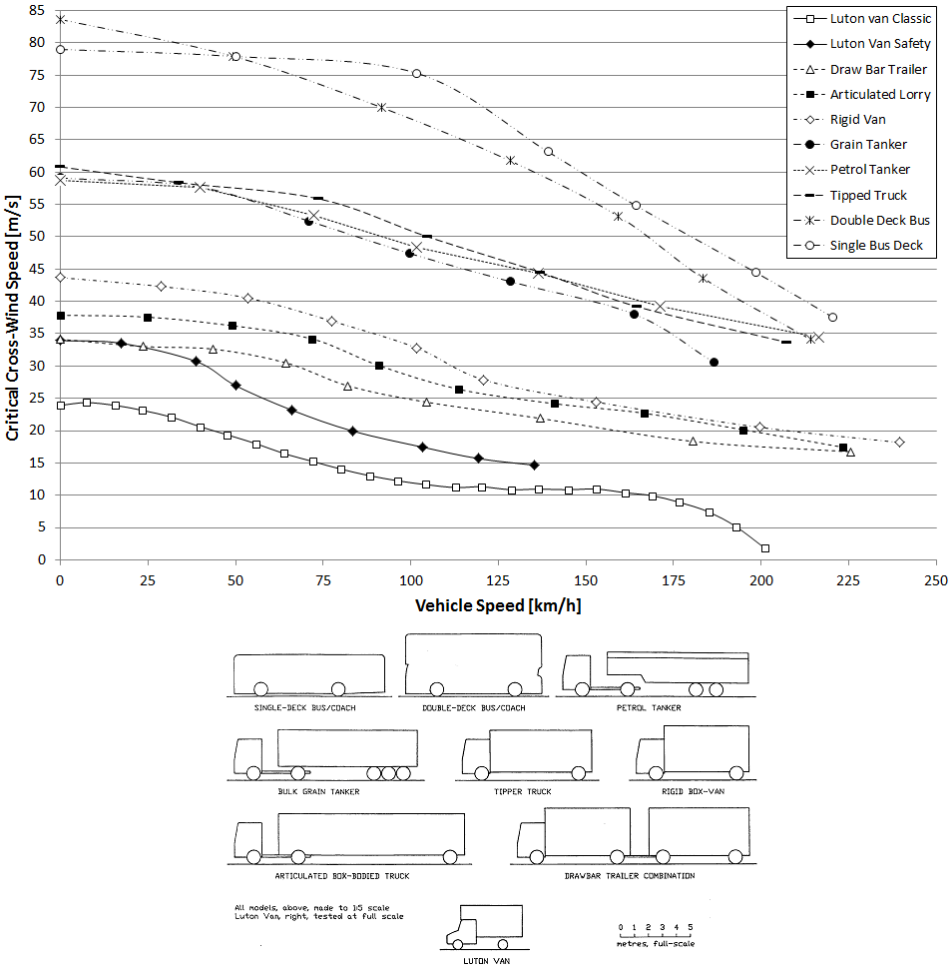

Fig. 2.13 Critical cross-wind speed for different high-sided vehicles (Carr *et al.*, 1993).

Although aerodynamic studies can enable the engineer to understand the factors that influence vehicle stability and the problems that might occur as a result, it is difficult to imagine how such studies could be used to prevent problems with empty, light bodies, bluff caravans and trailers, or prevent accidents caused by losing loads. As far as the form of the vehicle is concerned, manufactures have concentrated their efforts on reducing drag, with little or no attention to wind effects. Indeed some of the skirts and wheel details that they have introduced to provide lower C_D values, may well be detrimental to cross-wind stability. Changes in vehicle design over the next half century are likely to be radical whereas a bridge designed today is expected to be operational for much longer period. Current trends towards lighter vehicle structures to maximise payloads may take vehicle handling in cross-wind more critical.

2.3 Wind effects on pedestrians

The earliest systematic work on the effects of wind was performed by Admiral Sir Francis Beaufort, whose scale of wind force, devised in 1806, is still in use today.

Originally designed to be used in the sea field, it has been extended and revised for estimating wind speeds on land, and is a particularly suitable starting point for the present discussion on forces on the human body. Table 2.1 lists Beaufort numbers, wind speed ranges and some descriptions.

Beaufort Number	**Speed [m/s]**	**Description of the effects on pedestrians**
0 ÷ 1	0 ÷ 1.5	Calm, no noticeable wind
2	1.6 ÷ 3.3	Wind felt on face
3	3.4 ÷ 5.4	Wind extend light flags
		Hair is disturbed
		Clothings flaps
4	5.5 ÷ 7.9	Raises dust, dry soil and loose paper
		Hair disarranged
5	8.0 ÷ 10.7	Force of wind felt on body
		Drifting snow becomes air-borne
		Limit of agreeable wind on land
6	10.8 ÷ 13.8	Umbrellas used with difficulty
		Hair blown straight
		Wind noise on ears unpleasant
		Wind-borne snow above head height
7	13.9 ÷ 17.1	Inconvenient felt when walking
8	17.2 ÷ 20.7	Generally impedes progress
		Great difficulty with balance in gusts
9	20.8 ÷ 24.4	People blown over by gust

Table 2.1 Summary of wind effects on pedestrians (Penwarden, 1973).

In order to compare these descriptions with other information it is important to know how the time scale and whether gusts or long-term average speeds are involved. The Beaufort scale (*BRF*) is not explicit on this point, but it seems that the speeds quoted are fairly long-term averages, perhaps over a period from 10 minutes to one hour. In order to develop Table 2.1, some observations were made using the wind tunnel of Building Research Station in 1972 (*BRS*). A few members of BRS staff were observed while standing and walking in the tunnel in a steady wind up to 7.5 m/s. Only objective assessments of mechanical effects were attempted because subjective reactions could be disturbed by factors such as fan noise, lighting and enclosure. At higher speeds some observations were made in the natural wind using a hand-held anemometer to measure average speeds over a few minutes. Further relevant information in the BRF scale comes from a study of soil erosion by Chepil (1945) and from the book on human physiology by Evans (1949).

The adverse effects of gust speeds around 20 m/s have been reported by Melbourne and Joubert (1971) in Australia, who have measured speeds near tall university building when people were struggling against high winds. They observed that with a wind gusting regularity up to 20 m/s everyone had a great difficulty with

balance, particularly when a gust caught them sideways. On separate occasions two girls were unbalanced to the extent that they came down onto their hands and knees; this was with a maximum gust of 23 m/s rising from 12 m/s in two to three seconds. The authors commented that a person can stand in a much higher steady velocity, but that it is the unexpected nature of the gust which takes people by surprise. The descriptions listed in Table 2.1 form a basis for assessing the effects of wind on pedestrians, and allow limits of acceptability to be suggested.

2.3.1 Wind actions on human body

The wind force on a stationary person depends on the dynamic pressure of the wind, the area of the body exposed to the wind and the drag coefficient of the body. This aerodynamic force can be calculated as follows:

$$F = \frac{1}{2}\rho u^2 \cdot A_p \cdot C_D \tag{2.4}$$

where: F is the drag wind force on the body; u is the wind speed; ρ is the mass density of the air; A_p is the projected area of the body normal to the wind and C_D is the drag coefficient of the human body.

The dynamic pressure is easily calculated, but the area and drag coefficient can only be determined experimentally. In experiments on three men walking on a treadmill inside a wind tunnel, Pugh (1971) measured the projected area A_p of the three subjects from photographs taken while they were walking, and also estimated their total surface area A_{Du}. His measurements showed that the ratio A_p/A_{Du} had the same value (0.31) for all subjects. Experiments made by Hoerner (1965) gave a value of 0.84 m^2 for the drag area (that is A_pC_D) and of 0.33 for the ratio A_p/A_{Du} that was quite close to the value obtained by Pugh (1971). The total surface area of a person can be found from the DuBois (1916) formula:

$$A_{Du} = 0.203 \cdot W^{0.425} \cdot h^{0.725} \tag{2.5}$$

where: W is the body weight and h is the height.

Then the frontal area of a walking person can be taken as $0.31 \cdot A_{Du}$. Considerable movement, as in running, will probably reduce the area exposed to the wind, as well as bending, turning sideways or leaning into the wind.

One of the most important works to understand the wind action on the human body has been developed by Penwarden *et al.* (1978). In the BRS wind tunnel the researchers positioned men and women standing, as per usual dressed, on an electronic and instrumented balance, in order to gain new information about the horizontal forces applied by the wind on pedestrians. The measurements on the people have been made following two types of conditions: people positioned facing to the wind and sideways to the wind, and in each case the respective areas A_F (*front*) and A_S (*side*), referring to the directions of the wind, were calculated. One of the aims of the experiments was to investigate whether the projected area of a person could be simply related to the total body area as calculated by the DuBois

formula (2.5). The relationship between the measured areas and the DuBois formula is shown in Fig. 2.14. As it is possible to notice, the ratios between the area facing to the wind A_F and the area sideways to the wind A_S respect to the area estimated from the DuBois formula A_{Du} show differences respectively of 6.7 % and 7.1 %. The difference is very small and to have an analogous result it is necessary to modify the exponents of DuBois formula from 0.425 to $0.2 \div 0.6$ and from 0.725 to $0.5 \div 1.25$. Since the results are comparable and given the uncertainties of the wind tunnel experiments, DuBois formula has been considered valid.

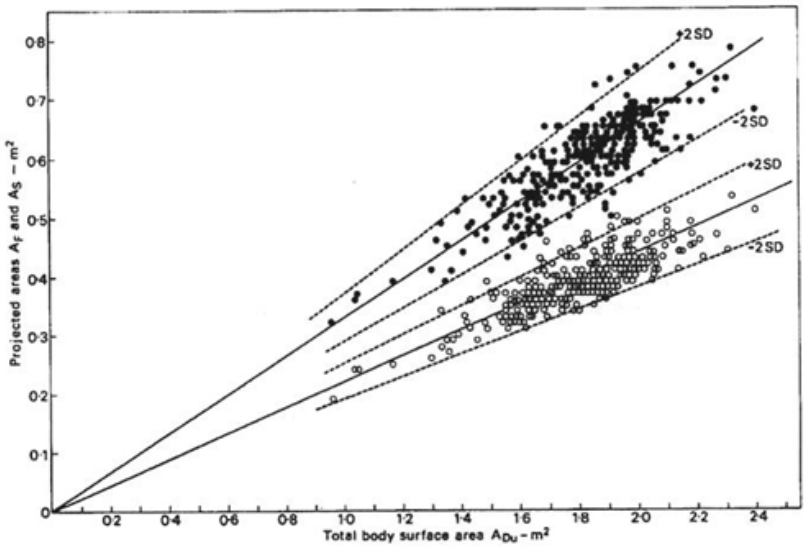

Fig. 2.14 Relation between the measured projected areas and the DuBois formula. • Facing to the wind A_F; ∘ Sideways to the wind A_S (Penwarden *et al.*, 1978).

The step forward of the analysis was to calculate the drag coefficients (Table 2.2) of the people as a function of the kind of clothing and the portion of body area directly invested by the wind.

Category	A_F/A_{Du}	A_S/A_{Du}	C_{DF}	C_{DS}
Skirt with shirt, sweater, buttoned jacket	0.30	0.21	1.08	0.95
Skirt with coat, open jacket	0.32	0.23	1.08	0.95
Trousers with shirt, sweater, buttoned jacket	0.32	0.22	1.17	1.01
As 3 carrying bag or clothing	0.35	0.23	1.17	1.01
Trousers with buttoned coat	0.35	0.24	1.17	1.01
Trousers with open coat	0.36	0.24	1.17	1.01
Trousers with jacket held open	0.34	0.22	1.23	1.06
Trousers with flapping coat, carrying clothes	0.35	0.26	1.33	1.12

Table 2.2 Summary of area ratios and drag coefficients (Penwarden *et al.*, 1978).

The values of the ratios A_F/A_{Du} and A_S/A_{Du}, that consider people invested by the wind respectively facing to the wind and sideways to the wind, have been

expressed depending on the type of the clothes. The former is in the interval between $0.30 \div 0.35$ and the latter in the range $0.21 \div 0.26$.

In Fig. 2.15 it is possible to observe a comparison between the wind force calculated with the analytic formula (2.4) and the wind force assessed by wind tunnel tests. Measurements related to people walking facing to the wind show values of forces larger than the ones faced by people walking sideways to the wind; this effect is due to the larger portion of area directly invested by the wind.

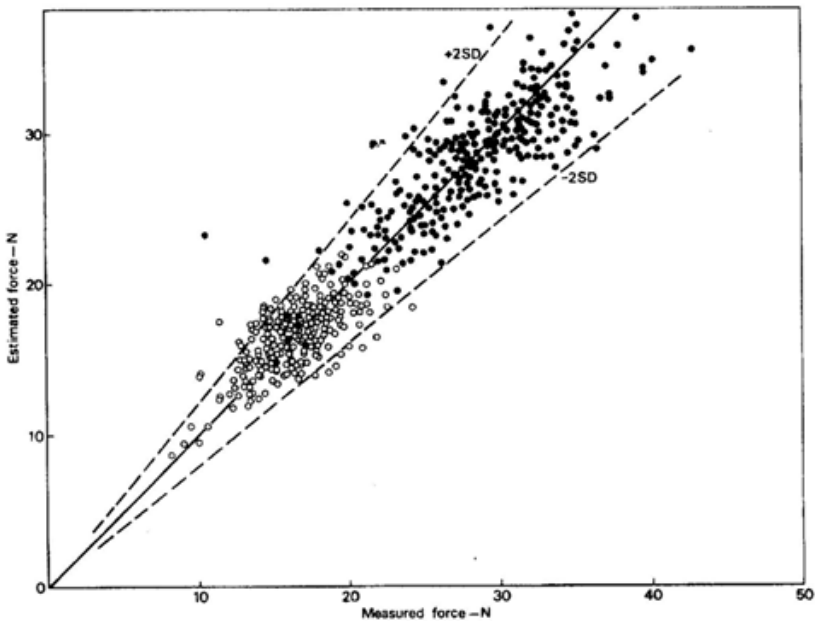

Fig. 2.15 Comparison between measured and estimated wind forces on pedestrians. • Facing to the wind A_F; ∘ Sideways to the wind A_S (Penwarden *et al.*, 1978).

Another important result of Penwarden *et al.* (1978) is directly linked to the differences between the forces measured and the ones calculated by the analytical formula. The measurements on people walking sideways to the wind highlighted double forces respect to the ones that are possible to obtain by analytic calculations. The authors suggest that this problem can be derived from natural deviations of walking pedestrian style when they are subject to high cross-wind forces. Moreover if considering a crowd of people in motion there is not only an increment of area A_p, as it can be easily expected, but also an increase of drag coefficient which is 40 % larger respect to the drag coefficient of one single person.

For a person standing in a steady wind, it is possible to define an angle θ of inclination of the walk due to wind effects, given by the equation:

$$tan\ \theta = \frac{wind\ force}{body\ weight} \tag{2.6}$$

As θ increases, the frontal area decreases and from equation (2.6) it is possible to create a graph which shows the variations of equilibrium angle θ with the wind speed for a standard man (Fig. 2.16).

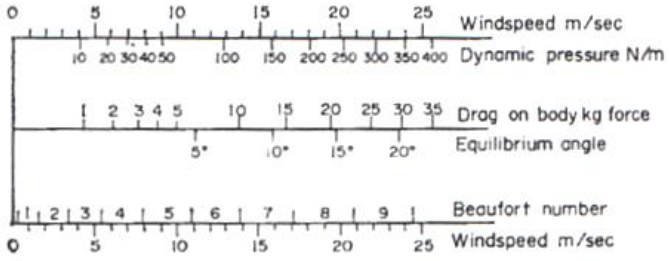

Fig. 2.16 Relationship between equilibrium angle and wind speed (Penwarden *et al.*, 1978).

A useful check on equation (2.6) is contained in a study made by Loewe (1972). It shows a man leaning into 45 m/s wind, in an area of Antarctic where extremely high speed winds blow steadily for hours. In this conditions it is possible to lean on 45 m/s wind so far forward that the hand can touch the ground. The equation above predicts an equilibrium angle of 45° for this wind speed. It agrees quite well with the average body angle, although the posture adopted to reduce wind drag makes comparison awkward. For example, an angle of 5° is unstable in the absence of wind, and is associated with a wind of about 10 m/s, a speed in which it is difficult to walk steadily. A full study of the mechanical effects of wind on a person would take into account the wind response of a person due to unsteady turbulent wind forces. Hunt and Poulton (1972) provide a basis for such a study and suggest that gusts having a duration of $0.1 \div 0.5$ s are likely to cause difficulty with balance.

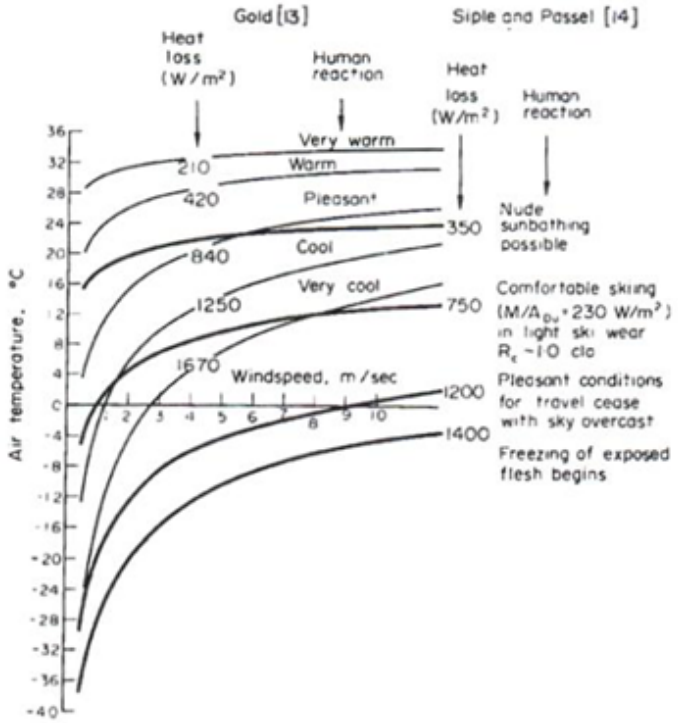

Fig. 2.17 Thermal effects of wind after Gold (1935) and Siple and Passel (1945) .

In addition to the mechanical effects described so far it is also necessary to consider the thermal ones. The heat balance of the human body and the related sensations of thermal comfort or discomfort have been studied for many years and there is a considerable volume of literature relating to indoor conditions. However the outside environment is much more variable and people are engaged in a wider range of activities, dressed with more varied clothing. As it is difficult to evaluate the comfort in open areas, there have been done few attempts of analysis; the most important studies in this sector have been performed by Gold (1935) and Siple and Passel (1945). They report the sensations of comfort or discomfort in terms of heat loss, measured by a thermometer with a silvered bulb, and build a relationship between the wind speed and the air temperature (Fig. 2.17).

2.3.2 Comfort criteria

It is generally agreed that the most appropriate approach to assess or predict human environmental wind comfort is the use of wind speed threshold values, defined for specific types or categories of pedestrian activities and/or particular areas, in combination with allowable frequencies of occurrence or exceedence and time duration. The main differences between the various methods are the number of defined pedestrian activities and areas and the definition of the corresponding threshold values given in terms of pedestrian limit wind speeds. Assuming a particular pedestrian activity, a limit wind speed of acceptable comfort u_{lim} has to be defined.

The general criteria assessing whether the investigated location fulfils the requirements for the intended utilization are defined by the following fundamental equations:

$$u_g = \overline{u} + g \cdot \sigma_u \leq u_{lim} \tag{2.7}$$

$$p_{(u_g \geq u_{lim})} \leq p_{comfort} \tag{2.8}$$

where: u_g is the gust wind speed, $\overline{u}$ is the mean wind speed, g is peak factor, σ_u is the standard deviation of the wind speed, u_{lim} is the maximum tolerable value for the wind speed, $p_{(u_g \geq u_{lim})}$ is the probability with which u_g exceeds u_{lim} within a given period of time T and $p_{comfort}$ is the maximum allowable probability of exceedance for a defined comfort level.

Almost each parameter contained in the two equations above differs from criterion to criterion, not only in value but also in meaning. The gust wind speed u_g defined in equation (2.7) is interpreted by Melbourne (1978) as the peak gust wind speed, whereas Davenport (1972), Isyumov and Davenport (1975), Gandemer (1975), Hunt *et al.* (1976), Gandemer (1978), Isyumov and Davenport (1978), FORCE-Technology (2002) see u_g as an effective wind speed since probably neither the mean wind speed nor the maximum gust speed are entirely appropriate as a yardstick of the wind effects particularly in blustery situations. Principally the wind comfort criteria are divided into two groups: the first group considers only the hourly mean wind speed (g = 0) as fundamental parameter to assign the comfort level; the second group is based also on the peak factor (g $\neq$ 0) and has the function to include the fluctuations of the mean wind speed.

The publication of Ratcliff and Peterka (1990) compares the conclusions of five reliable comfort criteria: Penwarden and Wise (1975), Isyumov and Davenport (1975), Lawson and Penwarden (1975), Hunt *et al.* (1976) and Melbourne (1978). The five wind comfort criteria for pedestrians in urban area are briefly summarized in the scheme reported in Fig. 2.18.

Comfort criteria compared by Ratcliff and Peterka (1990)

Penwarden and Wise (1975)
Hourly mean wind speed ($g = 0$)
Onset for remedial actions is $u_{mean} = 5$ m/s

Isyumov and Davenport (1975)
Gust ($g = 1.5$) and hourly mean wind speed ($g = 0$)
A Long: u, $u_g > 3.58$ m/s for $T < 1.5\%$ and > 5.37 m/s for $T < 0.3\%$
B Short: u, $u_g > 5.37$ m/s for $T < 1.5\%$ and > 7.61 m/s for $T < 0.3\%$
C Stroll: u, $u_g > 7.61$ m/s for $T < 1.5\%$ and > 9.85 m/s for $T < 0.3\%$
D Walking: u, $u_g > 9.85$ m/s for $T < 1.5\%$ and > 12.53 m/s for $T < 0.3\%$
Unpleasant for all other cases
Dangerous for $u_g > 15.22$ m/s for $T > 0.02\%$ of the time (year)

Davenport presented these criteria in 1972 (Davenport, 1972) without specifying which wind speed should be applied on the threshold values but suggested already that the mean wind speed might not be the correct quantity to apply. In frame of this comparison both the mean wind speed and the effective (gust) wind speed is used.

Lawson and Penwarden (1975)
Gust ($g = 2.68$) and hourly mean wind speed (g = 0)
A Covered area: $u > 3.35$ m/s for $T < 4.0\%$ and $u_g > 5.7$ m/s for $T < 4.0\%$
B Standing area: $u > 5.45$ m/s for $T < 4.0\%$ and $u_g > 9.3$ m/s for $T < 4.0\%$
C Walking area: $u > 7.95$ m/s for $T < 4.0\%$ and $u_g > 13.6$ m/s for $T < 4.0\%$
D Unacceptable: $u > 13.85$ m/s for $T < 2.0\%$ and $u_g > 23.7$ m/s for $T < 2.0\%$
Uncomfortable all other cases

Hunt et al. (1976)
Gust ($g = 3$) and hourly mean wind speed ($g = 0$)
For comfort and little effect on performance: $u_g < 6$ m/s for $T = 10.0\%$
Most performance unaffected: $u_g < 9$ m/s for $T = 10.0\%$
Control of walking: $u_g < 15$ m/s for $T = 10.0\%$
Safety of walking: $u_g < 20$ m/s for $T = 10.0\%$
Unacceptable if $u_{mean} > 9$ m/s for $T = 1\%$ of the time (year)

The list of comfort criteria given in Ratcliff and Peterka (1990) is supplemented with further information given by the authors of the study.

Melbourne (1978)
Gust ($g = 3.5$) and hourly mean wind speed ($g = 0$)
Generally acceptable: $u_g > 10$ m/s for $T = 0.025\%$
A Long: $u_g > 10$ m/s for $T = 0.025\%$
B Short: $u_g > 13$ m/s for $T = 0.025\%$
C Walking: $u_g > 16$ m/s for $T = 0.025\%$
D Unacceptable: $u_g > 23$ m/s for $T = 0.025\%$
Uncomfortable for all other cases.

Fig. 2.18 Definition of various comfort criteria by Ratcliff and Peterka (1990), (Koss, 2006).

After the collection of criteria by Ratcliff and Peterka (1990), a recent attempt to orientate the community of researchers and engineers about the assessment and evaluation of pedestrian wind comfort has been performed by the research group of European-C14 (2001). The research team has gathered the various comfort criteria that are currently used for wind comfort investigations in several European institutes. In this case the comfort criteria are summarized in function of the proposers in Fig. 2.19.

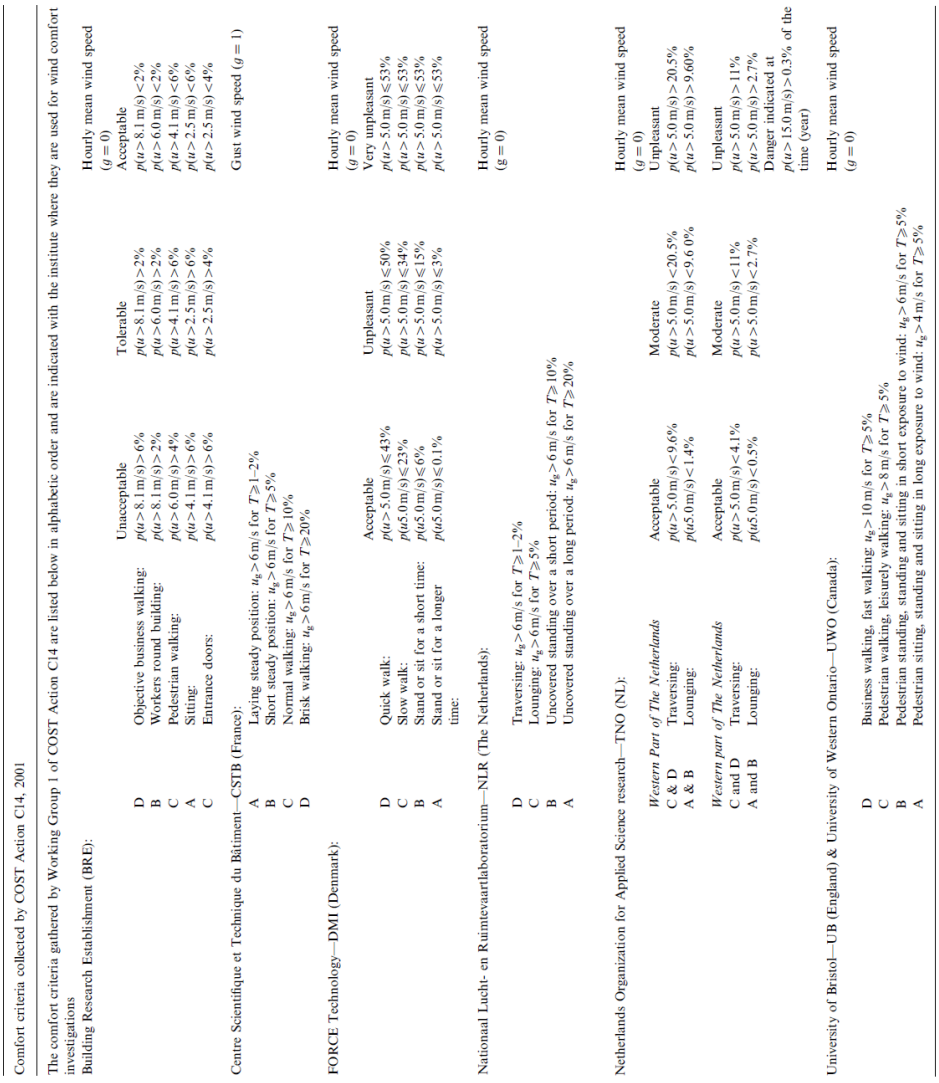

Comfort criteria collected by COST Action C14, 2001

The comfort criteria gathered by Working Group 1 of COST Action C14 are listed below in alphabetic order and are indicated with the institute where they are used for wind comfort investigations

Building Research Establishment (BRE):					Hourly mean wind speed ($g = 0$)
			Unacceptable	Tolerable	Acceptable
	D	Objective business walking:	$p(u > 8.1\,\mathrm{m/s}) > 6\%$	$p(u > 8.1\,\mathrm{m/s}) > 2\%$	$p(u > 8.1\,\mathrm{m/s}) < 2\%$
	B	Workers round building:	$p(u > 8.1\,\mathrm{m/s}) > 2\%$	$p(u > 6.0\,\mathrm{m/s}) > 2\%$	$p(u > 6.0\,\mathrm{m/s}) < 2\%$
	C	Pedestrian walking:	$p(u > 6.0\,\mathrm{m/s}) > 4\%$	$p(u > 4.1\,\mathrm{m/s}) > 6\%$	$p(u > 4.1\,\mathrm{m/s}) < 6\%$
	A	Sitting:	$p(u > 4.1\,\mathrm{m/s}) > 6\%$	$p(u > 2.5\,\mathrm{m/s}) > 6\%$	$p(u > 2.5\,\mathrm{m/s}) < 6\%$
	C	Entrance doors:	$p(u > 4.1\,\mathrm{m/s}) > 6\%$	$p(u > 2.5\,\mathrm{m/s}) > 4\%$	$p(u > 2.5\,\mathrm{m/s}) < 4\%$
Centre Scientifique et Technique du Bâtiment—CSTB (France):					Gust wind speed ($g = 1$)
	A	Laying steady position: $u_g > 6\,\mathrm{m/s}$ for $T \geqslant 1$–2%			
	B	Short steady position: $u_g > 6\,\mathrm{m/s}$ for $T \geqslant 5\%$			
	C	Normal walking: $u_g > 6\,\mathrm{m/s}$ for $T \geqslant 10\%$			
	D	Brisk walking: $u_g > 6\,\mathrm{m/s}$ for $T \geqslant 20\%$			
FORCE Technology—DMI (Denmark):					Hourly mean wind speed ($g = 0$)
			Acceptable	Unpleasant	Very unpleasant
	D	Quick walk:	$p(u > 5.0\,\mathrm{m/s}) \leqslant 43\%$	$p(u > 5.0\,\mathrm{m/s}) \leqslant 50\%$	$p(u > 5.0\,\mathrm{m/s}) \leqslant 53\%$
	C	Slow walk:	$p(u5.0\,\mathrm{m/s}) \leqslant 23\%$	$p(u > 5.0\,\mathrm{m/s}) \leqslant 34\%$	$p(u > 5.0\,\mathrm{m/s}) \leqslant 53\%$
	B	Stand or sit for a short time:	$p(u5.0\,\mathrm{m/s}) \leqslant 6\%$	$p(u > 5.0\,\mathrm{m/s}) \leqslant 15\%$	$p(u > 5.0\,\mathrm{m/s}) \leqslant 53\%$
	A	Stand or sit for a longer time:	$p(u5.0\,\mathrm{m/s}) \leqslant 0.1\%$	$p(u > 5.0\,\mathrm{m/s}) \leqslant 3\%$	$p(u > 5.0\,\mathrm{m/s}) \leqslant 53\%$
Nationaal Lucht- en Ruimtevaartlaboratorium—NLR (The Netherlands):					Hourly mean wind speed ($g = 0$)
	D	Traversing: $u_g > 6\,\mathrm{m/s}$ for $T \geqslant 1$–2%			
	C	Lounging: $u_g > 6\,\mathrm{m/s}$ for $T \geqslant 5\%$			
	B	Uncovered standing over a short period: $u_g > 6\,\mathrm{m/s}$ for $T \geqslant 10\%$			
	A	Uncovered standing over a long period: $u_g > 6\,\mathrm{m/s}$ for $T \geqslant 20\%$			
Netherlands Organization for Applied Science research—TNO (NL):					Hourly mean wind speed ($g = 0$)
	Western Part of The Netherlands		Acceptable	Moderate	Unpleasant
	C & D	Traversing:	$p(u > 5.0\,\mathrm{m/s}) < 9.6\%$	$p(u > 5.0\,\mathrm{m/s}) < 20.5\%$	$p(u > 5.0\,\mathrm{m/s}) > 20.5\%$
	A & B	Lounging:	$p(u5.0\,\mathrm{m/s}) < 1.4\%$	$p(u > 5.0\,\mathrm{m/s}) < 9.6\,0\%$	$p(u > 5.0\,\mathrm{m/s}) > 9.60\%$
	Western part of The Netherlands		Acceptable	Moderate	Unpleasant
	C and D	Traversing:	$p(u > 5.0\,\mathrm{m/s}) < 4.1\%$	$p(u > 5.0\,\mathrm{m/s}) < 11\%$	$p(u > 5.0\,\mathrm{m/s}) > 11\%$
	A and B	Lounging:	$p(u5.0\,\mathrm{m/s}) < 0.5\%$	$p(u > 5.0\,\mathrm{m/s}) < 2.7\%$	$p(u > 5.0\,\mathrm{m/s}) > 2.7\%$
					Danger indicated at $p(u > 15.0\,\mathrm{m/s}) > 0.3\%$ of the time (year)
University of Bristol—UB (England) & University of Western Ontario—UWO (Canada):					Hourly mean wind speed ($g = 0$)
	D	Business walking, fast walking: $u_g > 10\,\mathrm{m/s}$ for $T \geqslant 5\%$			
	C	Pedestrian walking, leisurely walking: $u_g > 8\,\mathrm{m/s}$ for $T \geqslant 5\%$			
	B	Pedestrian standing, standing and sitting in short exposure to wind: $u_g > 6\,\mathrm{m/s}$ for $T \geqslant 5\%$			
	A	Pedestrian sitting, standing and sitting in long exposure to wind: $u_g > 4\,\mathrm{m/s}$ for $T \geqslant 5\%$			

Note: The conversion of Beaufort scale to (m/s) differs in between the values given in Ratcliff and Peterka (1990) for the wind speed limits defined in Davenport (1972) and Isyumov and Davenport (1975) and the conversion applied for wind speed values. The differences are small and do not affect the comparison.

Fig. 2.19 Comfort criteria collected by European-C14 (2001), (Koss, 2006).

2.4 Concluding remarks

This chapter reports a short review of the principal actions that are induced by wind on the users of the civil engineering infrastructures. More in detail the wind effects on ground vehicles (rail and road) and on pedestrians are discussed.

Road vehicles are more prone to wind-induced accidents because they are in general rather smaller and lighter than the rail vehicles. In addition, their motion is not constrained by the rails. In fact, unlike the trains, road vehicles are subject to two different types of accident: the classical overturning (typical also for rail vehicles) and the course deviation of the vehicle (side-slip).

The wind effects on pedestrians are usually expressed by means of comfort criteria, in function of a critical threshold for the mean or gust wind speed. The assessment of comfort levels is at present still an open issue in several research fields as they are very complex to evaluate due to their subjective characteristics.

Chapter 3

Flow through screens

3.1 Generality

In recent years the more accurate control during the design, construction and exercise phases of structures have led to a wider use of accessory elements, chosen and studied to guarantee higher and higher standard of life. Among them the use of porous structures has had a strong development because this kind of elements presents many functionalities. Firstly, the temperature regulating function helps to avoid the heat loss during night-time. Secondly, the shading function has the purpose to mitigate the solar radiation entering a building. Lastly there is the wind-breaking effect that contrasts the wind speed. Both the temperature regulating function and the shading one become fundamental for the buildings for which it is necessary to reach high energetic standards. In fact, for the energetic sustainability the new international regulations are more and more demanding and less tolerating the energetic losses. On the other hand referring to the windbreak effect, this is mostly present in the realization of windbreak shields for many important infrastructures, such as main roads, bridges, viaducts and footbridges. In these cases the introduction of such mitigation devices implies the reduction and control of wind speed, in order to safeguard the users of those structures.

In the literature there are many experimental studies, along with theoretical studies of the flow through porous media [Miguel (1998); Bejan *et al.* (2004)], and numerical CFD analysis on porous materials [Fatnassi *et al.* (2003); Teitel *et al.* (2009)]. As an alternative to the analysis of porous media, there are also experimental works with the typical approach of the hydraulic resistance [Annand (1953); Pinker and Herbert (1967); ESDU81039 (1985); Brundrett (1993); Idelchik (1994); Valli *et al.* (2009)].

3.2 Flow through a porous medium

3.2.1 Introduction

The flow through a porous medium is encountered everywhere, both in nature and in technology: for instance, the phenomena of the uptake of water and the flow of sap and gums in trees, the flow of blood in vessels and in various organs with porous

boundaries. Further examples are found in the flow of fluids through textile fabrics, pulp fibres, woven and non-woven filters, and in coffee and cigarette filters. The classical examples include the groundwater hydraulics, flow in fractured rocks and their contamination by non-Newtonian oil pollutants, flow in saturated aquifers, aerosol filtration, filtration of slurries, sludge and polymer melts using sand pack beds, screens, and metallic filters. This limited list of porous media flows is concluded by mentioning the use of packed beds as a calming section to eliminate turbulence in a fluid stream prior to entering a test section and in each case where separation and filtration among various materials is sought. In view of such a wide occurrence of porous media flows, it will not be exaggerate saying that the phenomenon is ubiquitous. It is readily recognized that the understanding and mathematical modelling of transport processes in porous media requires a detailed description of both the porous medium and the process itself. Ever since the pioneering work of Darcy in the 19^{th} century, a huge body of knowledge concerning the fluid flow in porous media has occurred, and excellent treatises dealing with various aspects of porous media per se and the phenomenon of fluid flow through it are available in literature, though a large part of this body of knowledge relates to the flow of Newtonian fluids [Collins (1961); Bear (1972); Chhabra (1993); Bejan *et al.* (2004)].

3.2.2 Fundamentals of porous media

A porous medium consists of a solid structure with void spaces that are in general complicated and distributed throughout the structure. The opening spaces can be interconnected or not. The traditional view of porous media was inspired by porous structures found in nature, for example packed sand saturated with water that seeps through the pores (*3D porous medium*) or a flow of air through a perforated plate (*2D porous medium*). Clearly, a porous medium is characterized by specifying the manner in which voids are present in the matrix, their location, size or size distribution, shape, interconnectedness. Natural porous structures have random features, such as irregular pore shapes and sizes, and irregular connection between the pores. Broadly speaking about the artificial porous structures it is possible to distinguish two particular cases with respect to the characteristics of the pores. On the one hand there are the modern complex porous structures, such as adsorption membranes and multi-part separation layers; on the other hand the very simple geometries and shapes such as physical filters and grids with a specific distribution of the pores. Even porous media of the same type can be different. When the voids are irregular, as in many porous media that occur in nature, the pore dimensions may be concentrated in a narrow range, or they may be distributed (smoothly or discretely) over a wide range of values.

It is generally known that there are two distinct levels of description of a porous medium: microscopic and macroscopic. The microscopic description of a porous medium is really equivalent to a statistical description of the pore size distribution, even if the description itself may be quite arbitrary. The second approach, that is the macroscopic description, involves the use of bulk quantities averaged over scales much larger than the size of pores. Both approaches are complementary and extensively used; the choice, however, varies from one application to another. For instance, the

use of microscopic description is a necessity while trying to understand the physics of fluid flow at a molecular level, whereas the macroscopic description of a porous medium is quite adequate for engineering design calculations involving fluid flows in porous media. Once again, bearing in mind the goals of this work, the macroscopic approach for describing porous media is more appropriate for porous windscreens. Several macroscopic parameters have been proposed to characterize non-ideal porous media (Dullien, 1992), but the parameters reported in the following sections have gained wide acceptance in describing the flow of single-phase and multi-phase fluids in a porous medium in terms of gross engineering parameters.

3.2.2.1 Porosity

Porosity is the measure of the effective pore or void volume per unit volume of the matrix. Depending upon the nature of the porous medium, the porosity (also known as *void age*) may vary from near zero to almost one.

The porosity is a scalar quantity and expresses the capability of the medium to contain fluids. Considering a sample of a porous material having a volume V, composed of a solid matrix with some amount of fluid inside, the volume fraction of the fluid phase is:

$$\varepsilon_v = \frac{V_v}{V} \tag{3.1}$$

where: ε_v is the volume porosity, V_v is the volume of fluid within the solid matrix and V is the total volume of the porous medium. For instance, certain rocks, sandstones, may have very low values of porosity ($\sim 0.15 \div 0.2$) whereas fibrous beds, glass wool, porous screens, structured packings, may take high values (~ 0.4 or even more).

Since porous screens are always made of thin materials, it is useful to define the porosity as a surface quantity:

$$\varepsilon_a = \frac{A_a}{A} \tag{3.2}$$

where: ε_a is the area porosity, A_a represents the surface area filled with air, and A is the total area of the screen. Within the context of fluid flow, it is important to distinguish between the so-called interconnected or effective voids (which contribute to fluid flow) and the so-called non-connected voids; the latter obviously are passive pores as far as the flow is concerned. Evidently, when a single value of the porosity is used to characterize a porous medium, the detailed structure of the matrix is unimportant. Thus, it is possible that two porous media having identical values of porosity may have completely different micro-structures, for example, pore size distribution, type of networks, etc.

3.2.2.2 Permeability

Henry Darcy, a French civil engineer, in his 1856 publication laid the real foundation of the quantitative theory of the flow of homogeneous fluids through porous media (Fig. 3.1). As a civil engineer, he was interested in the flow characteristics of sand

filters used for public water in the city of Dijon in France. Permeability can be simply defined as the capability of a porous medium to be gone through, via the Darcy's law as:

$$\frac{Q}{A} = \frac{K}{\mu}\left(\frac{\Delta p}{L}\right) \tag{3.3}$$

Equation (3.3) is a physical and empirical law, like the Newton's law of viscosity, relating the volumetric flow rate (Q) through a porous medium having a cross sectional area normal to the flow (A) under the pressure gradient ($\Delta p/L$); μ is the dynamic viscosity of the fluid, and K is the permeability of the porous medium. In other words, it is a measure of the resistance to fluid flow, and generally depends upon the pore size, distribution, length, entrances and exits of the pores, etc.

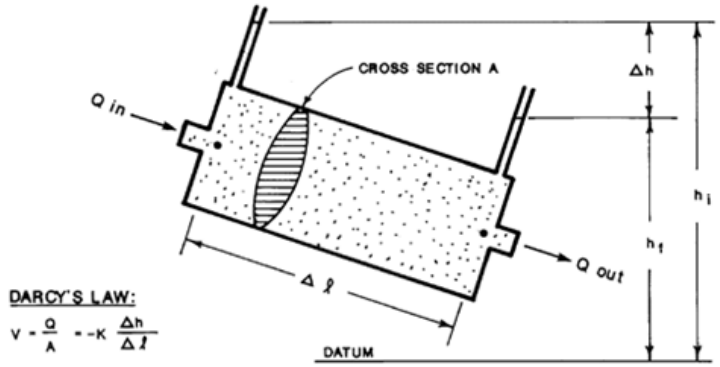

Fig. 3.1 Darcy's experiment.

Intuitively, it is reasonable to anticipate a connection between the porosity and the permeability, since a medium with zero porosity will have zero permeability. However, the porosity cannot be estimated from the permeability alone and vice versa. The permeability of a porous medium is measured in terms of Darcy. A porous material is said to have the permeability of 1 Darcy if a pressure difference of 1 atm results in a flow of 1 cm^3/s of a fluid having a viscosity of 1 cP (*centipoise*) through a cube (*of porous matrix*) having sides of 1 cm. In SI units, it is expressed as m^2 and 1 Darcy $\approx 10 \div 12\ m^2$.

Contrary to the porosity, the permeability is a vectorial quantity as it depends on the direction considered and should be expressed like a second-order tensor and to be more precise by its nine components. However, even if permeability is characterized by nine components, there are usually some preferential directions where the fluid flows more easily.

3.2.2.3 Other relevant characteristics

In this part other important characteristics of porous structures are described, although they have an irrelevant weight with regard to surface porous structures such as windbreaks. This kind of properties is typical for volume porous media because they are related to the three-dimensional hole matrix.

One of these characteristics is tortuosity. It is the measure of the tortuous zigzag paths traversed by fluid elements in a porous matrix. The tortuosity is defined as the ratio of the average length of the flow paths to the actual length of the porous medium in the direction of mean flow. Clearly, tortuosity can be seen as a macroscopic measure of both sinuousness of the flow path and pore size variation along the direction of flow. Once again, though tortuosity bears some correlation with permeability, these parameters cannot be obtained from the other.

Specific surface area is fundamental quantity for packed bed because it influences both its structure and the resistance to the flow. It is defined as the surface area per unit volume of the bed, and is directly related to the specific area of the packing via the bed porosity. It is readily seen that, for a given particle shape, the specific surface area is inversely proportional to the particle size.

Finally, other macroscopic and microscopic parameters such as connectivity, formation resistivity, pore size distribution, pore networks are currently in use for characterizing a porous material.

3.2.3 Darcy flow and more advanced models

In the fluid mechanics of porous media, just as in turbulence, the role of momentum equations or force balances is replaced by experimental observations summarized in simple models. Such observations were firstly reported and modelled by Darcy (1856) who, based on measurements alone, discovered that the area-averaged fluid velocity through a column of porous material is proportional to the pressure gradient along the column. Darcy's empirical equation is a statistical average of classical hydrodynamic equation over the minute and detailed variation of the geometric boundaries occurring in the individual pores; it gives a simplified macroscopic representation.

The Darcy flow model is based on the following assumptions of the phenomenon:

- Darcy's law assumes laminar or viscous flow (creep velocity); it does not involve the inertial term (the fluid density). This implies that the inertial or acceleration forces in the fluid are neglected when compared to the classical Navier-Stokes equations;
- Darcy's law assumes that in a porous medium a large surface area is exposed to fluid flow, hence the viscous resistance will greatly exceed acceleration forces in the fluid unless turbulence sets in.

Darcy's empirical flow model represents a simple linear relationship between flow rate and pressure gradient in a porous medium; any deviation from the Darcy flow scenario is termed non-Darcy flow. Physical causes for these deviations are grouped under the following headings: high velocity flow effects, molecular effects, ionic effects and Non-Newtonian fluids phenomena. Subsequent studies showed that the velocity is inversely proportional to the dynamic viscosity (μ) of the fluid seeping through the porous material. With reference to the one-dimensional flow configuration shown in Fig. 3.1, the Darcy flow model states:

$$u = \frac{K}{\mu}\left(-\frac{dp}{dx}\right) \quad or \quad \nabla p = -\frac{\mu}{K} \cdot \mathbf{v} \tag{3.4}$$

The dimension of K can be seen by comparing equation (3.4) with the equation (3.5) for Hagen-Poiseuille flow of mean velocity u through a tube of diameter D (Bejan, 1995):

$$u = \frac{D^2}{32\mu}\Big(-\frac{dp}{dx}\Big) \tag{3.5}$$

Nield and Bejan (1995) claim that Darcy's model (3.4) is not a balance of forces averaged over a representative elementary volume. In fact, the similarity between equations (3.4) and (3.5) suggests that the Darcy flow is the macroscopic manifestation of highly viscous flow through the pores of the permeable structure, and $K^{1/2}$ is a length scale representative of the effective pore diameter. By considering a small-scale network of channels of well-known geometry, and assuming Hagen-Poiseuille flow through each channel, it is possible to derive equation (3.4) so that K is function of the network geometry. Due to this parallelism using $K^{1/2}$ as a length scale, it is possible to define the Reynolds number (Re_K) and the friction factor (f_K) of the porous medium:

$$Re_K = \frac{uK^{1/2}}{\nu} \tag{3.6}$$

$$f_K = \Big(-\frac{dp}{dx}\Big)\frac{K^{1/2}}{\rho u^2} \tag{3.7}$$

where: Re_K is the Reynolds number of the porous medium based on permeability; f_K is the friction factor of the porous medium; u is the fluid velocity through the medium; ρ and ν are respectively the density and the kinematic viscosity of the fluid. Using the Reynolds number definition (3.6) and the friction factor (3.7) it is possible to rewrite the Darcy law (3.4) as:

$$f_K = \frac{1}{Re_K} \tag{3.8}$$

This form is reminiscent of the friction factor for Hagen-Poiseuille flow. Experimental measurements have shown that equations (3.4) and (3.8) are valid when Re_K is in the range from 1 to 10 (Fig. 3.2). If Re_K exceeds 10, inertial effects flatten the $f_K(Re_K)$ curve in a similar way to the friction factor curve in turbulent flow over a rough surface, and it is necessary to rewrite the relation for f_K:

$$f_K = \frac{1}{Re_K} + c_f \tag{3.9}$$

where: c_f is an empirical constant originally believed to be approximately equal to 0.55. A more general friction factor model is due to Dupuit's modification (1863) of the Darcy model, later modified by Forchheimer (1901).

Fig. 3.2 shows the generic relationship between the friction factor (pressure drop) and the Reynolds number (flow rate) for a given porous medium. At very low Reynolds numbers, this relationship is characterized by a slope equal to one and this corresponds to the Darcy regime or the creeping flow conditions. On the other

hand, at very high Reynolds numbers, the friction factor is nearly independent from Reynolds number, but depends on particle roughness and pore structure.

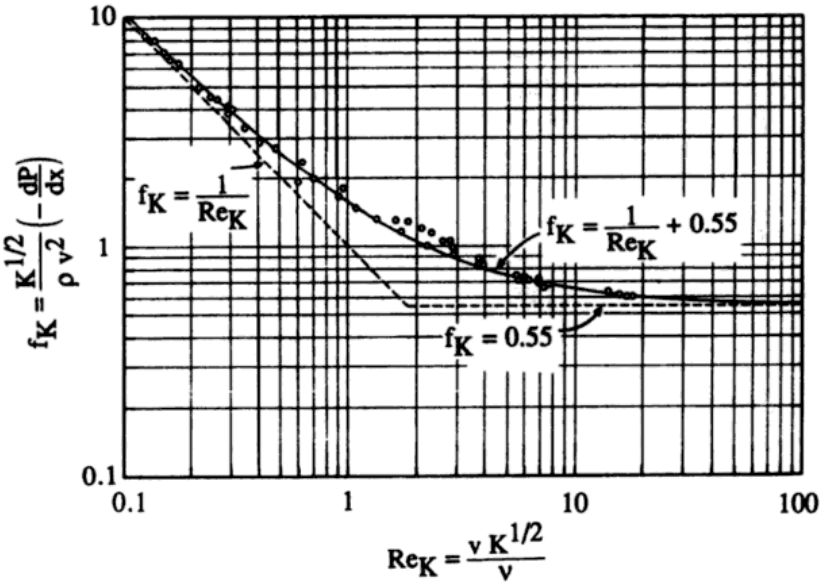

Fig. 3.2 The transition from the Darcy regime to the Forchheimer regime (Ward, 1964).

In 1901, Philippe Forchheimer, while studying gas through coal beds, discovered that the relationship between flow rate and pressure gradient is non-linear at sufficiently high velocity, and that this non-linearity increases with the flow rate. He initially attributed this non-linear increase to turbulence in the fluid flow (it is now known that this non-linearity is due to inertial effects in the porous media), which he determined to be proportional to u^2 through a constant a. Cornel and Katz (1953) gave a value of $\beta\rho$ to a, where β is called the inertial factor and ρ is the density of the fluid flowing through the medium. The total pressure drop is thus given by Forchheimer empirical flow model (3.10) stated traditionally as:

$$-\frac{dp}{dx} = \frac{\mu}{K}u + \beta\rho u^2 \quad or \quad \nabla p = -\frac{\mu}{K}\mathbf{v} - c_f \rho K^{1/2}|\mathbf{v}|\mathbf{v} \tag{3.10}$$

As shown in the Forchheimer equation, the increase of pressure drop can be calculated by adding to the linear term of the equation one more quadratic term of the velocity, multiplied by the non-Darcy flow coefficient β and the mass density of the fluid. The non-Darcy flow coefficient has a lot of names, related to its different meanings, such as turbulence factor, coefficient of inertial drag and Forchheimer coefficient. The additional pressure drop due to inertial losses is primarily due to the acceleration and deceleration effects of the fluid as it travels through the tortuous flow path of the porous medium.

The transition from Darcy flow (3.4) to Darcy-Forchheimer flow (3.10) occurs when Re_K is of order $100 \div 200$; this wide range depends on the typology of porous medium. Given a particular velocity, the loss of pressure is larger than the one

provided by the Darcy law, or for a certain gradient of pressure the final velocity of the flow is smaller than the velocity calculated through Darcy law.

In case of fully turbulent flow through porous media, the linear term of Forchheimer equation can be neglected (because the inertial characters of motion are predominant with respect to the viscous ones), and the equation (3.10) can be further modified as:

$$-\frac{dp}{dx} = \beta\rho u^2 \quad or \quad \nabla p = -c_f \rho K^{1/2} |\mathbf{v}|\mathbf{v} \tag{3.11}$$

where: β is an empirical constant, that includes the inertial effects due to the flow.

The transition to turbulence in porous media and the modelling of the turbulent flow continue to be an attractive research issue (Masuoka and Takatsu, 2002). In this regard the literature is full of a big variety of models and inferences. For instance, [Wodie and Levy (1991); Skjetne and Auriault (1999); and Koch and Ladd (1997)] suggest to correct the equation (3.11) replacing the usual u^2 term with a u^3 term, in order to take into account the weak inertial effects. More complex models of turbulent flow through porous media have been developed by Dullien (1992); Antohe and Lage (1997); Pedras and de Lemos (2000); Kuwahara *et al.* (2006).

3.2.4 Flow regimes and pressure loss in porous media

The literature available on the flow of Newtonian fluids in porous media is voluminous. A cursory inspection of the relevant literature shows that the majority of the research efforts has been directed to elucidate the macroscopic aspects of the flow in porous media, with particular attention to the characterization of flow regimes and pressure loss.

Similarly to flow in pipes and conduits, several researchers have also tried to define flow regimes in porous media. Typically, for flows in pipes and conduits the Reynolds number is used to delineate flow regimes. A Reynolds number less than 2100 implies laminar flow, while larger values imply turbulent flow. However in porous media there is no clear limit that defines this transition.

The non-linearity experienced in non-Darcy flow is not a result of turbulence but of inertial effects as stated earlier, hence non-Darcy flow is known to occur in porous media at a much lower Reynolds number, and it is not initiated by a change of the flow regime. The detailed kinematics and structure of the flow field prevailing in a porous medium directly determine the macroscopic effects such as pressure loss, dispersion, rates of heat and mass transfer [Sederman *et al.* (1997); Shibu *et al.* (2001)]. Therefore, many authors have reported on these aspects in porous medium flows; a big variety of experimental techniques has been employed to establish the nature of flow in porous media including optical methods and colored plumes [Jolls and Hanratty (1966); Karabelas *et al.* (1973); Stephenson and Stewart (1986)], electrochemical methods [Latifi *et al.* (1989); Rode *et al.* (1994); Seguin *et al.* (1998); Comiti *et al.* (2000); Lesage *et al.* (2004)], hot wire anemometry to ascertain the level of turbulence [Mickley *et al.* (1965); van der Merwe and Gauvin (1971)], laser anemometry [Ganoulis *et al.* (1989); Hall and Hiatt (1996)], particle image velocimetry (Saleh *et al.*, 1993), photo luminescent volumetric imaging (Montemagno

and Gray, 1995), and lattice Boltzmann simulations (Hill and Koch, 2002).

While some of these studies have endeavoured to provide qualitative insight into the flow characteristics, such as locating the stagnant zones, regions of back flow, or the onset of convection, others have attempted to deduce quantitative information about the velocity distribution in two and three dimensional porous systems and about the onset of turbulence. Notwithstanding the importance of such detailed information, it is probably adequate to talk in terms of the various flow regimes that grossly relate the dependence of the pressure drop to the flow rate or to the mean velocity. Indeed, depending upon the nature of the fluid, the type of porous medium and the flow rate, different flow patterns have been observed and documented in the literature. The ultimate objective of all these studies is to establish criteria for predicting the transition from a flow regime to another. This purpose is realized in terms of an appropriately defined Reynolds number (Re_K), which, of course, hardly takes into account the detailed structure of the medium. Depending on the flow velocity and the nature of porous media, different flow patterns have been observed. However four major regimes were proposed by Dybbs and Edwards (1984) (using laser anemometry and visualization techniques). The main flow patterns can be summarized as follows:

- **Darcy (creeping flow) regime:** This flow region is dominated by viscous forces and the local velocity is determined primarily by local geometry. Since boundary layers begin to develop near the pore walls at about $Re_K \approx 1$, the Darcy regime ceases to exist at this value of the Reynolds number.

- **Inertial flow regime:** As the flow rate is progressively increased so that $Re_K > 1$, boundary layer effects dominate and an inertial core appears outside the boundary layer. The flow is still steady, but the pressure drop-flow rate relationship moves away from the linear dependence, typical of the Darcy regime. While it is difficult to identify the onset of this steady non-linear flow regime, it occurs somewhere in the range $1 < Re_K < 10$ and persists up to about $Re_K = 150$. Although there might be pockets of local turbulence in some pores, this flow regime is also known as non-linear laminar flow regime.

- **Unsteady laminar flow regime:** In the range $150 \leq Re_K \leq 300$, the flow in a porous medium is characterized by the formation of waves thereby imparting an unsteady character to the flow.

- **Turbulent flow regime:** At high Reynolds numbers ($Re_K > 300$), the flow conditions are dominated by eddies that closely resemble the ones of turbulent flow in pipes. In literature, this regime is also known as *highly chaotic* flow pattern.

There is large variation in limiting Reynolds numbers for these transition zones, therefore there are no categorical definitions about limits and transition zones. Fig. 3.3 is a diagrammatic representation of the flow regimes in a porous medium proposed by Basak (1977).

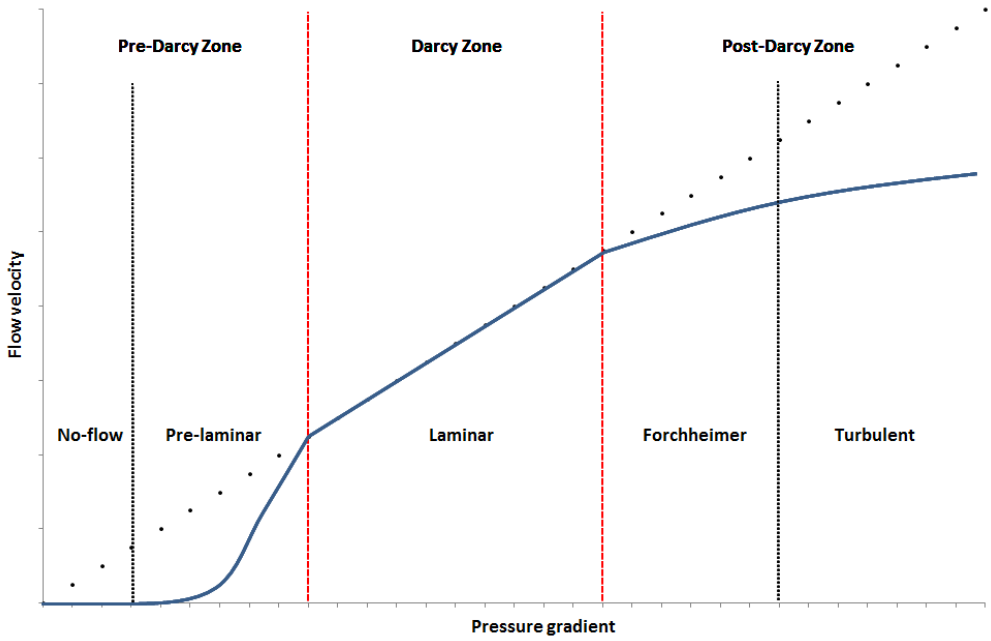

Fig. 3.3 Flow regimes in porous media (Basak, 1977).

Considering the flow regime proposed by Dybbs and Edwards (1984), it is appropriate to make four observations: firstly, there is always a degree of arbitrariness and subjectivity inherent in the interpretation of flow visualization studies. Secondly, transition from one flow regime to another occurs gradually over a range of conditions rather than abruptly, as it may seem looking at the limit of Reynolds numbers. Thirdly, much confusion exists in literature about the occurrence of turbulence in porous media (Niven, 2002) and therefore some authors (Scheidegger, 1974) have attributed the deviation from Darcy's law to the distortion of streamlines (thereby emphasizing the role of inertial forces) rather than to true turbulence. Finally, transition is also strongly influenced by the type of medium and the pore structure and therefore the critical values of the Reynolds number denoting the transition of flow regimes for one medium may not apply to a different porous medium. Consequently, considerable confusion exists in literature about the limit of the Darcy regime.

A part of this confusion can be attributed also to the variety of definitions of the Reynolds number used in the literature. For example, Sabiri and Comiti (1997) have promoted the use of a Reynolds number based on the pore characteristic size and on the velocity inside the pore, Re_{pore}, and they asserted that when $Re_{pore} = 0.83$ the Darcy's regime ends. Wegner *et al.* (1971) proposed the end of the non-linear laminar regime to occur somewhere in the range $90 \leq Re_K \leq 120$ and for the transition to the fully turbulent flow conditions, they reported values of the Reynolds number in the range from 200 to 300.

In summary, considering the complex interactions between the structure of the porous medium and the resulting flow field, it is really neither justifiable nor possible to offer universally applicable transition criteria in terms of a single value of the Reynolds number. This difficulty is further accentuated by the fact that each porous

medium is unique in its characteristics. From an engineering point of view, however, it is possible to work in terms of the three broad flow regimes, namely the Darcy regime, non-Darcy flow regime and the turbulent flow regime.

Another important key parameter is the drop of pressure due to the percolation of the fluid in a porous medium. In the past many studies have been carried out to estimate the pressure gradient that it is required to maintain a fixed flow rate through a porous medium. The results in this field are frequently expressed in terms of dimensionless parameters such as friction factor or Reynolds number.

3.3 Hydraulic resistance approach

Resistance to flow is an important subject; it is applicable to every branch of engineering where flows of liquids and gases occur. A few areas where the knowledge of the resistance to flow is a normal requirement in the design and operation are fluid loops, circuits, air conditioning and ventilation systems. But in more general terms the hydraulic resistance has an important relevance in many branches of engineering, such as aeronautical, mechanical, civil and chemical. The importance of exact values of flow resistance is, primarily, a question of determining the pumping or energy requirements for any apparatus or, eventually, for the entire plant involved in the motion of fluid.

3.3.1 Flow resistance fundamentals

In each flow system a portion of the total energy that is expended to overcome the resistance forces arising from the flow of real (viscous) fluids through medium is irretrievably lost. This loss of energy is due to irreversible conversion of mechanical energy into heat (the work of resistance forces). Therefore, the term fluid resistance, or hydraulic loss, represents the irreversible loss of total energy over a given system length. The ratio of the total stream energy loss to the kinetic energy or of the total pressure loss to the velocity pressure over an arbitrary flow section is called *the coefficient of hydraulic resistance*, and usually it is represented by the letter K. In a generic system it is possible to distinguish two types of pressure losses:

- Pressure loss resulting from friction (frictional drag), Δp_{fr};
- Local pressure loss (local resistance or shock), Δp_{loc}.

The fluid friction loss is due to the viscosity (both molecular and turbulent) of real liquids or gases in motion, and results from momentum transfer between the molecules (in laminar flow) and between the individual particles (in turbulent flow) of adjacent fluid layers moving at different velocities.

The local losses of total pressure are caused by local disturbances of the flow, such as separation from walls, formation of vortices, strong turbulent agitation of the flow in zones where the fluid stream passes obstructions. All of these phenomena contribute to the exchange of momentum between the moving fluid particles, thus enhancing energy dissipation. The phenomena of flow separation and eddy formation are associated with the differences of velocities and with positive pressure gradients along the flow.

The two kinds of losses are summed according to the principle of superposition of losses:

$$\Delta p_{tot} = \Delta p_{fr} + \Delta p_{loc} \tag{3.12}$$

In fact, the value of Δp_{fr} should be taken into account only for those parts of the system where the drop of pressure due to friction component is higher than the local one, or when Δp_{fr} is commensurable with Δp_{loc}.

Hydraulic calculations use dimensionless coefficients of fluid resistance, which conveniently have the same value in dynamically similar flows, that is, flows over geometrically similar configurations and with equal Reynolds numbers or other pertinent similarity criteria, irrespective of the kind of fluid or of the flow velocity and characteristic dimensions of the systems considered. The fluid resistance coefficient K_{tot} is defined as the ratio of the total energy lost over a given part of the system to the kinetic energy in a reference point:

$$K_{tot} = \frac{\Delta p_{tot}}{\frac{1}{2}\rho U^2} \tag{3.13}$$

where: U a reference velocity, which takes into account the kinetic load of the system. It is possible to reach this analytic expression if the fluid density (ρ) is considered constant along the streamlines. Also, in accordance with the arbitrarily accepted principle of superposition of losses, it is possible to express the total loss coefficient as follows:

$$\begin{aligned} K_{tot} &= K_{fr} + K_{loc} \\ \frac{\Delta p_{tot}}{\frac{1}{2}\rho U^2} &= \frac{\Delta p_{fr}}{\frac{1}{2}\rho U^2} + \frac{\Delta p_{loc}}{\frac{1}{2}\rho U^2} \end{aligned} \tag{3.14}$$

The friction loss coefficient (K_{fr}) depends on superficial roughness and on the flow regime related to the Reynolds number. The local resistance coefficient (K_{loc}) is mainly a function of the geometric parameters of the system and also of some general flow features, such as the velocity distribution profile, the degree of turbulence and the flow regime characterized by Mach and Reynolds numbers.

3.3.2 Loss coefficient for incompressible flow through screens

There has been a lot of work both experimental and theoretical, with the aim to describe the flow through gauzes and screens made of fibres (or wires) under various kinds of flow conditions. The industrial applications of these elements are numerous including: reduction of turbulence in wind tunnel experiments and in other aerodynamic applications, various water-removal processes in paper making and drying, and many filtering processes. Common examples of screens for aerodynamic applications are arrays of parallel rods, honeycombs, perforated plates and wire-gauze screens.

The literature on the topic of flow through screens can be divided into three categories (Laws and Livesey, 1978):

- Investigations on the flow properties of the screens;
- Investigations on the effect of a screen on time-averaged velocity distributions;
- Investigations on the turbulence distribution downstream of gauze screens.

In a certain sense, the flow through the screen could be modelled respect to the actuator-sheet theory, because the presence of the screen can be regarded as a finite discontinuity in the flow.

In case of confined screen element, the momentum normal to the screen is conserved, then drag force F_D on the screen is due only to the pressure loss through each orifice. Considering the flow through a single gauze element or orifice (Fig. 3.4) a possible manner to write the non dimensional drag coefficient is $C_D = 2F_D/\rho U^2 S$; where: U is the undisturbed flow velocity and S a typical orifice or gauze area.

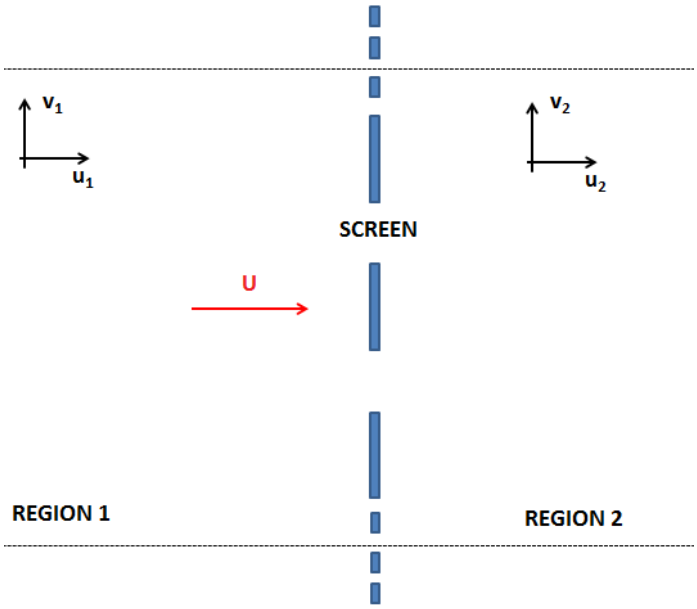

Fig. 3.4 Schematic view of the flow through a screen element.

For wire-gauze screens specified by wire diameter d and wire spacing l, the area usually taken as S is the solid area of the mesh expressed as $(1-\varepsilon)$ and represents the complementary of the porosity level (fullness). Using this definition, the drag coefficient can be defined as:

$$C_D = \frac{\Delta p}{\frac{1}{2}\rho U^2 (1-\varepsilon)} \tag{3.15}$$

and remembering the definition of loss coefficient (K) in the equation (3.13), it is easy to find the relationship between the drag coefficient and the loss coefficient for porous screens with porosity ε:

$$C_D = \frac{K}{(1-\varepsilon)} \tag{3.16}$$

On the basis of the measured pressure drop, one usually tries to find how this quantity depends on the Reynolds number and screen porosity. As there is no unambiguous theory for these dependencies, one is often satisfied with empirical correlations. Annand (1953), Grootenhuis (1954), Cornell (1958) and Brundrett (1993) presented several correlations for earlier data. The results of Annand (1953), Grootenhuis (1954) and Cornell (1958) were briefly reviewed by Pinker and Herbert (1967), who also compared these with their own measurements on the pressure drop for the air flow through screens with porosities varying between 0.3 and 0.7. Pinker and Herbert (1967) examined many previous attempts to separate the pressure drop coefficient or loss coefficient (K_0) defined for flow perpendicular to the screen ($\theta = 0$) in terms of the screen pressure drop Δp and upstream velocity U. The pressure drop for fluid flow through screens, Δp, is usually written as follows:

$$\Delta p = K_0(\varepsilon, Re_L) \cdot \frac{1}{2}\rho U^2 \tag{3.17}$$

where: U and ρ are respectively the upstream fluid velocity and the density of fluid, Re_L is the local Reynolds number (based on the orifice dimension and on the velocity inside the orifice) and K_0 is a dimensionless resistance coefficient. The porosity (ε) is defined as the ratio of the open area of the screen to its total area in the orthogonal projection (3.2). Annand (1953) has analysed the data of several experiments on different screens and showed that, for a large range of screen porosities, the dependence of coefficient K_0 on Reynolds number is very similar. Therefore, it is generally assumed that the dependence of K_0 on screen porosity and Reynolds number can be separated as:

$$K_0(\varepsilon, Re_L) = G(\varepsilon) \cdot F(Re_L) \tag{3.18}$$

where: G and F are functions whose exact forms are not known. Thus, it is possible to conclude that K_0 can be separated into two independent contributions, a screen porosity function $G(\varepsilon)$ and a function based on the wire-orifice Reynolds number $F(Re_L)$. As these functions are difficult to obtain analytically, most of the previous work has been based on experimental correlations, and there are several suggestions for the functional form of $G(\varepsilon)$. A good review of this topic for regular woven screens is given by Pinker and Herbert (1967). They examined four different $G(\varepsilon)$ functions:

Weighardt (1953) $$G_1(\varepsilon) = \frac{1-\varepsilon}{\varepsilon^2} \tag{3.19}$$

Annand (1953) $$G_2(\varepsilon) = \frac{1-\varepsilon^2}{\varepsilon^2} \tag{3.20}$$

Pinker and Herbert (1967) $$G_3(\varepsilon) = \frac{(1-\varepsilon)^2}{\varepsilon^2} \tag{3.21}$$

Grootenhuis (1954) $$G_4(\varepsilon) = \frac{1-\varepsilon_v}{{\varepsilon_v}^2} \tag{3.22}$$

where: ε_v is a *volumetric porosity* which permits skin friction losses to be computed for the total surface area of the warp and weft wires. The authors suggested that the best correlation with the data is given by:

$$G(\varepsilon) = \frac{1-\varepsilon^2}{\varepsilon^2} \tag{3.23}$$

This function has been also used by Hoerner (1965), Munson (1988), Groth and Johansson (1988) and Brundrett (1993). In Fig. 3.5 Richards and Robinson (1999) report a typical effect of porosity level on the loss coefficient for a round wire mesh screen. It is simple to notice that to low levels of porosity correspond high values of loss coefficient and vice versa.

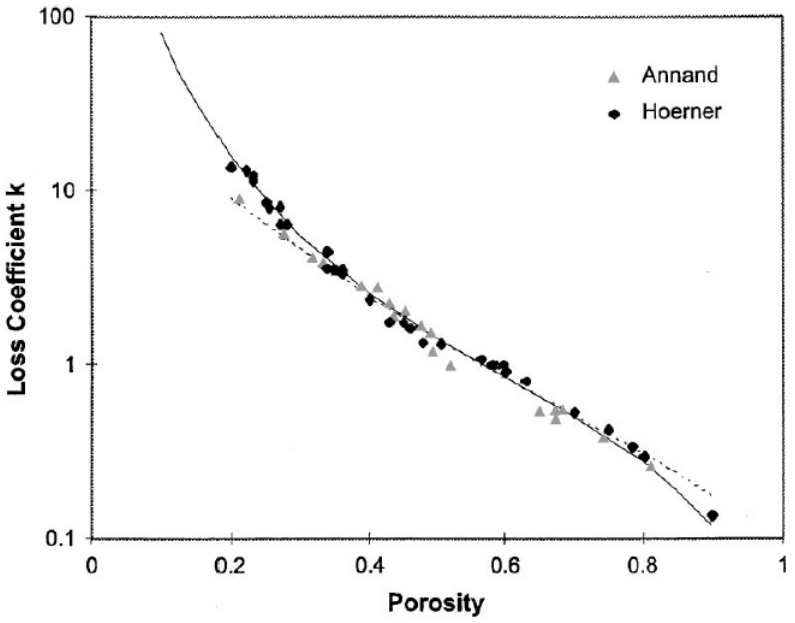

Fig. 3.5 Loss coefficient for round wire mesh screens (Richards and Robinson, 1999).

As it has been already shown, the loss coefficient K is a function of porosity, Reynolds number and, in case of compressible flow, also Mach number (Laws and Livesey, 1978). Richards and Robinson (1999) observed that K_0 decreases with Re_L

until $Re_L < 2000$; after that point, K_0 is a function of porosity only (ε).

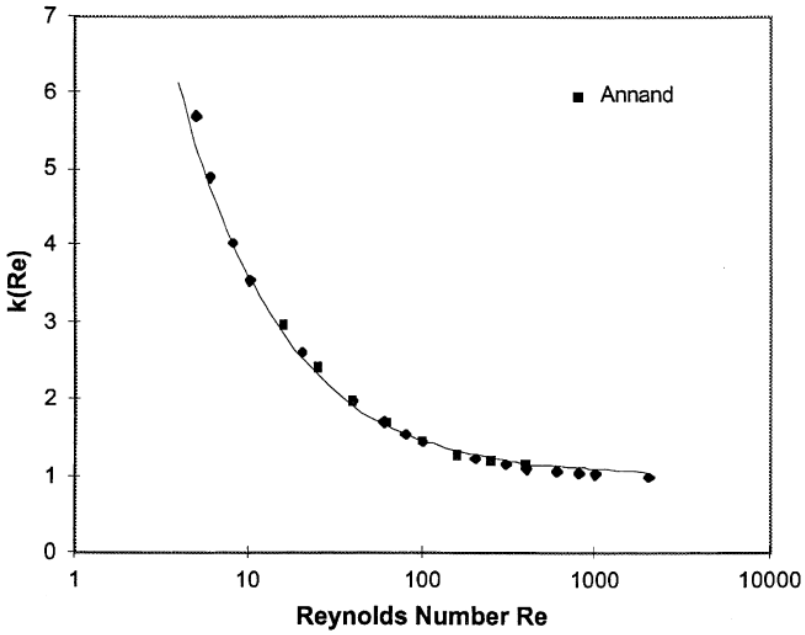

Fig. 3.6 The influence of Reynolds number on the loss coefficient for round wire mesh screen (Richards and Robinson, 1999).

The optimum expression for this functional relationship has been found by Pinker and Herbert (1967) and Reynolds (1969) to be as follows:

$$K_0 = A \cdot \frac{(1-\varepsilon^2)}{\varepsilon^2} \tag{3.24}$$

where: A is equal to 1.0 for low porosity and 0.52 for high porosity. This relationship is valid only when the dependence on Reynolds number is removed, therefore when Re_L is higher than 2000.

The previous flow studies have mainly focused on regular screens with moderate or large Reynolds numbers, as this kind of problems is abundant in industrial applications. Much less information on flow through screens in the low Reynolds-number regime is available. Munson (1988) has performed experiments on flow of silicone oil through woven fibrous screens of varying porosity, mounted in a pipe connecting two reservoirs. For low Reynolds numbers (the creeping-flow regime), the pressure drop across the screen is proportional to the flow velocity and therefore to the Reynolds number Re_L. Therefore, the Reynolds-number dependent part F of factor K_0 has to be set as inversely proportional to the Reynolds number:

$$F(Re_L) = \frac{2C}{Re_L} \tag{3.25}$$

The value of the coefficient $2C$ depends on the velocity profile. Munson (1988) found that his experimental data could be well described with the screen-porosity function of equation (3.23) together with the Reynolds-number dependence given by equation (3.25), for Reynolds numbers $10^{-4} < Re_L < 0.1$. The value of the coefficient $2C$ was found to be 4.75 when the average flow velocity in the tube was adopted for U. Brundrett (1993) suggested a *universal form* for the function F based on the existing data for a wide range of Reynolds numbers. For low Reynolds numbers he used the pipe-flow data of Munson (1988), and for higher Reynolds numbers the uniform-flow data of Schubauer *et al.* (1948) and Groth and Johansson (1988). For consistency, Brundrett first converted the pressure-drop data of Munson to correspond to those for a uniform profile. This was done by multiplying the data by a numerical factor 1.5 obtained from an analysis (Brundrett, 1993) in which the flow profile was assumed to be parabolic in Munson's experiments. Brundrett function consists of three terms whose coefficients were found via a trial and error procedure. Dependence on the flow direction is also included in this function, in this case for laminar pipe flow or for uniform upstream conditions. If, for simplicity, uniform flow orthogonal to the planar screen is assumed, Brundrett function can be expressed in the following form:

$$F(Re_L) = \frac{7.125}{Re_L} + \frac{0.88}{log(Re_L + 1.25)} + 0.055 log(Re_L) \tag{3.26}$$

For creeping flow, corresponding to the limit of vanishing Reynolds number, only the first term in the Brundrett function, $F(Re_L)$, is retained. The pressure drop is then proportional to the inverse of the upstream velocity U, as it should be, because of the linearity of the Stokes equation. The region of validity of this linearity assumption can be estimated from the ratio of the sum of the last two terms on the right-hand side of equation (3.26) to the first term. This analysis suggests that the error made by assuming linearity is less than about 10 % for $Re_L < 0.5$, and less than 50 % for Re_L up to 15.

Schubauer *et al.* (1948) extended their investigation for upstream flow angles other than perpendicular as defined by approach angle θ ($\theta = 0$ for perpendicular flow). They found that the empirical correlation of pressure loss coefficient K_θ versus approach angle θ was satisfactorily provided plotting $K_\theta / cos^2(\theta)$ versus $Re_L cos(\theta)$, for the range $0 \leq \theta \leq 45°$. Therefore the resistance (or pressure loss) coefficient K_θ at an approach angle θ is defined by the following relationship:

$$K_\theta = K_0 \cdot cos^2(\theta) \tag{3.27}$$

where: K_0 is the resistance coefficient at normal incidence $\theta = 0$. Hence, the general expression for K_θ, using also the decomposition explained in the equation (3.18), results:

$$K_\theta = cos^2(\theta) \cdot G(\varepsilon) \cdot F(Re_L \cdot cos(\theta)) \tag{3.28}$$

3.3.2.1 Pressure losses through orifice and perforated plates

The literature review by Ward Smith (1971) shows that much work has been done on the pressure drop characteristics of orifice and perforated plates in ducts and channels. Barriers that are distributed uniformly over the cross section of tubes and channels are able to create a uniform resistance to the flow; these devices include grids, orifice and perforated plates, screens, fabrics, beds, crosswise bundles of tubes, etc (Fig. 3.7). Orifice plates are mainly used as devices of flow measurements for fluid system. In heating, ventilation and air-conditioning systems, duct cross sections are generally large, so installation of such a plate results in considerable extra fan power being required. Perforated plates with multiple openings have been widely used in the study of experimentally simulated nearly isotropic turbulence (Liu *et al.*, 2007). On the other hand, perforated plates and screens are often used to reduce the non-uniformities of flow in air conditioning systems or to create uniform flow diffusion from supply air outlets. In the sector of civil engineering perforated plates are mainly used as flow-permeable elements in the architectural design of structures or mitigation devices like windbreak shields.

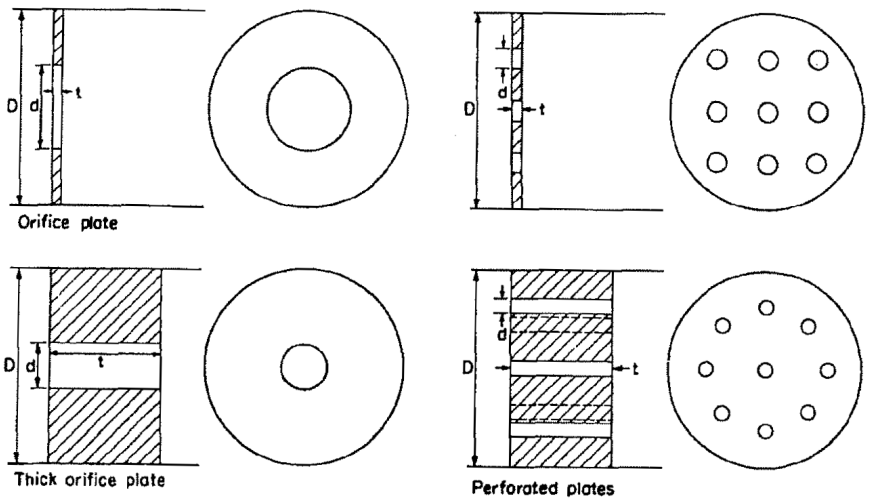

Fig. 3.7 Orifice and perforated plates (ESDU81039, 1985).

According to many authors such as ESDU81039 (1985) and Idelchik (1994), the resistance created by plane grids (perforated sheets), with the same porosity or free-area ratio (ratio between the surface occupied by the overtures and the total surface of the screen) placed in a straight tube, is the same as the one created by the flow passage through an orifice plate.

Gan and Riffat (1997) do not agree with ESDU81039 (1985) and Idelchik (1994) and demonstrated that the loss coefficient of orifice plates is lower of about 10 % than the loss coefficient of perforated plates. Their results are related to orifice and perforated plates with porosity level equal to 0.5 and positioned in a tube having non circular section.

Objects such as orifice plates, perforated plates and cylindrical tube orifices present the same geometries and flow characteristics. In fact, these elements imply a sudden sharp contraction of the flow area followed by a sudden enlargement (Fig. 3.8).

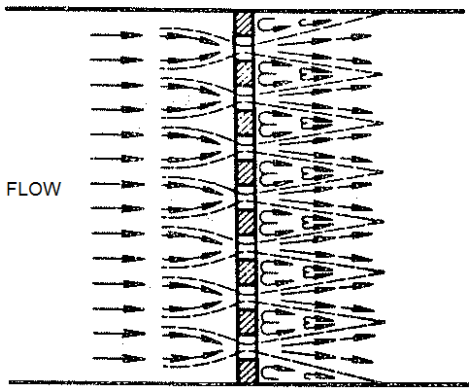

Fig. 3.8 Pattern of flow through grids, perforated plates and screens (Idelchik, 1994).

For a thin orifice plate this occurs as a single-jet flow, whereas for a thin perforated plate the fluid contracts during its passage through the plate orifices and leaves the plate as separate jets. The pressure losses for the thin plates are thus associated with the entry into orifices and with the sudden expansion at their exit. For a thick orifice plate (*cylindrical tube orifice*), the total losses include not only the sudden contraction and sudden expansion losses but also friction losses in the orifice.

The resistance coefficient of a perforated plate (grid) depends on the porosity, the shape of the orifice edges and the Reynolds number, calculated as:

$$Re = \frac{w_{or} d}{\nu} \tag{3.29}$$

where: w_{or} and d are respectively the velocity of fluid inside the orifice and the hydraulic diameter of the orifice, and ν is the kinematic viscosity of the fluid.

At small values of the level of porosity of the perforated plate, the velocity of the flow in the orifice and especially in the narrowest section of the jet in the orifice can turn out to be very high even at low inlet velocities. In some cases the velocity of the flow in the contracted section of the jets can approach the sonic velocity ($Ma \approx 1$). Under these conditions the resistance coefficient of a perforated plate or orifice becomes a function also of the Mach number.

In the general case of the flow passing from a volume into another through an opening in the wall, the following phenomena shown in (Fig. 3.9) are observed. The flow passes from channel 1, located before the partition A with an opening of diameter D_0, into channel 2, located behind the partition. Flow passage through the openings is accompanied by distortion of the trajectories of particles with the

result that they continue their motion toward the axis of the opening. This reduces the initial area of the jet cross section F_1 until the area F_c (*section c-c*) is smaller than the area of the opening cross section F_0. Starting with the *section c-c*, the trajectories of the moving particles are straightened and thereafter an abrupt jet expansion takes place.

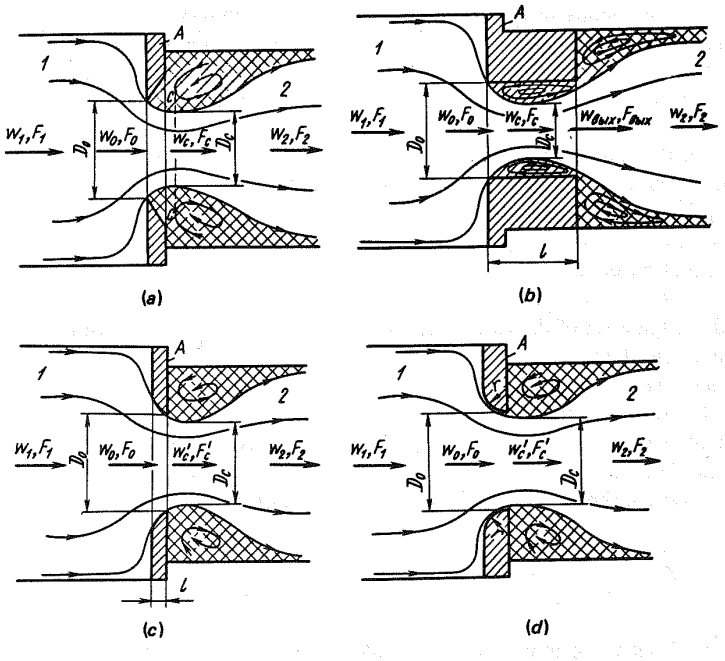

Fig. 3.9 Flow passage through orifices (Idelchik, 1994).

Thickening (Fig. 3.9b), bevelling (Fig. 3.9c) or rounding (Fig. 3.9d) of the orifice edges reduces the effect of the jet contraction in the opening, that is, decreases the jet velocity in its smallest section. Since this velocity determines the shock losses at discharge from the orifice, the total resistance to the flow created by the screen is decreased compared with a barrier with the same pattern but sharp-edged orifices (Fig. 3.9a). At very low values of local Reynolds number (Re less than about 10), the flow remains attached to the orifice. As the Reynolds number increases, the flow separates from the surface at the orifice entry to form a jet downstream of the hole. At sufficiently high Reynolds number, transition from laminar to turbulent flow takes place in the jet and the nature and geometry of the flow are largely insensitive to further increase of Reynolds number.

The resistance coefficient of a flow through a perforated plate inside a pipe depends not only on the geometric parameters of the screen, but also on the flow regime. In fact, in case of flow through perforated plate it is possible to distinguish:

- The laminar regime, in which the loss coefficient depends linearly on Re;
- The transition regime, in which the linear dependence is violated;
- The turbulent regime (the region of quadratic resistance law), in which there is no effect of the Reynolds number on the resistance coefficient.

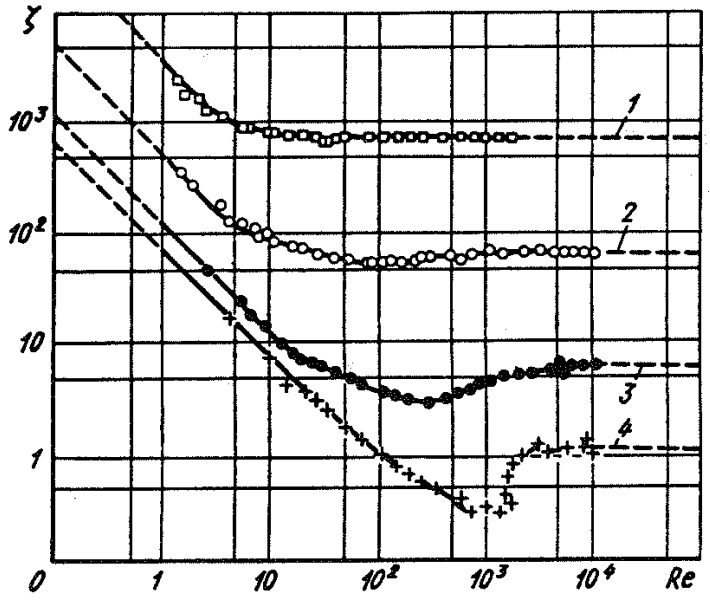

Fig. 3.10 Effects of Reynolds number on loss coefficient (Idelchik, 1994);
1) Porosity =5%; 2) Porosity =16%; 3) Porosity =43%; 4) Porosity =64%.

Fig. 3.10 shows the loss coefficient as a function of the Reynolds number (3.29) and four levels of porosity. The graph highlights that for Reynolds number higher than 1000 for intermediate porosity and 10,000 for high porosity, the Reynolds effects on the loss coefficient are negligible. A similar trend is reported in ESDU81039 (1985), where the authors suggest that for practical purposes, for an orifice plate and for multiple holes, a value of 10,000 can be taken as the critical limit value: over this threshold, the Reynolds number effects can be neglected.

The characteristics of the flow through an orifice depend on whether the jet which forms downstream of the orifice entry remains separated or whether it reattaches to the orifice wall. The influence of the ratio t/d, between thickness (t) and the hydraulic diameter (d) of the orifice, on the separation and reattachment of the flow has been investigated (Ward Smith, 1971) and various incompressible flow regimes have been identified. The corresponding flow patterns are shown in Fig. 3.11. In the fully-separated flow regime (over a range of small t/d) shown in Fig. 3.11a and Fig. 3.11b, the flow remains separated from the surface of the orifice. As t/d increases, the jet tends to converge on the inner wall of the orifice and this is known as the marginally-separated flow regime (Fig. 3.11c). With further increase in t/d, the jets just reattach to the orifice walls and immediately separate again, as shown in Fig. 3.11d. This situation can be called the marginally-reattached flow regime. In the fully-reattached flow regime (t/d large) shown in Fig. 3.11e, the flow separates from the orifice entry and, for the high Reynolds numbers under consideration, reattaches in the form of a turbulent boundary layer. The two intermediate stages of marginally-separated (Fig. 3.11c) and marginally-reattached flow (Fig. 3.11d) represent an uncertain region where, for a given value of t/d, either reattached or separated flow regimes can occur. Therefore, it is possible to identify two different

types of flow regime, distinguished in separated and reattached flow.

Except for very low Reynolds numbers (Valli *et al.*, 2009) or at conditions where compressibility effects are significant, the flow through a sharp-edged orifice initially separates from the sharp entrance edge. Downstream of this, the flow may either remain separated right through the orifice or may reattach to the wall of the orifice. The orifice t/d ratio, at which the flow changes from one condition to the other will be influenced by flow parameters such as Reynolds and Mach numbers and by geometrical parameters such as the level of porosity (ε).

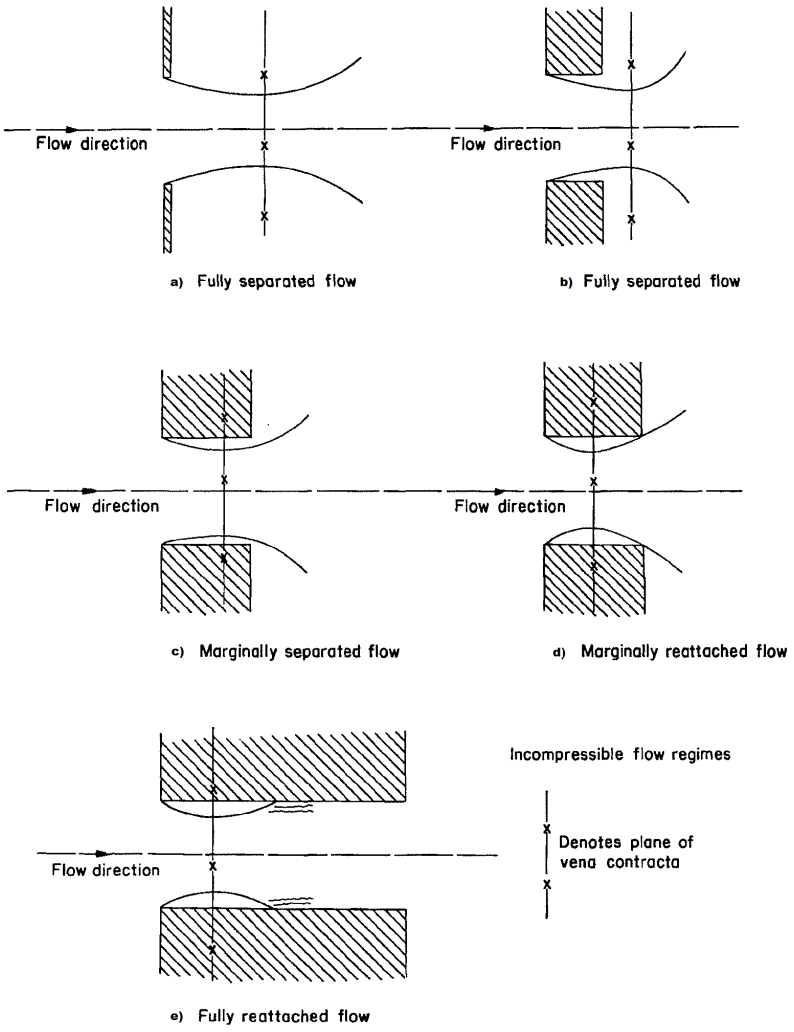

Fig. 3.11 Effect of orifice ratio t/d (ESDU81039, 1985).

Ward Smith (1971) collected a large number of experimental data for the incompressible flow loss coefficient of orifice plates, perforated plates and thick orifice plates and he suggested limits for separated flow and reattached flow. Greater scatter of the experimental data in the region of $0.6 < t/d < 1.0$ suggests that this represents a probable overlap region between the separated and reattached flow regimes. The paper highlights that the use of orifices in the overlap range t/d should be avoided

because of the uncertain nature of the flow. The experimental data are not able to define exactly the value of t/d that divides the two main flow regimes, but it is necessary to evaluate the effective value by appropriate tests. In case of flow through orifice and perforated plates, the ESDU81039 (1985) suggests to set the division between the two regimes at $t/d = 0.8$ for all values of porosity level (ε): for $t/d \geq 0.8$ reattached flow is expected while for $t/d < 0.8$ the flow should be separated.

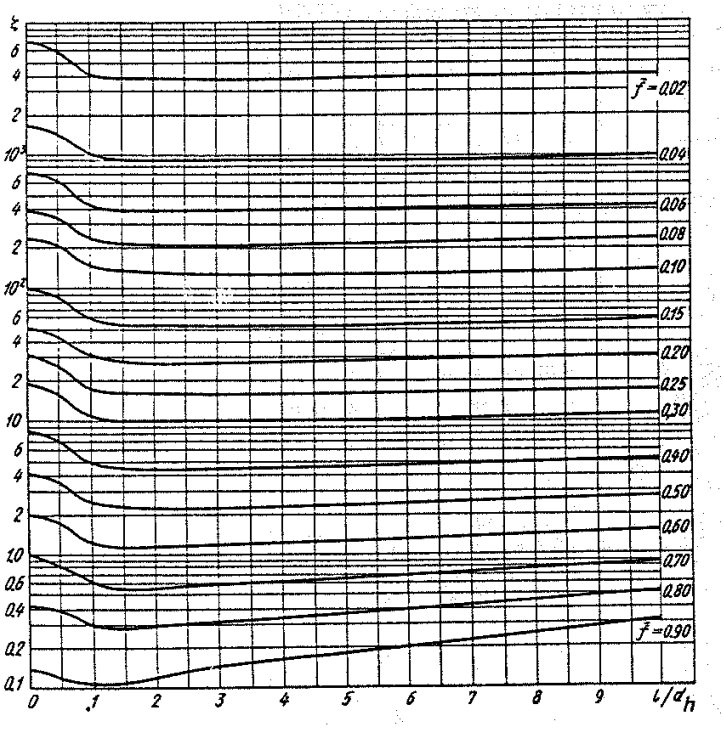

Fig. 3.12 Loss coefficient versus l/d_h ratio (Idelchik, 1994).

Fig. 3.12 reports the relationship between the loss coefficient, indicated with (ξ) and the ratio l/d_h that is an equivalent of ratio thickness-diameter t/d, in correspondence of different values of porosity level ($\overline{f}$). Considering the previous diagram given by Idelchik (1994) it is possible to notice that, in the initial part of the graph, there is a decrease of the loss coefficient. In addition, Fig. 3.12 confirms that the loss coefficient decreases up to values of the ratio l/d_h equal to 1.0; after this value, the loss coefficient can either remain stable (for low-medium porosity values) or grow (for high porosity values).

Gan and Riffat (1997) carried out some experimental and CFD tests on perforated and orifice plates with the aim to investigate the effect of the thickness-diameter ratio on the loss coefficient. They concluded that the loss coefficient decreases considerably when the thickness is increased up to half the orifice diameter. This trend is also confirmed by ESDU81039 (1985), Idelchik (1994) and Liu *et al.* (2007) and it is related to the transition between the separated and reattached flow regime.

3.4 Windbreak barriers

Since the beginning of history, in every part of the world, the human being had been trying to relate with natural elements, in particular with the wind. In this respect Kahun's location, 2.000 b.C. Egyptian town, is significant. The city was built in order to guarantee to the rich districts on the one hand a significant shelter effect from hot desert winds and on the other hand the possibility to soak up the pleasant breezes coming from the North (Borri and Briganti, 2006). Windbreaks are the earliest devices used to interact with and to mitigate windy climatic conditions in order to serve human needs. They are widely used in coastal, arid and cold areas to reduce wind and to control sand and snow drift, and have been studied in a systematic manner since the 1940's with the objective to find the optimal windbreak configuration that yields the best protection at the minimum cost (Plate, 1971). The first fences used in the past were the natural windbreaks made of trees and hedgerows, in order to defend dwelling areas and agriculture from wind storms. Thanks to the progress and development of technology and industrialization, materials used to build the barriers have become more and more varied, such as plastic, wooden, synthetic and metallic materials, with many shapes and characteristics. Some of the first serious windbreak researches started in the Dust Bowl years in the U.S. Midwest where years of removing trees and of finely tilling the soil had created a classic wind erosion problem. To analyse the effect of windbreaks, the researchers built small fences using laths. Some of the technology was borrowed from snow fences which had been in use since the 1850's and were undergoing a revival in popularity at that time. The researchers varied the spacing of the laths, then measured the effects on the wind and the erosion of the soil. They discovered that solid fences were not the best solution, but a certain porosity was required.

3.4.1 Use, characteristics and classification

The terms windbreak, wind fence, wind shelter, shelter fence and wind screen are interchangeable. The windbreaks have the objective to create a physical and artificial barrier between two portions of territory: the first one is subject to the external wind action, and the other one is internal for which it is necessary to mitigate that action. Usually when in a precise context a porous wind screen is introduced, the principal target is to be able to mitigate the main effects of the wind, such as its mean wind speed, and its turbulent component. While doing that it is likely to solve an aspect of the problem, without considering the possible consequences due to the windbreak introduction, for example protecting an urban area, and disregarding the effects and interactions of the presence of barriers on the interested area and on the surrounding one. The main objective of this kind of screens is to create a wide shelter area behind the barrier which can be used with different aims. The efficiency of a fence depends on many parameters which are often very complex to identify and evaluate.

The best screen, from the point of view of protection, as it is easy to understand, is represented by a very high and solid fence which contrasts the wind flow. Unfortunately this can be realized very rarely due to many reasons. The main problems are linked to: the environmental impact of the structure on the territory, the large costs of building a filled screen, the internal forces due to the wind loads the fence

is subject to and the bad aerodynamic behaviour of the barrier. Consequently there is the need to conceive screens with a certain porosity defined as the ratio of the screen area which the flow passes through to the total screen area.

The most important structural feature of a fence is its porosity (Heisler and Dewalle, 1988). The function of a windbreak is to reduce wind velocity within a certain distance. Maximum wind reductions are closely related to porosity, with low porosity producing the maximum reductions. However, fences with very low porosity create more turbulence downwind than medium and high-porosity fences. The higher turbulence produced by low-porosity fences may result in the recovery of mean horizontal wind velocities to levels equal to upwind velocities at a distance closer to the fence, thereby decreasing the shelter distance [Plate (1971); Laws and Livesey (1978); Perera (1981); Lee and Kim (1999)]. Consequently, there should be a fence porosity that provides the optimal shelter effect by balancing the reduction of wind speed with the effects on shelter distance.

Windbreaks are now in use in many applications throughout the world. Even if they are applied in different fields and with various implementations, the aerodynamic design fundamentals are the same. The principal application fields are:

- Agriculture and horticulture, with the aim to protect and defend plantations;
- Industrial sites use windbreaks to avoid blowing dust onto their neighbours;
- Mines and desert areas, controlling sand and dusts;
- Main roads and highways, to mitigate the wind effect on vehicles;
- Bridges and footbridges, to protect vehicular traffic and pedestrian comfort;
- Pollution dispersion's control in particular contexts.

Fences that are always constructed to have optical porosities greater than zero (Guan *et al.*, 2003) are important artificial windbreaks. They can be classified as upright, horizontal, griddled, holed-plank fences and wind screens (Fig. 3.13), depending on the available materials (Dong *et al.*, 2007). One of the main aspects in building a porous wind fence is the geometry characterization of its components. Upright fences, horizontal fences and gridded fences are usually made of wooden bars, bunches of straws or reeds, or tree branches and are widely used to check drifting sand and drifting snow because of their easy availability, low cost and simple construction. If the fence is required to be more durable and stronger, it is very common the use of metallic materials, especially light alloys consisting of a combination of aluminium, copper, zinc, manganese, silicon or magnesium. In many applications it is possible to find also barriers made of plastic materials, as polymethylmethacrylate, that provide a very good mechanical strength and a low visual impact as they are often used in a transparent version.

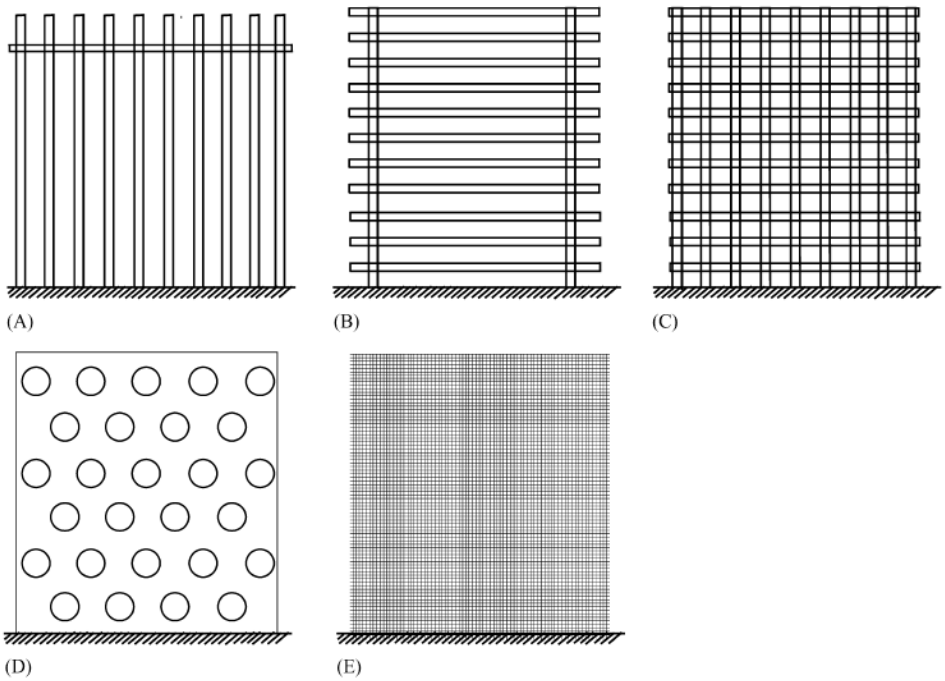

Fig. 3.13 Types of fences: A) upright fence; B) horizontal fence; C) gridded fence; D) holed-plank fence; E) wind screen (Dong *et al.*, 2007).

The horizontal elements which form the windbreaks have sections of different type: the classical rectangular shape, circular, the one typical of metallic structural elements, up to the most progressive and complex like wing profiles and ropes consisting of a single or a group of steel wires.

Holed-plank fences are mostly realized with panels of holed and pressed plates, in standard steel, stainless steel or aluminium. In this kind of barriers there is a big variety of designs of holes, different for shapes (circular, square, hexagonal, oblong or with many possible geometric variants) and for position (in staggered rows, linear or random). They are widely used to build road windbreak shields and façades for hi-tech buildings, or in industrial dust control systems.

Wind screens are grids, characterized by low values of porosity and made of synthetic materials, such as HDPE polyethylene and polyester (texture, non-texture or crossed mesh), or metallic micro-holed panels: they are used in agriculture to protect the plantations, to control the dusts and to decrease pollutants. For each one of these five kinds of screens a fundamental role is played by porosity, in particular by the geometry of the openings, because with identical porosity but different kind of screen (for example horizontal fence or gridded fence) there are completely dissimilar flow responses and consequently different shelter effects.

The height of the fence is also very important as it should be able to protect all the internal levels of the area to be covered. Therefore the screen height is a fundamental design parameter that, as well as the porosity, has to be evaluated very carefully when applying aeolian mitigation measures. The first tests carried out in the 1960's on wind and snow fences in wind tunnel took into account only the efficiency or non-efficiency of a screen, assuming the length of protected area as a

multiple of the fence height.

Another category of wind barriers includes the fences typical of naturalistic engineering, the so-called *living windbreaks* (Fig. 3.14), that are artificial barriers made of vegetable species carefully chosen and allocated in order to create a protected zone from the wind flow. Brandle and Finch (1991) carried out a very important study trying to understand the behaviour of the living windbreaks. They considered the shield effect of the natural screen consisting of deciduous and conifer during their realization, their complete development in time and during seasonal changes.

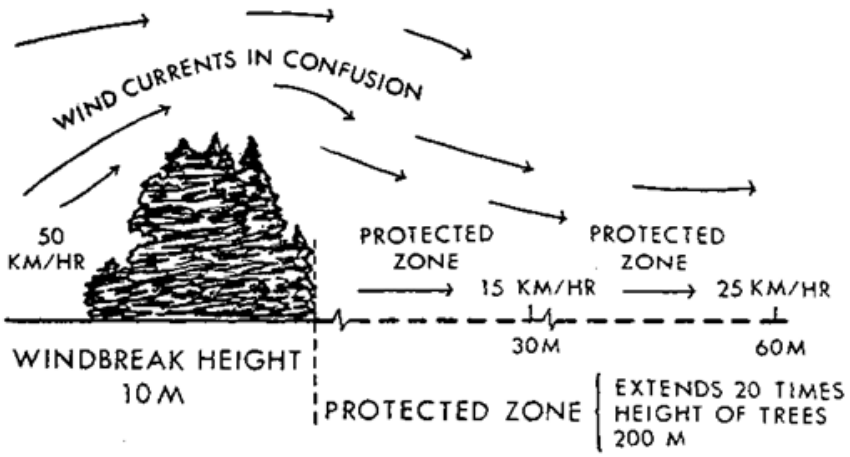

Fig. 3.14 Effects of living windbreaks (Brandle and Finch, 1991).

3.4.2 State of art on windbreak aerodynamics

The majority of studies related to the flow around windbreaks or other porous structures do not usually consider the physical aspects of the problem. They tend to approach it in a simplified and qualitative manner, especially trying to define the optimal porosity of the screens. These efforts include field measurements that are difficult to validate [Hagen and Skidmore (1971); Miller *et al.* (1975) Jacobs (1985); Bofah and Alhinai (1986); Schwartz *et al.* (1995); Wilson (1997); Boldes *et al.* (2001)], and simulations in the wind tunnel on small scale models without defining a law of scale [Iversen (1981); Raju *et al.* (1988); Papesch (1992); Judd *et al.* (1996); Lee *et al.* (2002); Guan *et al.* (2003); Park and Lee (2003)]. The previously mentioned studies had the aim to perform flow visualization analysis using the non-intrusive PIV technique on small samples of barriers. Finally some other studies have been carried out by CFD simulations [Wilson (1985); Fang and Wang (1997); Pattone *et al.* (1998); Packwood (2000); Vigiak *et al.* (2003); Alhajraf (2004)].

A common way to explain the aerodynamic effects of a porous barrier is by considering its resistance to the flow, or in dimensionless terms by using the drag coefficient [Raine and Stevenson (1977); Jacobs (1985)]. Many publications show that the drag coefficient decreases with the increasing of the porosity of the screen [Hoerner (1965); Hagen and Skidmore (1971); Seginer (1972); Wilson (1985); Guan *et al.* (2003)]. This entails that shields having low porosity are able to provide a very

good shelter effect and that completely solid screens (with porosity equal to zero) are the best if one considers only the shelter effect. The drag coefficient only cannot define the optimal porosity even if it is the fundamental parameter to understand the interference with the air flow due to the presence of screens. There are also other parameters involved that are able to define and describe the shelter effects and the aerodynamics of these particular structures.

Several authors have concentrated their efforts in the research of the optimal porosity value for a given examined system. A review of published results shows that the optimal porosity ranges from 0.3 to 0.5. Hagen and Skidmore (1971) field measurements indicated that a windbreak with a porosity of 0.4 produced the lowest wind velocity over the largest downwind area.

Fig. 3.15 Blowing-sand shelter system in the Chinese desert (Dong *et al.*, 2007).

Field tests by Lin *et al.* (1984) on the south-eastern edge of China's Tengger Desert suggested that porosities of $0.3 \div 0.4$ should be used for fences $0.8 \div 1.0$ m tall to avoid sand accumulation upwind of the fence (Fig. 3.15). The wind tunnel results of Lee *et al.* (2002) showed that a porous wind fence with a porosity of 0.3 was the most effective for abating windblown sand particles because it produced the greatest decrease in the wind velocity required to initiate sand movement behind the fence. The wind tunnel simulation by Dong *et al.* (2006) indicated that fences with porosities of $0.3 \div 0.5$ (depending on fence height) had the maximum relative threshold wind velocity and maximum effective shelter distance, and thus were most suitable for controlling wind erosion. As it is possible to expect there must be some inherent link between shelter efficiency and the flow regime characteristics behind fences, but how these parameters are correlated is not clear, yet.

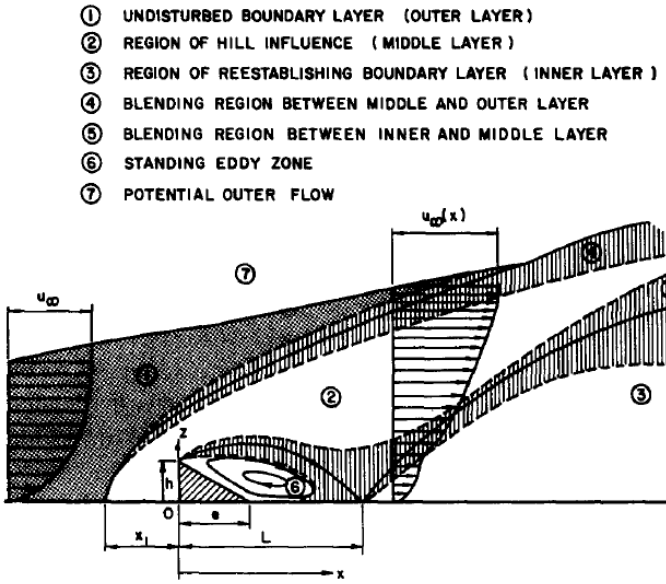

Fig. 3.16 The flow zones of a boundary layer disturbed by a shelter belt (Plate, 1971).

The complexity of the flow around a wind shelter is evident from the scheme shown in Fig. 3.16. A boundary layer flow is approaching a wedge-shaped obstruction which has been placed on a flat plate. Not less than seven flow zones can be distinguished. In Zone 1, far upstream from the wedge, the flow field is mostly determined by the condition of undisturbed boundary layer. In Zone 2, the flow field is displaced and distorted due to the presence of the wedge, with the lower boundary of Zone 2 given by the separation induced shear layer which starts at the edge of the wedge and forms the transition to the highly retarded flow in Zone 3. When the wedge is solid, back flow may occur, leading to a separation bubble with a reattachment point, at a distance L downstream of the wedge. Downstream of the reattachment point the flow is again in the direction of the oncoming wind, and in the layer 5 it gradually increases in velocity until at some large distance the inner layer 5 has blended with the outer flow. Therefore a new and thicker boundary layer is formed which adjusts to the local boundary conditions at the ground until the effect of the obstruction can only be inferred by comparing the boundary layer thickness with that one which would have existed if the wedge had not been there. The flow in the region downstream of reattachment is due to the adjustment of an initial velocity profile to the local boundary conditions, and can be determined in principle from an initial profile downwind of reattachment by methods of boundary layer calculations, as Plate (1971) for distances larger than $35h$, where h is the height of the obstruction.

Several researchers [Perera (1981); Borges and Viegas (1988); Wilson (1997); Lee and Kim (1998); Lee and Kim (1999); Dong *et al.* (2006)] attempted to define the optimal porosity by measuring and analysing velocity, turbulence, shear stress, pressure and sediment susceptibility to wind transport behind fences (Fig. 3.17). They found noticeable changes in the flow characteristics at porosity levels around 0.3 or 0.4. Nevertheless, Raine and Stevenson (1977) demonstrated in their tests that a

fence with a porosity of 0.2 gave the best reduction in leeward mean velocity.

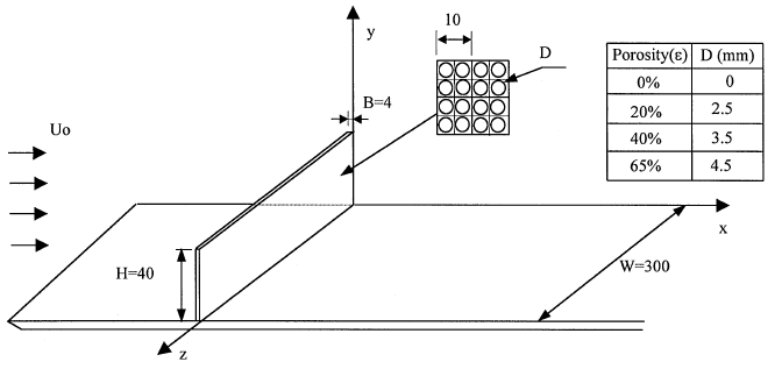

Fig. 3.17 Experimental set-up of windscreens in wind tunnel (Lee and Kim, 1999).

Perera (1981) found that the Reynolds shear stress and turbulent kinetic energy were strong behind the fence when the porosity was less than 0.3, whereas the bleed flow (air passing through the fence rather than over it) was strong when the porosity was greater than 0.4. By measuring the velocity field and surface pressure distributions (on the windward side of the barrier), which directly influence the shelter effect produced by wind fences, Lee and Kim (1998, 1999) found a porous fence with a porosity level of $0.3 \div 0.4$ to be the most effective for reducing the mean velocity and surface pressure fluctuations.

Porous fences have been widely used also as turbulence manipulators. They have been also chosen to reduce the flow velocity or abating wind erosion by small particles transported by the flow. For the cases of screens and grids, Baines and Peterson (1951) mentioned that the screens should have porosity of more than 50 % to avoid the jet coalescence effect for minimizing turbulence generation from the screens. Many previous studies on the porous fence had revealed that the most important parameter affecting the fence wake is the porosity. Castro (1971) found that there was no vortex street behind a porous plate located in a uniform flow, when its porosity is larger than 30 %. Perera (1981) studied the wake flow behind porous fence in a simulated atmospheric boundary layer using a pulsed hot-wire anemometer system. No recirculation region behind the fences with porosity above 30 % was observed. He mentioned that the hole shape was a less important factor, compared to other parameters affecting the wake flow characteristics such as the dimension of the openings and the thickness of the fence. However, Raine and Stevenson (1977) claimed that fine holes would be more efficient in reducing the turbulence level. Villermaux and Hopfinger (1994) investigated the flow structure of co-flowing jets behind a perforated plate of low porosity (13 %), located in a uniform flow. They found a low-frequency oscillation of merging distance at moderate values of jet Reynolds numbers.

However, technological limitations have prevented precise measurements of the characteristics of flow regimes, particularly near the fences. The leeward flow has often been measured using conventional anemometers, but hot-wire anemometers

provide much more detailed information about turbulence characteristics and were soon used by researchers. However, both conventional anemometers and hot-wire anemometers have difficulties in obtaining detailed measurements close to fences and both may influence the flow field.

The development of particle image velocimetry (PIV) improved the ability to measure the flow velocity field because the technique is non-intrusive, and this is the reason why it is finding more and more applications in theoretical studies. The hole diameter effect on the turbulence wake for porous fences with the same porosity has not been deeply studied yet. Therefore, a detailed study on this effect is still needed to understand the wake characteristics and to optimize the fence hole size. After the success of their publication in 1999, Lee *et al.* (2002) have developed an interesting study to evaluate the influence of hole diameter on the wake behind the screens. To do that, they have considered three different types of windscreens with the same porosity of 38.5 % but with different hole dimensions. The tests have been carried out in a water tunnel and the velocity and turbulence fields downstream of the fences have been determined with the Particle Image Velocimetry technique. The results showed that the screen with the best behaviour had the smallest hole diameter, because this configuration was able to decrease the wind velocity upstream of the fence and at the same time to generate few and small vortices downstream (Fig. 3.18). Lee *et al.* (2002) also showed that the larger is the hole diameter, the larger is the dimension and the number of vortices.

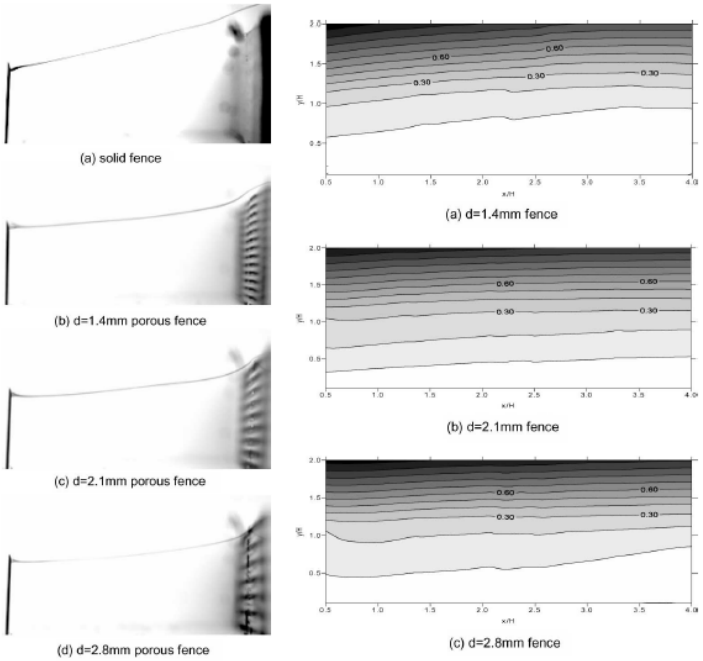

Fig. 3.18 Upstream flow visualizations and velocity contour maps in the region behind the porous fence (Lee *et al.*, 2002).

The most frequent design requirement is the maximum wind speed to be guaranteed up to a certain distance. The selection of the most efficient shelter has been the

objective of much of the research on windbreaks. Numerically the problem is very complex since it requires the solution of the full turbulent Navier-Stokes equations for a complete treatment and it is not surprising that most wind fence researches have been done experimentally and by trial and error, by evaluating the wind speed reduction of existing belts. Nageli (1941) obtained an optimum solution by showing that a medium dense screen reduced the velocity by at least 20 % over a larger distance than either a very dense screen or one with very high porosity. Similar results were found in the wind tunnel by Buccolieri *et al.* (2009) for a living windbreak. As far as shape is concerned, an optimum generally accepted solution has not been found and field researches were conducted on existing shelter fences for a post facto assessment of their effect.

The only theoretical formulation of the flow around a wind fence was given by Kaiser (1959) who assumed that the sheltering results from diffusion of the momentum defect downwind from the shelter as if it were a passive scalar. This model is physically unrealistic and somewhat oversimplified, but it does point out the decisive role played by drag in the sheltering problem and it leads to a prediction of velocity profiles in the sheltered region. Indeed, it would be too much to expect an analytical solution which covers all details of the shelter belt flow.

Another important contribution was given by Dierickx *et al.* (2003) who carried out some tests in the wind tunnel on windbreak shields positioned perpendicularly to the wind flow, inclined against the wind and in the wind direction respectively of 30°, 45° and 60°(Fig. 3.19).

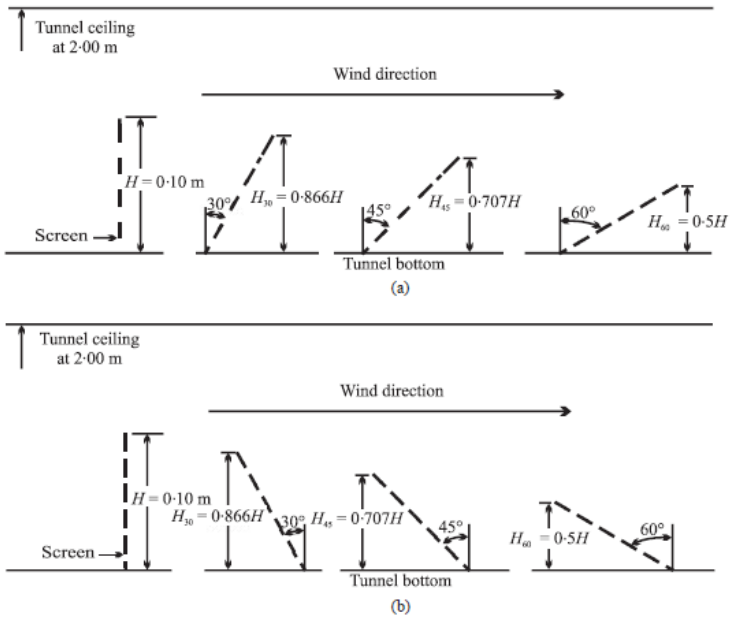

Fig. 3.19 Position of the wind barriers (a) in the wind direction and (b) against the wind direction, as studied in the wind tunnel (Dierickx *et al.*, 2003).

The analysed screens had porosities of 35.7 %, 49.1 %, 62.6 %; only one had zero porosity. During the tests a technical roughness was introduced on the floor of the wind tunnel in order to simulate the logarithmic profile of the wind velocity. In the

other cases the tests were performed with smooth flow. During all the simulations the wind velocity downstream of the windbreak screens was measured by a row of hot wire anemometers vertically lined up in the centre of the analysed fence. After the wind tunnel test campaign, it was possible to state that the inclined screens with the best behaviour in terms of shelter effects were the ones leaning against the wind and not in its direction. However, for each porosity value the best screens were the vertical ones because they had the height vertical component larger than the inclined ones. Furthermore, the study suggests that strong wind velocity reductions, even better than vertical screens, would be possible with an inclined screen of 30°, with low porosity and with the same projected height of the vertical fences.

An additional important issue to mention in this brief review is the characterization of the wind load on this kind of structures. It strongly depends on the resistance offered to the flow, which may be characterized by the loss and drag coefficients. Although the wind loads on such structures are similar to those on solid structures the flow through the porous barriers modifies the pressure distribution around the barrier and therefore requires special consideration. In general the wind loads on planar porous surfaces are affected by the porous medium characteristics and the overall geometry of the structure: the size, shape and angle to the wind. Richards and Robinson (1999) made tests in the wind tunnel at Auckland University on different types of wind fences in order to calculate the loss and drag coefficients. The first barriers analysed consisted of round wire mesh and it was pointed out that the loss coefficient of the screens was very much linked to the porosity level. For other screens, such as the holed-plank fences, it was noticed that the loss coefficient was not only function of the porosity of the screen but also of the geometrical aspects of the holes.

3.5 Concluding remarks

In this chapter the state-of-the-art on the flow through porous screens and windbreak barriers is reviewed. The study of flow through screens is analysed following two different methodologies: the porous media approach and the hydraulic resistance one. In the porous media approach three different flow models are encountered during the review: the Darcy model (laminar flow regime), the Forchheimer equation (transition regime) and the non-linear model (turbulent regime). Due to the complexity of the phenomenon the transition between the three flow regimes is not clearly identified by the Reynolds number alone.

In the second approach the hydraulic resistance for incompressible flow through screens is identified by the loss coefficient. The loss coefficient (K) can be separated into two different functions: one depending on porosity and the other on the Reynolds number. In case of perforated plates the effects of Reynolds number, screen thickness and diameter of the holes on K are discussed.

Finally, a general overview on uses, characteristics and classifications of the windbreak barriers is outlined. In addition, with the aim to highlight the general problems encountered by researchers a brief literature review is presented.

Chapter 4

Scaling problems of porous elements in wind tunnel

4.1 Dimensional analysis and similitude

A mathematical model describes the behaviour of a physical system in terms of mathematical equations. These equations represent the relations between the relevant properties of the system under consideration. In these models the fundamental characteristics are *parameters* and *variables*. There are two different types of variables: *dependent* and *independent*. For example, in mechanical systems one is often interested in the position of the different points as a function of time, so in these systems the positions act as the dependent variables and time as the independent variable. Parameters are properties like masses, lengths, temperatures, etc. The *solution* of a mathematical model is known if it is possible to determine the relations between dependent and independent variables.

4.1.1 Dimensions and units

The most important variables or parameters involved in a model correspond to physical properties and they have physical dimensions. The *fundamental dimensions* used in this work are given in the following table:

Dimension	**Symbol**	**SI Unit**
Length	L	m (meter)
Mass	M	kg (kilogram)
Time	T	s (second)
Temperature	Θ	°C (degree Celsius)
Current	I	A (Ampere)

Table 4.1 Five fundamental dimensions and units.

The dimension of any physical quantity can be expressed in terms of combinations of the five fundamental dimensions. For most quantities this is clear from the definition. For example:

Quantity	**Dimension**	**SI Unit**
Area	L^2	m^2
Volume	L^3	m^3
Velocity	LT^{-1}	ms^{-1}
Acceleration	LT^{-2}	ms^{-2}
Mass density	ML^{-3}	$Kg\ m^{-3}$

Table 4.2 Characteristic derived quantities.

In other cases the dimension of a quantity is deduced from the fact that all terms in a particular equation must have the same dimension. For example, the dimension of force directly follows from the second Newton's law, which states that for a single mass, the mass times the acceleration equals the total force exerted on the mass (in standard notation, $F = ma$). The dimension of a force F, denoted as $[F]$, is equal to the dimension of the product of mass (m) and acceleration (a). Since $[ma] = [m][a]$, it can be concluded that $[F] = MLT^{-2}$. In this way other derived dimensions can be simply defined as:

Quantity	**Dimension**	**SI Unit**
Force	MLT^{-2}	$kg\ ms^{-2}$
Energy	ML^2T^{-2}	$kg\ m^2s^{-2}$
Pressure	$ML^{-1}T^{-2}$	$kg\ m^{-1}s^{-2}$
Dynamic viscosity	$ML^{-1}T^{-1}$	$kg\ m^{-1}s^{-1}$
Kinematic viscosity	L^2T^{-1}	m^2s^{-1}

Table 4.3 Other derived quantities.

In dimensional analysis, which will be treated in the next paragraphs, dimensionless quantities play a central role. The existence of these so-called dimensionless numbers allows to draw important conclusions about the system without solving the governing mathematical model.

4.1.2 Modelling and similitude

Although many practical engineering problems involving fluid mechanics can be solved by using equations and analytical procedures, there is still a large number of problems that rely on experimentally obtained data for their solution. The solution of many problems is achieved through the use of a combination of analytical methods and experimental data. Thus, engineers working on fluid mechanics problems should

be familiar with the experimental approach to these problems so that they can interpret and make use of data obtained by others, or be able to plan and execute the necessary experiments in their own laboratories. An obvious goal of any experiment is to make the results as widely applicable as possible.

Most engineering projects involving structures, aircraft, ships, rivers, harbours, dams, air and water pollution, and so on, frequently involve the use of models. Although the term *model* is used in many different contexts, the *engineering model* generally conforms to the following definition. A model is a representation of a physical system that may be used to predict the behaviour of the system in some desired respects. The physical system for which the predictions are to be made is called the prototype. Even if analytical or computational models may also conform to this definition, our interest will focus on physical models, that is, models that resemble the prototype but are generally of a different size, may involve different fluids, and often operate under different conditions (pressures, velocities, etc.). Usually a model is smaller than the prototype. Therefore, it is more easily handled in the laboratory and less expensive to construct and operate than a large prototype. Occasionally, if the prototype is very small, it may be advantageous to have a model that is larger than the prototype so that it can be more easily studied. With the successful development of a valid model, it is possible to predict the behaviour of the prototype under a certain set of conditions. To achieve this aim, the concept of *similitude* is often used so that measurements performed on one system (for example, in the laboratory) can be used to describe the behaviour of similar systems (outside the laboratory). From these model studies, empirical formulations can be developed, or specific predictions of one or more characteristics of similar systems can be made. To do this, it is necessary to establish the relationship between the laboratory model and the prototype.

The fundamental cornerstone of experimentation on models is the principle of similitude. The similitude is a concept used in engineering, which describes a real system using a physical scaled model. In order to get a complete similitude between model and prototype three necessary conditions have to be respected: geometric similitude, kinematic similitude and dynamic similitude. The geometric similitude indicates that the model has to have the same shape of the prototype, or in other terms, it is necessary to have one single relationship between the scale lengths of model and prototype. The kinematic similitude indicates that exists a similarity of motion between prototype and model. The condition is reached if the ratios of the velocity and the acceleration at the corresponding points in the model and at the corresponding points in the prototype are the same. The geometric similitude is the necessary condition to have kinematic similitude. In particular if the kinematic similitude is fulfilled the flow net formed by streamlines and the equipotential line for the model and the prototype are geometrically similar (i.e., changing in the scale, flow net of model and the prototype can be superimposed). If both geometric and kinematic similitude exist between the model and the prototype, then dynamic similitude for model and the prototype is attained. This third condition means that the ratio between all forces acting on homologous points in the model and the prototype are equal. Fig. 4.1 summarizes in a graphical way the three conditions of similitude.

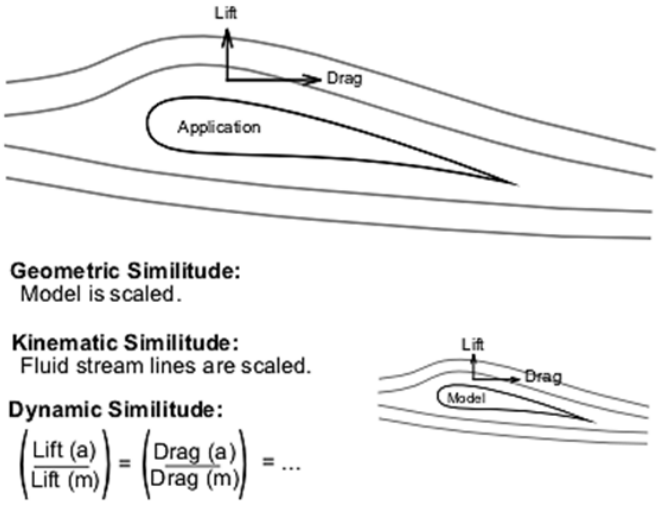

Fig. 4.1 The three conditions of similitude.

To determine the conditions of similarity a technique called dimensionless analysis or dimensional analysis is very useful and effective. The principal applications of dimensional analysis are:

- to obtain dimensionless parameters that may help in the design phase of the investigations (physical or numerical) and in the comprehension of the results;
- to obtain scaling laws so that starting from the model behaviour it is possible to trace the prototype one;
- to hypothesize the relationship between the involved dimensionless parameters.

This technique was born in fluid mechanics and it is very important when it is necessary to lead and design experimental campaigns of measurement.

4.1.3 Dimensional analysis and Π theorem

Nondimensionalizing a mathematical model is a constructive way to formulate the model in terms of dimensionless quantities only. A big achievement is that dimensional analysis yields insight in the scaling relations of the system without using knowledge of any governing equation. An advantageous corollary is that the total number of variables and/or parameters is minimal. Reduction of the number of parameters is also the purpose of scaling, a technique to be dealt with at the end of this section. However, dimensional analysis is more general than scaling because it is based on a transformation of both variables and parameters on the same footing, whereas in scaling only the variables are transformed. Another difference is that scaling starts from the governing equations, whereas dimensional analysis more basically starts from the dimensions involved in the system, and it may even predict from them some quantitative features of the model without knowledge of the model equations. The premise of dimensional analysis is that the form of any physically significant equation must be such that the relationship between the actual physical quantities remain valid independently of the magnitudes of the base units.

4.1.3.1 Step 1: The independent variables

Supposing to be interested in some particular physical quantity Q_0 that is a *dependent variable* in a well defined physical process or event, the first and most important step in dimensional analysis is to identify a *complete* set of *independent* quantities $Q_1, ..., Q_n$ that determines the value of Q_0,

$$Q_0 = f(Q_1, Q_2, ..., Q_n) \tag{4.1}$$

A set $Q_1, ..., Q_n$ is *complete* if, when the values of the variables are specified, no other quantity can affect the value of Q_0, and *independent* if the value of each variable can be adjusted arbitrarily without affecting the value of any other variable.

Starting with a correct set $Q_1, ..., Q_n$ is as important in dimensional analysis as it is in mathematical physics to start with the correct fundamental equations and boundary conditions. If the starting point is wrong, so is the answer. The relationship expressed symbolically in equation (4.1) is the result of the physical laws that govern the phenomenon of interest. Its form must be such that, once the values $Q_1, ..., Q_n$ are specified, the equation holds regardless of the base units in terms of which the quantities are measured.

4.1.3.2 Step 2: Dimensional considerations

At this point it is important to create a list that contains the dimensions of the dependent variable Q_0 and the independent variables $Q_1, ..., Q_n$. As discussed in §4.1.1, each variable can be written in the system M, L, T. More in detail, all physical quantities have dimensions which can be expressed as products of powers of the set of base dimensions. Alternatively, it is possible to express the dimension of one quantity as a product of powers of the dimensions of other quantities which are not necessarily base quantities. For example, supposing to deal with a purely mechanical problem, all quantities have dimensions of the form:

$$[Q_i] = L^{l_i} M^{m_i} T^{t_i} \tag{4.2}$$

where: the exponents l_i, m_i and t_i are dimensionless numbers that follow from each quantity definition.

A subset $Q_1, ..., Q_k$ of the set $Q_1, ..., Q_n$ is *dimensionally independent* if none of its members has a dimension that can be expressed in terms of the dimensions of the remaining members. The subset is also *complete* if the dimensions of all the remaining quantities $Q_{k+1}, ..., Q_n$ of the full set *can* be expressed in terms of the dimensions of the subset $Q_1, ..., Q_k$.

From the complete set of physically independent variables $Q_1, ..., Q_n$, a *complete, dimensionally independent subset* $Q_1, ..., Q_k$ $(k \leq n)$ is chosen, and the dimensions of each of the remaining independent variables $Q_{k+1}, ..., Q_n$ and of the dependent variable Q_0 are expressed as a product of powers of $Q_1, ..., Q_k$.

The dimensionally independent subset $Q_1, ..., Q_k$ is selected by trial and error. Its variables may be chosen in different ways, but the *number* k of dimensionally independent quantities, in the full set $Q_1, ..., Q_n$, is unique to the set, and cannot exceed the number of base dimensions which appear in that set. For example, if

the dimensions of $Q_1, ..., Q_n$ involve only length, mass, and time, then $k \leq 3$. Having chosen a complete, dimensionally independent subset $Q_1, ..., Q_k$, the dimensions of Q_0 and the remaining quantities $Q_{k+1}, ..., Q_n$ can be expressed in terms of the dimensions of $Q_1, ..., Q_k$. These will have the following form:

$$[Q_i] = [Q_1^{N_{i1}} Q_2^{N_{i2}} \ ... \ Q_k^{N_{ik}}] \tag{4.3}$$

if $i > k$ or $i = 0$. The exponents N_{ij} are dimensionless integers numbers and in most cases can be found quickly by inspection, although a formal algebraic method can be used. The formal procedure can be illustrated with an example where length, mass and time are the only base quantities, in which case all dimensions have the form of equation (4.2). Considering Q_1, Q_2, and Q_3 as the complete dimensionally independent subset and equating the dimension given by formula (4.2) with that of equation (4.3), are obtained three expressions:

$$l_i = \sum_{j=1}^{3} N_{ij} l_j, \tag{4.4a}$$

$$m_i = \sum_{j=1}^{3} N_{ij} m_j \tag{4.4b}$$

$$t_i = \sum_{j=1}^{3} N_{ij} t_j. \tag{4.4c}$$

which can be solved for the three unknowns N_{i1}, N_{i2}, and N_{Ni3}.

4.1.3.3 Step 3: Dimensionless variables

Now it is necessary to define *dimensionless* forms of the $n-k$ remaining independent variables by dividing each one with the product of powers of $Q_1, ..., Q_k$ which has the same dimension,

$$\Pi_i = \frac{Q_{k+i}}{Q_1^{N_{(k+i)1}} Q_2^{N_{(k+i)2}}, ..., Q_k^{N_{(k+i)k}}} \tag{4.5}$$

where: $i = 1, 2, ..., n-k$ and a dimensionless form of the dependent variable Q_0,

$$\Pi_0 = \frac{Q_0}{Q_1^{N_{01}} Q_2^{N_{02}}, ..., Q_k^{N_{0k}}} \tag{4.6}$$

4.1.3.4 Step 4: Final step and Buckingham's theorem

An alternative form of equation (4.1) is the following:

$$\Pi_0 = f(Q_1, Q_2, ..., Q_k; \Pi_1, \Pi_2, ..., \Pi_{n-k}) \tag{4.7}$$

in which all quantities are dimensionless except for $Q_1, ..., Q_k$. They cannot be put into dimensionless form since they are (by definition) dimensionally independent of each other. From the principle that any physically meaningful equation must be dimensionally homogeneous, it follows that $Q_1, ..., Q_k$ must be absent from equation (4.7), that is,

$$\Pi_0 = f(\Pi_1, \Pi_2, ..., \Pi_{n-k}) \tag{4.8}$$

This equation is the final result of the dimensional analysis, and contains:

Buckingham's theorem (or Π theorem)**.** *When a complete relationship between dimensional physical quantities is expressed in dimensionless form, the number of independent quantities that appear in it is reduced from the original n to n-k, where k is the maximum number of the original n that are dimensionally independent.*

The Π theorem derives its name from Buckingham's use of the symbol for the dimensionless variables in his original paper dated 1914. The Buckingham's theorem states that, because all complete physical equations must be dimensionally homogeneous, a restatement of any such equation in an appropriate dimensionless form will reduce the number of independent quantities in the problem by k. The theorem merely confirms the *number* of dimensionless quantities that affect the value of a particular dimensionless dependent variable. It does not indicate the forms of the dimensionless variables. Nor does the Π theorem say anything about the form of the functional relationship expressed by equation (4.8). That form has to be discovered by experimentation or by solving the problem theoretically.

4.1.4 Dimensionless parameters and similitude models

In the scientific sector, a dimensionless group (or dimensionless parameter) is a quantity that describes a particular physical system. This group is usually defined as product or ratio of dimensional reference quantities, so that the result is a pure number; the choice of the reference quantities is critical, since an arbitrary choice would lead to an useless result. The dimensionless groups are widely used in all fields of science and engineering to describe a large amount of physical phenomena and to establish, under appropriate conditions, if it is possible to neglect or not the influence of less important phenomena involved in the problem. Through the theorem of Buckingham it is possible to obtain the number of dimensionless groups that are necessary to describe any physical phenomenon. In equation (4.8) Π_1, Π_2, ..., Π_{n-k} are known as similarity parameters. If two physical phenomena are similar, they will be described by the same function. Denote the similarity parameters of

the model and the prototype by the superscripts m and p, respectively. Then, if the two systems are similar, their similarity parameters must be the same:

$$\Pi_1^{(p)} = \Pi_1^{(m)}, ..., \Pi_{n-k}^{(p)} = \Pi_{n-k}^{(m)} \tag{4.9}$$

Therefore, in order to have an accurate physical model of a prototype and to guarantee the perfect similitude, first of all it is necessary to identify the similarity parameters, that are predominant in the phenomena involved and it has to be insured that they are maintained equal, passing from the model to the prototype. The principal dimensionless parameters that are used in experimental fluid dynamics are reported in (Table 4.4).

Dimensionless group	**Name, symbol**	**Interpretation**
$\frac{\rho V \ell}{\mu}$	Reynolds number, Re	$\frac{\text{inertial force}}{\text{viscous force}}$
$\frac{V}{\sqrt{g\ell}}$	Froude number, Fr	$\frac{\text{inertial force}}{\text{gravitational force}}$
$\frac{p}{\rho V^2}$	Euler number, Eu	$\frac{\text{pressure force}}{\text{inertia force}}$
$\frac{\rho V^2}{E_\nu}$	Cauchy number, Ca	$\frac{\text{inertial force}}{\text{compressibility force}}$
$\frac{V}{c}$	Mach number, Ma	$\frac{\text{inertial force}}{\text{compressibility force}}$
$\frac{\omega \ell}{V}$	Strouhal number, St	$\frac{\text{inertial (}\textit{local}\text{) force}}{\text{inertia (}\textit{convective}\text{) force}}$
$\frac{\rho V^2 \ell}{\sigma}$	Weber number, We	$\frac{\text{inertial force}}{\text{surface force tension}}$

Table 4.4 Dimensionless groups in fluid mechanics.

Variables: *gravity acceleration, g; bulk modulus, E_ν; characteristic length, ℓ; density, ρ; frequency of oscillating flow, ω; pressure, p, Δ_p; speed of sound, c; surface tension, σ; velocity, V; dynamic viscosity, μ.*

The list is obviously not exhaustive but indicates a broad range of variables likely to be found in a typical problem. Fortunately, not all of these variables are encountered in all problems. However, when combinations of these variables are present, it is standard practice to combine them into some of the common dimensionless groups (Π terms). It is also often possible to provide a physical interpretation for the Π terms which can be helpful in assessing their influence on a particular application.

Equation (4.9) provides the model design conditions, also called similarity requirements or modelling laws. If it is possible to maintain equal all the Π terms passing from the model to the prototype, this condition is called complete similitude or true model. Although the general idea behind establishing similarity require-

ments for models is straightforward, usually it is not possible to carry out analysis on model in complete similitude with the prototype, or rather, it is impossible to maintain all dimensionless parameters equal passing from the model to the reality. If one or more of the similarity requirements are not met, for example, for a problem characterized by two Π terms, if $\Pi_2^{(p)} \neq \Pi_2^{(m)}$ then it follows that the above equation $\Pi_1^{(p)} = \Pi_1^{(m)}$ is not true. Models for which one or more of the similarity requirements are not satisfied are called distorted models. In this case it is necessary to establish an incomplete similitude, and guarantee the equality of only these parameters that mainly characterize the phenomena. Distorted models are rather common, and they can be necessary for a variety of reasons. Distorted models can be successfully used, but the interpretation of results obtained with this type of model is obviously more difficult than the interpretation of results obtained with true models for which all similarity requirements are met. There are no general rules for handling distorted models, and essentially each problem must be considered separately. The success of using distorted models depends on a large extent on the skill and experience of the investigator responsible for the design of the model and in the interpretation of experimental data obtained from the model.

4.2 Modelling of porous structures

The fundamental cornerstones of modelling are particular rules that enable to extend to reality what is measured at small scale in the wind tunnel. This practice finds an important basis in the dimensionless analysis and similitude criteria. Maintaining the same key parameters between the wind tunnel model and the real scale, it is possible to extend one-to-one the results and to analyse with tests at small scale what is very difficult to measure in reality. Obviously there are some difficulties when the exact equality between the similitude parameters cannot be maintained. As regards the scale modelling, it is hard to represent at the common wind tunnel scales the fundamental elements of the prototype that have reduced dimensions compared to the predominant ones.

Fig. 4.2 Windbreak shields on a railway.

Considering the case of wind-tunnel modelling of road with windbreak shields, it is very complex to analyse the real shelter effects offered by the barrier and the related behaviour. In fact the screens are made of small elements, and they are difficult to represent at reduced scale (Fig. 4.2). Other examples where the scale modelling is hard to realize refer to the Aeolian loads evaluation on high-rise buildings with permeable façades, or the control and reduction of air flow turbulence in such particular areas where very high standards are required. Consequently the objects that are more complex to study and assess are those which can be schematized like porous media and that cannot be treated as solid surfaces.

4.2.1 Dimensional analysis of porous elements

In order to study an innovative problem, like the modelling in wind tunnel of porous elements, it is important to correctly understand the variables involved in the studied system. A good instrument to do that is the dimensionless analysis or more in particular the results of dimensionless analysis could be an important starting point to solve the problem.

In this work the reference porous element is represented by a metallic perforated thin plate. The fundamental characteristics of porous materials, consisting of holes, are represented by porosity (ε), the index able to express the relationship between the voids respect to the filled parts, dimensions and geometrical shape of the holes and thickness. Fig. 4.3 reports two different kinds of perforated plates, the first with round holes and the second with square holes.

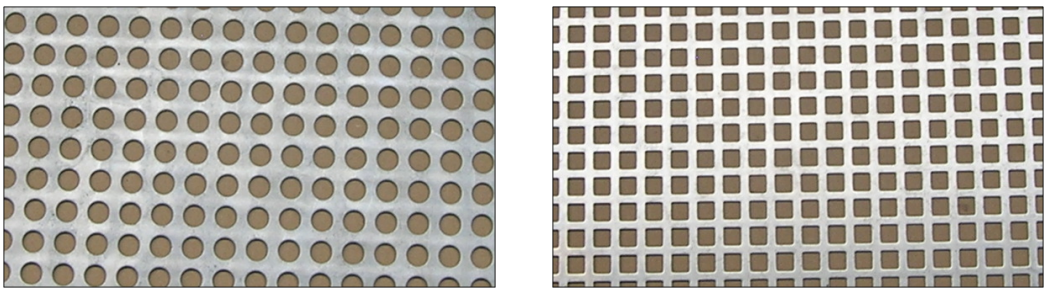

(a) Round holes (b) Square holes

Fig. 4.3 Perforated plates.

Consider the flow field schematically represented in Fig. 4.4, where a perforated plate is confined in a one-dimensional fluid flow. The fluid flow comes from the left direction and passes through the perforated plate. The principal variables that are included are the characteristics of the fluid flow, like the mean velocity (V), the density (ρ) and the dynamic viscosity (μ) and the properties of the porous material, such as the porosity (ε), the holes characteristic length (D) and the thickness (t). It is necessary to consider also other derived variables from the fluid motion like the drag force (F_D) and the drop of pressure (Δp) upstream and downstream of the porous object. The fluid is assumed to be incompressible with ρ and μ constant in all points of the fluid, and for the continuity also the mean velocity remains constant

in the front and in the rear part of the plate. The resistance offered by the walls, where the flow is confined, is neglected because the transversal dimension of the grid (L) is much larger than the boundary layer thickness that develops on the walls. The influence of the gravity (g) is not considered insofar as the motion is developed at the same level without abrupt height variation.

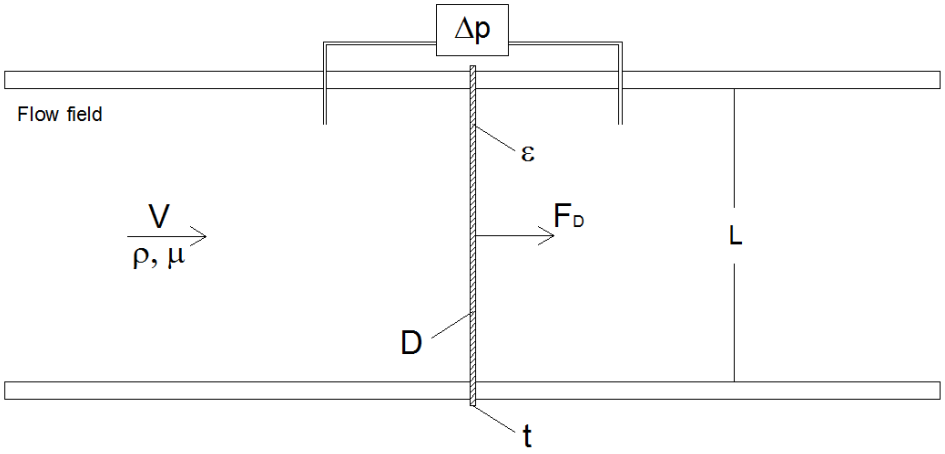

Fig. 4.4 Scheme of flow field.

Suppose that in this application it is necessary to establish a dimensionless relation between the resistance force (F_D) and the other parameters of the problem. This functional link can be expressed as follows:

$$F_D = f(V, \rho, \mu, \varepsilon, t, D, \Delta p) \tag{4.10}$$

Then, it is possible to apply the dimensionless analysis in order to find the dimensionless groups that play a fundamental role for the phenomenon considered.
The parameters involved in the problem are eight ($n = 8$):

$$[V, \rho, \mu, \varepsilon, t, D, F_D, \Delta p]$$

An important phase in dimensionless analysis is covered by the evaluation of the parameter dimension:

$$[V] = LT^{-1} \qquad [\rho] = ML^{-3}$$
$$[\mu] = ML^{-1}T^{-1} \qquad [\varepsilon] = M^0L^0T^0$$
$$[t] = L \qquad [D] = L$$
$$[F_D] = MLT^{-2} \qquad [\Delta p] = ML^{-1}T^{-2}$$

The problem has a fluid dynamic nature, and the fundamental dimensions are three M, L and T. Therefore j=3, where j represents the number of fundamental dimensions involved. The number of the Π parameters can be estimated by the relation: $\#\Pi = n - j$. In this fluid dynamic problem the dimensionless parameters

are five ($\#\Pi = 8 - 3 = 5$). As $j = 3$, it is necessary to identify three independent variables. The choice of the three independent variables is complicated because it is not possible to consider variables that have the same dimension, like in this case $[D]$ and $[t]$, or parameters that are already dimensionless like ε. In this application of dimensionless analysis $[\rho]$, $[V]$, $[D]$ are taken as dimensionless independent quantities. Before proceeding to the estimation of the five Π terms it is significant to verify that the three dimensionless quantities chosen are independent. In other terms, it is not possible to find three coefficients α, β, $\gamma \neq 0$ such that:

$$[\rho]^{\alpha}[V]^{\beta}[D]^{\gamma} = M^0L^0T^0 \tag{4.11}$$

Remembering the dimensions of the chosen parameters,

$$[V] = LT^{-1} \qquad [\rho] = ML^{-3} \qquad [D] = L$$

substituting in the equation (4.11):

$$(ML^{-3})^{\alpha}(LT^{-1})^{\beta}(L)^{\gamma} = M^0L^0T^0 \tag{4.12}$$

and solving the equation (4.12) for α, β, γ

$$\begin{aligned} M^0 &= M^{\alpha} \\ L^0 &= L^{-3\alpha} \cdot L^{\beta} \cdot L^{\gamma} \\ T^0 &= T^{-\beta} \end{aligned}$$

it is possible to obtain:

$$\alpha = 0 \qquad \beta = 0 \qquad \gamma = 0$$

Therefore, it has been proved that $[\rho]$, $[V]$ and $[D]$ are independent quantities.

4.2.1.1 Identification of Π_0

At this stage it is possible to start with the determination of the dependent parameter as follows:

$$\begin{aligned} \Pi_0 &= M^0L^0T^0 = [F_D][\rho]^{\alpha}[V]^{\beta}[D]^{\gamma} \\ \Pi_0 &= M^0L^0T^0 = (MLT^{-2})(ML^{-3})^{\alpha}(LT^{-1})^{\beta}(L)^{\gamma} \end{aligned} \tag{4.13}$$

Imposing that the parameter Π_0 is dimensionless,

$$\begin{aligned} M^0 &= M \cdot M^{\alpha} \\ L^0 &= L \cdot L^{-3\alpha} \cdot L^{\beta} \cdot L^{\gamma} \\ T^0 &= T^{-2} \cdot T^{-\beta} \end{aligned}$$

it results that:

$$\alpha = -1 \qquad \beta = -2 \qquad \gamma = -2 \tag{4.14}$$

The first dimensionless group, using the coefficients in (4.14), is equal to:

$$\begin{aligned} \Pi_0 &= F_D(\rho)^{-1}(V)^{-2}(D)^{-2} \\ \Pi_0 &= \frac{F_D}{\rho V^2 D^2} \end{aligned} \tag{4.15}$$

This dimensionless number is also called *Newton number* (Ne) and represents the ratio of the resistance forces to the inertia forces.

4.2.1.2 Identification of Π_1

After that it is possible to start with the determination of the first independent parameter as:

$$\begin{aligned} \Pi_1 &= M^0L^0T^0 = [\Delta p][\rho]^{\alpha}[V]^{\beta}[D]^{\gamma} \\ \Pi_1 &= M^0L^0T^0 = (ML^{-1}T^{-2})(ML^{-3})^{\alpha}(LT^{-1})^{\beta}(L)^{\gamma} \end{aligned} \tag{4.16}$$

Imposing that the parameter Π_1 is dimensionless,

$$\begin{aligned} M^0 &= M \cdot M^{\alpha} \\ L^0 &= L^{-1} \cdot L^{-3\alpha} \cdot L^{\beta} \cdot L^{\gamma} \\ T^0 &= T^{-2} \cdot T^{-\beta} \end{aligned}$$

it results that:

$$\alpha = -1 \qquad \beta = -2 \qquad \gamma = 0 \tag{4.17}$$

The second dimensionless group, using the coefficients in (4.17), can be written as:

$$\begin{aligned} \Pi_1 &= \Delta p(\rho)^{-1}(V)^{-2}(D)^{0} \\ \Pi_1 &= \frac{\Delta p}{\rho V^2} \end{aligned} \tag{4.18}$$

This dimensionless number is also called *Euler number* (Eu) and represents the ratio of the pressure forces to the inertia forces.

4.2.1.3 Identification of Π_2

Similarly it is possible to obtain the second independent parameter as:

$$\begin{aligned} \Pi_2 &= M^0L^0T^0 = [\mu][\rho]^{\alpha}[V]^{\beta}[D]^{\gamma} \\ \Pi_2 &= M^0L^0T^0 = (ML^{-1}T^{-1})(ML^{-3})^{\alpha}(LT^{-1})^{\beta}(L)^{\gamma} \end{aligned} \tag{4.19}$$

Imposing that the parameter Π_2 is dimensionless,

$$\begin{aligned} M^0 &= M \cdot M^{\alpha} \\ L^0 &= L^{-1} \cdot L^{-3\alpha} \cdot L^{\beta} \cdot L^{\gamma} \\ T^0 &= T^{-1} \cdot T^{-\beta} \end{aligned}$$

it results that:

$$\alpha = -1 \qquad \beta = -1 \qquad \gamma = -1 \tag{4.20}$$

Remembering the definition of kinematic viscosity ($\nu = \mu/\rho$) and using the coefficients in (4.20), the third dimensionless group is equal to:

$$\begin{aligned} \Pi_2 &= \mu(\rho)^{-1}(V)^{-1}(D)^1 \\ \Pi_2 &= \frac{\mu}{\rho V D} = \frac{\nu}{VD} = \frac{1}{Re} \end{aligned} \tag{4.21}$$

so, by a simple inversion:

$$\Pi_2 = \frac{VD}{\nu} \tag{4.22}$$

This dimensionless number is also called *Reynolds number* (Re) and represents the ratio of the inertia forces to the viscous forces.

4.2.1.4 Identification of Π_3

Consequently it is possible to obtain the third independent parameter as follows:

$$\begin{aligned} \Pi_3 &= M^0 L^0 T^0 = [t][\rho]^{\alpha}[V]^{\beta}[D]^{\gamma} \\ \Pi_3 &= M^0 L^0 T^0 = (L)(ML^{-3})^{\alpha}(LT^{-1})^{\beta}(L)^{\gamma} \end{aligned} \tag{4.23}$$

Imposing that the parameter Π_3 is dimensionless,

$$\begin{aligned} M^0 &= M \cdot M^{\alpha} \\ L^0 &= L \cdot L^{-3\alpha} \cdot L^{\beta} \cdot L^{\gamma} \\ T^0 &= T^{-\beta} \end{aligned}$$

it results that:

$$\alpha = 0 \qquad \beta = 0 \qquad \gamma = -1 \tag{4.24}$$

The fourth dimensionless group, using the coefficients in (4.24), is equal to:

$$\begin{aligned} \Pi_3 &= t(\rho)^0(V)^0(D)^{-1} \\ \Pi_3 &= \frac{t}{D} \end{aligned} \tag{4.25}$$

This dimensionless number is not famous like the previous ones but it represents the ratio between the characteristic lengths (t and D).

4.2.1.5 Identification of Π_4

The last independent parameter is very simple to evaluate because the porosity (ε) is in itself dimensionless, then the fifth dimensionless group is:

$$\Pi_4 = \varepsilon \tag{4.26}$$

4.2.1.6 Final remarks

The final functional relationship between the drag force and the other parameters can be written as follows:

$$\begin{aligned} \frac{F_D}{\rho V^2 D^2} &= f(\frac{\Delta p}{\rho V^2}, \frac{VD}{\nu}, \frac{t}{D}, \varepsilon) \\ Ne &= f(Eu, Re, t/D, \varepsilon) \end{aligned} \tag{4.27}$$

Observation:
Through the application of the Buckingham's theorem it has been possible to define a functional link with a remarkable advantage. The starting problem, reported in the equation (4.10) foresees the determination of seven variables [$f(V, \rho, \mu, \varepsilon, t, D, \Delta p)$] to solve the problem. On the other hand with the dimensionless analysis it has been possible to simplify and solve the problem using only four parameters [$f(Eu, Re, t/D, \varepsilon)$].

In order to reach a *complete similitude* between prototype and model it is necessary to respect the condition reported in the equation (4.9). For this application example this condition can be written as:

$$\begin{aligned} Eu^{(p)} &= Eu^{(m)} \\ Re^{(p)} &= Re^{(m)} \\ \left(\frac{t}{D}\right)^{(p)} &= \left(\frac{t}{D}\right)^{(m)} \\ \varepsilon^{(p)} &= \varepsilon^{(m)} \end{aligned} \tag{4.28}$$

4.2.2 Inadequacy of geometric scaling

Supposing to have to carry out some tests on a scaled model in the wind tunnel or water tunnel with porous elements, it is necessary to consider the similitude requirements found in the equation (4.28) in order to get correspondences between prototype and model. In this section the feasibility of these prescriptions will be analysed and commented for each dimensionless group.

4.2.2.1 Reynolds similitude

An important parameter for many simulations in laboratory is the Reynolds number. In this case it is important to maintain the following dimensionless group passing from the prototype to the model:

$$\begin{aligned} \left(\frac{VD}{\nu}\right)^p &= \left(\frac{VD}{\nu}\right)^m \\ \frac{V_p D_p}{\nu_p} &= \frac{V_m D_m}{\nu_m} \end{aligned} \tag{4.29}$$

Considering that the fluid in use in the wind tunnel is the air in normal conditions of pressure and temperature, the dynamic viscosity for the prototype and for the model is the same ($\nu_p = \nu_m$).

$$\begin{aligned} V_p D_p &= V_m D_m \\ V_m &= V_p \frac{D_p}{D_m} \end{aligned} \tag{4.30}$$

In order to have the same Reynolds numbers for the prototype and model, it is necessary that the velocity scale is inversely proportional to the geometric scale. Remembering that models are commonly built in appropriate geometric scales, it is possible to define the ratio: $\frac{D_p}{D_m} = \frac{1}{s}$ (where s is the inverse of the scale factor). Applying this definition at the equation (4.30) one obtains:

$$V_m = V_p \cdot \frac{1}{s} \tag{4.31}$$

If the model is built at scale 1:50, the air speed in the wind tunnel should be 50 times the speed of the prototype. It is easy to notice that a simple geometric scale cannot be applied. Imagining to measure the drag force on a perforated plate due to a wind speed of 10 m/s in the reality, it would be necessary to have in the wind tunnel an air velocity of 500 m/s. Regardless the feasibility of this condition in the common wind tunnels, the model will be subject to a different condition of motion; in fact at 500 m/s the motion is supersonic ($Ma > 1$) while in the prototype the motion is subsonic and in the incompressible range.

4.2.2.2 t/D similitude

Another important dimensionless parameter found is the ratio t/D, where t is the thickness of the perforated plate and D the hydraulic diameter of the hole. Also for this parameter it is necessary to maintain the same value from prototype to model:

$$\begin{aligned} \left(\frac{t}{D}\right)^{(p)} &= \left(\frac{t}{D}\right)^{(m)} \\ \frac{t_p}{D_p} &= \frac{t_m}{D_m} \end{aligned} \tag{4.32}$$

Expressing in terms of model parameters and the geometric scale:

$$\begin{aligned} t_m &= t_p \frac{D_m}{D_p} \\ t_m &= t_p \cdot s \end{aligned} \tag{4.33}$$

Considering the same geometric scale 1:50, the second parameter leads that the thickness of the model is 1/50 the thickness of prototype. This condition is impossible to realize because referring to grids or perforated plates with thickness in the order of 0.5 ÷ 10 mm it would be necessary to build a model with thickness in the range of 0.01 ÷ 0.2 mm. Leaving aside the possibility of respecting this prescription, the result would be a micro-material very thin difficult to handle, highly fragile and then not suitable for the models manufacturing.

4.2.2.3 ε similitude

It is necessary to have the same porosity level passing from model to prototype as expressed by the formula:

$$\begin{aligned} \left(\varepsilon\right)^{(p)} &= \left(\varepsilon\right)^{(m)} \\ \varepsilon_p &= \varepsilon_m \end{aligned} \tag{4.34}$$

Nowadays the industrial processing of perforated plates and grids is able to realize many typologies of porous elements almost without limits, especially for the dimensions of holes, shape and thickness. The mainly used shapes are square, round, oblong, cross, hexagonal. The limiting factor in this case is the porosity level and consequently the position of the holes. In fact porosity levels in the range 2 % ÷ 80 % can be reached. The porosity level could be maintained equal from model to prototype neglecting the geometric scale of dimensions, thickness and shapes. Hence a grid totally different from the real one in terms of dimension and shape of holes and thickness is often obtained.

4.2.2.4 Euler similitude

In this case the pressure force respect to the inertia force plays an important role and the Euler number is an important parameter that has to be maintained between reality and laboratory:

$$\begin{aligned} \left(\frac{\Delta p}{\rho V^2}\right)^p &= \left(\frac{\Delta p}{\rho V^2}\right)^m \\ \frac{\Delta p_p}{\rho_p {V_p}^2} &= \frac{\Delta p_m}{\rho_m {V_m}^2} \end{aligned} \tag{4.35}$$

Also in this case the fluid in use in the wind tunnel is air in normal conditions of pressure and temperature, therefore the air density for the prototype and model is the same ($\rho_p = \rho_m$).

$$\begin{aligned} \frac{\Delta p_p}{{V_p}^2} &= \frac{\Delta p_m}{{V_m}^2} \\ \Delta p_m &= \Delta p_p \frac{{V_m}^2}{{V_p}^2} \end{aligned} \tag{4.36}$$

Remembering the relationship between the velocity scale and the length scale, obtained by the Reynolds similitude ($\frac{V_p}{V_m} = \frac{1}{s}$), the equation (4.36) can be modified as follows:

$$\Delta p_m = s^2 \cdot \Delta p_p \tag{4.37}$$

Consequently, the pressure drop on model is equal to the square of the inverse of the scale factor (s^2) multiplied by the pressure drop of prototype. This condition, being a strictly consequence of Reynolds similitude, results impossible to realize on the scaled models.

4.2.2.5 Concluding remarks

Nowadays modern design of structures requires an increased application of accessory elements, chosen and studied to guarantee higher and higher standards of performance. Over the past decades, the interest for macro-porous materials in building and bridge engineering has grown tremendously, because of their use in many different fields. This kind of porous elements is mainly used like accessory elements of a structure or infrastructure, such as the wind shields for bridge decks and the permeable façades for many technological buildings.

When it is necessary to get a deep comprehension of the behaviour of porous elements by specific tests in the wind tunnel, it is required that the similitude criteria are known. The existing literature is a bit evasive and elusive, or at least there is no criterion in the research community. Using the dimensionless analysis it has been possible to identify the major parameters involved in the phenomena, and the relative problem of geometrical scaling. In fact, it may be hard or almost impossible to realize a geometrically scaled modelling on the porous element. This depends on the difficulty to realize scaled features that are little in reality, such as the small openings of the grids or the thickness of the screens. As a consequence, it has been shown that the complete similitude between prototype and model cannot be reached. Then, it is necessary to establish an incomplete similitude in order to guarantee the equality of the only parameters that mainly characterize the phenomenon. A good approach to understand the behaviour of a perforated plate respect to the air flow is to carry out several wind tunnel tests on porous plates, with various levels of porosity, dimensions and shape of holes and thickness, for different flow conditions, in order to find a general law of modelling for this kind of items.

4.3 Wind tunnel experimentation

The effects of wind are essential elements in the design of structures (tall buildings, long span bridges and slender structures) and in the evaluation of a series of phe-

nomena in the field of environmental engineering (dispersion of gaseous pollutants).

The correct quantification of actions and wind effects on structures is a complex operation that requires the use of various techniques that can be distinguished in two categories: numerical or experimental. Nowadays the numerical techniques, that are enclosed in the acronym CFD (*Computational Fluid Dynamics*), are not mature yet, especially in the case of turbulent flows around complex bodies. This is due to the uncertainty for the use of different grid generation algorithms and the turbulence models, to the high expenditure of computational resource and to the long run times for the convergence. For this reason, it is often necessary to use auxiliary helps like results coming from an experiment at full scale or on models, in this case through wind tunnel tests, which are essential for the proper quantification of the phenomena. These tests must be carried out in boundary layer wind tunnel, that is in particular conditions of physical similarities with the natural air flow. There are different types of wind tunnels, depending on the type of application and their inherent characteristics. Typically they are distinguished in:

- **Boundary Layer Wind Tunnel:** are suitable for environmental studies (atmospheric pollutant diffusion and pedestrian comfort) and structural studies (interaction between wind and structures). These are subsonic wind tunnels where the thickness of boundary layer has a relevant dimension respect to the dimension of the test section. This layer can be created naturally (if the wind tunnel is long enough), or using turbulence promoters, artificially placed in the proximity of the inlet and using a distribution of surface roughness on the floor of the tunnel;
- **Aerodynamic Wind Tunnel:** can be subsonic, transonic or supersonic; they are primarily used for aerodynamic studies on cars, aircraft and space applications. They are generally wind tunnels with low level of turbulence and without boundary layers, which are sometimes sucked away from the test section.

With respect to the working modality, wind tunnels can also be divided into:

- **Open-circuit wind tunnels:** are sensitive to external conditions, in particular to the distortion of flow and contamination from dust (Fig. 4.5).

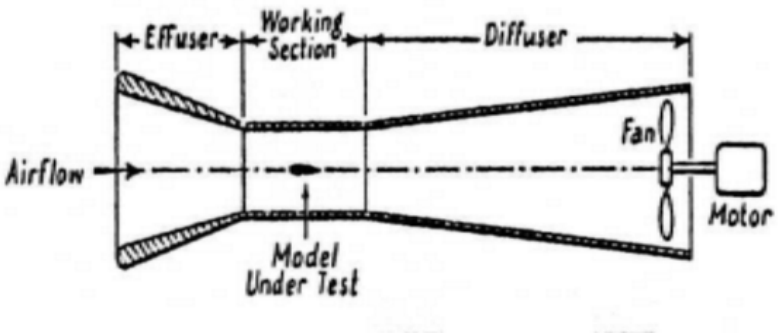

Fig. 4.5 Open-circuit wind tunnels (*Eiffel type*).

- **Closed-circuit wind tunnel:** are less sensitive to external conditions. The flow must be anyway monitored and controlled in order to have stable conditions during the experimental tests (Fig. 4.6).

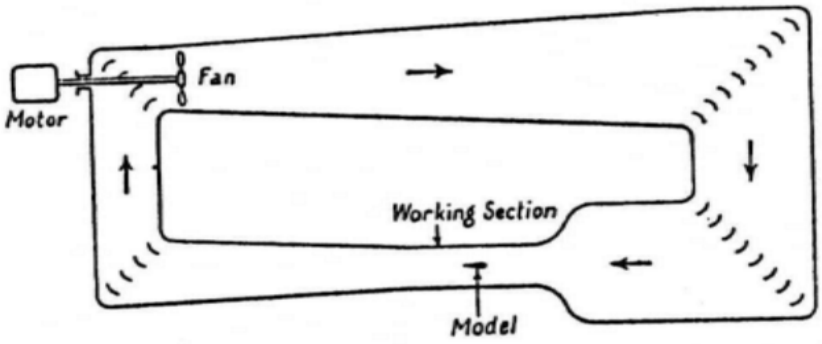

Fig. 4.6 Closed-circuit wind tunnels (*Prandtl type*).

4.3.1 CRIACIV Wind Tunnel

The CRIACIV is the Inter−University Research Centre on Building Aerodynamics and Wind Engineering, established in 1992 by the University of Florence and the University of Rome (La Sapienza). Since 1996 are part of CRIACIV the University of Perugia, and the University of Trieste, and since 2004 also the Universities of Chieti−Pescara and Venice (IUAV) are involved in the centre. The wind engineering laboratory is active since 1993, it is located in *Polo Universitario di Città di Prato*, a branch of the University of Florence. The CRIACIV boundary layer wind tunnel is an open-circuit wind tunnel (Fig. 4.7).

Fig. 4.7 Picture of CRIACIV boundary layer wind tunnel.

The wind tunnel cross-section is rectangular with sides of 2.2 m by 1.6 m (at the inlet section), slightly divergent from the inlet to the working section whose dimensions are 2.4 m by 1.6 m. The global length of the wind tunnel from inlet to the end of the T-shaped diffusers (Fig. 4.8) is about 22 m.

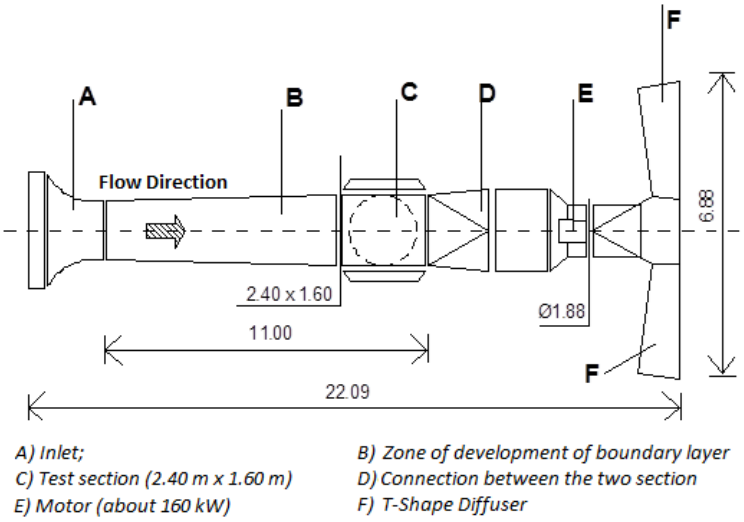

Fig. 4.8 Geometry of CRIACIV boundary layer wind tunnel.

The supporting structure of the BLWT is made of steel, closed with wooden panels and glasses and a wooden floor. The overall longitudinal dimension for the development of the boundary layer is about 11 m (8 m upstream of the test section and 3 m at the test section). Motor and fan, with a nominal power of 156 kW, are located downstream of the test section. The air flow can be changed continuously in the range $0 \div 30$ m/s, through a double regulation system: the variation of the pitch angle (from 7.7° to 15.4°) of the ten blades of the fan; and the variation of the r.p.m. of the motor which is controlled through an inverter up to 52.5 Hz.

In order to simulate correctly the test conditions in the testing chamber a boundary layer with appropriate characteristics must be generated in the wind tunnel. This boundary layer can be obtained positioning for the entire length used for the development particular devices that provide an appropriate surface roughness and reproduce the correct quantities of turbulent flow characteristics. The surface roughness is often reproduced using horizontal wooden panels made of a series of alternating wooden cubes. With the purpose to create a boundary layer totally developed in test section of the wind tunnel it is necessary to have a development zone the longest possible and thus a very long wind tunnel. Usually this requirement cannot be respected, and it is necessary to find a compromise between the length of development and the boundary layer thickness. For this reason, in addition to surface roughness, devices capable of increasing the height of the boundary layer are frequently added in wind tunnel. They are usually adjusted at the inlet of the tunnel, and are composed of vertical (*spires*) or horizontal elements (*barriers*).

In the case where tests do not require to create a boundary layer and an incident wind speed profile, it is sufficient to reproduce the turbulent character of the air motion. The CRIACIV wind tunnel has the ability to create three different configurations of air flow turbulence: the low ($I_t < 1$ %), the medium ($I_t = 3.3$ %) and the high turbulence intensity ($I_t = 17$ %), where I_t is the turbulence index and represents the ratio between the wind speed standard deviation and the mean wind speed. In the first case (low turbulence) there is no need to introduce any device at the inlet of the wind tunnel to recreate the smooth flow. The other two cases can be obtained by the use of two wooden grids put in the inlet area of the tunnel (Fig. 4.9).

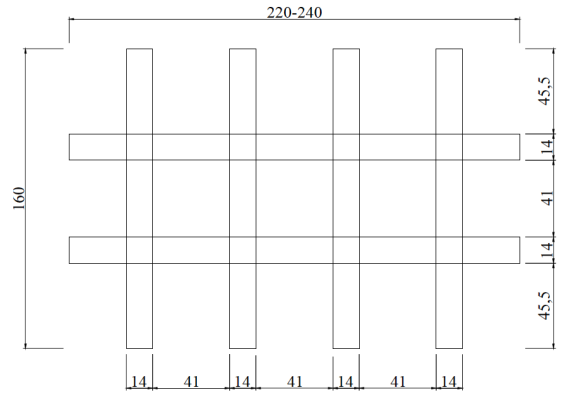

(a) High turbulence intensity (I_t=17 %)

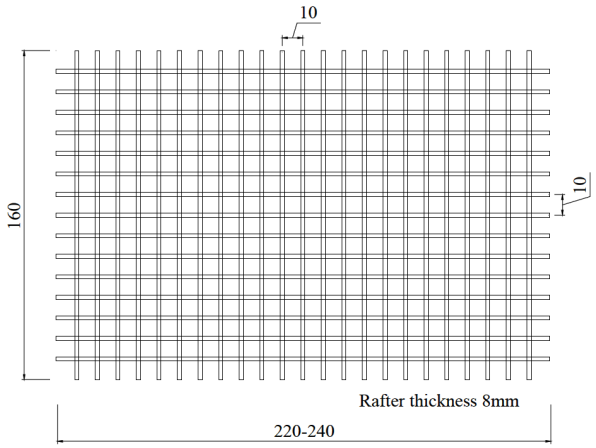

(b) Medium turbulence intensity (I_t=3.3 %)

Fig. 4.9 Wooden grids in use at CRIACIV.

Chapter 5

WT tests on porous elements

5.1 Introduction

The core of this section will be the search for a rule of scale or its approximation for porous elements. In this part of the analysis porous materials are represented by perforated plates, the so-called holed plank fences. Before proceeding with the scaling process of the porous material (*perforated plate*) it is necessary to have a deep comprehension of the behaviour of perforated plates respect to the air flow. With the aim to find the lead parameters of the problem, the general study of the topic becomes fundamental.

The principal issue is to obtain real measurements on samples of porous materials. The options are mainly two: performing tests on prototype of screens in open field, or in wind tunnel on samples of screens. For the present work many tests in Boundary Layer Wind Tunnel of CRIACIV on screen samples with variable porosity have been performed, because the experiments in open fields are very complex and expensive especially regarding the control of the flow incident the screen. The starting idea is to analyse the behaviour of porous screens with respect to the air flow in wind tunnel in order to define the hypothetical equivalence between the prototype and the wind tunnel model and with the aim of determining some possible similitude and general scaling criteria. With the purpose of analysing this kind of materials it is necessary to know the fields of pressure and velocity in front and behind the porous screens, the aerodynamic forces on the barrier and the related dimensionless coefficients of drag and loss for a perforated plate. The dimensionless key parameters that have been examined are: drop of pressure, loss coefficient and drag coefficient, all depending on the presence of the holed plank fences. The fundamental characteristics of porous structures, consisting of holes, are represented by porosity, the index able to express the relationship between the voids respect to the filled parts; dimensions and geometrical shape of the holes and thickness.

5.2 Experimental set-up

The preparation of the experimental set-up has been very accurate also in terms of design and realization phases. It was necessary to build an experimental apparatus that was able to measure pressures, forces and velocity with high level of precision.

The main idea is to use the air flow generated by Boundary Layer Wind Tunnel of CRIACIV and to canalize the flow in a particular sub-channel equipped with measuring instruments. The experimental equipment consisted in a cylinder positioned in the test section of the wind tunnel, where a porous screen was placed inside. It had the aim to channel the wind stream in order to control the approaching flow on the grid sample and recreate a controlled measured environment. Thanks to this device it was possible to obtain full-scale measurements for portion of porous objects in confined flow condition. This idea can be observed in a general picture (Fig. 5.1) where a schematic view of the designed set-up is reported.

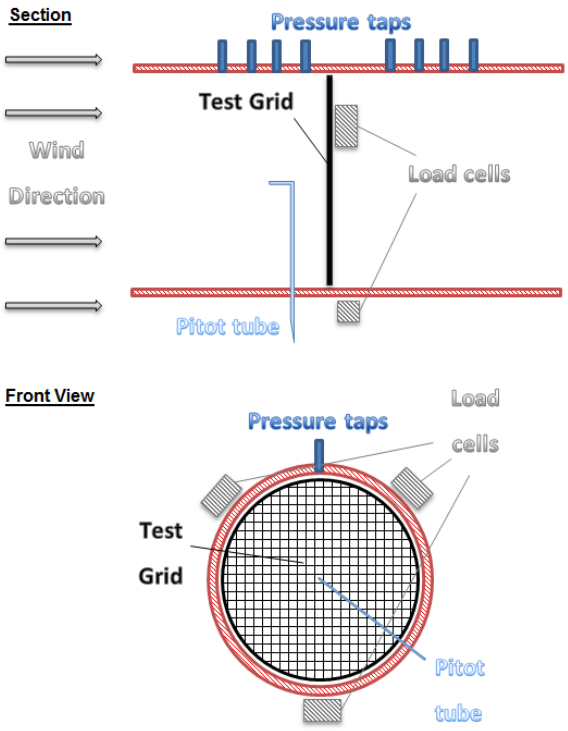

Fig. 5.1 Experimental set-up scheme, section and front view.

The air flow in the wind tunnel comes from the left direction and passes through the screen. In order to study the flow field, the pressure taps are able to evaluate the pressure pattern near the grid and the three load cells measure the drag force on the grid. The pitot tube has the aim to check the incident flow velocity during all test phases.

The sub-channel consists of a classical Polyvinyl-chloride (PVC) pipe used in drainage and sewage system having an external diameter (ϕ_{ext}) equal to 400 mm, thickness equal to $5 \approx 6$ mm and length of 1.5 m. The choice has fallen on this kind of material because it has a lot of advantages, for example it is economic (*about 15* €*/mt*), easy to find, lightweight and simple to handle and presents a surface roughness very low, in the order of 0.01 mm. The PVC pipe presents also a little disadvantage related to the high deformability after the external loads, that usually can be lead up to a permanent deformation of the cross section, from circular to oval

shape. In order to have a perfect internal cross section of the pipe (ϕ_{int}) equal to 395 mm and avoid any kind of deformation problem, three steel rings are positioned around the pipe next to the grid test section (Fig. 5.2).

Fig. 5.2 View of three steel rings.

As shown in Fig. 5.2 the sub-channel is collocated on a particular birch wooden support that has the function to sustain the pipe. The wooden support is designed for increasing the stiffness of all the apparatus and to keep the pipe in a steady position during the test phase, respect to the central part of the test chamber of wind tunnel. The pipe is linked to the ground of the wind tunnel by four wooden legs that are fixed on the floor by screws. To increase the global leg stiffness the front legs are connected with the rear legs with a wooden crossbar. The legs of the support, both right and left, anterior and posterior, are joined with a steel threaded rod. The solution of sub-channel allows to fix a solid blockage ratio equal to 5% and to minimize the blockage effects in the wind tunnel (Takeda and Kato, 1992). The pressure patterns and drop of pressure have been measured with an appropriate system of pressure taps linked to pressure piezoelectric transducers.

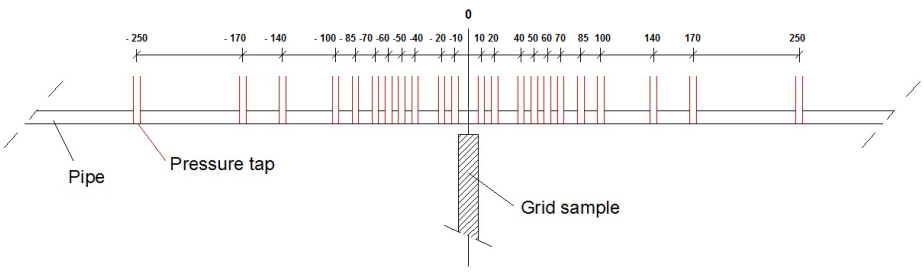

Fig. 5.3 Disposition of pressure taps.

The pipe is provided with static pressure taps that are made of little brass pipes with an internal diameter in the order of 1 mm. The taps are positioned on the upper part of the pipe at fixed positions with respect to the grid test section (Fig. 5.3). In the picture below (Fig. 5.4) a global view of pipe equipped with the pressure taps is reported.

Fig. 5.4 Global view of pressure taps.

With the purpose of enabling the instrumented set-up to measure the drag force due to wind flow through the screen, the experimental apparatus has been equipped with three extensometric load cells strictly connected to the sample under testing. Each load cell has been connected to the PVC pipe by a dedicated system of anchorage that is shown in the following figure (Fig. 5.5).

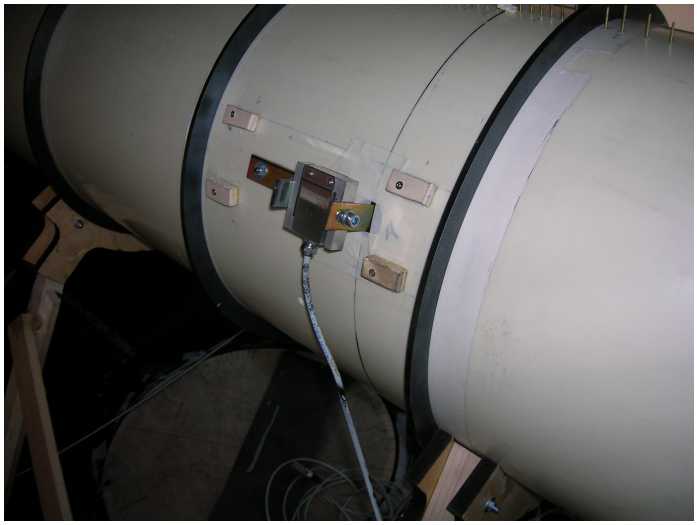

Fig. 5.5 Particular of load cell position.

The anchorage system has been realized with a metallic L-shaped profile solidly linked to the load cell and the pipe by screws, and a metal board platen that connects the grid sample with the upper part of the load cell (Fig. 5.6).

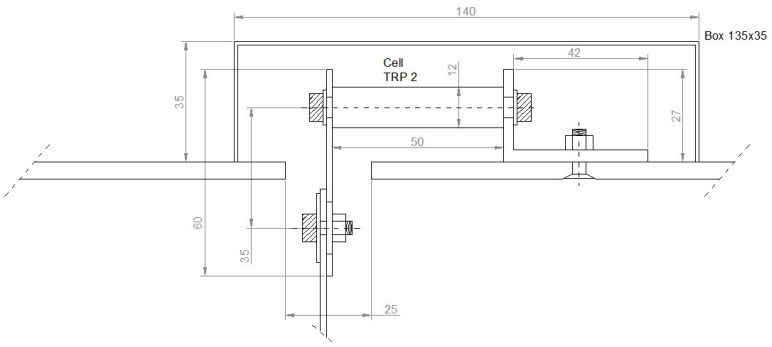

Fig. 5.6 Scheme of load cell anchorage.

With this system of anchorage it was possible to obtain three rigid points where the grid under testing, suitably drilled, could be fixed (Fig. 5.7). It was also able to avoid zones of contact between the internal part of the PVC pipe and the grid.

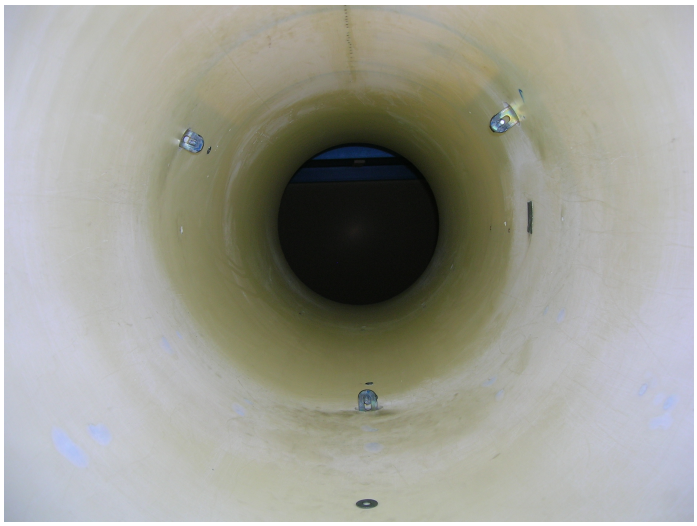

Fig. 5.7 Three rigid points of connection.

Afterwards the load cells have been covered with opportune aerodynamic boxes that were able to isolate the load cells from the external air flow, thus ensuring an uncontaminated environment of measurement.

5.2.1 Instruments of measure

Before entering into details of the experimental campaign it is necessary to describe the general characteristics of the measurement instruments that have been used and the relative limits.

5.2.1.1 Pressure system (*PSI*)

The pressure system that has been used in the experimental campaign is composed by twenty-two pressure taps linked to piezoelectric transducers. The transducers or ESP Pressure Scanners are miniaturized electronic differential pressure measurement units consisting of an array of silicon piezoresistive pressure sensors, one for each pressure port (Fig. 5.8).

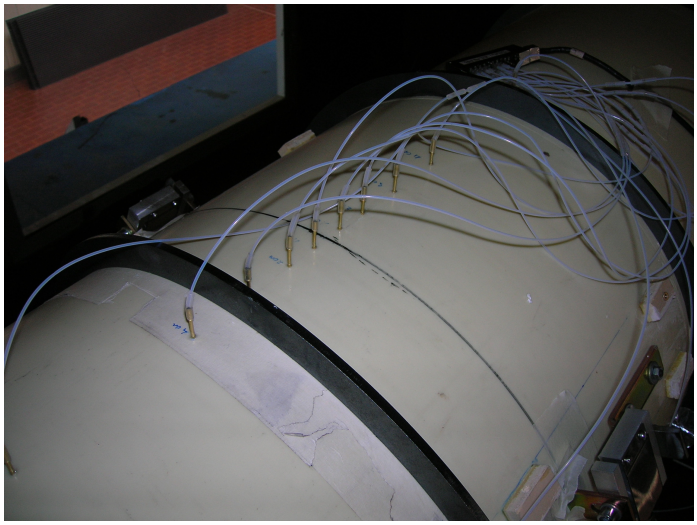

Fig. 5.8 ESP Pressure Scanners in use.

Pressures can be measured with a sampling frequency up to 1 kHz. The number of acquisition channels used are inversely proportional to the sampling frequency. For example, for the maximum number of pressure signals that can be simultaneously measured (128), the sampling frequency decreases to 250 Hz per channel.

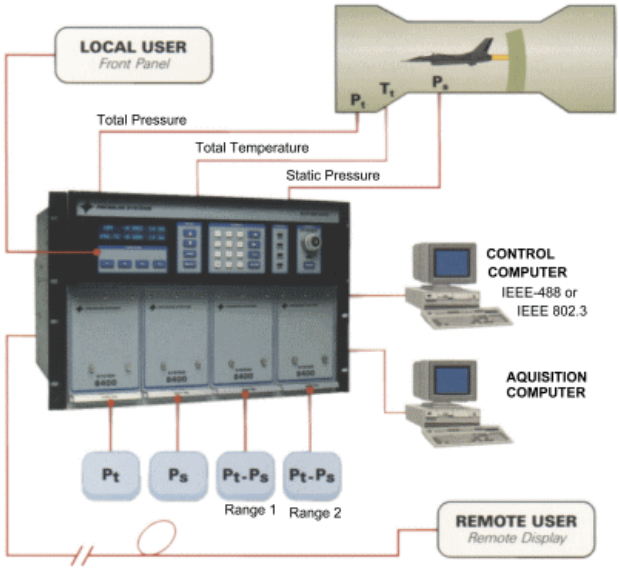

Fig. 5.9 Pressure acquisition system PSI 8400.

Two peripheral scanners, each with 16 miniaturized piezoelectric pressure transducers, are controlled by a Pressure System unit, PSI 8400 (Fig. 5.9), for calibration, acquisition and analogic-digital conversion of the data. The pressure is indirectly determined by measuring the resistivity variation of a piezoelectric crystal, caused by the pressure itself. As the pressure is not a fundamental quantity, it is measured indirectly from the ratio between the force and the area where the force is applied. The deformation is used to generate a voltage signal that is sampled by the acquisition board. Thanks to their small dimensions (13 x 21.5 x 69 mm for the system in use) the ESP scanners can be located directly on the experimental set-up (Fig. 5.8). Before any measurement the transducers must be calibrated because the output depends on the air pressure and temperature inside the working section of the wind tunnel. Once the measurement range is evaluated, the calibration is carried out by means of a pressure calibration unit (PCU). During the calibration, every transducer reads five reference pressure values generated by the PCU. These values can be changed by the operator depending on the required range which must be within ± 254 mm of water. The measured points are interpolated by a fourth order polynomial. The accuracy of the calibration procedure is ± 0.05% of the maximum allowed pressure. The error of the pressure measurements is ± 0.2% of the maximum allowed pressure. Considering the range of measurements typical for this application, the precision of the unit PSI in use at CRIACIV can be expressed in terms of water height and more precisely the measurements are subject to error in the range of ± 0.25 mm of water column (≈ 2.5 Pa). The pressures measured up-wind and down-wind the grid test section are transmitted to the sensor without distortions through small highly flexible plastic tubes, manufactured in Teflon.

5.2.1.2 Force system (*Extensometric load cells*)

During the test phase in wind tunnel only the force component in the wind direction (*drag force*) has been measured by three extensometric load cells.

Specifications	**Values**
Capacity	$0 \div 20$ N (FS = 20 N)
Nominal sensitivity	2mV/V
Repeatability	$\leq \pm$ 0.02 % FS
Zero temperature coeff.	$\leq \pm$ 0.005 % FS
Nominal load creep (20')	$\leq \pm$ 0.03 % FS
Combined error	$\leq \pm$ 0.05 % FS
Electrical excitation	$2 \div 15$ V
Safe overload	150 % FS
Operating temp. range	$-20 \div +70$ °C

Table 5.1 Characteristics of load cell TRP 2.

Regarding the other forces and moments exercised by the air flow on the perforated plates, these components, considering their little entity with respect to the drag force, have been neglected. The choice of the technical characteristics of the

cell has been a fundamental step of the experimentation, because it was necessary to have a small load cell that could measure low entity of forces with high precision. After an accurate market analysis, the load cell that best meets these requirements is a tension-compression load cell, model TRP 2 manufactured by Metior s.r.l., having the specifications reported in Table 5.1 (Fig. 5.10).

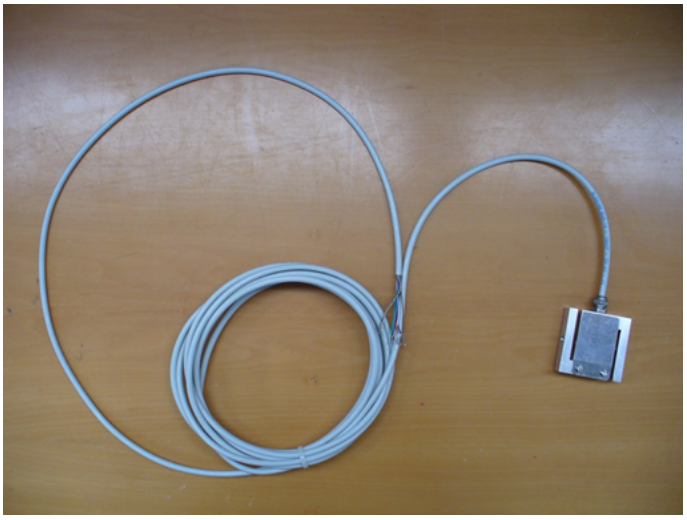

Fig. 5.10 Tension-Compression load cell (TRP 2).

A load cell is a transducer that is used to convert a force into an electrical signal. This conversion is indirect and is obtained in two stages. Through a mechanical arrangement, the force being sensed deforms a strain gauge. The strain gauge converts the deformation (*strain*) into electrical signals. A load cell usually consists of four strain gauges in a Wheatstone bridge configuration. The electrical signal output is typically in the order of a few millivolts (mV) and requires amplification before being used (Fig. 5.11).

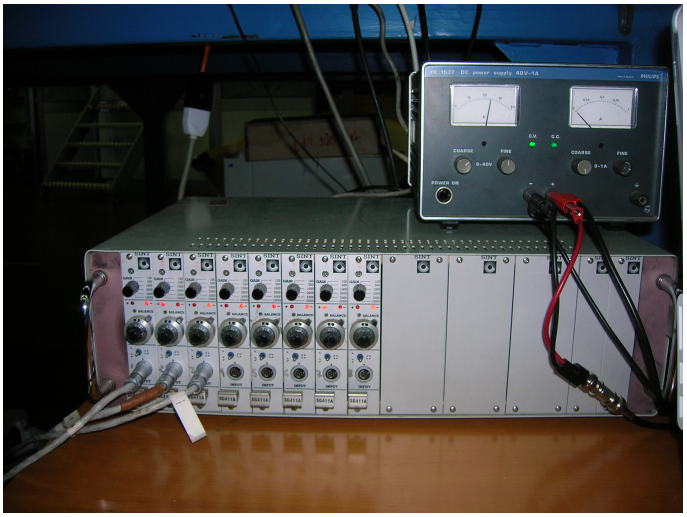

Fig. 5.11 Amplification system SINT SG411A.

The signal has been amplified and subsequently conditioned, acquired and converted in a digital signal by an acquisition card NI cDAQ-9174 of National Instruments. Thanks to an appropriate interface, the data acquired by the card NI cDAQ-9174 are saved as digital data on PC.

A phase that has a great importance is the calibration of the three load cells, that has been performed for each grid before the measurements. It has the function of obtaining the calibration matrix (k) that allows to convert electric signals (mV), into data of force (N). The matrix k has been obtained imposing four known weights having mass: P_1=499.2 g, P_2=499.6 g, P_3= 501.2 g and P_4= 499.3 g for each load cell, using load incremental steps (Fig. 5.12).

Fig. 5.12 Calibration phase.

Considering the data in output provided by the calibration, it was possible to evaluate the effective precision of this measurement system, thus the intrinsic error of the measurement is within the range ± 0.01N.

The experimental campaign has been carried out recording the signals acquired by the three cells for 120 seconds at sampling frequency of 1000 Hz, in order to have a very long time history of measurements.

5.2.1.3 Velocity system (*Pitot tubes and hot-wire*)

The instrumentation devices used during the wind tunnel tests were the hot wire anemometer for the dynamic measurements of the wind speed and the classic Pitot-Prandtl tube (Fig. 5.13). The Pitot tube allows to measure the mean kinetic pressure of the incoming flow and therefore indirectly the mean wind speed. Two Pitot tubes were used during the measurements in order to record the wind speed during the tests, while the hot wire anemometer was employed during the characterization and study of the flow field inside the pipe. The Pitot tubes were linked to Setra System (*Model. 239*) pressure transducers, which sent the electrical signal to an A/D converter. The A/D converter sampled the signal and made it available to processing.

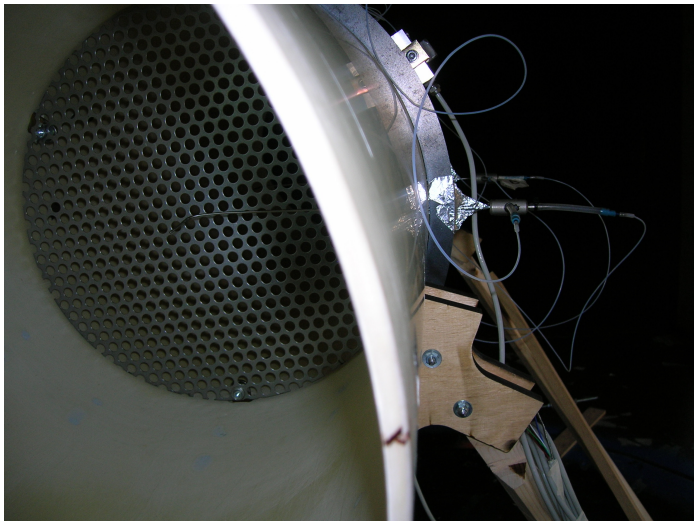

Fig. 5.13 Particular of the Pitot tubes used.

The anemometric channel DANTEC 65C01 was instrumented with one mono-component hot wire probe. The channel had both low-pass and high-pass filters and selectable gain. The analogical signal switched to an A/D converter IOTECH ADC488/8SA that sent it to the PC for processing.

5.2.2 Characteristics of the perforated plates

The perforated plates used in this study are provided by MEVACO. This is one of the leading manufacturers and suppliers of perforated sheeting and expanded metals in Europe. The perforated sheets are built with many types of materials: steel, stainless steel, zinc-coated steel, copper, aluminium and zinc-titanium. They are characterized by a certain level of porosity (ε), thickness, shape and dimension of holes. Principally remembering the definition of porosity like the ratio between the open area respect to the total area of the sample, various levels of porosity can be reached by modifying the area of the open part of the screen. The range of porosity that has been investigated in the experimental tests in wind tunnel is 22.68% $\div$ 69.40%. Regarding the shape of holes at the present time there is a big variety of shape starting from the most common geometric shape as round, square, triangular, rhomboidal, hexagonal until the creative line like oblong shape, cross-shape and shape manufactured on request. These shapes can be obtained in a wide range of dimensions, as the industrial construction process can realize many geometries in almost all the dimensions. The commercial range is from 0.5 mm to 30 mm but on request it is possible to obtain also very particular dimensions. The level of porosity, that can be expected, is reached varying the dimension, the shape but also the position of the holes. The position of the holes that are commonly in use are in line, staggered, square mesh, triangular mesh and random. Regarding the shape of holes under testing there are round, square, oblong, hexagonal and cross, with different dimensions in the range 1.5 $\div$ 10 mm, and thickness variable from 1 to 6 mm. In Table 5.2 are reported the grid samples tested in wind tunnel subdivided by Porosity, Thickness, Hydraulic Diameter (D_h) and Shape. Recourse to the Hydraulic

Diameter (D_h) is a general practice in order to standardize the dimension of holes especially for the less regular shapes, and it can be defined as:

$$D_h = \frac{4 \cdot A_{Hole}}{2p_{Hole}} \tag{5.1}$$

with: A_{Hole} and $2p_{Hole}$ are the area and the perimeter of the single hole.

Model	**Porosity %** (ε)	**Thickness [mm]**	D_h**[mm]**	**Shape**
R1.5T3	22.68	1.5	1.5	Round
R3T5	32.65	1.0	3.0	Round
R10U15	34.88	1.5	10.0	Round
C3U5	36.00	1.0	3.0	Square
C5U8	39.06	1.0	5.0	Square
R2T3	40.31	1.0	2.0	Round
R4T6	40.31	1.0	4.0	Round
R4T6	40.31	2.0	4.0	Round
R4T6	40.31	3.0	4.0	Round
R4T6	40.31	4.0	4.0	Round
R4T6	40.31	5.0	4.0	Round
R4T6	40.31	6.0	4.0	Round
R6T9	40.31	1.0	6.0	Round
R8T12	40.31	1.0	8.0	Round
R10T15	40.31	1.0	10.0	Round
LR5x20	43.81	1.0	8.5	Oblong
C10U15	44.40	1.0	10.0	Square
R10U14	44.40	1.0	10.0	Round
C6U9	44.44	1.0	7.0	Square
C8U12	44.44	1.0	8.0	Square
R7T10	44.44	1.0	7.0	Round
C7U10.5	44.44	1.0	7.0	Square
Nr.152	45.00	1.0	6.0	Cross
R5T7	46.28	1.0	5.0	Round
R10T14	46.28	1.0	10.0	Round
C8U10	64.00	1.0	8.0	Square
H2T90	64.00	1.0	2.0	Hexagonal
C10U12	69.40	1.5	10.0	Square

Table 5.2 Grid typologies.

The perforated plates are commercialized in sheets having dimension of 1000 mm x 2000 mm as regards the small thickness (1 $\div$ 2 mm), and 1000 mm x 1000 mm for high thickness ($>$ 2 mm). In order to obtain samples of grid that can be contained within the experimental set-up, the perforated sheets were subject to laser cutting, so that it was possible to have samples of screen with diameter of 390 mm (Fig. 5.14).

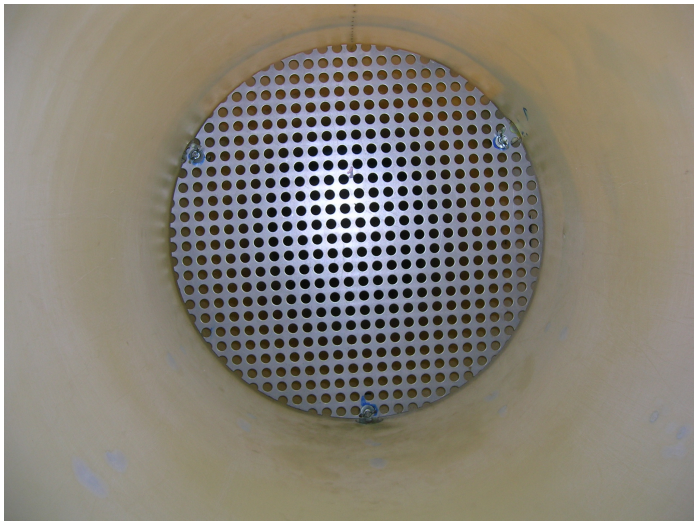

Fig. 5.14 Grid sample (model R10U15, $\varepsilon = 34.88\%$).

Tests have been performed on twenty-eight grid samples at several wind velocities with the flow coming perpendicularly to the screen. Thirteen of the twenty-eight samples of screens were tested in CRIACIV wind tunnel and differed each other for porosity, dimensions and shapes of holes, and thickness, in order to evaluate the role of porosity. With the purpose of understanding the effects of hydraulic diameter other five samples had the same porosity, same shape, but they were different for the dimension of the holes. To evaluate the influence of the thickness of the medium, six additional samples, with same porosity level and same hole shape and dimension, have been investigated. Finally the shape effect has been checked on four grid samples having the same porosity level, same hydraulic diameter, but with round or square shape of the holes.

5.3 Study of the flow inside the PVC pipe

A fundamental phase of the test is the characterization of the flow field inside the instrumented PVC pipe. The set-up has been designed in order to have a controlled system of flow approaching the grid samples under testing. The test section for the screens is positioned at 50 cm from the inlet section, and this location has been chosen with the purpose to have a clean zone of flow. In the test zone the main idea is to have a flat wind speed profile, and a small sub-zone of boundary layer. This short entrance length of inlet in the pipe has the function of avoiding the fully developed velocity profile with the characteristic parabolic shape. Fig. 5.15 illustrates laminar flow in the entrance region of circular pipe. The flow has uniform velocity profile at the pipe entrance, and increasing the distance from the entrance, the speed profile becomes sharper. It is well known that the velocity at the wall is zero and a boundary layer develops along the walls of the channel. There is an *entrance region* where a nearly inviscid upstream flow converges and enters the tube. Viscous boundary layer grows downstream, retarding the axial flow $u(r, x)$ at the wall and thereby accelerating the centre-core flow to maintain the incompressible

continuity requirement (*flow rate is constant along all sections of the pipe*). At a finite distance from the entrance, the boundary layers merge and the inviscid core disappears. Downstream of the entrance length (L_e) the velocity profile is constant, the wall shear is constant and the pressure drop decreases linearly with the distance (x) for both laminar and turbulent flow. The shape of the velocity profile in the pipe depends on whether the flow is laminar or turbulent, as does the length of the entrance region. As with many other properties of pipe flow, the dimensionless entrance length correlates quite well with the Reynolds number. For very low Reynolds number ($Re = 10$) flows, the entrance length can be quite short in order of $L_e = 0.6D$ whereas for large Reynolds number ($Re > 2100$) flows, it may take a length equal to many pipe diameters before the end of the entrance region is reached for $L_e \approx 20D$. The choice to fix the grid test section at 50 cm from the inlet, thus fix $L_e = 50$ cm, is a good compromise between avoiding the development of thick boundary layer and having a bad incident wind profile.

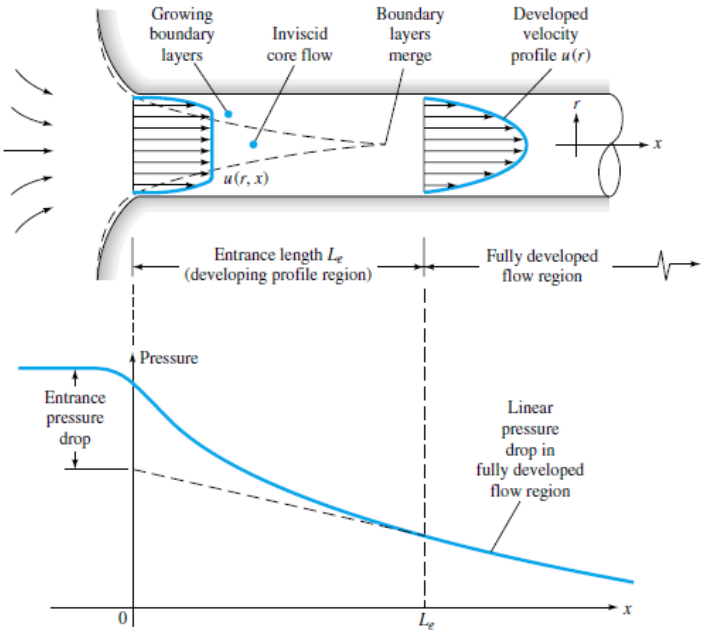

Fig. 5.15 Flow in the entrance region of a pipe (White, 2001).

The transition from laminar to turbulent flow in a pipe occurs, under normal condition, at Re $\approx$ 2100, and the Reynolds number is defined as:

$$Re = \frac{UD}{\nu} \tag{5.2}$$

where: U is the flow velocity inside the pipe; D the internal diameter of the pipe and ν the flow kinematic viscosity. If considering the air speed at temperature of 20 °C, with kinematic viscosity $\nu = 1.5 \cdot 10^{-5}$ and pipe diameter D = 395 mm it is possible to calculate the threshold of wind speed that establishes the transition between two regimes. Executing this simple calculus the threshold of air velocity is equal to 0.09 m/s. The speed value obtained is very low and confirms that the air flow inside

the experimental set-up is always in turbulent regime. Due to the characteristics of wind tunnel in use, it is almost impossible to have an incident mean velocity less than 1 m/s, so the tests were carried out on perforated plates in turbulent motion. Leaving aside the theoretical approach of the problem the wind speed profile inside the pipe in turbulent motion is more flattened than in laminar case (Fig. 5.16). Thus a turbulent velocity profile is very flat in the central core and drops off sharply to zero at the wall.

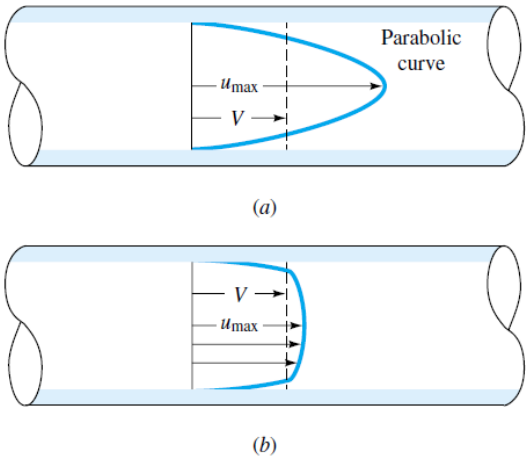

Fig. 5.16 Comparison of pipe-flow speed profiles.
a) laminar b) turbulent (White, 2001).

The turbulent velocity profile is a positive achievement because it is very close to the idea of investing the sample of the grid by a uniform and constant wind speed, respect to the laminar case where the wind speed is less homogeneous and the wind profile is sharper.

In order to have a deep comprehension of the flow field inside the pipe in correspondence of the grid test section many experimental measurements with hot wire anemometer were made. In the grid test section, for fifteen different flow rate values (*from 0.56 to 2.75* m^3/s), the wind speed and the intensity of turbulence mean profiles were examined. As the PVC pipe has circular section it is well established that the horizontal and vertical velocity profiles are supposed to be equal. In this experimental work the two fundamental profiles are measured with the aim to check on one hand if there is any asymmetry of flow due to the wrong collocation of the experimental apparatus respect to the external airflow; on the other hand to have a global characterization of the flow field inside the pipe. With the purpose of creating a minimal disturb of the confined flow two small openings have been made on the PVC pipe and through them it has been positioned a hot wire anemometer. The holes are placed on the grid test section in vertical direction and horizontal direction. The profiles have been measured using an external mechanical robot arm, where thanks to three step by step motors it was possible to move the hot wire anemometer inside the pipe with very high precision, in the order of $\pm$ 0.1 mm, and create excellent profiles (Fig. 5.17).

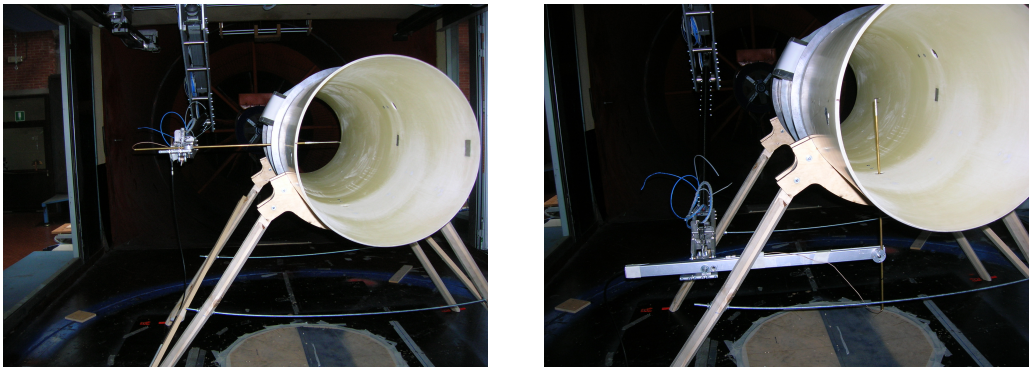

(a) Horizontal (b) Vertical

Fig. 5.17 Measurement of profiles inside the PVC pipe.

During the measurement phase the experimental data are acquired for 120 seconds with sampling frequency equal to 2000 Hz. The profiles are created using 39 points of measure, spaced 15 mm ÷ 20 mm apart in the central area, where it is assumed that the flow was flat and smooth; by contrast, in the area close to the walls, in order to estimate the boundary layer thickness, the spacing was reduced in the range 2 ÷ 5 mm. Profiles of velocity and turbulence measured horizontally and vertically are identical. This shows that the experimental set-up is well positioned respect to the external air flow, and there are no problems of flow deviation. The speed profile is flat and smooth in the central area of the tube, as expected, while near the wall, it is influenced by the viscous effects. In this zone the profile has an almost linear decrease so that the velocity vanishes at the wall, thus respecting the no-slip conditions (Fig. 5.18).

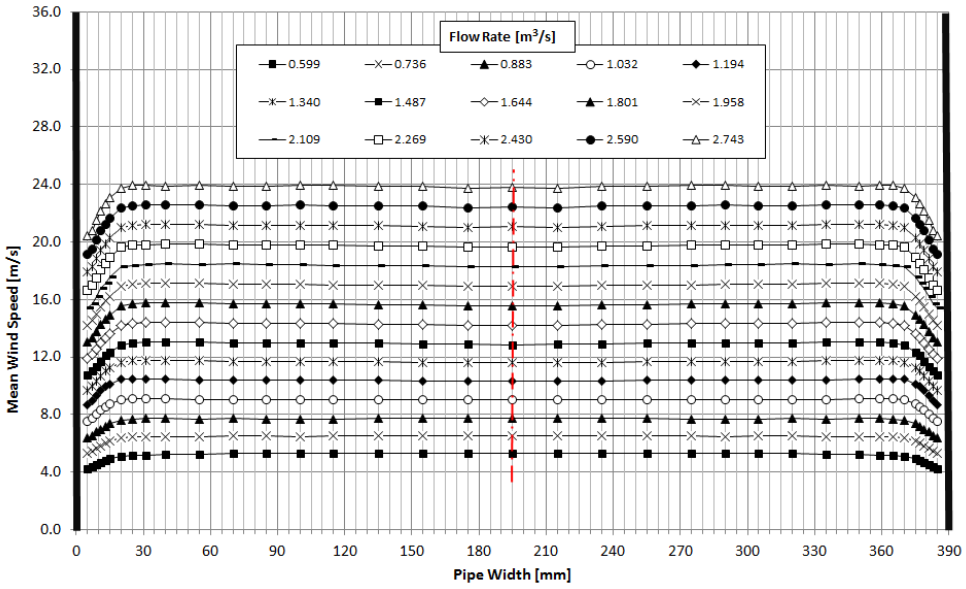

Fig. 5.18 Horizontal mean wind speed profile.

The wind speed value in proximity of the wall has not been measured because it was not possible to put the hot wire probe too close to the wall. This problem is due to the size of the sensor of measure, in fact the first measure to the wall has been taken at a distance of 5 mm, which represents the thickness of the hot wire. The relative graph shows also the presence of a small boundary layer thickness approx. 15 mm ÷ 20 mm. Before showing the other profile relative to the turbulence intensity it is necessary to explain briefly what represents this quantity and how it can be defined. The turbulence intensity index is a parameter able to give a numerical quantification of turbulence level and it is defined as follows:

$$I_t = \frac{\sigma_u}{U_m} \tag{5.3}$$

where: σ_u is the standard deviation of the time history of wind speed and U_m is the mean component of wind speed. Also in this case the horizontal and vertical profiles are equivalent. In Fig. 5.19 the horizontal one is reported.

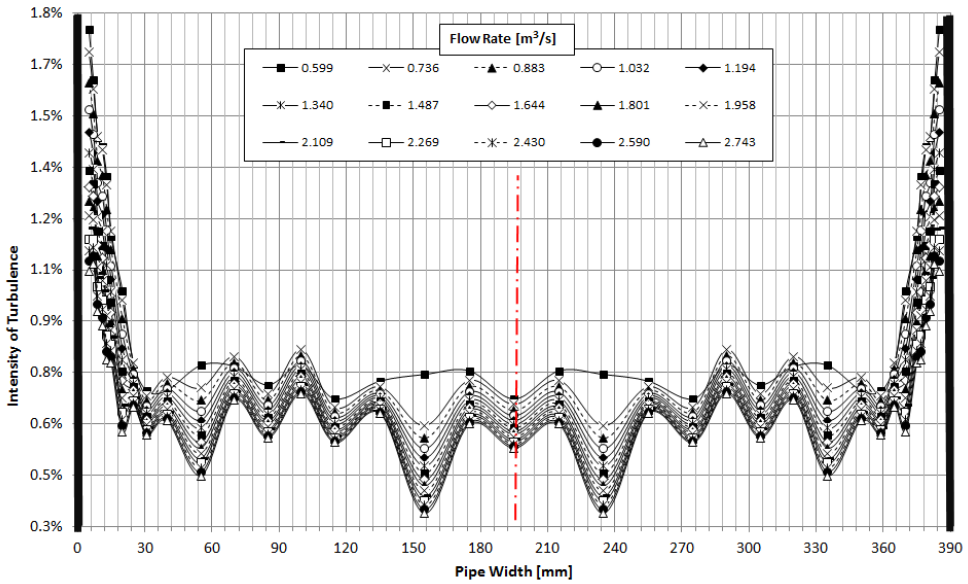

Fig. 5.19 Horizontal intensity of turbulence profile.

The profile of turbulence intensity is the opposite of the speed's, in fact there are high values of the index in close proximity to areas of high turbulence and low values in areas with little turbulence. In correspondence to the wall the index grows from 0.6% to 1.8%, this is attributable to the presence of a thin boundary layer. Outside the boundary layer and inside the inviscid core flow, the turbulence intensity is more uniform and it is in the range 0.6% ÷ 0.8%. Considering both mean wind speed profile and intensity of turbulence profile, it is possible to confirm the high quality of the flow field inside the experimental PVC apparatus. Indeed the low level of turbulence (lower than 2%) and the regularity of velocity profiles imply that there is not huge mixing of flow and that the boundary layer is confined close to the wall. The flow that has been obtained meets the required test conditions, i.e. a controlled flow environment, with uniform velocity profile and low-turbulence intensity.

5.4 Experimental measurements

To support this activity, as already shown, a particular measurement set-up has been realized. It had the purpose of describing the behaviour of the perforated plate by evaluating the wind speed and the patterns of pressure upstream and downstream of the obstacle, the related drop of pressure and the drag force on the perforated plate. To consider possible asymmetries in the screen structure, the experiments were carried out with air flowing in both direction through the grid sample. None of the 28 samples tested exhibited any signs of dirt accumulation, deformation or structural failure before or after the experimental campaign. Tests have been completed in correspondence to 15 different values of flow speeds. The three extensometric TRP 2 load cells recorded signals for 120 seconds with sampling frequency of 1000 Hz, while the PSI instrumentation acquired pressure signals for 60 seconds with a sampling frequency of 333 Hz. Finally, to check the flow velocity incident the screen, the two pitot tubes acquired data for 120 seconds at sampling frequency of 1000 Hz. The air flow approaching the samples under testing was generated by the wind tunnel fan and subsequently canalized into the PVC pipe.

Quantity	**Unit**	**Instrument**
U_{mean}	$[m/s]$	Pitot BLWT
U_{std}	$[m/s]$	Pitot BLWT
Q_{in}	$[m^3/s]$	Hot-wire
u_{mean}	$[m/s]$	Pitot Up-wind
u_{std}	$[m/s]$	Pitot Up-wind
u'_{mean}	$[m/s]$	PSI Up-wind
u'_{std}	$[m/s]$	PSI Up-wind
v_{mean}	$[m/s]$	Pitot Down-wind
v_{std}	$[m/s]$	Pitot Down-wind
v'_{mean}	$[m/s]$	PSI Down-wind
v'_{std}	$[m/s]$	PSI Down-wind
$Drag_{mean}$	$[N]$	Three load cells
$Drag_{std}$	$[N]$	Three load cells
$Pressure_{mean}$	$[mm_{H_2O}]$	Pressure taps PSI
$Pressure_{std}$	$[mm_{H_2O}]$	Pressure taps PSI

Table 5.3 Quantities measured in wind tunnel.

The actual air-channelled inside the pipe depends upon the level of porosity of the grid because screens at low porosity offer testing velocity values reduced respect to the screens with high porosity.

The main quantities that have been acquired during the test phase are subdivided in function of the reference measuring instruments and are reported in Table 5.3. Using a fixed pitot tube it was possible to measure the mean and standard deviation of reference airflow velocity in the test chamber of the wind tunnel. It was recorded in an external zone respect to the set-up $[U_{mean}; U_{std}]$ and it was useful to operate a comparison between the inner and outer air flow. The flow rate at the inlet of the

PVC pipe $[Q_{in}]$ was measured by a simple integration of the mean wind speed profile along the tube cross section. With two pitot tubes located at a distance of ± 25 cm with respect to the grid test section, in up-wind and down-wind position the mean and standard deviation of wind speed in front and behind the grid were evaluated $[u_{mean}; v_{mean}; u_{std}; v_{std}]$. In order to have a double control of the approaching airflow on the perforated plate samples the mean values of velocities and standard deviation were calculated also with a PSI system $[u'_{mean}; v'_{mean}; u'_{std}; v'_{std}]$. By combining the output signals from three load cells and using the calibration matrix (k) it was possible to evaluate the mean and standard deviation of drag force induced by the wind on the porous plate $[Drag_{mean}; Drag_{std}]$. The pressure patterns and drop of pressure have been measured with an appropriate system of 22 pressure taps. More in details in correspondence to each pressure tap the mean and standard deviation of pressure data were determined $[Pressure_{mean}; Pressure_{std}]$. In Fig. 5.20 a general view of the system of acquisition data and a sketch of the recording phase are reported.

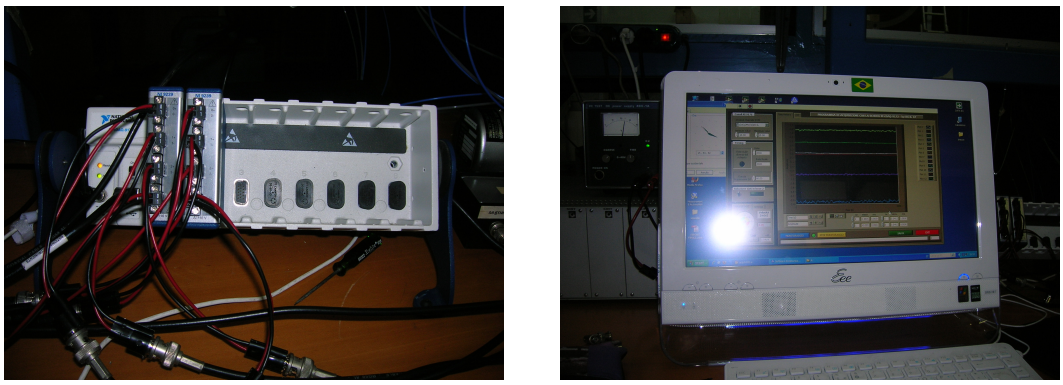

(a) Acquisition card (b) Signal acquisition monitor

Fig. 5.20 Particulars of signal acquisition system.

For each sample, three fundamental graphs have been created. One reports the patterns of pressure as a function of the distance up-wind and down-wind from the porous grid; another one indicates the trends of drag and loss coefficients; the third graph is related to the drop of pressure with respect to the velocity through the screen, in order to complete a typical analysis of flow through porous media.

5.5 Experimental results

With the help of the particular set-up built in the CRIACIV Boundary Layer Wind Tunnel, it was possible to obtain experimental data for twenty-eight grid samples. The analysis of experimental data is divided into two parts, the first one is related to the elaboration of pressure data acquired by the PSI unit and the second one refers to the force data sampled by the three load cells.

5.5.1 Pressure data

Before going into details of the analysis it is necessary to briefly summarize some fundamental concepts related to the theoretical behaviour of static pressure when an obstruction, in this case represented by porous grids, is inserted in a pipe or duct. Fig. 5.21 shows a typical experimental static pressure distribution along the axis of a pipe containing a perforated plate, represented in the picture with the term *Component*.

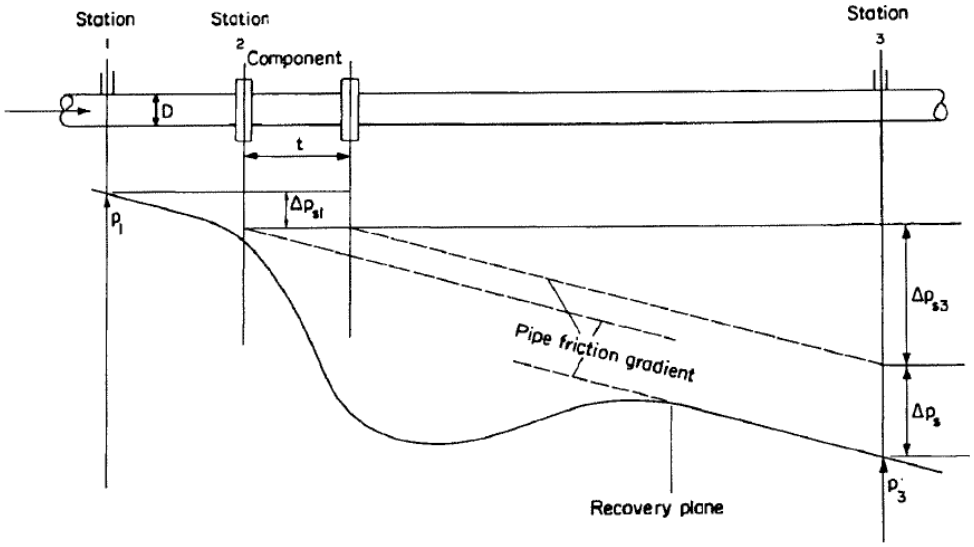

Fig. 5.21 Distribution of pressure along the axis of pipe (ESDU81039, 1985).

The recovery plane is variable but often is approximately fixed at $6D_h$ downstream a single orifice. ESDU81039 (1985) and Idelchik (1994) suggest for a perforated plate a value of $6D_h\sqrt{\varepsilon}$ to be taken for the distance of the recovery plane from the grid. D_h is the hydraulic diameter of hole and it is already defined in equation (5.1) and ε is the porosity of the grid.

The static pressure drop is defined as:

$$\begin{aligned} \Delta p_s &= (p_{m1} - \Delta p_{s1}) - (p_{m3} - \Delta p_{s3}) \\ \Delta p_s &= p_1 - p_3 \end{aligned} \tag{5.4}$$

where: p_{m1} and p_{m3} are static pressures measured in the system at stations (1) and (3) respectively and p_1 and p_3 are static pressures at the same points but corrected for pipe friction losses up to entry and beyond the exit of the component (*for perforate plate the friction losses are negligible*). Stations (1) and (3) are strictly taken to be in regions where a sudden contraction does not influence the wind speed profile.

The total pressure loss Δp is equal to Δp_s in case of incompressible flow and is given by:

$$\Delta p_s = \Delta p = \frac{1}{2}\rho\overline{u}^2 K \tag{5.5}$$

and the loss coefficient K can be calculated by a simple inversion of the equation (5.5), as follows:

$$K = \frac{\Delta p}{\frac{1}{2} \cdot \rho \cdot \overline{u}^2} \tag{5.6}$$

where: Δp is the total drop of pressure up-wind and down-wind, ρ is the air density and $\overline{u}$ is the testing mean wind speed inside the PVC pipe.

The values of velocity ($\overline{u}$) are achieved averaging the two values of wind speed in up-wind position obtained by pitot tube (u_{mean}) and PSI system (u'_{mean}) and the two speed values in down-wind location always provided by pitot tube (v_{mean}) and PSI system (v'_{mean}). This assumption is valid because the difference between the velocity values measured by the two instruments is negligible (about 2 %). For each one of the twenty-eight grid samples an opportune graph with the same shape of Fig. 5.21 has been created. Fig. 5.22 shows for one sample of perforated plate (R1.5T3) the pressure distribution, in correspondence to the instrumented static pressure taps along the axis of the PVC pipe, respect to fifteen different flow rate values.

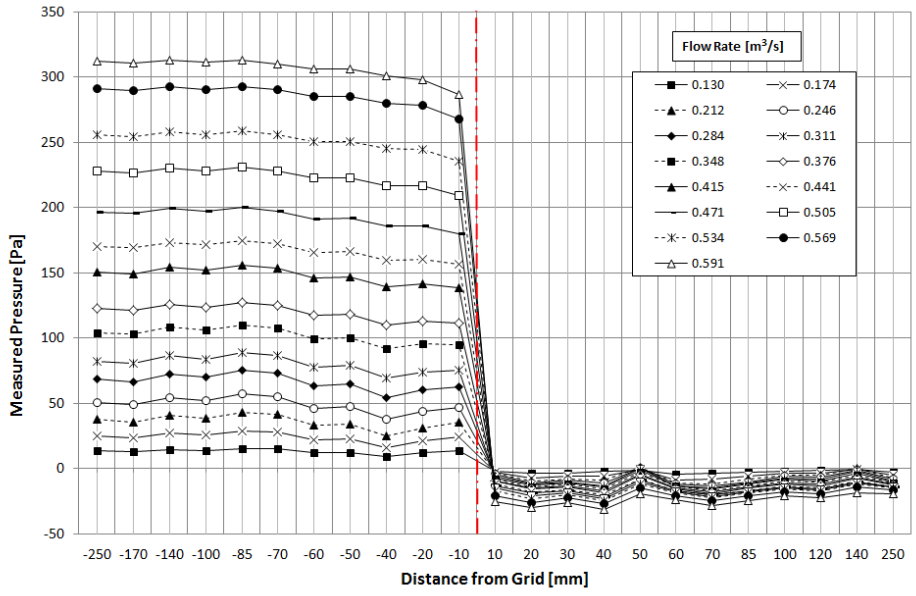

Fig. 5.22 Pressure distribution for grid R1.5T3 (ε=22.68 %, D_h=1.5 mm and t=1.5 mm).

It can be seen that upstream of the plate there is a gradual decrease of the pressure due to the friction at the PVC pipe wall. In the immediate neighbourhood of the plate there are rapid variations of pressure. The static pressure in correspondence of the perforated plate surface (*represented by red dot broken line*) declines suddenly due to contraction of the air passage. However, there is a rise in the static pressure on the wall surface just before the plate. Part of the pressure is recovered when air flows out of the plate as a result of conversion of kinetic energy to static pressure.

From the graph it is not possible to establish with high precision where the maximum recovery occurs, because the first useful pressure tap is positioned at 10 mm from the grid. Further down-wind the pressure distribution again settles down due to duct wall friction.

Regarding the total pressure drop (Δp) it has been estimated by a simple difference between the up-wind pressure ($\Delta p_{up-wind}$) and the down-wind pressure ($\Delta p_{down-wind}$).

$$\Delta p = \Delta p_{up-wind} - \Delta p_{down-wind} \tag{5.7}$$

The reference pressure values (up-wind, down-wind) have been obtained using the pressure pattern reported in Fig. 5.22 and especially considering the constant pressure values that are not influenced by the presence of the screen. The reference up-wind pressure is defined averaging the pressure values in the first three pressure taps located respectively at -250, -170, -140 mm. Instead for the down-wind reference pressure the values are averaged on the last three pressure taps at 250, 140, 120 mm. Making this subtraction it is possible to estimate 15 drops of pressure in correspondence of the 15 different flow rate levels.

Using the values of drop of pressure measured and applying the equation (5.6), it is possible to calculate the loss coefficient K, in correspondence of each flow rate value for all the samples tested. It is common practice in fluid dynamics to express the relationship between the variables involved in dimensionless terms, with the purpose to have a dimensionless relationship. The loss coefficient as it is defined, is already a dimensionless quantity, while the 15 testing velocities or flow rates are dimensional parameters. The fundamental dimensionless parameter which provides a dimensionless representation of variables like velocity or flow rate is the Reynolds number. In this study it is necessary to give two different definitions of Reynolds number: the Global Reynolds number (Re_G) and the Local Reynolds number (Re_L).

$$Re_G = \frac{\overline{u} \cdot D}{\nu} \tag{5.8}$$

$$Re_L = \frac{w_0 \cdot D_h}{\nu} \tag{5.9}$$

where: D is the diameter of the screen sample, fixed in 390 mm; D_h is the hydraulic diameter; ν is the kinematic viscosity of air and w_0 is the wind speed through the permeable material, calculated as the ratio between the testing mean wind speed and the porosity level ($w_0 = \overline{u}/\varepsilon$).

In Fig. 5.23 the dimensionless graph reports the relationship between the loss coefficient K respect to the Local and Global Reynolds number. This kind of diagram has been realized for all the samples tested and it has the function of highlighting the influence of Reynolds effects on loss coefficient. Black and white dots represent the results of experimental tests on model R1.5T3 and a comparison with the available literature (Idelchik, 1994) is represented by a black broken line. The experimental data are in accordance with the empiric model of Idelchik and this can be demonstrated by analysing the little discrepancy between the experimental data and the ones from Idelchik. The graph shows also that the viscous effects are important for values of Local Reynolds number below 2000 and become less relevant when the inertia forces are predominant with respect to the viscous effect, if Re_L is higher than

2000. This reasoning can be extended also to the global Reynolds number below 110,000 for the viscous region and beyond 110,000 for the inertial zone.

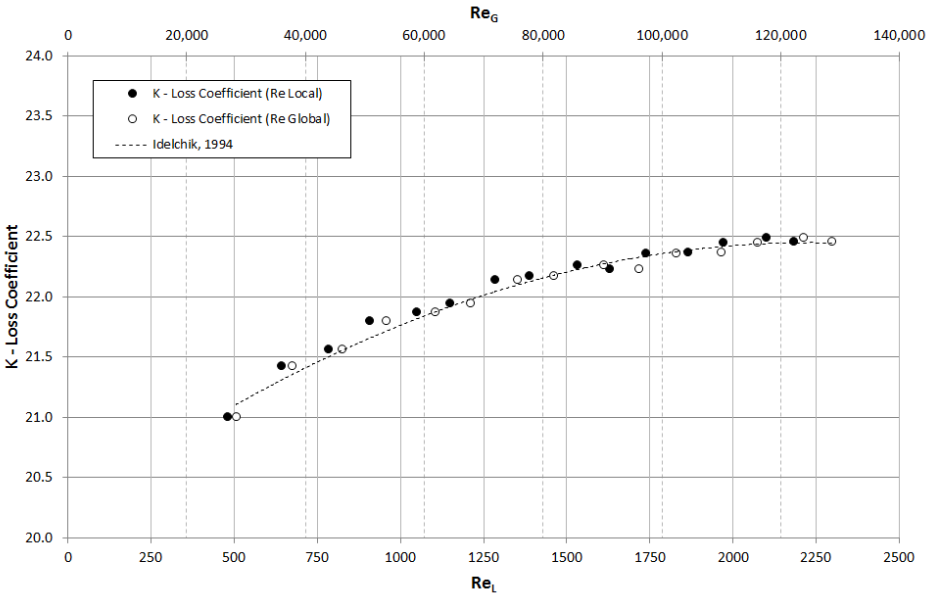

Fig. 5.23 K vs. Re_L; Re_G for grid R1.5T3 (ε=22.68 %, D_h=1.5 mm and t=1.5 mm).

For each grid sample tested, the data resulting from the experiments performed were plotted also as pressure drop versus the testing mean wind speed $\overline{u}$ (*superficial fluid velocity*), as shown in Fig. 5.24. In all the samples tested, the equation that best seemed to fit the curves obtained was a second order polynomial $\Delta p = a\overline{u}^2 + b\overline{u} + c$. In literature [(Miguel *et al.*, 1997); (Miguel, 1998); (Teitel *et al.*, 2009)] the zero order term c can be neglected compared with the other terms due to its small entity and relevance. Then, the best fitting function in use is a modified polynomial $\Delta p = a\overline{u}^2 + b\overline{u}$. This type of equation in this case needs to be further simplified as $\Delta p = a\overline{u}^2$ because the linear term $b\overline{u}$ is strictly related to the viscous effects and its exact estimation can be obtained only testing the samples at low Local Reynolds number ($Re_L \approx 1$). Carrying out experiments at low Reynolds numbers means testing grid samples at wind velocities in order of 1-2 mm/s. This kind of wind speed is totally insignificant for porous materials like windbreaks or permeable walls, because their application or scope is studied for higher wind speeds in order of metres per second and not millimetres per second. Thus the experiments done in wind tunnel are made in fully turbulent motion and they are able to capture only the quadratic part, thus the inertial effect of the motion. The relationship is well represented, as already shown in the Chapter 3, by the turbulent flow equation:

$$\textbf{Turbulent flow:} \qquad \frac{\Delta P}{L} = a\overline{u}^2 \tag{5.10}$$

where: L represents the thickness of the screen and a the fitting coefficient, in case of sample R1.5T3 a is equal to 13.48.

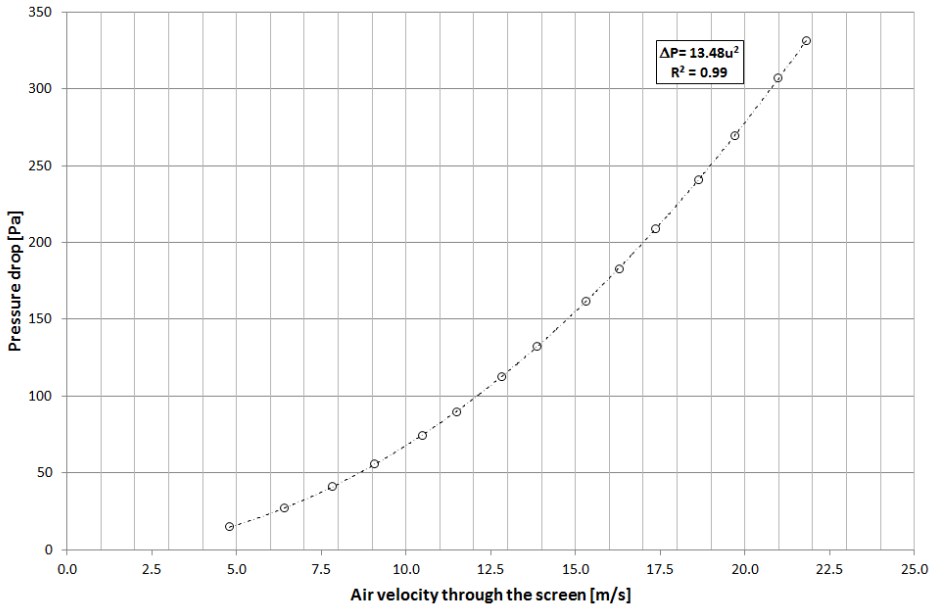

Fig. 5.24 Pressure Drop vs. $\overline{u}$ for grid R1.5T3 (ε=22.68 %, D_h=1.5 mm and t=1.5 mm).

For all the samples tested the a coefficients are collected but are not significant without the viscous effects quantification (b). Therefore it will be completed an elaboration in terms of loss coefficient K instead of a typical modelling of porous media in order to evaluate more in detail the effects of porosity, shape and dimension.

5.5.2 Force data

Whenever there is relative motion between a solid body and the fluid in which it is immersed, the body experiences a net force, $\vec{F}$, due to the action of the fluid. In general, the infinitesimal force, $d\vec{F}$, acting on an element of surface area, will be neither normal nor parallel to the element. This can be seen clearly when one considers the nature of the surface forces that contribute to the net force, $\vec{F}$. If the body is moving through a viscous fluid, both shear and pressure forces act on it:

$$\vec{F} = \int_{body\ surface} d\vec{F} = \int_{body\ surface} d\vec{F}_{shear} + \int_{body\ surface} d\vec{F}_{pressure} \tag{5.11}$$

The resultant force, $\vec{F}$, can be resolved into components parallel and perpendicular to the direction of motion. The component of force which is parallel to the direction of motion is the Drag force (F_D) and the force component that is perpendicular to the direction of motion is the Lift force (F_L). There are few cases in which the lift and drag can be determined without recourse to experimental results. The presence of an adverse pressure gradient often leads to separation; flow separation prohibits the analytical determination of the force acting on a body. Therefore, also when studying the behaviour of perforated plates respect to air flow it is necessary to resort to the use of experimental measure to compute the force involved. In case of perforated sheets the fundamental force exercised by wind on screen is due to the

pressure component (*drag*) that compared to lift has a bigger relevance.

The total drag force has been evaluated using the data acquired by three load cells. In Fig. 5.25 are reported for each load cell in use the values of drag force measured in correspondence of the flow rate across the sample R1.5T3. The graph reports the force recorded by load cells 1, 2, and 3 and the sum of these values reported under the name *Total Drag*, that represents the global drag force acting on the sample.

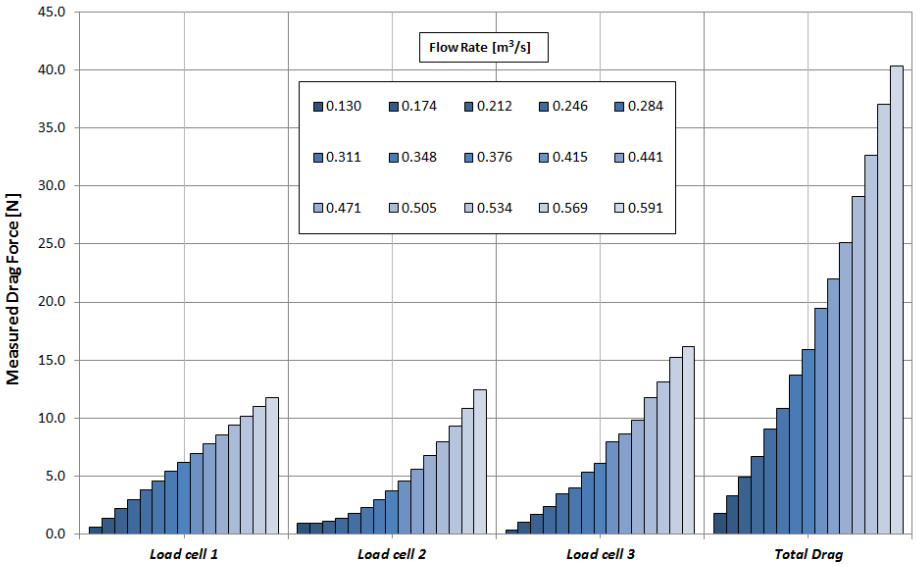

Fig. 5.25 Measured drag force for grid R1.5T3 (ε=22.68 %, D_h=1.5 mm and t=1.5 mm).

The previous graph (Fig. 5.25) has been realized for all of the twenty-eight samples, in order to evaluate the drag force due to the wind flow through the screens. Considering the flow through a perforated plate the dimensionless drag coefficient (C_D) is given as:

$$C_D = \frac{F_D}{\frac{1}{2} \cdot \rho \cdot \overline{u}^2 \cdot A} \tag{5.12}$$

where: F_D is the drag force on the grid, ρ is the air density, $\overline{u}$ is the mean wind speed inside the PVC pipe and A is the total full area of the sample under testing. This is one of the possible ways to define the dimensionless coefficient C_D respect to the independent quantity (ρ, $\overline{u}$, A).

As in the case of the loss coefficient, also for the drag coefficient it is necessary to express dimensionless relationship between the quantities. More in particular the trends C_D vs. Reynolds numbers (Re_L and Re_G) are shown in Fig. 5.26. The drag coefficient data are more sensible and less stable respect to the loss coefficient because they are more scattered. This dispersion is attributable to the high sensitivity of the load cell to small vibrations of the grid during the tests. This fact does not invalidate the measurements which are of good quality but highlights that in correspondence

of small value of porosity (in this case ε=22.68 %) little vibrations can occur. The dispersion is present only in this sample; in other grids with higher porosity levels the effect is never present. In spite of this, the graph shows that exists the same dependency of C_D respect to Reynolds numbers in the viscous zone ($500 < Re_L < 2000$ or $30,000 < Re_G < 110,000$). It also highlights an almost independence from Reynolds number ($Re_L \geq 2000$ or $Re_G \geq 110,000$) in the inertial region.

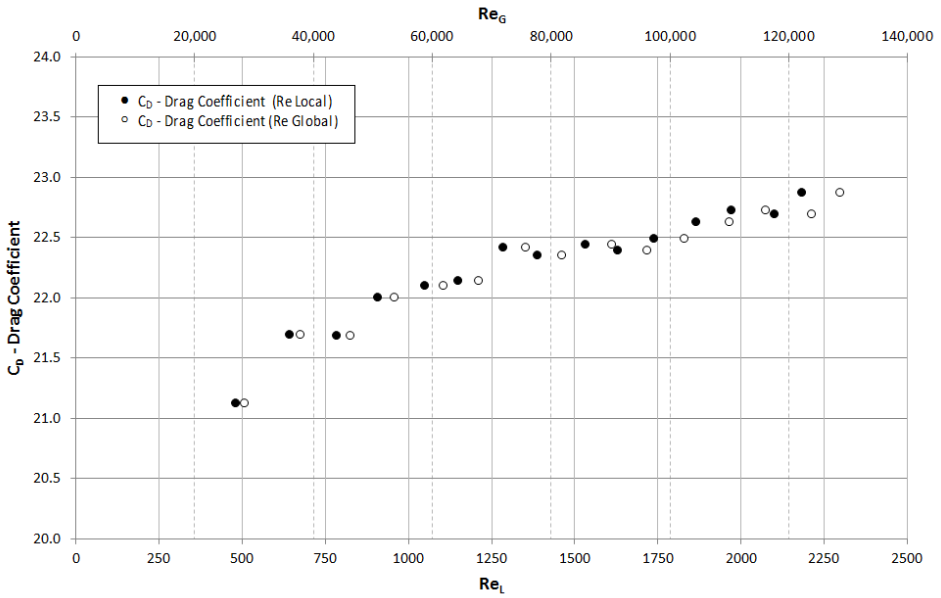

Fig. 5.26 C_D vs. Re_L and Re_G for grid R1.5T3 (ε=22.68 %, D_h=1.5 mm and t=1.5 mm).

5.5.3 Relationship $K - C_D$

The data of drag and loss coefficients are very close and they are included in the range of about 21 to 23 as both the diagrams show (Fig. 5.23 and Fig. 5.26). Thus it is fundamental to put in relation the two quantities with the purpose to find some correlation between the two dimensionless key parameters (Fig. 5.27). Since the momentum normal to the screen is conserved, the drag force (F_D) is equal to the drop of pressure due to the grid (Δp) multiplied by the area of porous sample (A) [$\Delta p \cdot A = F_D$]. So, by introducing in the previous statement the loss (5.6) and the drag coefficient (5.12) it is possible to arrive to:

$$\begin{gathered} K \cdot \frac{1}{2} \cdot \rho \cdot \overline{u}^2 \cdot A = C_D \cdot \frac{1}{2} \cdot \rho \cdot \overline{u}^2 \cdot A \\ K = C_D \end{gathered} \tag{5.13}$$

Thus, K and C_D are equal and can be used interchangeably to describe the behaviour of the screen respect to the air flow. This theoretical result is fully supported by the experimental data as shown in Fig. 5.27. In fact the discrepancy between the $K - C_D$ data is in the order of $1 \div 2$ % and falls in the range of measurement error, so it is possible to confirm what was anticipated by equation 5.13.

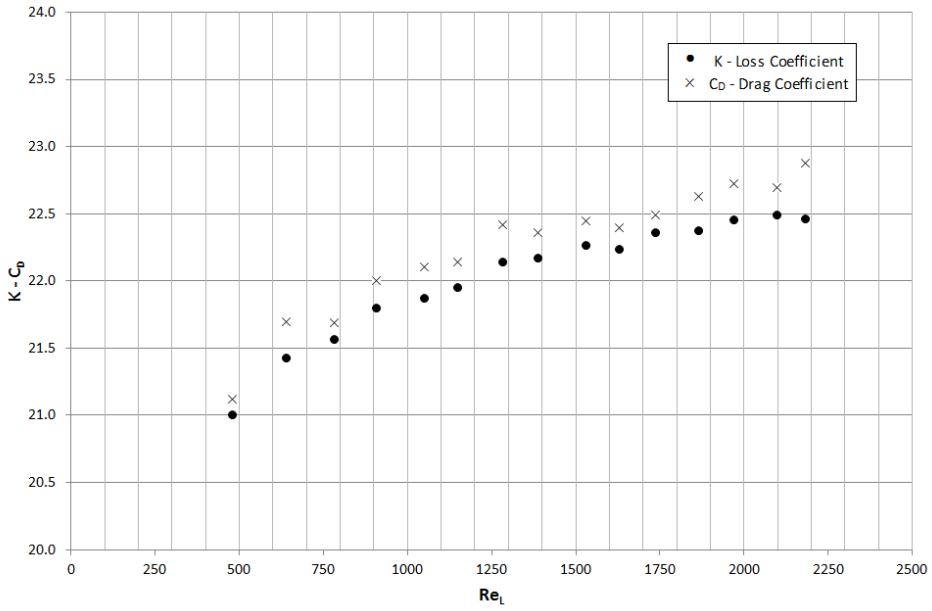

Fig. 5.27 $K - C_D$ vs. Re_L for grid R1.5T3 (ε=22.68 %, D_h=1.5 mm and t=1.5 mm).

The same trend is observed for all the 28 samples tested where the results show that K and C_D are very close and they are not much influenced by the Local Reynolds number if Re_L is higher than a critical threshold value.

5.6 Analysis of the data

In this paragraph the most relevant results of the experimental campaign in wind tunnel are reported and commented. Since both K and C_D have the same meaning and are identical in value, it was decided to consider only the loss coefficient (because it is more regular than drag coefficient) to explain the results of experimentation. All the elaborations presented will be expressed in function of the loss coefficient K and the Local Reynolds number (Re_L). These parameters are commonly used to characterize the behaviour of confined screens respect to air flow, and they can be easily compared with many important studies present in literature.

The discussion will be divided according to various parameters that are able to influence the loss coefficient. Indeed, the effects due to the level of porosity, Reynolds number, thickness of the perforated plate and dimension and shape of the holes will be considered. This subdivision has the aim to quantify and study more in detail the influence of various parameters involved in the loss coefficient, in order to find possible correspondences and key parameters.

5.6.1 Effect of porosity level and Reynolds number

As easily imaginable, the level of porosity is a key factor when studying the behaviour of permeable obstacle to air flow.

Fig. 5.28 reports for all the samples tested in wind tunnel the global effects of all variables involved respect to loss coefficient. The diagram is plotted in function of

only local Reynolds number Re_L and shows at first glance the influence of porosity on loss coefficient. It is possible to see from the graph that the K data are subdivided in function of porosity level and fall in the interval $0.95 \div 22.4$. As expected, high values of loss coefficient correspond to low values of porosity level and low values of K are found for high porosity.

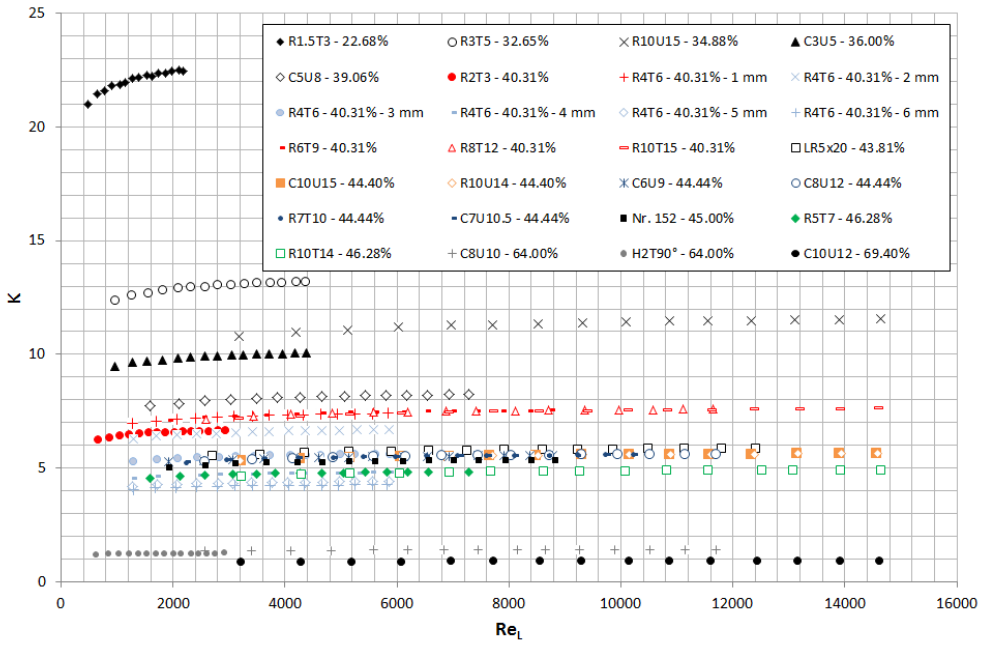

Fig. 5.28 K vs. Re_L for all the samples tested.

The most common practice, present in literature [Pinker and Herbert (1967); Brundrett (1993); Valli *et al.* (2009)], consists in separating the loss coefficient K in two distinguished functions: one depending on porosity (ε) and the other on the Local Reynolds number (Re_L), as follows:

$$K(\varepsilon, Re_L) = G(\varepsilon) \cdot F(Re_L) \tag{5.14}$$

where: $G(\varepsilon)$ and $F(Re_L)$ are respectively functions of porosity and Local Reynolds number.

For each typology of grid, considering the K data where the loss coefficient does not depend on Local Reynolds number *(in this case represented by the average of last three points of each K - Re_L diagram)*, it was possible to find the analytic expression of $G(\varepsilon)$ function by a simple fitting of the data.

Fitting the points of the graph (Fig. 5.29), the $G(\varepsilon)$ function has been estimated and the best fitting is represented by an exponential function:

$$G(\varepsilon) = 127.09e^{(-7.05\varepsilon)} \tag{5.15}$$

$$\textbf{with: } R^2 = 0.9967 \ ^1$$

[1] (R^2) is the determination coefficient.

The fitting curve works very well for all grids with the exception of the sample R1.5T3 where the porosity level is very low ($\varepsilon = 22.68\%$). For this perforated plate $G(\varepsilon)$ presents a slight overestimation in the order of 10% of the loss coefficient compared to the experimental measured value during the test in wind tunnel. The fitting data are congruent with the logical limits of K, in fact $K \to \infty$ as $\varepsilon \to 0$ and $K \to 0$ as $\varepsilon \to 1$.

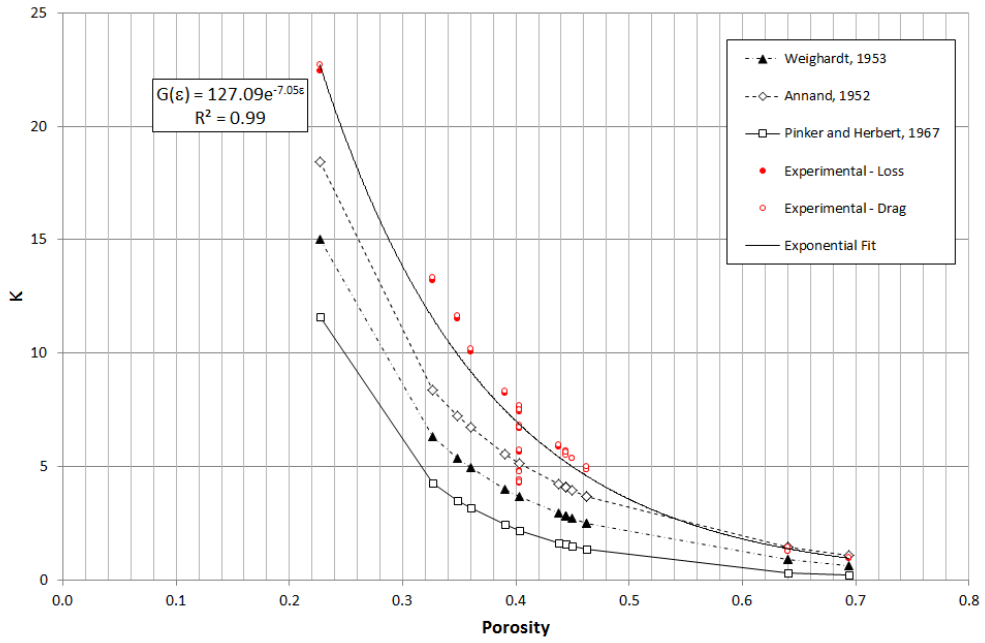

Fig. 5.29 $G(\varepsilon)$ fitting function.

Fig. 5.29 reports also a comparison with the empirical $G(\varepsilon)$ functions proposed in literature by several authors [Annand (1953); Weighardt (1953) and Pinker and Herbert (1967)]. Between the fitting curve and other empirical functions of the literature there is a noticeable difference especially as regards the values of K at low and medium porosity. These curves were obtained by testing screens made of round-wire gauzes normal to the flow and the differences seem to be imputable to different objects in testing.

Hence, it seems that the most important role is played by the porosity and that K does not depend on the Local Reynolds number when it is higher than 3000 as it can be seen from the graph K vs Re_L (Fig. 5.28). Also other studies present in literature [Brundrett (1993); Richards and Robinson (1999) and Valli *et al.* (2009)] seem to confirm these experimental results.
The Reynolds number dependency can be isolated dividing the $K(\varepsilon, Re_L)$ data, reported in Fig. 5.28, by the $G(\varepsilon)$ function found in equation (5.15). Then, the $F(Re_L)$ function can be defined as follows:

$$F(Re_L) = \frac{K(\varepsilon, Re_L)}{G(\varepsilon)} \tag{5.16}$$

In Fig. 5.30 (F vs Re_L) it is possible to see that the dependency on porosity has been removed, because the empirical data are not subdivided in function of the porosity level and the $F(Re_L)$ is included in the range $0.55 \div 1.08$.

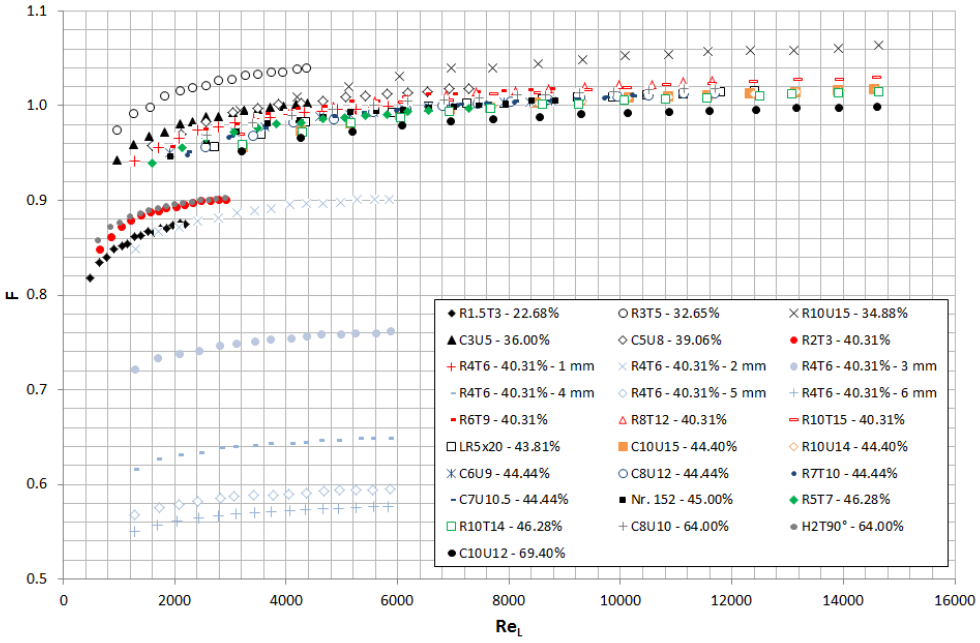

Fig. 5.30 F function vs. Re_L for all of samples tested.

The chart shows the Reynolds number effect for each sample of porous material. The diagram confirms that the effects of Reynolds become negligible when the local Reynolds number is higher than 3000. Looking closely at Fig. 5.30 the F function is called improperly $F(Re_L)$ because it highlights that there are not only Reynolds effects but also other issues due to additional parameters involved. This is pointed out by the eight curves that are found in the lower part of the graph which are related to perforated plates having different diameter and thickness of the holes. Therefore it may be conceivable that even the diameter, thickness and shape of the holes play fundamental roles in this situation.

5.6.2 Thickness effect

In order to study more in detail the influence played by the thickness of perforated plate, six different typologies of screen, with different thickness, have been tested during the experimental campaign of measurements. The screens had same level of porosity fixed equal to 40.31 %, same shape and dimension of holes, with the aim of removing possible dependencies on porosity, shape and dimension. The characteristics of grids used for thickness tests are summarized in the table (5.4).

Model	**Porosity % (ε)**	t **[mm]**	D_h**[mm]**	**Shape**
R4T6	40.31	1.0	4.0	Round
R4T6	40.31	2.0	4.0	Round
R4T6	40.31	3.0	4.0	Round
R4T6	40.31	4.0	4.0	Round
R4T6	40.31	5.0	4.0	Round
R4T6	40.31	6.0	4.0	Round

Table 5.4 Samples for thickness tests.

Also in this case an important diagram is reported where it is shown the influence of thickness respect to loss coefficient (K) in correspondence of different Reynolds numbers (Fig. 5.31).

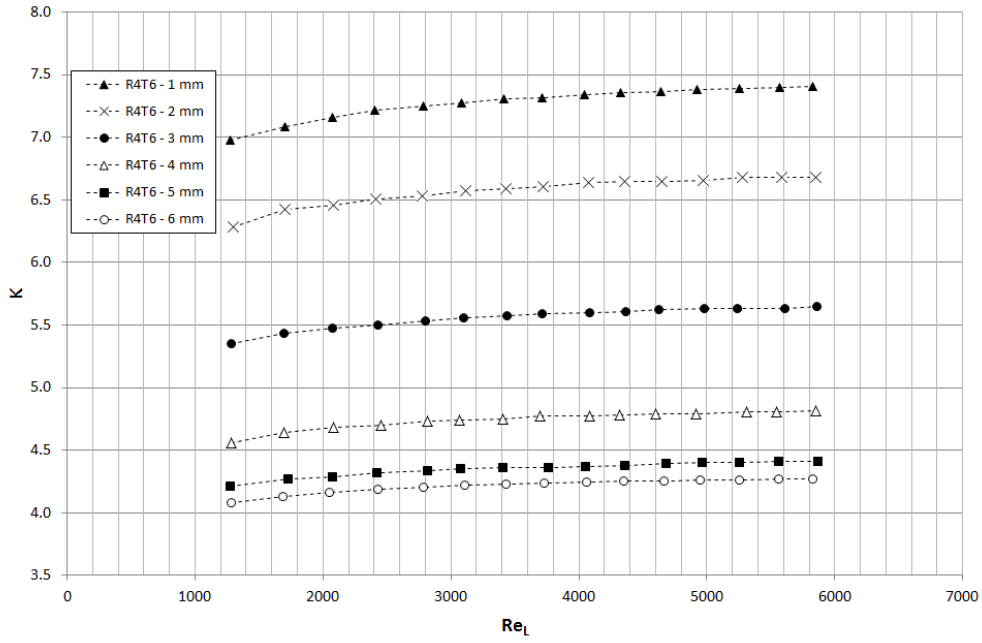

Fig. 5.31 K vs. Re_L for thickness tests.

The results emphasize that the loss coefficient is higher for the grid samples having the smallest value of thickness. In fact the highest value ($K \approx 7.5$) is found in correspondence of the sample with thickness equal to 1 mm and the lowest value ($K \approx 4.3$) is highlighted for sample having 6 mm of thickness. Considering only the asymptotic K values where the dependency on Reynolds number is not present (mean of last three points of the $K - Re_L$ trends in Fig. 5.31) it is possible to build a final graph that reports the thickness effect (Fig. 5.32).

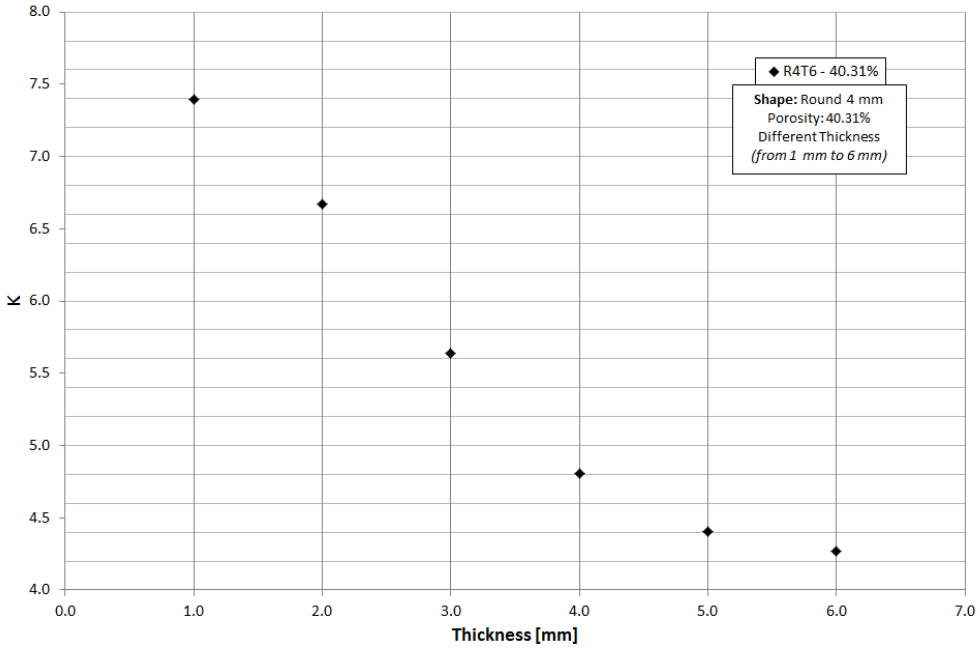

Fig. 5.32 K vs. Thickness.

Increasing the thickness of the perforated plate, the loss coefficient decreases and therefore the drop of pressure.

5.6.3 Dimension effect

In order to investigate more deeply the influence of the dimensions of holes of the perforated plate, five different typologies of screen, with different hole dimensions, have been tested during the experimental campaign. The screens had the same level of porosity fixed equal to 40.31 %, same shape and thickness of holes, with the aim of cutting away dependencies on porosity, shape and thickness. The table 5.5 summarizes the principal characteristics of the grids used for dimension tests.

Model	**Porosity % (ε)**	t **[mm]**	D_h**[mm]**	**Shape**
R2T3	40.31	1.0	2.0	Round
R4T6	40.31	1.0	4.0	Round
R6T8	40.31	1.0	6.0	Round
R8T12	40.31	1.0	8.0	Round
R10T15	40.31	1.0	10.0	Round

Table 5.5 Samples for dimension tests.

As for the thickness tests, also in this case a fundamental graph is created where the role of dimension of holes respect to loss coefficient (K) in correspondence of different Reynolds numbers is highlighted (Fig. 5.33).

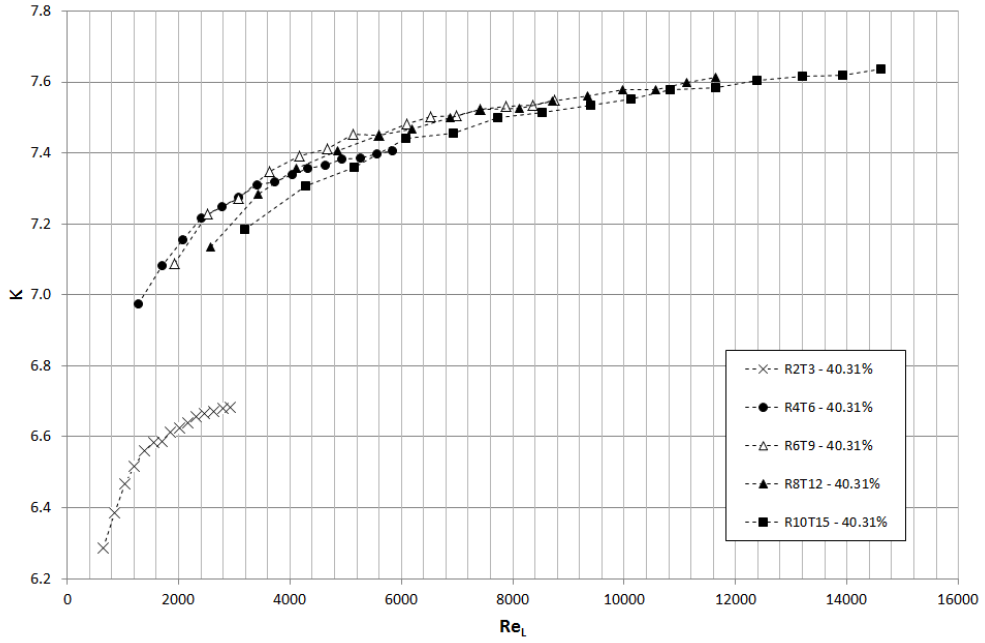

Fig. 5.33 K vs. Re_L for diameter tests.

The data plotted in Fig. 5.33 nearly overlap and it is difficult to understand at first sight which is the effect of diameter. With the aim of making more readable the previous graph a new figure is presented in terms of Global Reynolds number instead of Local Reynolds number (Fig. 5.34).

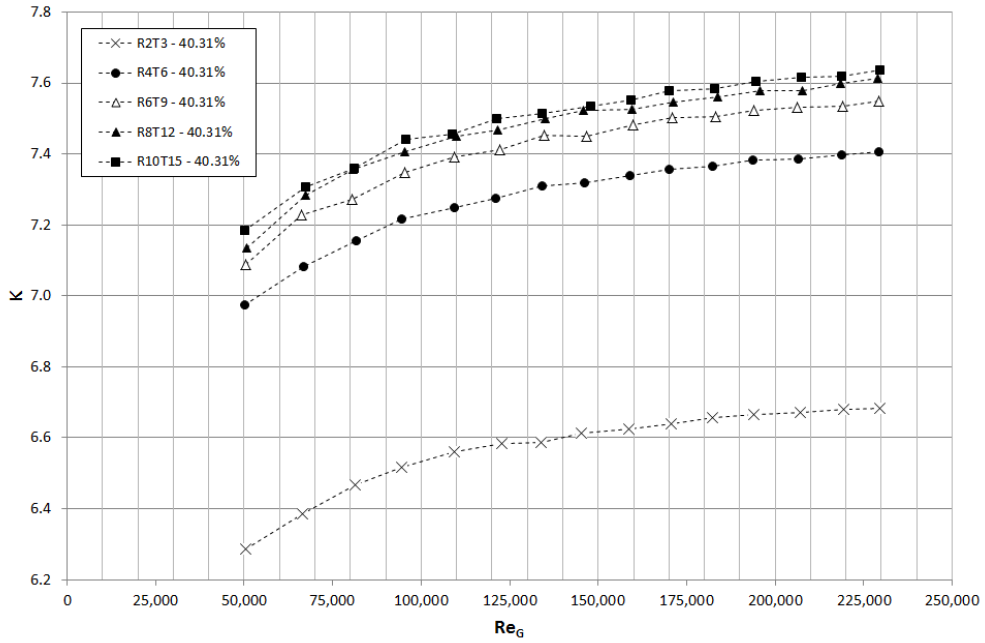

Fig. 5.34 K vs. Re_G for diameter tests.

The diagram in Fig. 5.34 clearly explains that higher values of loss coefficient are found in correspondence of large hydraulic diameters and vice versa. Following the same procedure that was adopted for the thickness tests (considering the asymptotic values of K that are independent of Reynolds) it is possible to realize a final graph that reports the effects of hydraulic diameter on loss coefficient (Fig. 5.35).

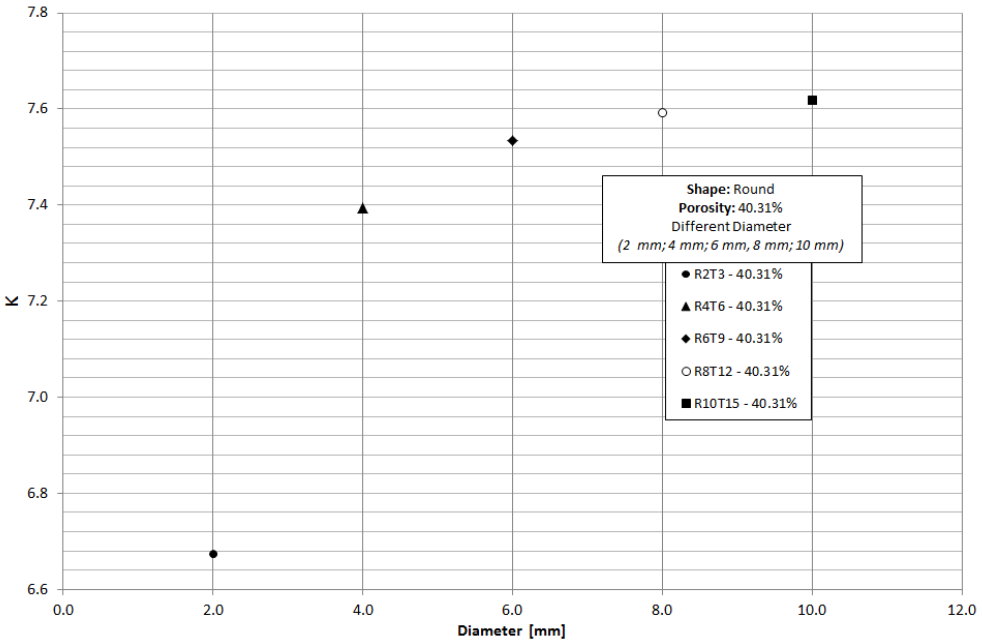

Fig. 5.35 K vs. Diameter.

Increasing the diameter of the perforated plate, the loss coefficient increases and consequently the drop of pressure.

5.6.4 Shape effect

In order to analyse the role of the shape of the holes, some other experiments were carried out on four samples in wind tunnel. The screens were different only for the shape of holes and had the same porosity level equal to 44.44 % and 44.40 %, same thickness and hydraulic diameter. The following table lists the main characteristics of the grids used for the shape test (Table 5.6).

Model	**Porosity % (ε)**	t **[mm]**	D_h**[mm]**	**Shape**
R7T10	44.44	1.0	7.0	Round
C7U10.5	44.44	1.0	7.0	Square
R10U14	44.40	1.0	10.0	Round
C10U15	44.40	1.0	10.0	Square

Table 5.6 Samples for shape tests.

The experimental measures have been made on two different shapes of holes, in particular perforated plates with round and square holes were tested, in correspondence of levels of porosity of 44.40 % and 44.44 %. As already done for thickness and diameter effects, also in this case an appropriate graph has been created that reports the dependency of loss coefficient (K) on the local Reynolds number (Re_L) in function of the two different shapes of holes (Fig. 5.36).

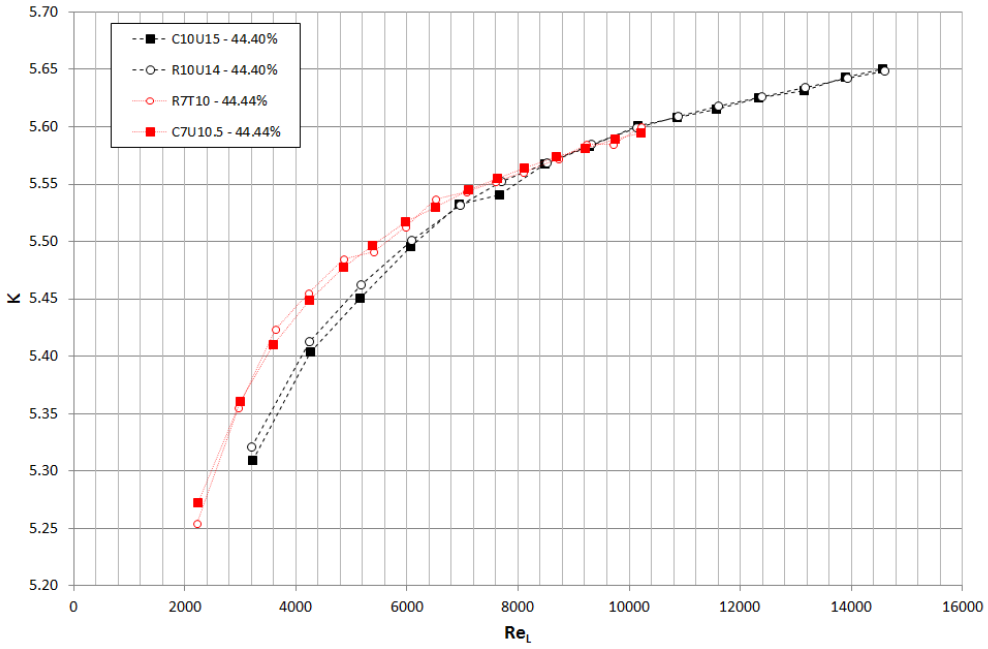

Fig. 5.36 K vs. Re_L for shape tests.

The picture represents with circular symbols the data related to grids having holes with round shape and with square symbols the measured data for the ones with square shape. The chart is further divided into two bands of hydraulic diameter represented by the colours red ($D_h = 7$ mm) and black ($D_h = 10$ mm). Evaluating carefully the graph it is possible to confirm that the effects of the shape of the holes are negligible. Therefore it is possible to state also that the shape of the holes from round to square with the same hydraulic diameter has not a predominant character and confirms what was said in ESDU81039 (1985) and Idelchik (1994).

5.6.5 Relationship t/D_h

The dimensional analysis carried out in Chapter 4 has shown the existence of an independent dimensionless parameter ($\Pi_3 = t/D$) that considers the influence of the diameter of hole and the thickness of grid. Since that parameter comes from the direct application of the Buckingham's theorem on a porous medium in confined walls and subjected to a flow, it becomes fundamental to consider the ratio t/D_h in the discussion in order to comprehend more in details the effects of diameter (D_h) and thickness (t) of hole.

A fundamental diagram has been built, it reports the asymptotic values of

F(Re_L) function, where the dependency of Reynolds is removed (mean of the last three points in Fig. 5.30), with respect to the ratio t/D_h for all of the samples tested.

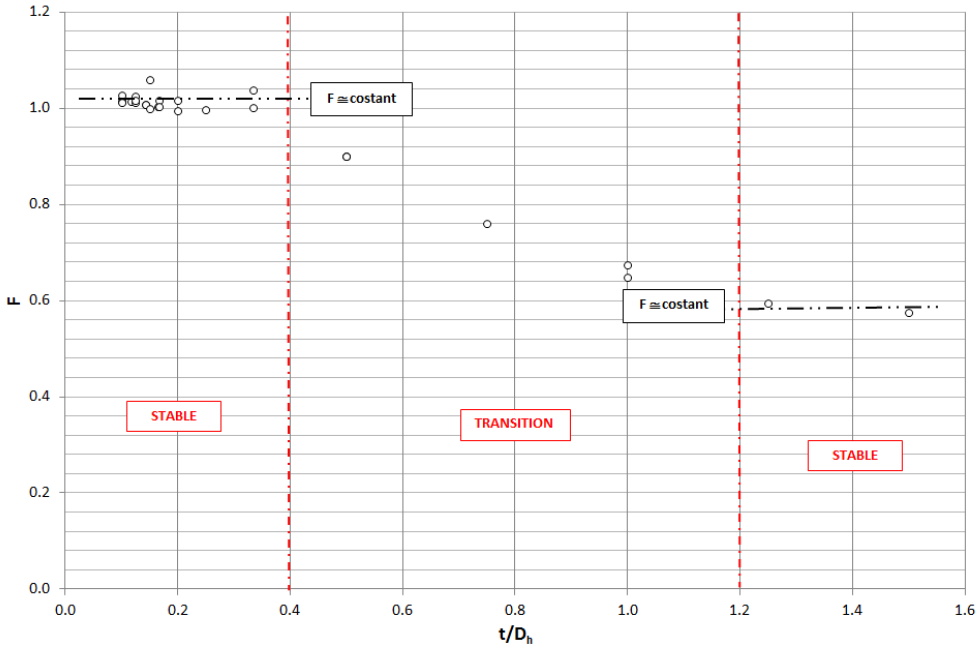

Fig. 5.37 F vs. t/D_h for all the samples tested.

Fig. 5.37 shows that three different regions are present, more in particular two stable regions and one zone of transition. The subdivision between the sectors of the diagram can be done in empirical way as follows:

- $t/D_h < 0.4$ **Stable**
- $1.2 > t/D_h \geq 0.4$ **Transition**
- $t/D_h \geq 1.2$ **Stable**

The F function results almost constant if $t/D_h \geq 1.2$ and $t/D_h < 0.4$. The separation in three different regions can be imputable to the typology of motion regime. ESDU81039 (1985) and Idelchik (1994) have supposed that there are two different regimes: separated and reattached flow. The proof of the existence of various types of regimes of motion can be found back in the study of the effects of thickness and diameter discussed in the previous paragraphs. In fact, during the tests a certain singularity of the loss coefficient trends was noted (Fig. 5.32 and Fig. 5.35), since this tended to grow or decrease in function of the diameter of the holes and thickness of the screen. With the aim of clarifying this aspect and understand the exact behaviour of porous plate when it is subject to airflow, it is required an application of Bernoulli's theorem. Consider the generalized scheme of flow obstruction shown in Fig. 5.38. The internal flow in the pipe of diameter D is forced through an opening of diameter d; the ratio m is a key parameter of the

system and can be defined as:

$$m = \frac{d^2}{D^2} \tag{5.17}$$

where m represents a sort of porosity level, or an index able to express the relation between the two characteristic diameters of the system.

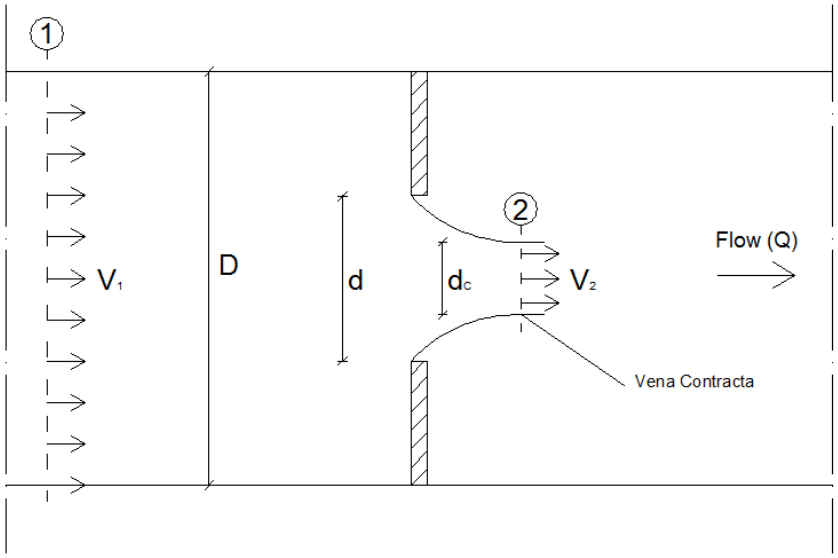

Fig. 5.38 Flow trough a generalized obstruction.

The air flow rate (Q) comes from the left direction (1) and passes through the obstruction; after leaving the opening, a flow contraction occurs, or more in particular the flow separation at the sharp edge of the hole throat causes a recirculation zone, as shown by the lines downstream the nozzle. The mainstream flow continues to accelerate from the opening throat to form a *vena contracta* at section (2) and then decelerates again to fill the entire section of the duct. At the *vena contracta*, the flow area is minimum, the flow streamlines are essentially straight and the pressure is uniform across the section. Another important index that has to be defined is:

$$C_c = \frac{A_2}{A_o} \tag{5.18}$$

This parameter is called *contraction coefficient* (C_c) and represents the ratio between the area of *vena contracta* A_2 and the area of the opening A_o. The theoretical flow rate may relate to differential pressure between sections (1) and (2) by applying continuity equation and Bernoulli theorem.

$$\textit{Continuity} \qquad Q = V_1 \cdot A_1 = V_2 \cdot A_2 \tag{5.19}$$

$$\textit{Bernoulli} \qquad z_1 + \frac{p_1}{\rho g} + \frac{V_1^2}{2g} = z_2 + \frac{p_2}{\rho g} + \frac{V_2^2}{2g} \tag{5.20}$$

where: p_1, V_1, A_1 and p_1, V_1, A_2 are respectively pressure, velocity and area in the corresponding section (1) and (2); g the gravity acceleration and ρ the air density. At the base of this application there are the following assumptions: steady and incompressible flow between the points (1) and (2), flow along a streamline, no viscosity, uniform velocity and pressure at sections (1) and (2) and flow is horizontal (thus, z_1=z_2). Therefore, the Bernoulli equation becomes:

$$\frac{p_1 - p_2}{\rho} = \frac{V_2^2 - V_1^2}{2} \tag{5.21}$$

and introducing the drop of pressure (Δp) upstream - downstream of the obstruction equal to $\Delta p = p_1 - p_2$, the equation (5.21) turns into:

$$\frac{2\Delta p}{\rho} = V_2^2 - V_1^2 \tag{5.22}$$

Using the continuity $[V_1 = V_2(\frac{A_2}{A_1})]$ and solving the equation (5.22) for the theoretical velocity, V_2:

$$V_2 = \sqrt{\frac{2\Delta p/\rho}{\left[1 - \left(\frac{A_2}{A_1}\right)^2\right]}} \tag{5.23}$$

The velocity in section (2), V_2, can be expressed in function of the flow rate as $V_2 = Q/A_2$ and substituting in equation (5.23),

$$Q = \frac{A_1 A_2}{\sqrt{A_1^2 - A_2^2}} \cdot \sqrt{2\Delta p/\rho} \tag{5.24}$$

Remembering the definition of contraction coefficient (5.18) as $A_2 = A_o C_c$ the equation (5.24) is modified as:

$$Q = \frac{A_1 A_o C_c}{\sqrt{A_1^2 - A_o^2 C_c^2}} \cdot \sqrt{2\Delta p/\rho} \tag{5.25}$$

Passing from the area to the diameter definition of the section using the following equations:

$$A_1 = \frac{\Pi}{4} D^2 \qquad\qquad A_o = \frac{\Pi}{4} d^2 \tag{5.26}$$

it is possible to rewrite the equation (5.25) as:

$$Q = \frac{C_c A_o}{\sqrt{\left[1 - \left(\frac{d^4}{D^4}\right) C_c^2\right]}} \cdot \sqrt{2\Delta p/\rho} \tag{5.27}$$

Substituting in the equation (5.27) the parameter m (5.17) it is possible to state the

final relationships for the flow rate (Q) and the contraction coefficient (C_c):

$$Q = \frac{C_c A_o}{\sqrt{1 - m^2 C_c^2}} \cdot \sqrt{2\Delta p/\rho} \tag{5.28}$$

$$\frac{C_c}{\sqrt{1 - m^2 C_c^2}} = \frac{Q}{A_o \cdot \sqrt{2\Delta p/\rho}} \tag{5.29}$$

The C_c coefficient is an index able to quantify the reduction of the area in the *vena contracta*. Remembering the definition of contraction coefficient (5.18), $C_c = 1$ if there is no contraction of the throat area and $C_c \lll 1$, if there is strong contraction of the area.

This kind of analysis can be applied to porous plates imagining to concentrate the distributed surface porosity level (ε), typical of perforated plates, in a single opening having the ratio (m) equal to porosity level (ε). More in particular the grids can be schematized as a single obstruction confined in a pipe having ratio d^2/D^2 equal to porosity level ε. With the purpose of demonstrating the existence of two regimes of flow, the contraction coefficients C_c have been determined for all the samples under testing during the study of thickness and diameter effects. The C_c coefficients have been determined in correspondence of same level of porosity equal to 40.31% only for round holes having variable thickness (*1, 2, 3, 4, 5, 6 mm*) and diameter (*2, 4 ,6, 8, 10 mm*). It was possible to carry out this analysis because all parameters that appear in the equation (5.29) are known and they have been determined during wind tunnel tests. Q represents the incoming air flow rate in the set-up channel, A_o is the obstruction opening area, Δp is the drop of pressure between the section (1) and (2), ρ the air density and m the porosity level. The results of the solution of the equation are shown in Table 5.7, reported for each grid tested.

Model	**Porosity (ε)**	D_h **[mm]**	t **[mm]**	t/D_h	C_c
R2T3	40.31%	2	1.0	0.500	0.8483
R4T6	40.31%	4	1.0	0.250	0.8071
R4T6	40.31%	4	2.0	0.500	0.8486
R4T6	40.31%	4	3.0	0.750	0.9167
R4T6	40.31%	4	4.0	1.000	0.9809
R4T6	40.31%	4	5.0	1.250	1.016
R4T6	40.31%	4	6.0	1.500	1.028
R6T8	40.31%	6	1.0	0.167	0.7996
R8T12	40.31%	8	1.0	0.125	0.7965
R10T15	40.31%	10	1.0	0.100	0.7950

Table 5.7 Contraction coefficient.

From the contraction coefficient (C_c) it is possible to define the expansion coefficient (C_e) as: $C_e = 1 - C_c$. C_e gives a measure of the area occupied by the expansion and growth of the jet wake respect to the effective opening area, characterized by the diameter d in Fig. 5.38.

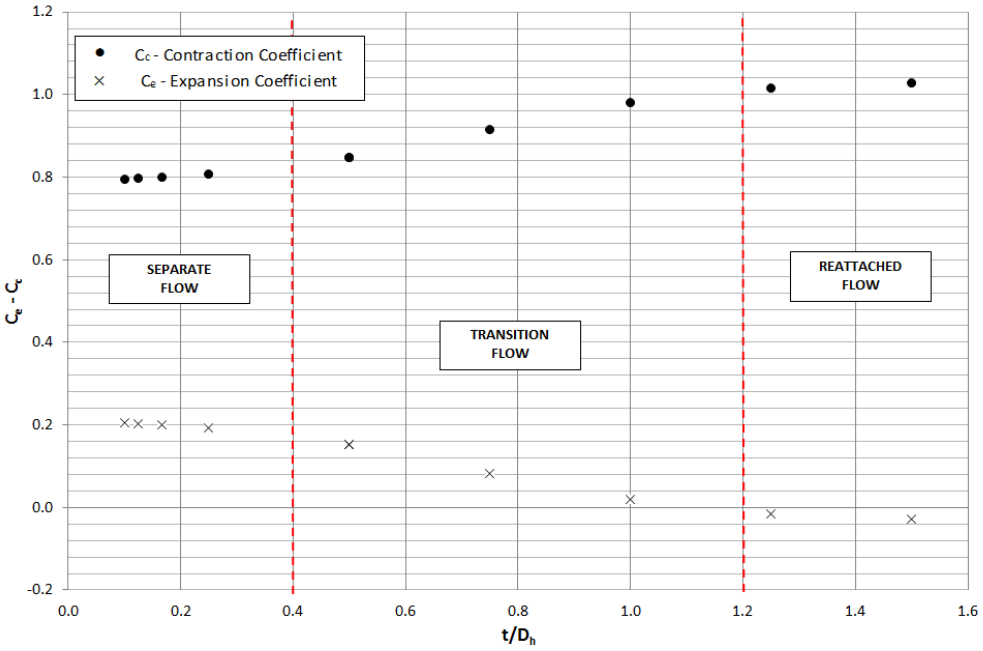

Fig. 5.39 Relationship C_c - C_e vs. t/D_h for samples reported in Table 5.7.

A general graph that reports the influence of ratio thickness-diameter versus the contraction and expansion coefficient has been created (Fig. 5.39). Before entering into detail of the analysis it is necessary to remember that both C_c and C_e are typically defined in the range $0 \div 1$. By contrast Fig. 5.39 and Table 5.7 report values higher than 1 or lower than 0; these values respect the physics of the phenomenon and indicate that downstream of the obstruction a flow expansion occurs. From this diagram it is possible to confirm the existence of two flow motion regimes insomuch as for values of t/D_h less than 0.4, the high values of C_e and the low values of C_c indicated that the jet wake growth takes place, typical of separated flow regime. In correspondence of the values of the relationship t/D_h higher than 1.2, the coefficient C_e is minimal and C_c is maximum and this demonstrates the existence of the reattached flow condition. Based on the above assumptions, the flow separation leads to the decrease of contraction coefficient that implies an increase of the mean wind speed (V_2), as well as of the pressure drop and consequently of the loss coefficient. Vice versa the reattached flow brings an increase of contraction coefficient and consequently a decrease of the wind speed in contracted zone, of the pressure drop and the loss coefficient.

The first appearance of two distinct regimes of motion had been already noticed plotting the $F(Re_L)$ function against the ratio t/D_h in Fig. 5.37. At this point it becomes fundamental to try to give a physical meaning to the $F(Re_L)$ function and to do that it is necessary to create a graph that reports the $F(Re_L)$ and the previously found coefficients (C_c and C_e) in function of the relationship t/D_h (Fig. 5.40). From the graph it is noticed that $F(Re_L)$ and C_e are dimensionless parameters that describe in a completely opposite manner the same aspects. Indeed, both are able to give an idea of the growth of the jet wake but they are expressed completely in

different scales. In fact F ranges between 0.5 and 1.0 and C_e between 0 and 0.2.

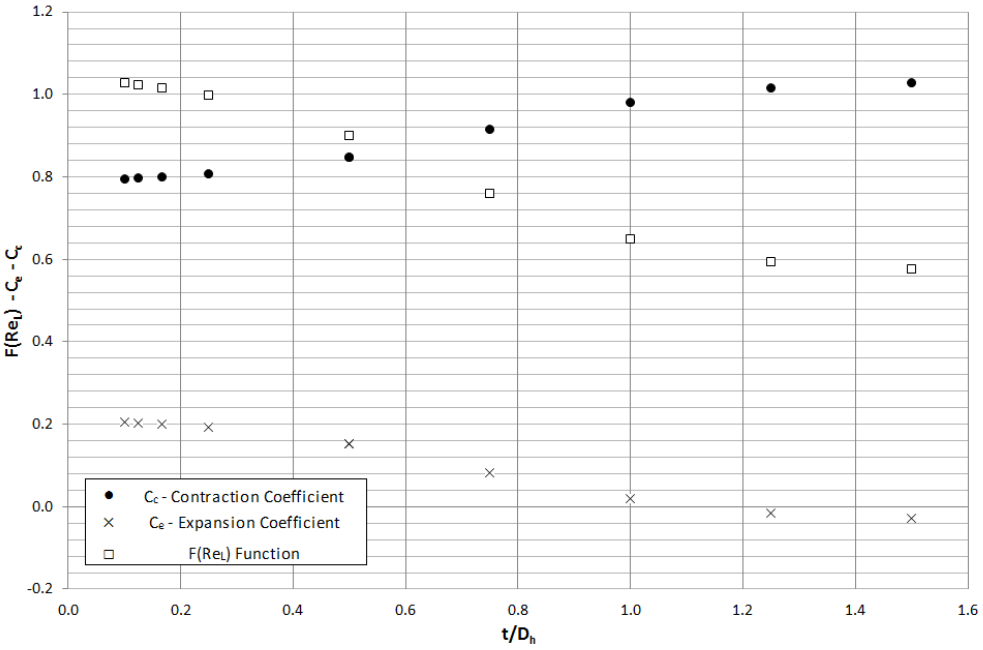

Fig. 5.40 Relationship $F(Re_L)$ function - C_c - C_e vs. t/D_h for grids in Table 5.7.

In order to understand the relationship between the $F(Re_L)$ function and the coefficient of contraction C_c, it is essential to construct a graph which relates the two key parameters (Fig. 5.41).

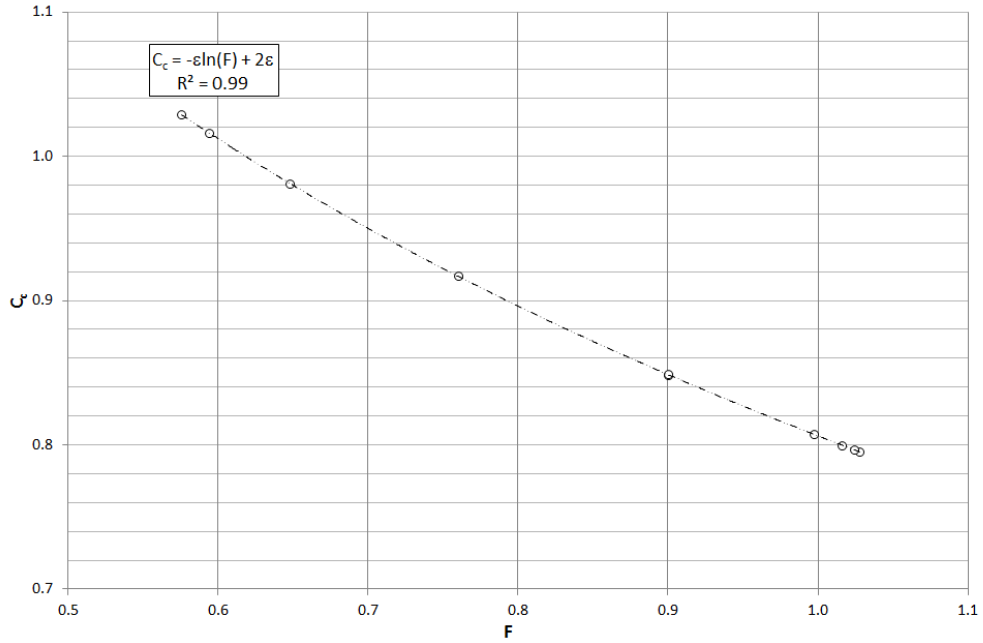

Fig. 5.41 Relationship $F(Re_L)$ function - C_c for grids in Table 5.7.

The best fitting function is reported in Fig. 5.41 with a black dotted line and it can be expressed in a more conventional way as:

$$C_c \approx -\varepsilon ln(F) + 2\varepsilon \tag{5.30}$$

$$\textbf{with: } R^2 = 0.9970$$

where ε is the porosity level of the grid, F function is obtained for experimental test and C_c is the theoretical coefficient of contraction achieved with Bernoulli theorem's application.

5.7 Proposed scaling criteria

Referring to what exposed in Chapter 4 the correct wind tunnel modelling of porous objects is far away from being completely clear. In fact the cornerstone of modelling is the geometric similitude or in other terms the scale modelling but as already explained in the relative chapter, for this kind of objects it cannot be applied. Thus, this is an open theme in wind engineering area because at today in literature there is not a single similitude criterion or a sort of law of modelling that can be used when it is necessary to carry out some experimental tests in laboratory on porous elements. In fact it is not possible to ensure the complete similarity between the model and prototype or in other terms the exact equality among all dimensionless groups, thus it is necessary to work in an incomplete similitude, trying to maintain constant between model and prototype only some key dimensionless parameters able to characterise more in detail the problem. The proposed rule of scale that will be exposed in this section is applicable only for porous elements that can be represented as perforated sheets characterized by porosity (ε), thickness of the plate (t), and shape and hydraulic diameter (D_h) of the holes.

Thanks to the results provided by the experimental campaign it is possible to study more in detail the behaviour of perforated plates with respect to air flow. The fundamental dimensionless key parameters under examination are: the loss coefficient (K) and the drag coefficient (C_D), the ratio t/D_h, the Local Reynolds number (Re_L), the G(ε) function and F(Re_L) function. Crossing all these parameters it has been possible to understand thoroughly which are the fundamental phenomena that develop due to the air motion through porous screens. The experiments have also confirmed the key role played by porosity (ε) through the definition of a particular function G(ε). The influence of viscous effects of the motion only in a restricted zone traces a clear separation between the viscous and inertial regime defining a fixed threshold value (Re_L). The characteristics of flow through an orifice depend on whether the jet formed downstream of the hole entry remains separated or it reattaches to the hole wall. The influence of t/D_h on separation and reattachment of the flow has been investigated and two different flow regimes have been identified. At this point using this information it is opportune to try to define a sort of scaling criteria for porous elements in wind tunnel simulation. The law of modelling can be obtained handling dimensionless parameters like porosity level, Reynolds number, shape of holes and ratio t/D_h.

5.7.1 Porosity effects

The porosity is the scale parameter that plays the most important role in the whole phenomenon. In fact variables like the loss coefficient (K) and drag coefficient (C_D) are heavily dependent on this key parameter. The demonstration of this can be seen at first sight in Figures (5.28) and (5.29). In fact, considering the decomposition of the loss coefficient as reported in equation (5.14) it is possible to isolate the contribution of porosity level respect to the loss coefficient through the definition of G(ε) function. Remembering that also the dimensionless analysis made in Chapter 4 defines the porosity level (Π_4) as independent parameter, and that the experimental measurements confirm its leading role, it is necessary to maintain the same porosity level passing from model to prototype as expressed by the formula:

$$\begin{gathered}\left(\varepsilon\right)^{(p)} = \left(\varepsilon\right)^{(m)} \\ \varepsilon_p = \varepsilon_m\end{gathered} \tag{5.31}$$

Maintain the same level of porosity (ε)

This first requirement affirms that the same level of porosity has to be maintained but it does not specify how this level must be achieved in terms of shape, dimension, position and thickness of holes. Today the industrial processing of perforated plates is almost able to build porous grids (ε in the range $2\% \div 80\%$) without any limitations, especially for the dimensions, thickness, position of holes and shape. Thus, if the prototype porosity falls in the interval mentioned above, it is quite simple to maintain this dimensionless parameter passing from real case to laboratory.

5.7.2 Reynolds effects

In order to correctly reproduce the viscous and inertial effects due to the air flow through the screen it would be correct to maintain the Reynolds similitude. In many cases of interest this similitude cannot be reproduced and thus it is necessary to use some particular methodologies that allow to respect the Reynolds similitude. These strategies include: the increase of dimension of the model, the change of fluid which is used in tests, the modification of the air pressure in the wind tunnel and the evaluation of Reynolds number independence.

Also in this case the separation of loss coefficient into two contributes, by the equation (5.14), leads to the definition of the F(Re_L) function. This is able to highlight the viscous and inertial region and relative threshold value for all the samples tested. Fig. 5.42 reports with different colours distinct zones of flow regime and more precisely in red the zone with low values of Re_L, where the viscous effects are relevant, and in blue the inertial zone, where the viscous effects are negligible.

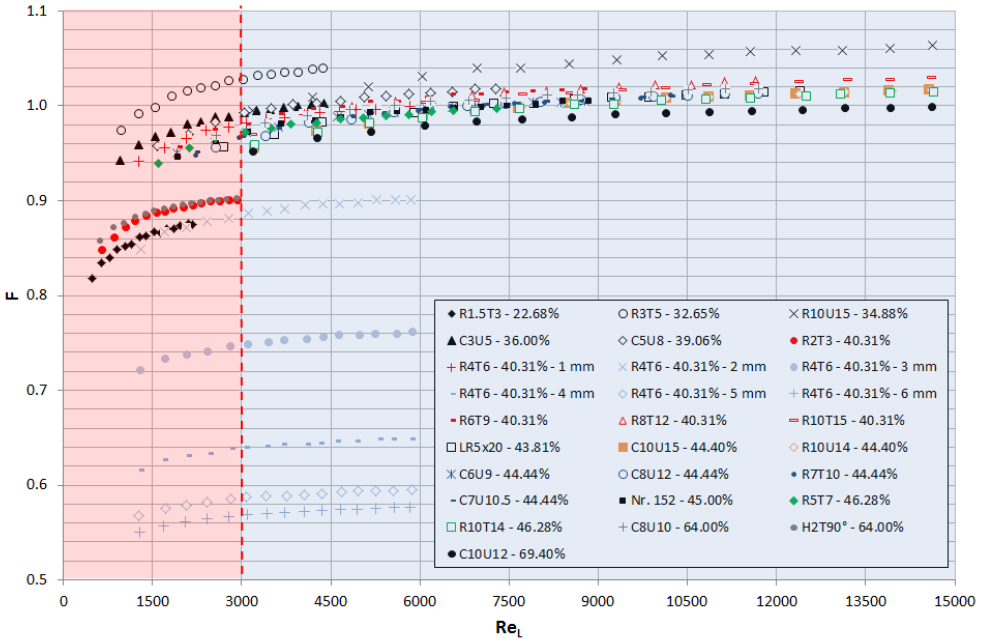

Fig. 5.42 Regions with different Reynolds effects.

The borderline between the two regimes is denoted by a red dash-dot line and it corresponds to a Local Reynolds number value equal to 3000. Thus if the $Re_L > 3000$ the phenomenon does not depend on Reynolds number. In order to avoid Reynolds effects and maintain a sort of Reynolds similitude between the prototype and the model, the second prescription that has to be considered is the following:

Performing tests at $Re_L \geq 3000$

Thus, the limit wind speed through the porous material (w_0) can be obtained by a simple inversion of the formula (5.9) as:

$$w_0 \geq \frac{3000 \cdot \nu}{D_h} \tag{5.32}$$

The minimal value of wind velocity that has to be used during the tests in wind tunnel is expressed by the equation (5.32) and it is a function of kinematic viscosity of the air (ν) and hydraulic diameter of hole (D_h) of the model. Considering air in standard conditions at 20 °C with $\nu = 1.5 \cdot 10^{-5}\ m^2/s$ it is possible to state that if $w_0 \cdot D_h \geq 0.045\ m^2/s$ the limitation on Local Reynolds number is totally satisfied. Therefore if the Re_L is higher than 3000 both in prototype and model, the influence of viscous effect and Reynolds number can be neglected. More in detail the equation

In case of prototype this condition is almost always satisfied

Then, the experimental data achieved for the wind tunnel model can be extended to the real case without distortion.

5.7.3 Shape effects

At today the manufacturers of perforated sheets are able to build different types of plates realized with the various shapes and positions of the holes. With the purpose of understanding which is the role played by these two parameters it is necessary to recourse to experimental results related to the shape effect tests. Many tests were carried out in wind tunnel on perforated plates having the same level of porosity, same hydraulic diameter of holes, same thickness and different shape and position of openings. They showed that the shape and position of holes do not influence the general behaviour offered by the samples respect to the air flow. More in detail the reference parameters like loss (K) and drag coefficient (C_D) remain constant in correspondence of different shape and position of holes (Fig. 5.36). Thus a new prescription for the similitude criterion is:

Indifferent shape ad arrangement of openings

This new statement emphasizes that the porous level, that has to be kept constant passing from prototype to model, can be reached with any shape and arrangement of the holes.

5.7.4 Ratio t/D_h

The final key parameter for which it is required special attention, as already proved by dimensional analysis, is the relationship t/D_h. This parameter has a fundamental role to define and to delimit the various types of flow regime that can develop inside the holes of the plates. Depending on the value assumed by t/D_h three fundamental regions are found (Fig. 5.37): two are stable and one is of transition. The two stable zones correspond to the fully reattached flow regime and the fully separated flow regime. Thus, in order to pass from prototype to model without changing the flow regime, it is important to conserve the same t/D_h ratio:

$$\begin{aligned} \left(\frac{t}{D_h}\right)^{(p)} &= \left(\frac{t}{D_h}\right)^{(m)} \\ \frac{t_p}{(D_h)_p} &= \frac{t_m}{(D_h)_m} \end{aligned} \tag{5.33}$$

Maintain the same constant relationship t/D_h

Going from real case to the laboratory without changing the relationship t/D_h means maintaining the same behaviour of the jet wake passing from prototype to model. More in particular if the ratio $t/D_h \lesssim 0.4$ the wake regime is fully separated; if $t/D_h \gtrsim 1.2$ the jet wake is fully reattached and if the ratio $0.4 \lesssim t/D_h \lesssim 1.2$ the regime is intermediate and the wake has transition features between the separated flow regime and the reattached one.

5.7.5 Summary of scaling rule

Considering the problem related to the correct analysis of porous element during wind tunnel measurements, a simple scaling criterion has been developed and can be summarized in function of some parameters that have to be maintained constant passing from prototype to model. The principal parameters that have to be kept constant are the following:

- Same level of porosity (ε);
- Test at $Re_L \geq 3000$;
- Same constant relationship t/D_h.

By contrast the scaling is not influenced by the shape and the position of holes.

This kind of law of modelling or rule of scale can be applied only to porous elements represented by perforated plates having any shape, arrangement, diameter and thickness of holes and for porosity level included in the analysed range. It is necessary to remember also that the rule of scale has to be used only to the portion of an object that can be schematized as porous medium.

Considering the general case of the windbreaks, subject of this work, where it could be necessary to carry out some tests in wind tunnel, the scaling criterion found can be applied in the porous part of the fence. Regarding the predominant geometrical dimensions of the windbreak the classical geometric scaling process can be used. The evaluation and the correct soundness of the geometric scaling process for the predominant geometrical dimensions of the elements will be analysed in the next chapter.

Chapter 6

WT tests on porous windbreaks

6.1 Introduction

As already mentioned, the scaling rule found in the Chapter 5 can be applied only to an internal portion of an object that can be schematized as a porous medium. Indeed, considering the general case of porous façades, windbreak screens, technical surfaces, the scaling criterion found can be used only for the porous core of the structure. On the other hand, regarding the predominant geometrical dimensions of the porous elements (the height in the case of windbreaks or the width times the height for porous surfaces) it is fundamental to understand whether the simple geometric scale can be adopted for modelling these dimensions or not. The evaluation and the correct soundness of the geometric scaling process with respect to the predominant geometrical dimensions of the elements will be analysed more deeply in this section. In this part, in order to highlight some possible correspondences with the confined case (obtained by sub-channel tests) the behaviour of unconfined perforated plates (represented by 2D porous windbreaks) respect to the air flow will be investigated more in detail.

The main idea is to create a new particular set-up of measurements in the CRIACIV Wind Tunnel that allows to recreate an unconfined 2D flow field around a porous windbreak. In this condition the air flow is able to move not only through the porous core (as the case of confined flow tests) but also around the barrier. With the aim of characterizing the behaviour of this kind of objects and to operate some comparison with the confined flow, it is necessary to know the aerodynamic forces and moments induced by the air motion on the windbreaks. The fences in use are made up of rectangular perforated plates with different levels of porosity, dimension, thickness and shape of holes.

6.2 Experimental set-up

The function of the set-up is double fold. At first, it aims to channelize the air flow and to recreate a two dimensional flow field approaching the windbreak. Secondly, it aims to support the windbreak samples for all the measurement phase and to act as a link between the tested barrier and the measuring equipment. The main characteristics are synthesized in a general figure (Fig. 6.1) that is able to give at

first sight a schematic and qualitative view of the new set-up.

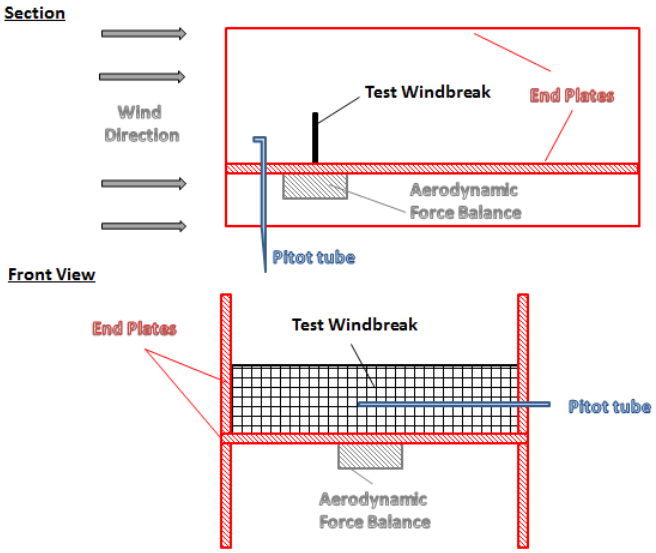

Fig. 6.1 Experimental set-up scheme, section and front view.

The experimental apparatus is composed of two main parts, the steel support and the end plates. The steel support is a sort of an instrumented stainless steel frame, able to keep fixed the screens under testing, linked to an aerodynamic force balance. It presents a circular base that has the aim to connect the frame with the measuring equipment, and in particular the frame has the duty to accommodate the porous sample. To keep fixed the model of windbreak on the frame there are 10 clamp screws installed, four of them are in the horizontal bars and three in each vertical element. The following figures report a constructive particular of the support with the related geometric dimensions (Fig. 6.2) and two views of the designed steel frame (Fig. 6.3).

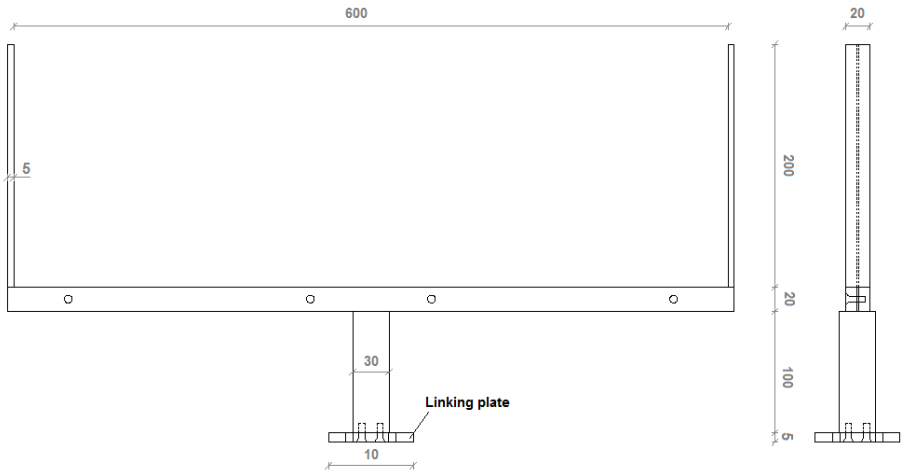

Fig. 6.2 Scheme of stainless steel frame.

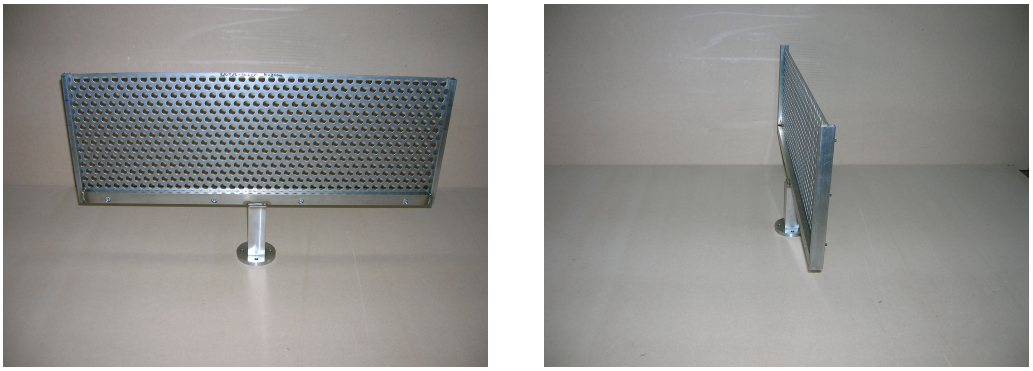

(a) Front View (b) Lateral View

Fig. 6.3 Particular of stainless steel frame equipped with sample.

The circular base is realized by a plate properly drilled and rigidly connected to an aerodynamic force balance using four screws (Fig. 6.4). Thanks to this connection it has been possible to measure all the vectorial components of the aerodynamic forces and moments acting on the unconfined porous samples with high levels of precision.

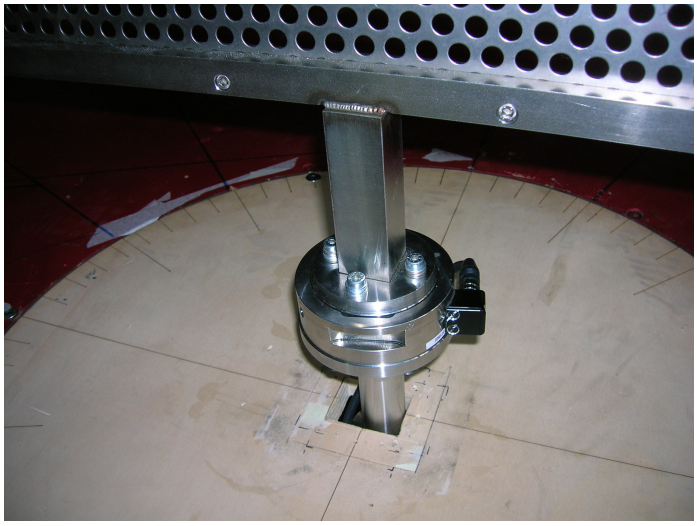

Fig. 6.4 Particular of aerodynamic force balance anchorage.

The end plates have the task of creating as much as possible a two dimensional flow field. In order to ensure the 2D condition of motion a ratio of 3 of the length of the barrier to its height has been guaranteed. In fact the length (L) and the height (H) of the windbreak have been fixed respectively to 600 mm and 200 mm.

The end plates are made of three plywood panels having rectangular dimensions of 600 mm times 1200 mm, with thickness of 18 mm. The original wood panels showed a strong surface roughness and bluff edges due to the natural property of the plywood and the related industrial phases of cutting and manufacturing process. These two aspects can lead to a strong modification of the air flow approaching the

samples in testing both in terms of quality of the wind speed profile and boundary layer development. Consequently, to avoid these issues the superficial roughness has been removed by smoothing process with belt sander and glass-paper. The bluff edges have been appropriately modified in a more aerodynamic shape thanks to the use of little wooden semi-NACA profiles in use in aircraft modelling. With the application of NACA it has been also possible to minimize the problem of boundary layer separation at the inlet of the end plates. The panels have been installed in *H shape position* and fixed to the wind tunnel floor by L-brackets and screws. In order to ensure a sort of channel stiffness and perfect uprightness to the end plates, four inclined wood props have been used (Fig. 6.5).

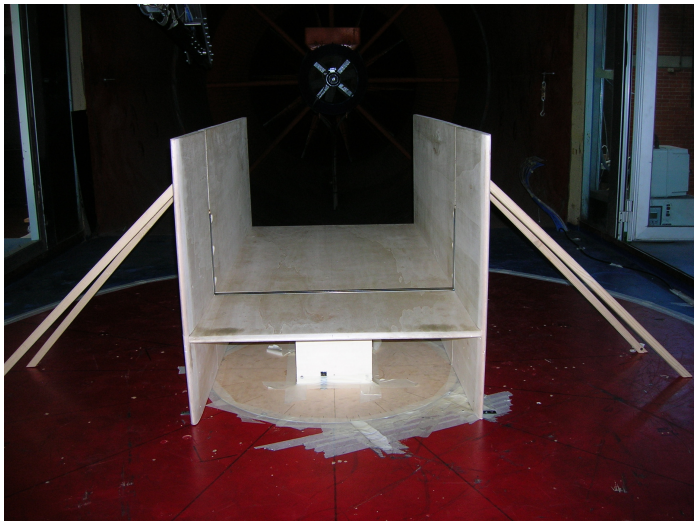

Fig. 6.5 Particular of experimental set-up.

Two of the three wood panels have been installed in a vertical position in order to define the horizontal flow field; the third one has been located horizontally to delimit the reference plane of the barrier. Within the end plates, at a distance of 20 cm from the inlet, through a little opening obtained in the wood was positioned the instrumented stainless steel frame. The choice of placing the equipped frame and then the barrier at that distance aimed to minimize boundary layer thickness. In fact the set-up has been conceived with the purpose to have a wind speed profile as uniform as possible, to minimize the boundary layer development and to fix a solid blockage ratio of 4%. All the parts of the frame have been hidden inside the thickness of the end plates through a precision milling of the plywood's thickness. The lower part of the frame and the measuring equipment were covered with an appropriate wooden box that was able to isolate the force balance from the external air flow and thus ensured a non-contaminated environment of measurement.

6.2.1 Instruments of measure

As already done in §5.2.1, also for this set of experimental measurements, it is necessary to explain the general characteristics of the measuring instruments employed with the related limitations.

6.2.1.1 High frequency force balance (*HFB*)

The forces and moments induced by the air motion on the sample of windbreak have been measured through an aerodynamic high frequency force balance. The choice has fallen on a particular type of load cell capable of measuring forces and moments with respect to the six-axis with a very high level of precision (Fig. 6.6).

Fig. 6.6 HFB FT-Delta SI-165-15.

The selected instrument is the HFB, model FT-Delta SI-165-15 manufactured by ATI Industrial Automation having the technical specification reported in Table 6.1.

Specifications	**Values**
Range of measurement, F_x, F_y	±165 N
Range of measurement, F_z	±495 N
Range of measurement, M_x, M_y, M_z	±15 Nm
Resolution, F_x, F_y	±1/128 N
Resolution, F_z	±1/64 N
Resolution, M_x, M_y, M_z	±1/2112 Nm
Repeatability	± 0.03 % FS
Full Scale Error, F_x, F_y	± 0.06 % FS
Full Scale Error, F_z	± 0.10 % FS
Full Scale Error, M_x, M_y, M_z	± 0.01 % FS
Resonance frequency	1.700 Hz
Operating temp. range	0 ÷ 70 °C

Table 6.1 Characteristics of HFB FT-Delta SI-165-15.

The HFB uses a Multi-Axis Force/Torque Sensor (F/T) system that measures the full six components of force and torque (F_x, F_y, F_z T_x, T_y, T_z) by means of a monolithic instrumented transducer. The F/T transducer uses silicon strain gauges for excellent noise immunity. Strain gauges (DMS) measure the strains applied in all six degrees of freedom (F_x, F_y, F_z T_x, T_y, T_z). The DMS signals are amplified in the sensor, subsequently conditioned, acquired and converted in digital signals by an acquisition card NI cDAQ-9174 of National Instruments. At this point the

data converted are saved in digital form on PC and are available for analytical elaborations.

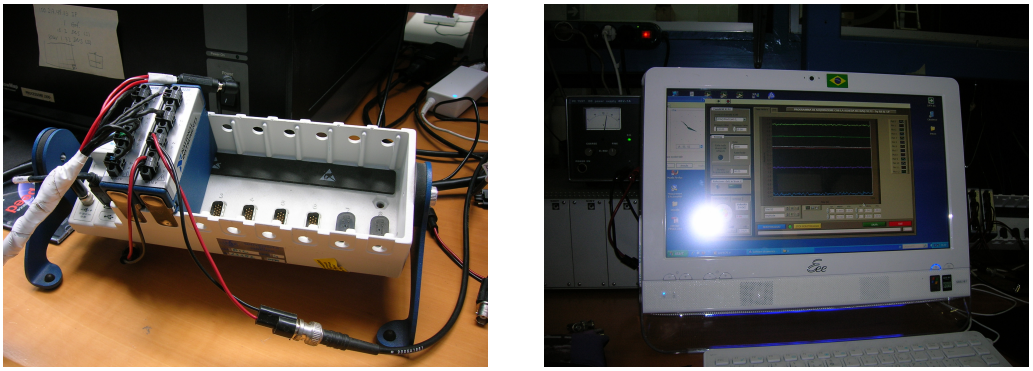

(a) Acquisition card NI cDAQ-9174 (b) PC in acquisition phase

Fig. 6.7 Acquisition system.

During the experimental measuring phase the signal coming from the six components of the HFB are acquired for 60 seconds at sampling frequency of 2000 Hz in order to obtain accurate time histories of forces and moments.

Also for this set of measurements a phase that has an important value is the calibration of the HFB. The calibration of the instrument has been done in the range $0 \div 120$ N imposing known weights and known moments for each axis. Thanks to calibration phase it has been possible to obtain the matrix of calibration (K) of HFB; multiplying K by the digital signals acquired have been obtained the single components of force and moment on the windbreak. From the analysis it has been quantified with high precision that the error accomplished by the HFB is included in the range $\pm$ 0.075 N for the force components and $\pm$ 0.01 Nm for the moment components.

6.2.1.2 Velocity system (*Pitot tubes and hot-wire*)

The laboratory equipment currently in use for measuring the wind speed during all experimental testing consisted of Pitot-Prandtl tubes and hot-wire anemometers. More precisely the hot-wire was employed in the part of tests related to the characterization of the flow inside the wooden end plates, like the estimation of the boundary layer thickness and the investigation of the index of turbulence. The two Pitot tubes were used during all campaign to check and measure the flow velocity.

With regard to the technical specifications of the instruments and related acquisition component it is necessary to refer to what has been already widely exposed in §5.2.1.3.

6.2.2 Characteristics of the porous windbreaks

Also for this experimental campaign, the samples of perforated plates were provided by MEVACO. The windbreak samples had a level of porosity in the range 22.68 % $\div$ 69.40 %, obtained by means of different dimensions, shapes and positions of the

holes. Referring to the porous materials tested the common shapes of holes were round, square, oblong, hexagonal and cross achieved with hydraulic diameter (D_h) in the interval from 1.5 mm to 10 mm and thickness (t) between 1 and 1.5 mm. Table 6.2 reports the main features of the perforated plates which the windbreaks are made of, distinguished for model, porosity, thickness, diameter and shape.

Model	**Porosity %** (ε)	**Thickness [mm]**	D_h**[mm]**	**Shape**
R1.5T3	22.68	1.5	1.5	Round
R3T5	32.65	1.0	3.0	Round
R10U15	34.88	1.5	10.0	Round
C3U5	36.00	1.0	3.0	Square
C5U8	39.06	1.0	5.0	Square
R2T3	40.31	1.0	2.0	Round
R4T6	40.31	1.0	4.0	Round
R6T9	40.31	1.0	6.0	Round
R8T12	40.31	1.0	8.0	Round
R10T15	40.31	1.0	10.0	Round
LR5x20	43.81	1.0	8.5	Oblong
C10U15	44.40	1.0	10.0	Square
R10U14	44.40	1.0	10.0	Round
C6U9	44.44	1.0	7.0	Square
C8U12	44.44	1.0	8.0	Square
Nr.152	45.00	1.0	6.0	Cross
R5T7	46.28	1.0	5.0	Round
R10T14	46.28	1.0	10.0	Round
C8U10	64.00	1.0	8.0	Square
H2T90	64.00	1.0	2.0	Hexagonal
C10U12	69.40	1.5	10.0	Square

Table 6.2 Windbreak typologies.

The choice of the features listed in the above table was dictated by the fact that it was necessary to maintain a ratio $(t/D_h) \leq 0.5$, in order to guarantee a fully separated wake flow regime. In fact, on the one hand it was important to study the ratio (t/D_h) more carefully in order to validate and compare the results with the ones found for the confined flow. On the other hand the fully separated wake flow regime is typical for the majority of porous elements used in civil engineering and especially for windbreaks.

In addition to this kind of windbreaks two additional barriers were tested, one with porosity level equal to zero ($\varepsilon = 0\%$) and the other with porosity equal to one ($\varepsilon = 100\%$). They represented the two extreme cases: respectively the solid barrier and the empty case without the presence of the barrier.

With the aim of validating the correct soundness of the geometric scaling hypothesis for the predominant dimensions of the barrier, five additional samples of windbreak with different geometric scale factors were tested and the related effects will be accurately explained in detail in this chapter.

Also for these experimental tests, as for the case of confined flow, the perforated sheets were subjected to laser cutting, with the purpose to have samples of windbreaks having the correct sizes to be placed in the instrumented stainless steel frame (Fig. 6.8).

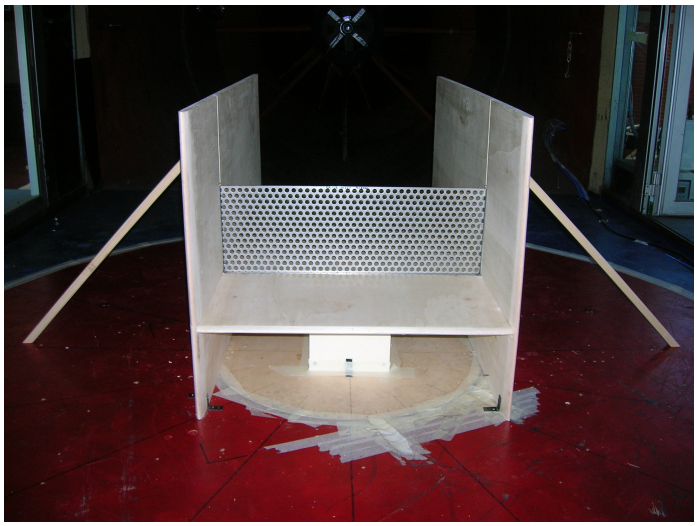

Fig. 6.8 Windbreak sample (model R10T15, $\varepsilon = 40.31\%$).

In this section, tests have been completed on 27 fence samples at several wind speeds, with flow coming perpendicularly to windbreaks without angle of inclination. Thirteen samples of barrier differing for the porosity level and were tested in wind tunnel with the purpose to investigate the role played by porosity. To study the effects of hole shape, two barriers with same porosity level, same thickness and hydraulic diameter but different only for the shape (*round and square*) were analysed. The t/D_h effect has been evaluated on five grid samples having the same porosity level, same shape and different t/D_h ratio (0.100; 0.125; 0.167; 0.250; 0.500).

6.3 Study of the flow inside the end-plates

Before moving to the measurement phase it is necessary to characterize with a high level of accuracy the flow field inside the end plates. In fact, the entire apparatus was planned in order to have a controlled flow approaching the wind barrier in testing. The measuring section was placed at 20 cm from the leading edge of the end-plates, as already said, with the purpose to have a flat wind speed profile and a thin boundary layer. Fig. 6.9 illustrates the classical boundary layer development on a flat plate. If the Reynolds number is small, the viscous effects are relatively strong and the plate affects the uniform upstream flow far ahead, above, below and behind the plate (Fig. 6.9a). If the Reynolds number is high the flow is dominated by inertial effects and the viscous ones are negligible everywhere except in the region very close to the plate and in the relatively thin wake area behind the plate, as shown in Fig. 6.9b. Since the fluid viscosity is not zero ($Re < \infty$), the fluid must stick to the solid surface. There is a thin boundary layer region over the plate in which the

fluid velocity changes from the upstream value to zero velocity on the plate. The layer thickness increases in the direction of flow, starting from zero at the leading edge of the plate. The flow within the boundary layer may be laminar or turbulent, depending on various parameters involved.

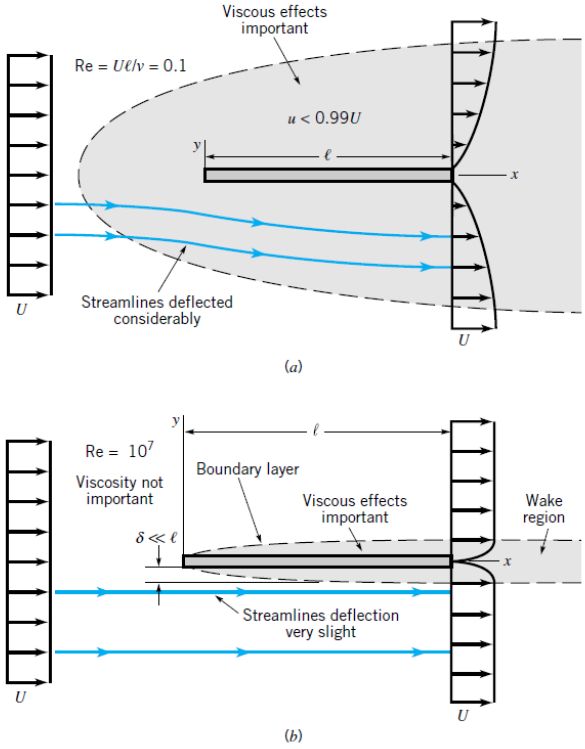

Fig. 6.9 Boundary layer development on flat plate (Munson *et al.*, 2002).

A better appreciation of the structure of the boundary layer flow can be obtained by considering what happens to a fluid particle that flows into the boundary layer.

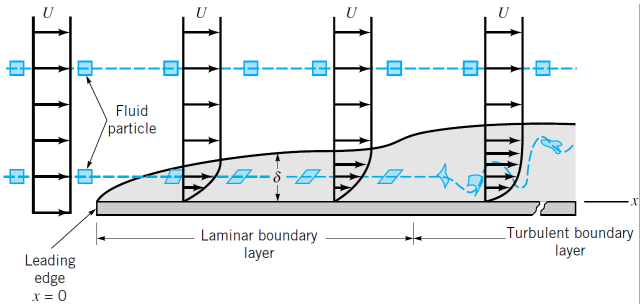

Fig. 6.10 Boundary layer growth on flat plate (Munson *et al.*, 2002).

As indicated in Fig. 6.10, a small rectangular fluid element retains its original shape as it flows in the uniform flow outside of the boundary layer. Once it enters the boundary layer, the particle begins to distort because of the velocity gradient within

the boundary layer; the top of the particle has a larger speed than its bottom. At certain distance downstream from the leading edge, the boundary layer flow becomes turbulent and the fluid particles become greatly distorted because of the random, irregular nature of the turbulence.

As a result of what exposed until now, the end plates and the relative length of entrance have been built with the aim to minimize the boundary layer growth, and obtain as much as possible a flat wind speed profile. These goals have been achieved using smoothing process and by adding the NACA profile at leading edge. Thanks to the use of these devices it was possible to avoid separation and huge growth of the layer, to ensure a laminar boundary layer with a reduced thickness and a good approaching velocity profile.

A hot-wire anemometry campaign was carried out, in correspondence of the testing section inside the end plates, to have a very accurate characterization of the wind speed profile, the relative turbulence level and boundary layer thickness. Two wind speed profiles (*vertical and horizontal*) were obtained by the use of a robot arm equipped with hot-wire anemometer and measured for 15 different wind tunnel wind speeds (*from 5.18 m/s to 26.79 m/s*) (Fig. 6.11).

(a) Vertical (b) Horizontal

Fig. 6.11 Measurement of profiles inside the end-plates.

In the measuring phase the anemometry experimental data were acquired for 120 seconds with sampling frequency of 2000 Hz. The vertical wind speed profile was created using 20 points of measure. The points were spaced 20 mm ÷ 40 mm outside of the boundary layer region where it was expected that the profile was flat and smooth. In the area next to the horizontal end-plates the measurement points were increased, to estimate the boundary layer thickness, and they were in the range 1 mm ÷ 2 mm. The vertical profile was measured in correspondence of the windbreak test section in the centreline of the channel delimited by the end-plates (Fig. 6.11a). The profile was obtained from 3 mm to 353 mm height and the lower limit was dictated by the size of the hot wire probe. Fig. 6.12 reports the vertical mean wind speed profile; at first glance it can be observed that there was no problem of flow distortion and that the experimental set-up was well positioned respect to the external wind tunnel air flow. In fact, as expected, the boundary layer is included in a small region near the horizontal wall, up to a maximum height of 13 mm, and the

remaining part is typical of a flat wind speed profile. In the lower part the velocity profiles tend to decrease so much that the velocity vanishes at the wall, so respecting the no-slip conditions.

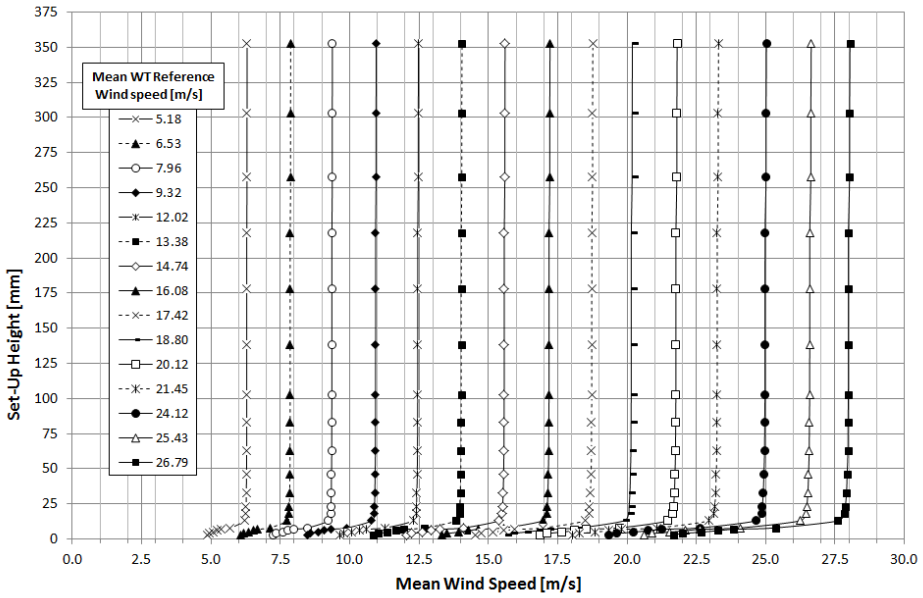

Fig. 6.12 Vertical mean wind speed profile.

As for the case of confined flow, also in this case it is good practice to create a profile of vertical intensity of turbulence in order to understand the turbulence characteristics of the flow (Fig. 6.13).

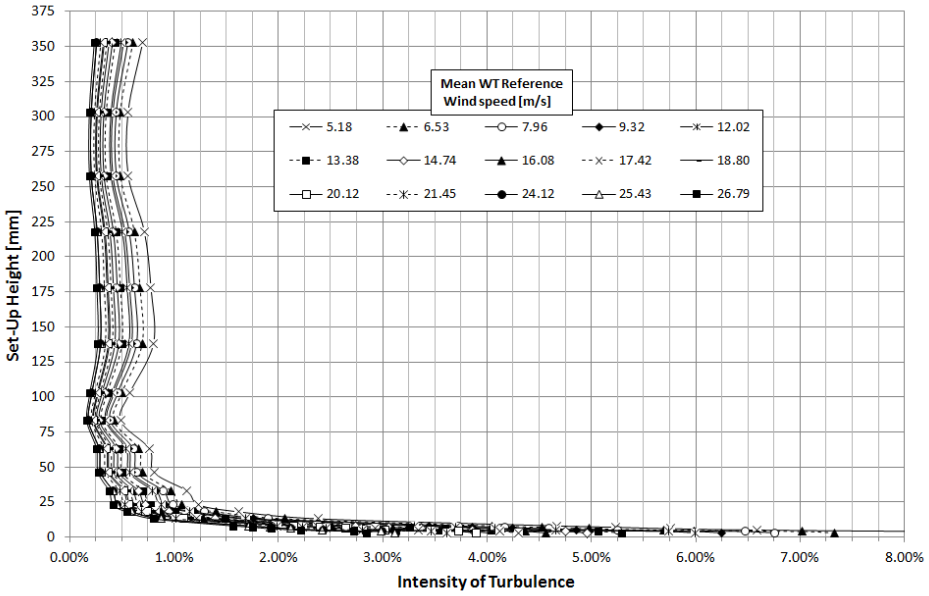

Fig. 6.13 Vertical profile of turbulence intensity.

This graph confirms very well what has been already shown through wind speed profiles. In fact, the zone near the wall is identified by high values of turbulence index that are a symptom of a strong viscous area in the range 2 % ÷ 8 % up to a maximum set-up height of 13 mm. In the higher part of the set-up outside the boundary layer and in the inviscid core flow, the index decreases until it sets to a more uniform turbulence level (0.5 % ÷ 0.8 %).

In order to have a global view of the entire flow field inside the end plates, Fig. 6.14 reports the horizontal mean wind speed profile. This was measured at a height of 100 mm from the horizontal wall (in correspondence of the half-height of the barrier) and had the principal purpose to check the flow quality in the horizontal plane to avoid any asymmetry and strange deviation of the flow field.

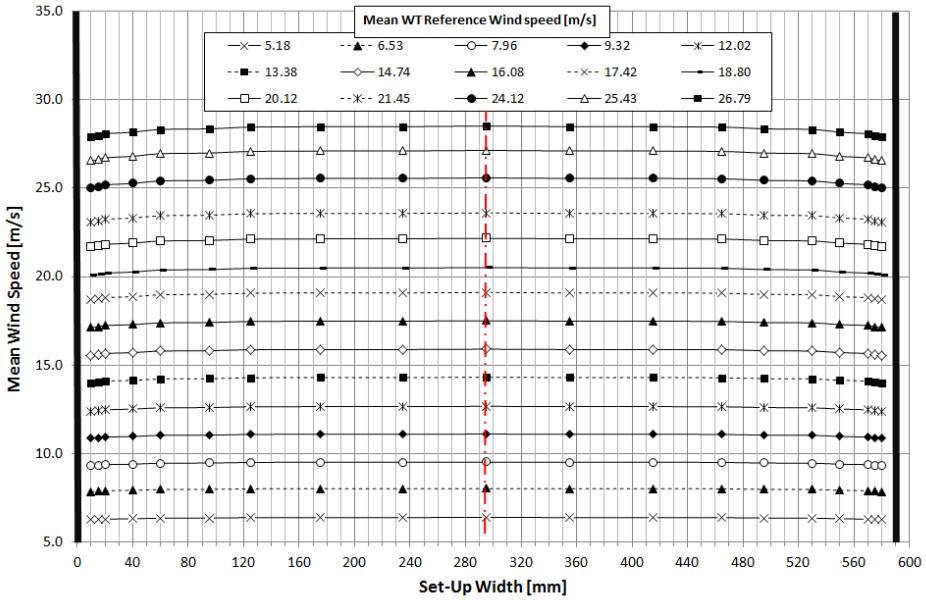

Fig. 6.14 Horizontal mean wind speed profile.

The horizontal wind speed profile has been obtained using 19 points of measure, spaced 20 mm ÷ 50 mm apart, in horizontal direction to cover the whole size of end plates with the exception of the zone near to the vertical walls. In fact this measure had the aim to check the flow quality without estimating the boundary layer, therefore the first and last points of measurement have been taken at a distance of 10 mm from the wall. The graph highlights that all the measured profiles are almost flat and regular. Increasing the testing wind speed the profiles tend to be more curved with maximum velocity values in the centre of the set-up. Inasmuch as the increase of wind speed in the centre of the profile is in the order of 2 % compared to the lowest measured wind speed, the curvature of the profile was considered totally negligible. The first point near to the wall is outside the boundary layer, consequently the boundary layer thickness is assumed to be in the same order of magnitude as the vertical one.

Thanks to this set of measures (mean vertical and horizontal wind speed profile and turbulence intensity) it is possible to state that the flow inside the designed

end-plates is good, because the boundary layer is all contained in a thickness of 13 mm and the wind speed profiles are flat and regular.

6.4 Experimental measurements

Thanks to the experimental set-up widely exposed in the previous paragraphs, it was possible to measure the aerodynamic forces and moments induced by the air motion on samples of porous windbreaks. Each of the 27 samples was tested in correspondence of 15 different wind speed values for 60 seconds at a sampling frequency of 2000 Hz. The porous samples were tested with air flowing in both directions through the barrier in order to take into account possible asymmetry in the screen due to the industrial manufacturing process. None of the porous windbreaks tested have shown any sign of deformation, dirt accumulation or structural failures.

The principal parameters that were measured during the tests are reported in Table 6.3 and are distinguished in function of the reference measuring instruments.

Quantity	**Unit**	**Instrument**
V_{mean}	$[m/s]$	Pitot BLWT
V_{std}	$[m/s]$	Pitot BLWT
u_{mean}	$[m/s]$	Pitot Up-wind
u_{std}	$[m/s]$	Pitot Up-wind
$F_{(x,y,z),mean}$	$[N]$	HFB
$F_{(x,y,z),std}$	$[N]$	HFB
$T_{(x,y,z),mean}$	$[Nm]$	HFB
$T_{(x,y,z),std}$	$[Nm]$	HFB

Table 6.3 Quantities measured in wind tunnel.

The CRIACIV BLWT is equipped with a fixed Pitot tube, positioned in an external zone respect to the set-up. With this device it was possible to measure mean and standard deviation of reference airflow in wind tunnel [V_{mean}; V_{std}]. Using a Pitot tube collocated upstream of the end-plates (placed at a distance of 70 cm), it was possible to know the mean and standard deviation of the undisturbed wind speed approaching the windbreaks [u_{mean}; u_{std}]. Six digital signals came from the aerodynamic high frequency balance (HFB) and then were converted by means of calibration matrix (K). Thanks to K, the three mean components of force and moment [$F_{(x,y,z),mean}$; $T_{(x,y,z),mean}$] and the relative standard deviations were obtained [$F_{(x,y,z),std}$; $T_{(x,y,z),std}$].

Fig. 6.15 shows two particular devices that were in use during all the measuring phase. The Setra transducer is able to convert the pressure signals coming from Pitot tubes in digital signals and the HFB power supply has the aim to regulate the electric power at the balance.

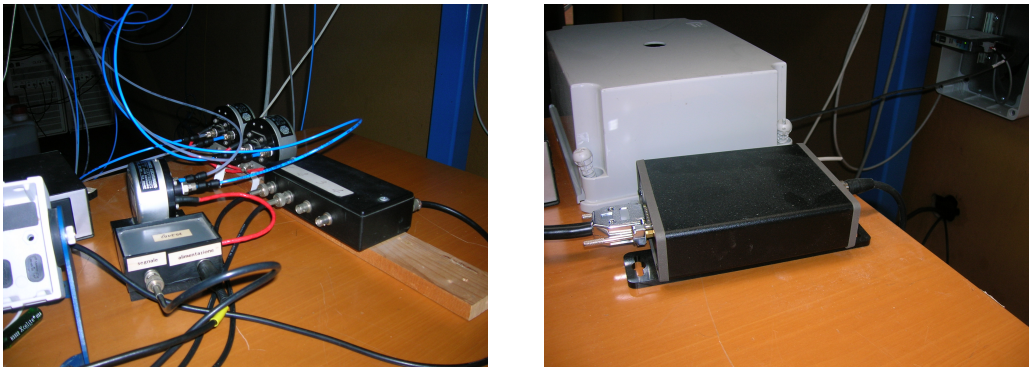

(a) Setra transducer for Pitot tubes (b) HFB Power supply

Fig. 6.15 Particular of devices in use.

For each kind of windbreak sample, three fundamental graphs have been created. One reported the pattern of aerodynamic forces and moments versus the mean reference wind speed on the barrier; another one indicated the relationship between the aerodynamic force and moment coefficients versus Reynolds number; the third graph was related to the points of application of the drag resultant force versus the Reynolds number.

6.5 Experimental results

Before entering into details of the acquired data it is necessary to specify which are the main components of force and moment acting on the windbreak in reference to the components measured by the HFB. Fig. 6.16 reports the reference system for the forces and moments that are adopted for the aerodynamic force balance.

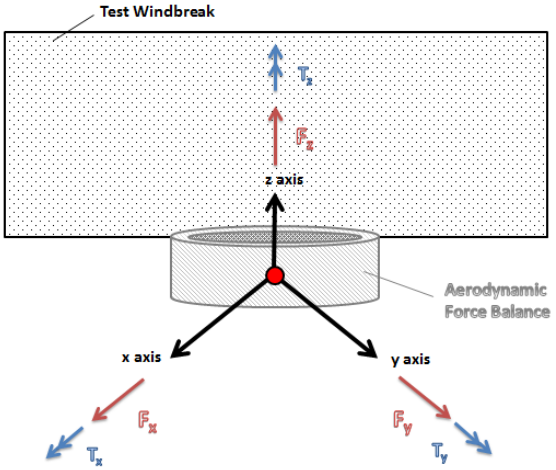

Fig. 6.16 Reference system for forces and moments.

In order to investigate the behaviour of porous windbreaks with respect to the air flow becomes fundamental to quantify the aerodynamic actions induced by wind

motion on the screen. The resultants of forces and moments can be simply determined by vectorial composition of forces and moments measured by HFB. The drag force and the moment induced by drag can be obtained by vectorial composition of the forces F_x and F_y and torque M_x and M_y. The lift force and the z-torque can be directly provided in output by the HFB through the force F_z and the torque T_z. As exposed so far the vectorial composition can be translated in purely mathematical terms in the following way:

$$\begin{aligned} Drag &= \sqrt{{F_x}^2 + {F_y}^2} \\ Moment &= \sqrt{{M_x}^2 + {M_y}^2} \\ Lift &= F_z \\ Z - Torque &= T_z \end{aligned} \tag{6.1}$$

In the Fig. 6.17 are reported in schematic manner the aerodynamic forces and moments that the airflow generates on the windbreak sample in wind tunnel.

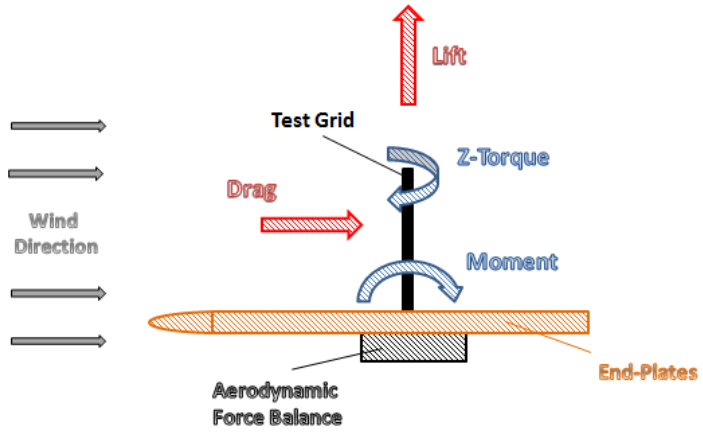

Fig. 6.17 Forces and moments acting on windbreak.

As expected the components that play a role of greater importance are the drag and the moment. This aspect confirms that the set-up is able to recreate almost perfectly a 2D flow model because the components of lift and above all z-torque have a small weight with respect to the others. Consequently the lift and z-torque components are neglected and for the analyses that follow only the drag and the moment were considered.

For each windbreak sample, the aerodynamic data resulting from the experiments performed were plotted in a graph reporting drag force and moment versus the undisturbed flow velocity (u_∞) (Fig. 6.18). The drag force and moment show a quadratic relationship with respect to the undisturbed wind speed. u_∞ is the reference velocity that is used to express dimensionless relationships; in this case it is represented by the wind speed measured, by means of the Pitot tube, upstream of the barrier.

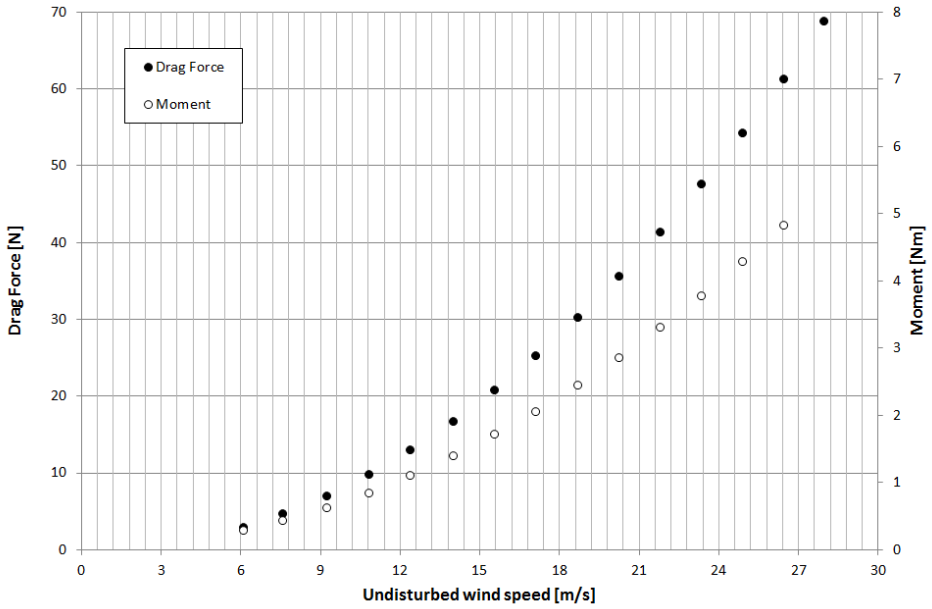

Fig. 6.18 Measured drag force and moment vs. undisturbed wind speed for the barrier R1.5T3 (ε=22.68 %, D_h=1.5 mm and t=1.5 mm).

In fluid mechanics and always when dealing with experimental data it is a good practice to express dimensionless relations between the many variables involved, with the goal to have dimensionless relationship. The first dimensionless parameter that it is necessary to introduce is the Reynolds number based on the height of the barrier. This parameter is able to represent the velocity in purely dimensionless term and can be defined as:

$$Re_H = \frac{u_\infty \cdot H}{\nu} \tag{6.2}$$

where: u_∞ is the undisturbed flow velocity; H is the height of the barrier, and for general tests it is equal to 0.2 m, and when testing the geometric scaling hypothesis, it is variable with the geometric scale; ν is the kinematic viscosity of the air.

The dimensionless parameters for aerodynamic force and moment are well represented by the relative aerodynamic coefficients of drag (C_D) and moment (C_M), as follows:

$$C_D = \frac{D}{\frac{1}{2} \cdot \rho \cdot u_\infty^2 \cdot L \cdot H} \tag{6.3}$$

$$C_M = \frac{M}{\frac{1}{2} \cdot \rho \cdot u_\infty^2 \cdot L \cdot H^2} \tag{6.4}$$

where: D and M are respectively the drag force and moment measured; ρ is the air density; L is the length of the barrier, always equal to 0.60 m, and H is its height.

In Fig. 6.19 the dimensionless graph reports the relationship between the drag and moment coefficients (C_D and C_M) versus the Reynolds number. This kind of diagram has been realized for all samples of windbreak tested in order to magnify the influence of Reynolds number on aerodynamic coefficients.

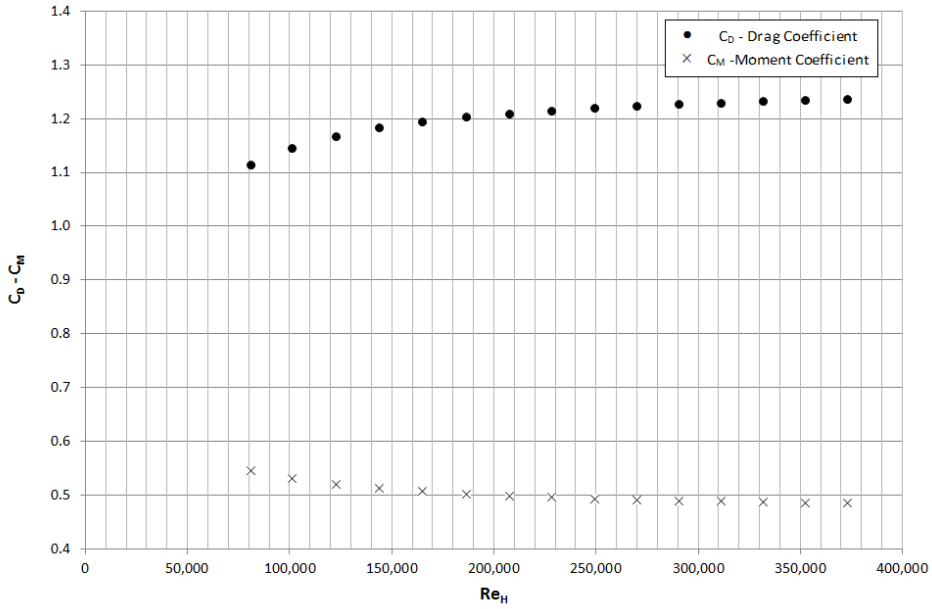

Fig. 6.19 C_D and C_M vs. Re_H for the barrier R1.5T3 (ε=22.68 %, D_h=1.5 mm and t=1.5 mm).

The graph shows that the viscous effects are important for value of Reynolds number in the range 80,000 ÷ 200,000 and become less relevant and even negligible when the inertial effects are predominant (when $Re_H > 200,000$).

A more immediate way to define the relationship between moment and drag is to resort to the point of application of drag force and the relative dimensionless parameter. The point of application of drag is a fundamental parameter, that is able to give an idea of the aerodynamic centre of the barrier and can be used to make some comparisons with the centre of gravity of the barrier itself. Remembering the definition of moment induced by drag force, the point of application (b) can be obtained as:

$$\begin{aligned} M &= D \cdot b \\ b &= \frac{M}{D} \end{aligned} \tag{6.5}$$

With the aim to have a more general dimensionless parameter it is common practice to define the ratio between the point of application of the drag and the height of the barrier as b/H. Fig. 6.19 reports for the sample R1.5T3 the pattern of drag coefficient (C_D) and ratio b/H versus the Reynolds number.

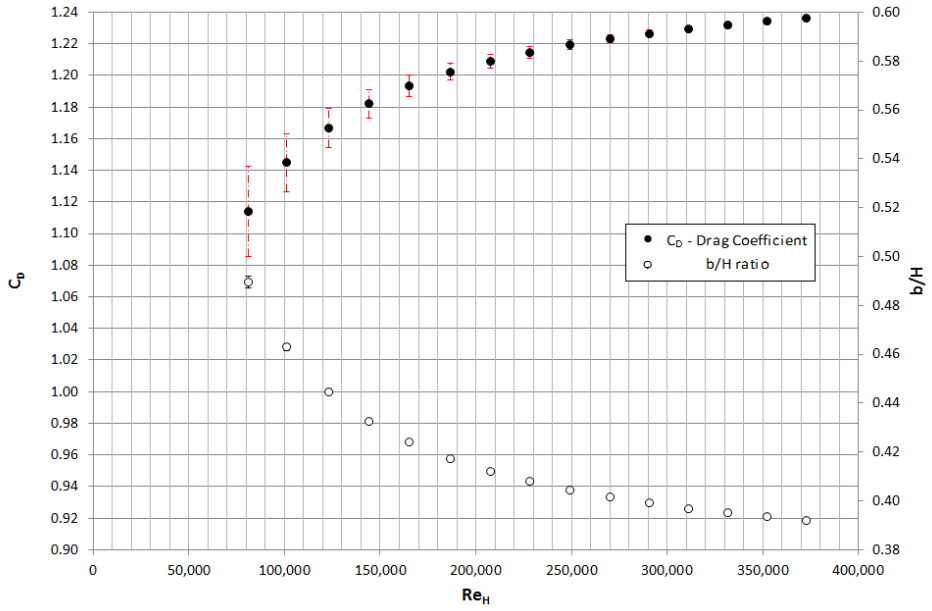

Fig. 6.20 C_D and b/H vs. Re_H for the barrier R1.5T3 (ε=22.68 %, D_h=1.5 mm and t=1.5 mm).

For each variable the diagram shows the relative pattern superimposed with error bars that are due to the uncertainty of the instrument of measure. More specifically the error bars have been determined introducing the full scale error of the HFB in correspondence of each component of force and moment. The red bars represent the errors made by the aerodynamic balance during the measure of the drag force and the black bars describe the errors in the estimation of the b/H ratio. As already shown in Fig. 6.19, also this graph confirms that the threshold between viscous and inertial effects can be fixed for Re_H equal to 200,000. The pattern of ratio b/H shows that the point of application of the drag force is at 40 % of the height of the barrier and that consequently the aerodynamic centre, for the sample studied, does not coincide with the centre of gravity of the barrier.

Similarly to the case of confined flow, the experimental data and the related treatment will follow the same descriptive procedure previously adopted.

6.6 Analysis of the data

In this section the main results related to unconfined flow around porous media will be reported and commented in detail. The key parameters that are considered are the drag and moment coefficients (C_D and C_M) and the ratio b/H. The choice has fallen on these parameters because they are fundamental quantities to characterize the behaviour of the barriers respect to the flow, and are easily comparable with the existing literature.

The analysis will be divided in function of the various factors that are able to influence the key parameters. Indeed, the effects due to the porosity level and Reynolds number, thickness, diameter and shape of the holes will be evaluated. In

addition, the geometric scaling hypothesis will be discussed in order to check the scaling criteria found in Chapter 5.

6.6.1 Effect of porosity level and Reynolds number

As already seen in the case of confined flow, the level of porosity is the key factor when dealing with permeable objects. Fig. 6.21 reports for all samples of windbreak the global effects of all variables involved with respect to the drag coefficient.

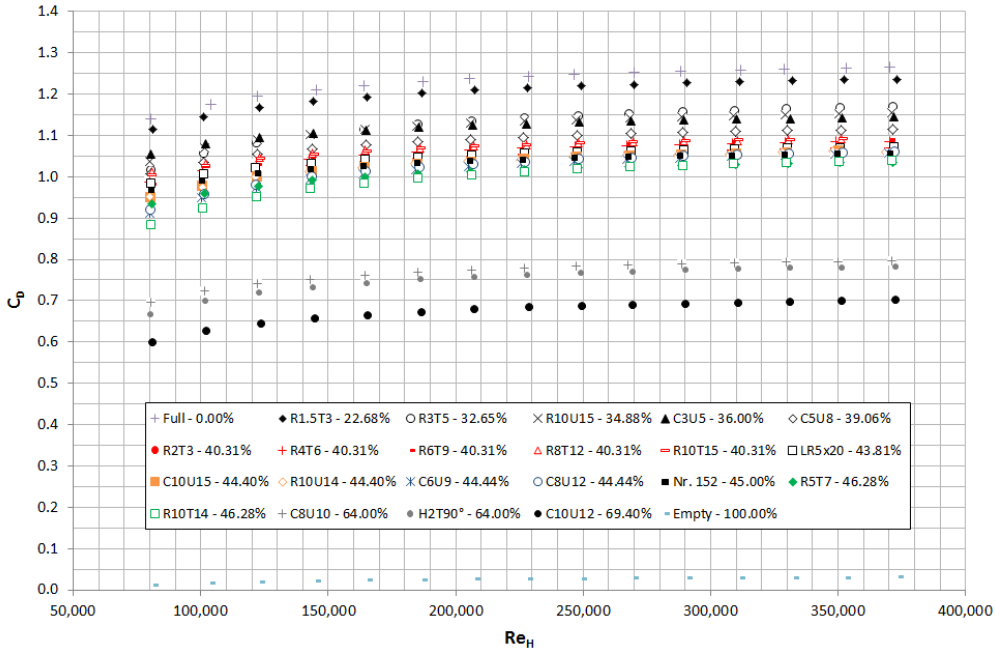

Fig. 6.21 C_D vs. Re_H for all of windbreak samples tested.

The graph is plotted in function of Reynolds number (Re_H) and shows the strong dependence of drag coefficients on porosity level. The experimental C_D data are subdivided in bands of porosity and are included in the interval $0.03 \div 1.26$. As expected, also in this case, the maximum values of the drag coefficient are found for low values of porosity and vice versa for high porosity level.

Following the same procedure adopted in literature [Pinker and Herbert (1967); Brundrett (1993); Valli *et al.* (2009)], it is possible to split the drag coefficient into two different functions: one depends only on porosity (ε) and the other only on Reynolds number (Re_H):

$$C_D(\varepsilon, Re_H) = G'(\varepsilon) \cdot F'(Re_H) \tag{6.6}$$

where: $G'(\varepsilon)$ is a function of porosity and $F'(Re_H)$ is a function of Reynolds Number.

This decomposition can be used for the moment coefficient as well as for the ratio b/H, but at this stage it will be applied to drag coefficient only. For each typology of windbreak, considering the C_D data where the drag coefficient does not depend

on Reynolds Number *(in this case represented by the average of last three points of each C_D - Re_H diagram)*, it was possible to find the analytic expression of $G'(\varepsilon)$ function by a simple fitting of the data.

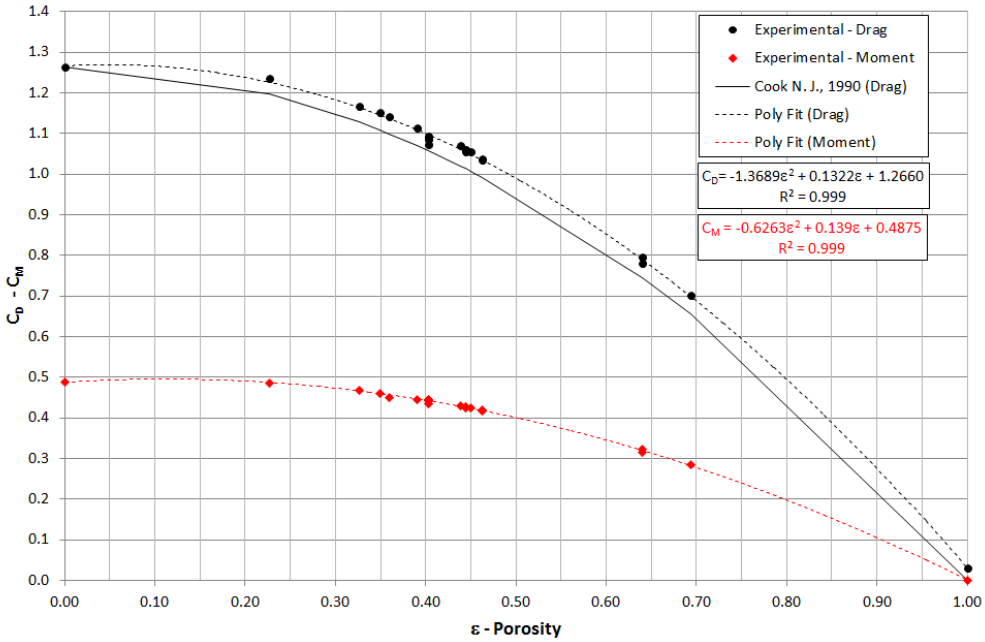

Fig. 6.22 $G'(\varepsilon)$ fitting function.

Fitting the black points of Fig. 6.22, the $G'(\varepsilon)$ function has been calculated and the best fitting is well represented by a polynomial function in the form:

$$G'(\varepsilon) = -1.3689\varepsilon^2 + 0.1322\varepsilon + 1.266 \tag{6.7}$$

$$\textbf{with: } R^2 = 0.999$$

Fig. 6.22 shows the influence of porosity level on drag (*black points*) and moment (*red points*) coefficients, and it reports also a comparison with the empirical function proposed in literature by Cook (1990). The fitting data are congruent with the logical limits of C_D, in fact $C_D \to 1.25$ [2D solid barrier] as $\varepsilon \to 0$ and $C_D \to 0$ as $\varepsilon \to 1$.

At this point, knowing the dependence of C_D on porosity level (ε) and the experimental function $C_D(\varepsilon, Re_H)$, the $F'(Re_H)$ function can be obtained as:

$$F'(Re_H) = \frac{C_D(\varepsilon, Re_H)}{G'(\varepsilon)} \tag{6.8}$$

Applying the equation (6.8) to all the data reported in Fig. 6.21 it is possible to obtain the $F'(Re_H)$ function for all samples in testing (Fig. 6.23). From Fig. 6.23 it is possible to notice that the dependence on porosity has been taken away, in fact the data are now contained in a narrow band in the range $0.85 \div 1.02$. The macro trend confirms that the effects of Reynolds number are negligible when $Re_H > 200,000$.

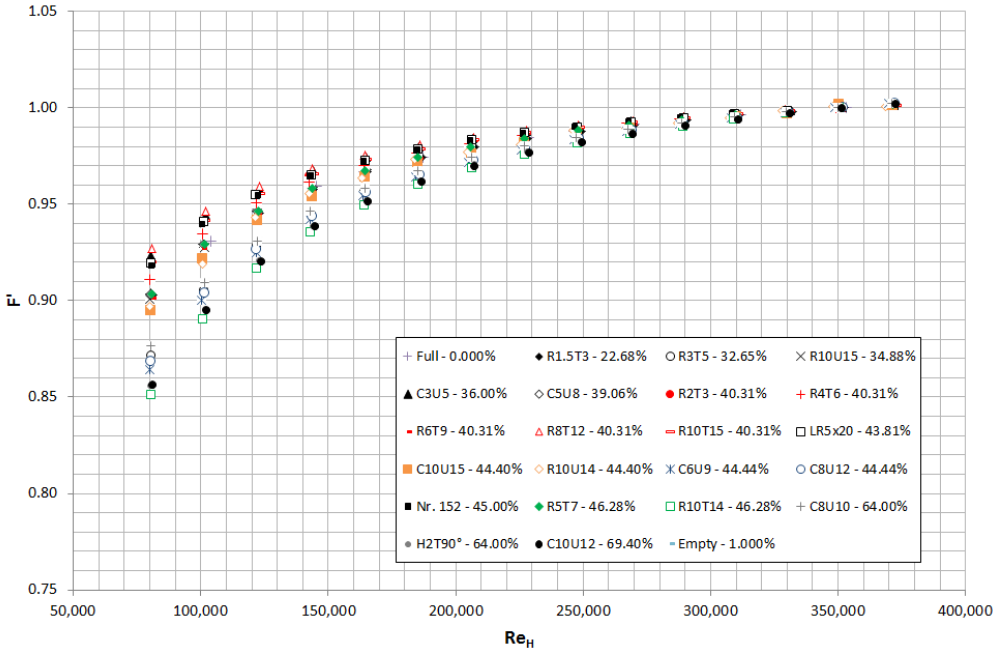

Fig. 6.23 F' function vs. Re_H for all of windbreak samples tested.

Using the ratio b/H it has been possible to evaluate the points of application of the drag force (b) respect to the global height of the barrier (H). In this part the influence of porosity level (ε) on the ratio b/H was evaluated and it is well represented by Fig. 6.24.

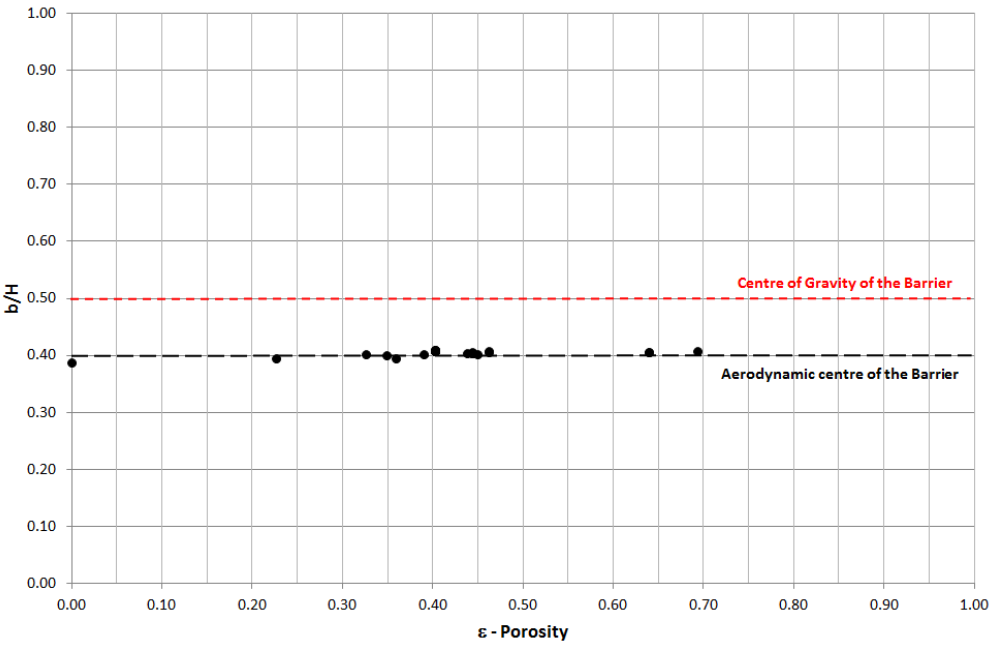

Fig. 6.24 b/H ratio vs. porosity for all windbreak samples tested.

In order to make it clearer, the graph contains also two dashed lines representing respectively the centre of gravity (*red line*) and the aerodynamic centre (*black line*) of the barrier. The black points reported in Fig. 6.24 are obtained considering, for all the samples of windbreak tested, only the asymptotic b/H values where the dependency on Reynolds number is not present (mean of the last three points of each b/H - Re_H diagram). The data for ratio b/H are included in the range $0.387 \div 0.406$ and the trend seems to highlight that the points of application slightly rise as the porosity level increases. It is fundamental to remember that the variation in the b/H data is in the order of 4 % and therefore it is comparable with the uncertainty of measurement. In virtue of this observation the ratio b/H remains almost constant increasing the porosity level of the windbreak with a value of approximately 0.40. Consequently the point of application of the drag force results not to be coincident with the centre of the mass but it is located below it at a distance of 20 mm. Showing the ratio b/H little dependence on a key parameter such as porosity, it was decided to assume as reference parameter, for the next analyses, only the drag coefficient.

6.6.2 Diameter and thickness effects

The tests performed in Chapter 5 have shown the existence of three different wake flow regimes depending on the t/D_h ratio. The experimental data do not define exactly the value of t/D_h that divides the three regimes and this has been hypothesized at $t/D_h \lesssim 0.4$ for the fully separated wake regime, and $t/D_h \gtrsim 1.2$ for the fully reattached flow. At values of $0.4 \lesssim t/D_h \lesssim 1.2$ the wake flow regime is intermediate and has transition features between the two previous regimes.

Regarding windbreaks and other porous elements used in civil engineering, the majority of these objects falls into the separated flow regime, because of their t/D_h ratio. To investigate more in detail this flow zone and to operate some comparison with the confined flow it has been decided to carry out experiments in the range of t/D_h from 0.1 to 0.5. The samples tested had the same porosity level fixed equal to 40.31 % and the same shapes of the holes (*round*), but different t/D_h ratio. Their main features are reported in Table 6.4.

Model	**Porosity % (ε)**	t **[mm]**	D_h**[mm]**	t/D_h	**Shape**
R2T3	40.31	1.0	2.0	0.500	Round
R4T6	40.31	1.0	4.0	0.250	Round
R6T8	40.31	1.0	6.0	0.167	Round
R8T12	40.31	1.0	8.0	0.125	Round
R10T15	40.31	1.0	10.0	0.100	Round

Table 6.4 Samples for diameter and thickness tests.

Fig. 6.25 highlights the influence of Reynolds number on drag coefficient (C_D) for all the samples subject to t/D_h tests. From the graph it is quite difficult to understand which is the influence of diameter and thickness because the data are very close to each other.

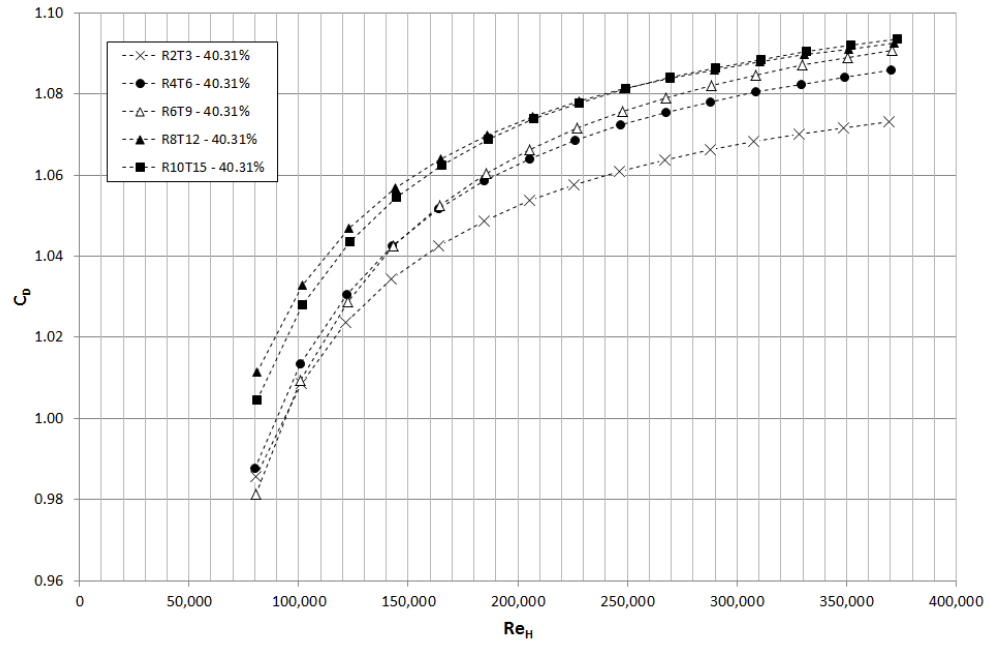

Fig. 6.25 C_D vs. Re_H for t/D_h tests.

Considering only the C_D data where the dependency on Reynolds number is not present (mean of last three points of the $C_D - Re_H$ trends in Fig. 6.25) and plotting C_D against the diameter of the holes (Fig. 6.26) and t/D_h ratio (Fig. 6.27), the data become more readable.

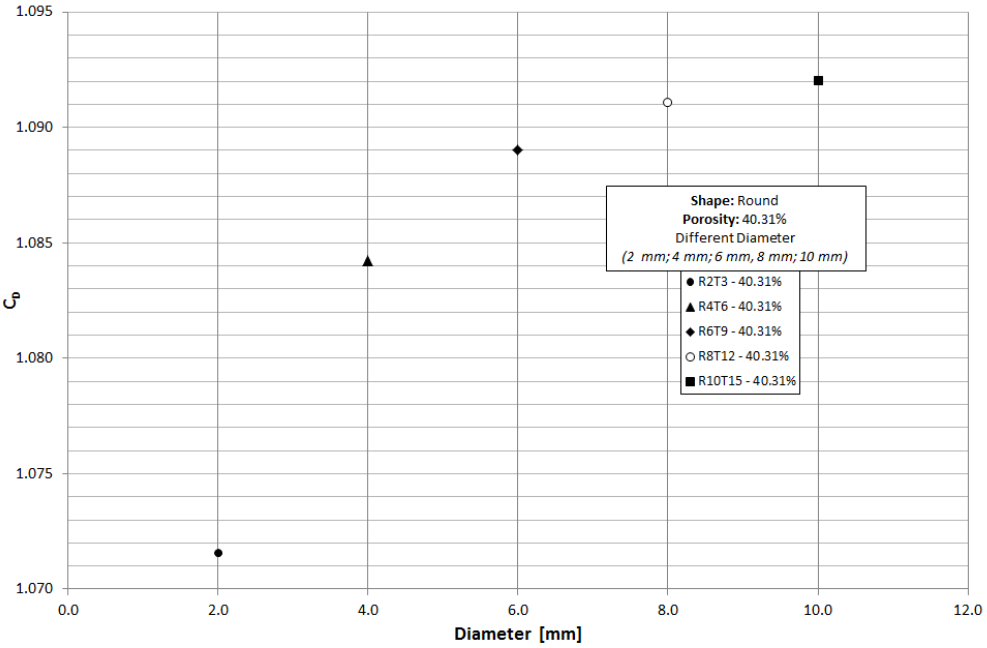

Fig. 6.26 C_D vs. Diameter.

Fig. 6.26 reports a trend similar to the one observed in the case of confined flow, in fact the highest values of drag coefficient are found for large hydraulic diameter of the holes and vice versa. Consequently it is possible to affirm that the windbreaks that show a major flow resistance are those with the largest diameter, but a deeper comprehension of the phenomenon can be obtained passing in the t/D_h domain.

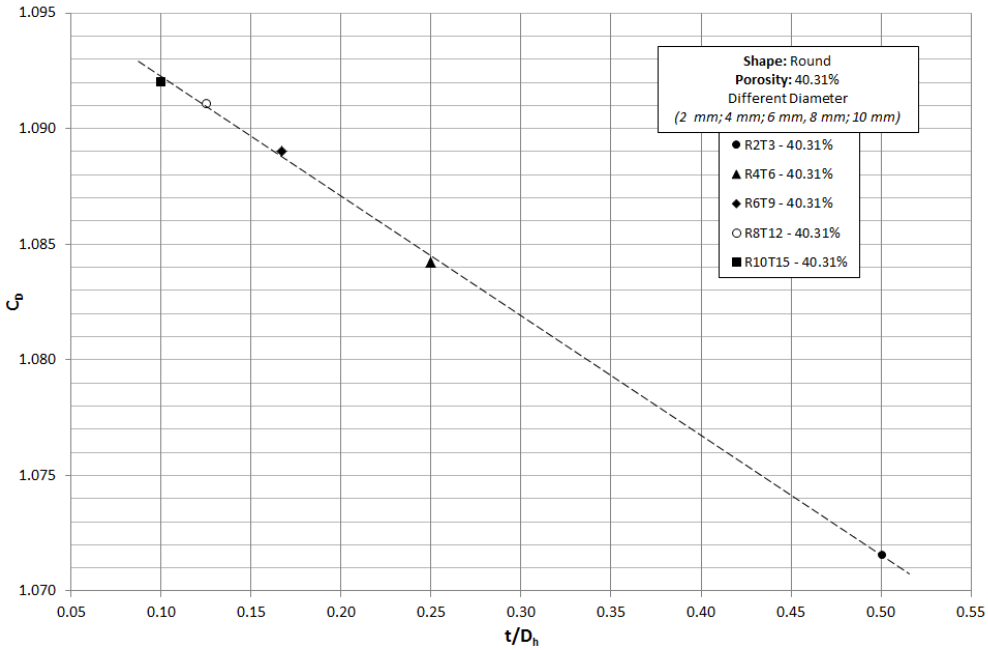

Fig. 6.27 C_D vs. t/D_h ratio.

In Fig. 6.27 it is possible to notice that exists a linear trend between C_D and t/D_h. Indeed, maximum C_D values are observed in correspondence of small t/D_h ratio and minimum C_D values for high t/D_h.

6.6.3 Shape effect

With the aim of investigating whether the effects played by the hole shape are present or not, some additional tests in wind tunnel were preformed on two samples. The windbreaks were different only for the shape of the holes and had the same hydraulic diameter, the same thickness and the same porosity level ($\varepsilon = 44.40$ %). In Table 6.5 the main characteristics of the samples in use for this test are briefly reported.

Model	**Porosity % (ε)**	t **[mm]**	D_h**[mm]**	**Shape**
R10U14	44.40	1.0	10.0	Round
C10U15	44.40	1.0	10.0	Square

Table 6.5 Windbreak samples for shape tests.

The shapes of the holes that were examined are round and square. An appropriate graph that reports the dependency of drag and moment coefficient on Reynolds

number in function of the two different shapes has been created.

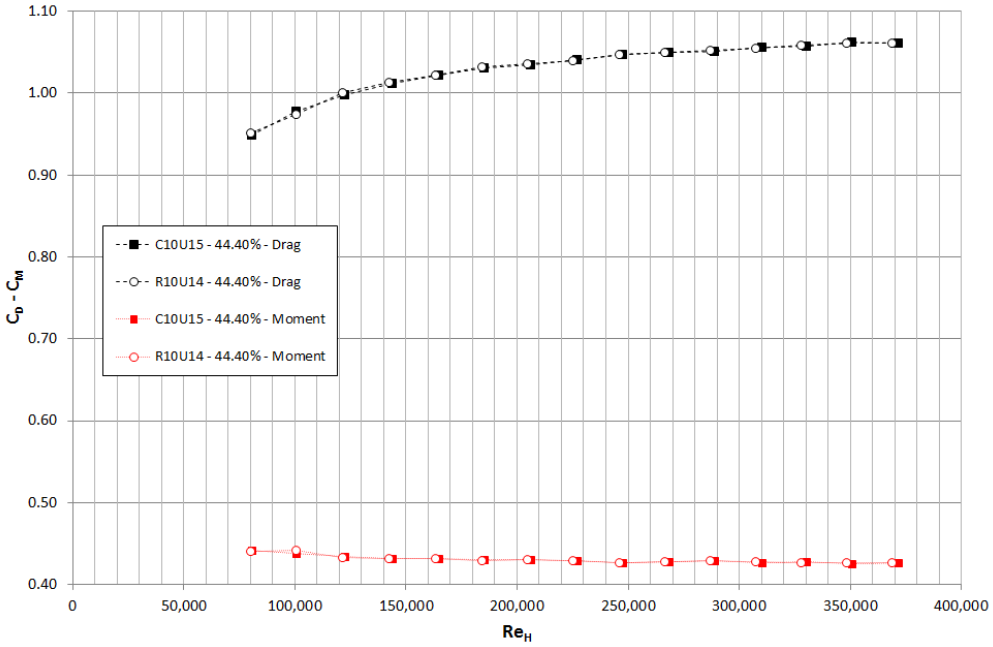

Fig. 6.28 C_D vs. Re_H for shape test.

Fig. 6.28 reports with square markers the data for barriers with square holes and with circular markers the measured data for round shape. The diagram is further divided into two bands of colours: red indicates the moment coefficient (C_M) and black the drag coefficient (C_D). From the graph it is possible to affirm that the effects of the shape of the holes are negligible and this is not fundamental parameter in the examined problem. This result confirms what was indicated by ESDU81039 (1985) and Idelchik (1994).

6.6.4 Geometric scaling effect

This subsection will analyse the feasibility of the geometric scaling hypothesis, paying particular attention to the errors that this procedure can cause. The reference structures for this kind of analysis are windbreak barriers.

Height[m]	**Porosity %** (ε)	t/D_h	**Shape**	**Scale Factor**
0.04	40.31	0.500	Round	1:5
0.08	40.31	0.250	Round	1:2.5
0.12	40.31	0.167	Round	1:1.67
0.16	40.31	0.125	Round	1:1.25
0.20	40.31	0.100	Round	1:1

Table 6.6 Windbreak samples for scale tests.

This typology of tests has been carried out on five different samples of windbreak at different geometric scales and the main features of the samples are summarized in the Table 6.6.

(a) Case without barrier

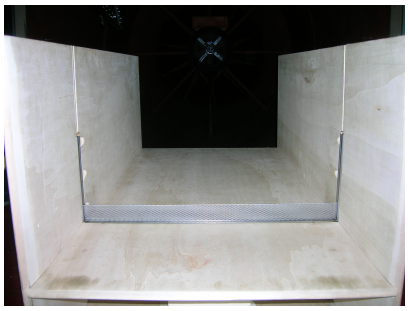

(b) Barrier at scale 1:5

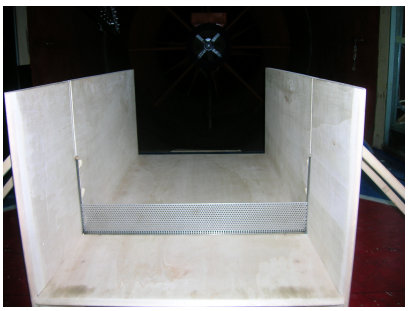

(c) Barrier at scale 1:2.5

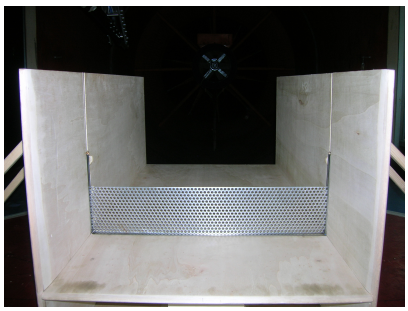

(d) Barrier at scale 1:1.67

(e) Barrier at scale 1:1.1.25

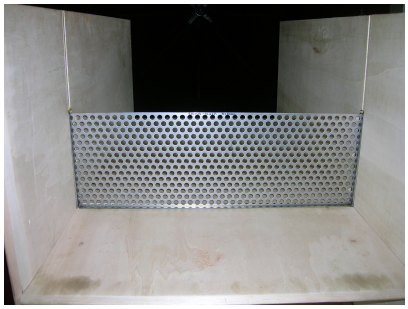

(f) Barrier at scale 1:1

Fig. 6.29 Windbreaks for scale tests.

To get an immediate idea of the experimental work, Fig. 6.29 reports all scaled barriers tested. The windbreak at scale 1:1 is a barrier that has a height of 200 mm, diameter of holes of 10 mm and a thickness of 1 mm. During the geometric scaling process the height of the barrier and the diameter of the holes have been scaled but not the thickness. This is justified by the fact that, as seen in the case of confined flow and confirmed by Fig. 6.27, if the value t/D_h is less than 0.4, the wake flow regime is permanently fully separated and then the discrepancy among the different t/D_h ratios is not important.

Fig. 6.30 shows the influence of Reynolds number (Re_H) on drag coefficient (C_D) for all geometrically scaled samples. Error bars have also been superimposed to the pattern C_D vs. Re_H with the purpose to present a confidence interval for

the measure. The error bars have been determined introducing the full scale error of HFB for each component of force measured.

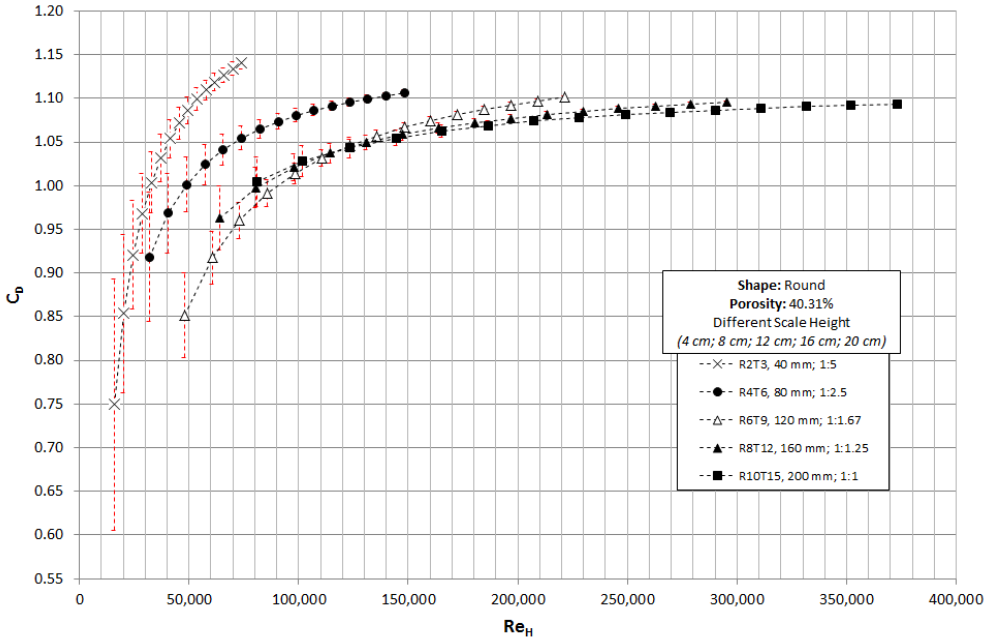

Fig. 6.30 C_D vs. Re_H for geometric scaling test.

It can be immediately noted that for the barriers at scale 1:5 the results are much more dependent on Reynolds number, and that the threshold value of 200,000 has not been reached. For the other windbreaks, with a little exception for the barrier at scale 1:2.5, it is confirmed that the Reynolds effects are not present if the value of 200,000 is exceeded.

In order to understand the effects of scale and the relative differences between the various barriers tested, it is useful to build a table that summarizes all the results. Table 6.7 reports for each windbreak the C_D value (it is the drag coefficient obtained for Reynolds number equal to 200,000) and the percentage error calculated with respect to the barrier at scale 1:1.

Height[m]	t/D_h	C_D	**Error %**	**Scale Factor**
0.04	0.500	1.158*	7.42	1:5
0.08	0.250	1.108*	2.79	1:2.5
0.12	0.167	1.0924	1.26	1:1.67
0.16	0.125	1.0804	0.15	1:1.25
0.20	0.100	1.0788	0.00	1:1

Table 6.7 C_D and percentage error for scale tests.

For the samples where the threshold value of Reynolds number has not been matched (*), the C_D values were obtained by the extrapolation of the C_D - Re_H

data in correspondence of $Re_H = 200,000$. To support the Table 6.7, a diagram reporting the C_D values versus the height of the barrier has been built (Fig. 6.31).

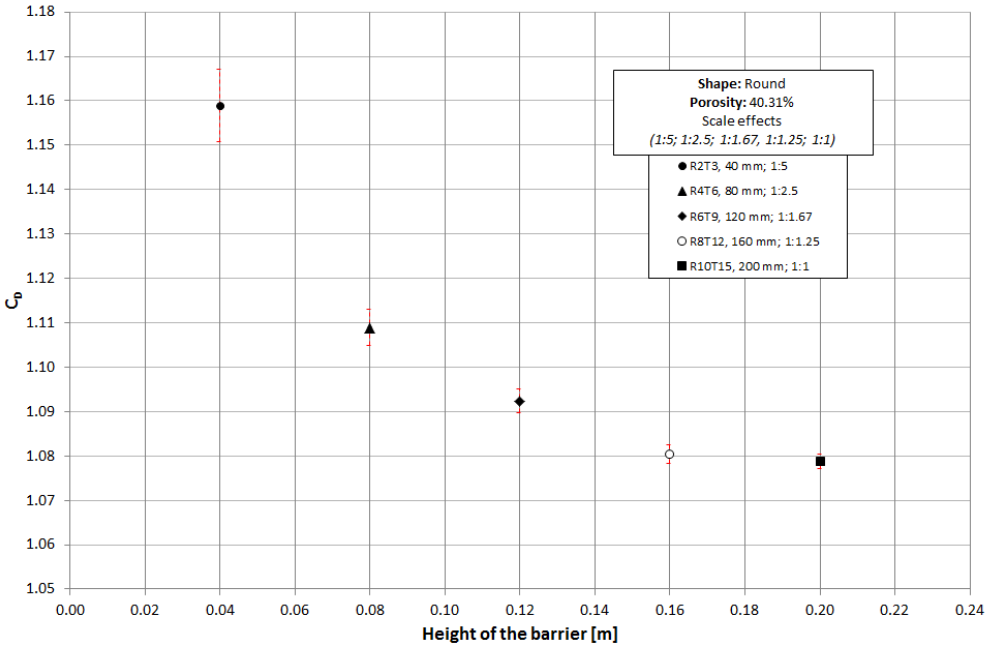

Fig. 6.31 C_D vs. height of the barrier.

The data related to the barrier on a smaller scale are affected by a difference of about 7.42 % and the data for the other scales show a percentage of discrepancy less than 3 % (that is comparable with the measurement error).

This difference on the data can be imputed to some experimental problems. The first issue is related to the boundary layer thickness that develops on the wall of the wooden end plates. In fact considering that boundary layer thickness is equal to 13 mm and the height of the fence is 40 mm, it is possible to confirm that the boundary layer thickness influences the 32.5 % of the height of the barrier. A second problem relates to the construction modality of the set-up and in particular to the introduction of the steel support on the wooden end-plates. This additional device can be positioned in a not perfect manner, resulting not aligned with the wooden end plates surface. As a consequence there can be some additional force contributions that remain negligible in the case of barrier at large scale. By contrast, in case of small scale, their effect becomes relevant. Thirdly, the instrumented steel frame was designed for windbreak samples of 20 cm but in this case it supports a sample having height of 4 cm only, thus it leaves a free portion of 16 cm. This can be seen very well in Fig. 6.29b where it is possible to notice the free upper part of the steel frame. The free portion of 16 cm, even if suitably covered, can take some contributions of force which become fundamental in view of the small forces acting on the tested sample. This aspect is fully supported by the results obtained for the case *Empty*.

Anyway the results demonstrate that initial hypothesis is valid. In fact applying the geometric scaling process for the height of the barrier and using the scaling criteria found for the porous core of the object, the experimental data confirm that

all scaled barriers in testing present almost the same drag coefficient and thus are equivalent.

6.6.5 Comparison between confined and unconfined flow

In this section all the results obtained for both cases of confined flow (*grid samples inside PVC pipe*) and unconfined flow (*samples of porous windbreaks*) will be compared. The main idea of this comparison is to relate the data coming from two different types of test. Also in this case the key parameters such as level of porosity, Reynolds number, dimension, thickness and shape of the holes will be examined one by one with the purpose to find some correspondences between the two cases.

6.6.5.1 Role of the porosity level

The porosity level (ε) is the most important parameter, in fact both cases presented strong dependence on it. The trends of loss coefficient (K), index able to characterize the flow resistance in confined flow, and drag coefficient (C_D), key parameter for unconfined flow, are reported in the following as a function of the porosity level (Fig. 6.32 and Fig. 6.33).

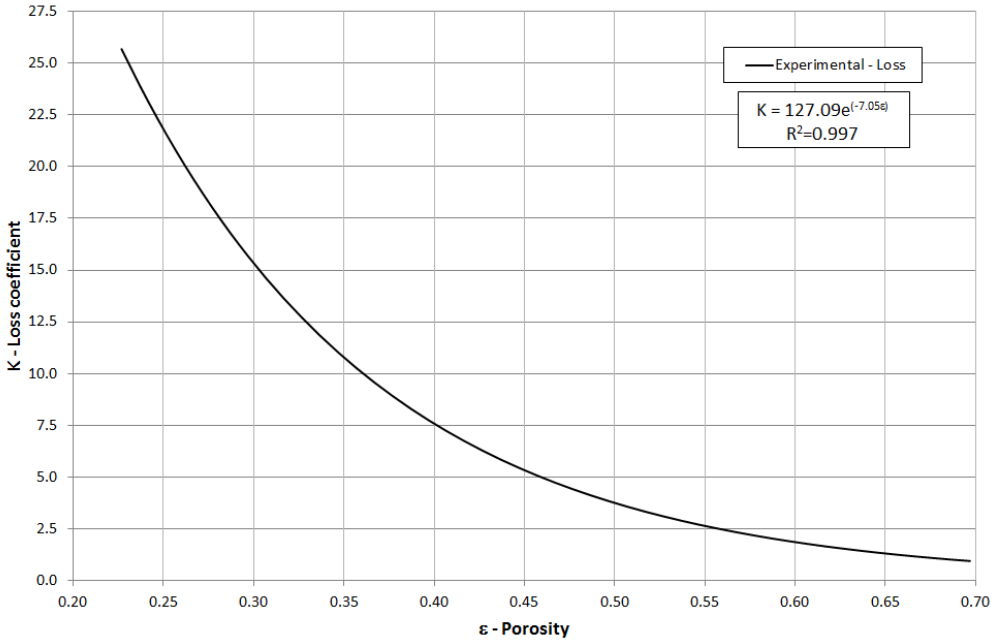

Fig. 6.32 K vs. porosity (confined flow).

The two graphs reported in Fig. 6.32 and Fig. 6.33 show the same tendency, in fact both parameters (K and C_D) tend to decrease as the porosity values increase, but with a different concavity of the curves. In case of confined flow the decrease is more pronounced and well described by negative exponential function unlike the case of unconfined flow where the decrease is less evident and it is well fitted by a second order polynomial function.

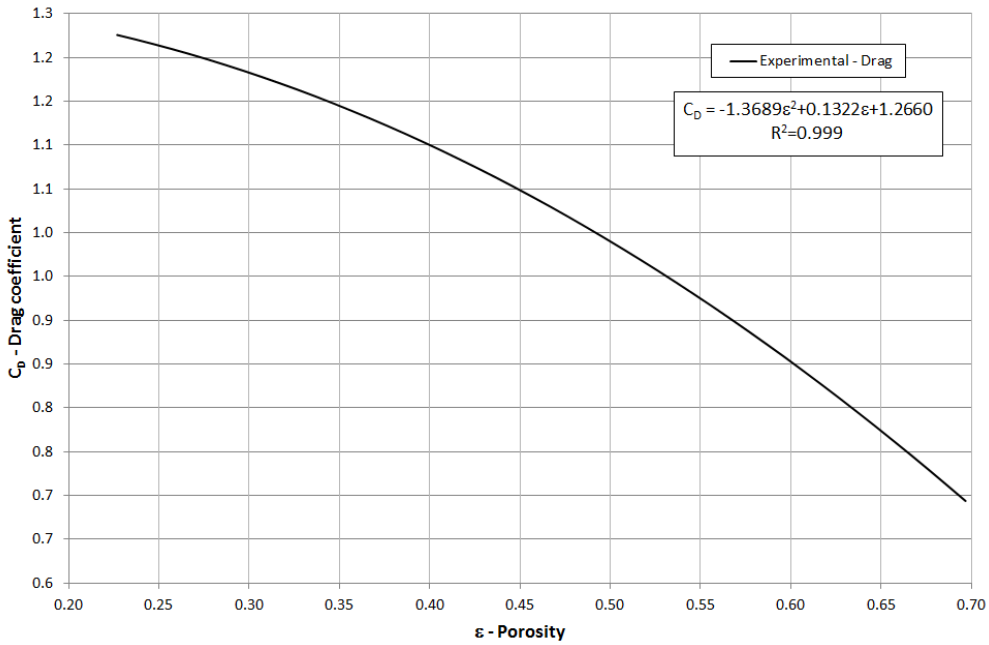

Fig. 6.33 C_D vs. porosity (unconfined flow).

It is difficult to compare the two trends, because they were obtained for two different conditions of air motion. This difference is mainly imputable to the different flow conditions: in the case of confined flow the momentum normal to the screen is conserved and for unconfined case it is not. In the confined flow the air is forced to pass only through the porous material and in case of windbreak the flow is able to move inside the porous core and also on the upper part of the barrier, similarly to a flow around a bluff body. In order to find a common description of the phenomenon, the only comparison that can be done is obtained by putting in relationship the loss coefficient (K) and the drag coefficient (C_D) in correspondence with the same level of porosity.

Fig. 6.34 shows the relation between the loss coefficient, obtained in case of forced flow, and the drag coefficient, achieved for external flow. It reports also on the second vertical axis the porosity level in order to make the chart more readable and intuitive. The best fitting between the two non-dimensional parameters is well provided by a rational function (6.9) with the following form:

$$C_D = \frac{K}{(0.436 + K)^{0.927}} \tag{6.9}$$

$$\textbf{with: } R^2 = 0.998$$

The formula in equation (6.9) is quite similar to some relations found in literature for round wire mesh screen, by Cook (1990) and Richards and Robinson (1999).

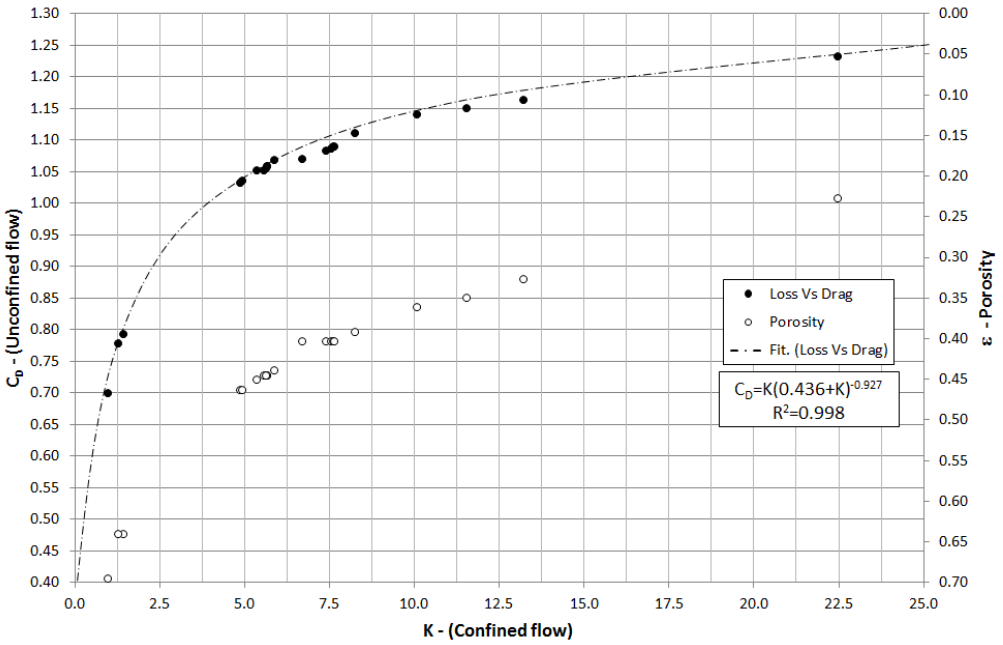

Fig. 6.34 K vs. C_D relationship.

6.6.5.2 Reynolds number effects

The Reynolds number is the key parameter that defines the boundary between the region where the viscous effects are not negligible and the region where those effects become less relevant (*inertial zone*). In the two cases of confined and unconfined flow several definitions of Reynolds number were given. As regards the confined flow, two definitions of Reynolds number were indicated, the Local Reynolds number (Re_L) and the Global Reynolds number (Re_G):

$$Re_L = \frac{w_0 \cdot D_h}{\nu} \tag{6.10}$$

$$Re_G = \frac{\overline{u} \cdot D}{\nu} \tag{6.11}$$

Re_L is Reynolds number based on the characteristics of the holes, in fact it depends on hydraulic diameter (D_h) of the holes and on the wind speed through the permeable material (w_0). Re_G has a more global definition and depends on the dimension of the samples (D) and on the testing mean wind speed inside the PVC pipe ($\overline{u}$). Turning to the case of unconfined flow the only adopted definition of Reynolds number (Re_H) is the one reported in equation (6.2). Re_H is a dimensionless parameter based on a characteristic dimension of the object, in this case the height of the barrier (H), and the undisturbed flow velocity (u_∞). In the case of unconfined flow it is impossible to give a definition of Local Reynolds number, due to the inability to determine the speed inside the barrier holes. In fact the conservation of momentum through the screen does not occur and the wind speed inside the holes cannot be uniquely correlated to approaching wind velocity and porosity level. Consequently the two typologies of test remain not comparable, in terms of Reynolds, and it is well

demonstrated by the two different patterns of Reynolds number that are encountered (Fig. 6.35 and Fig. 6.36).

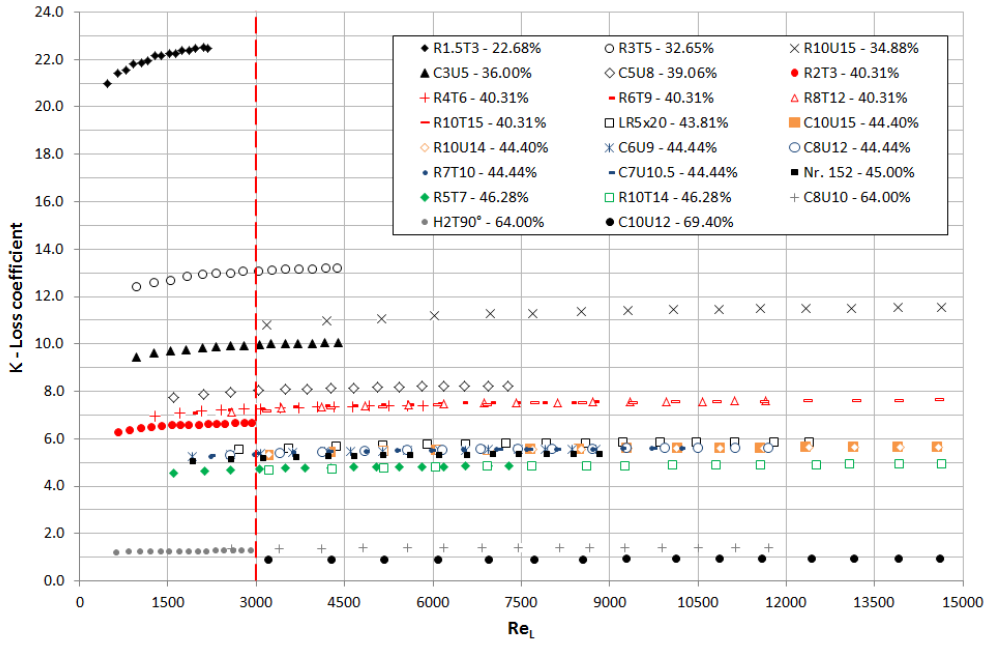

Fig. 6.35 K vs. Re_L (confined flow).

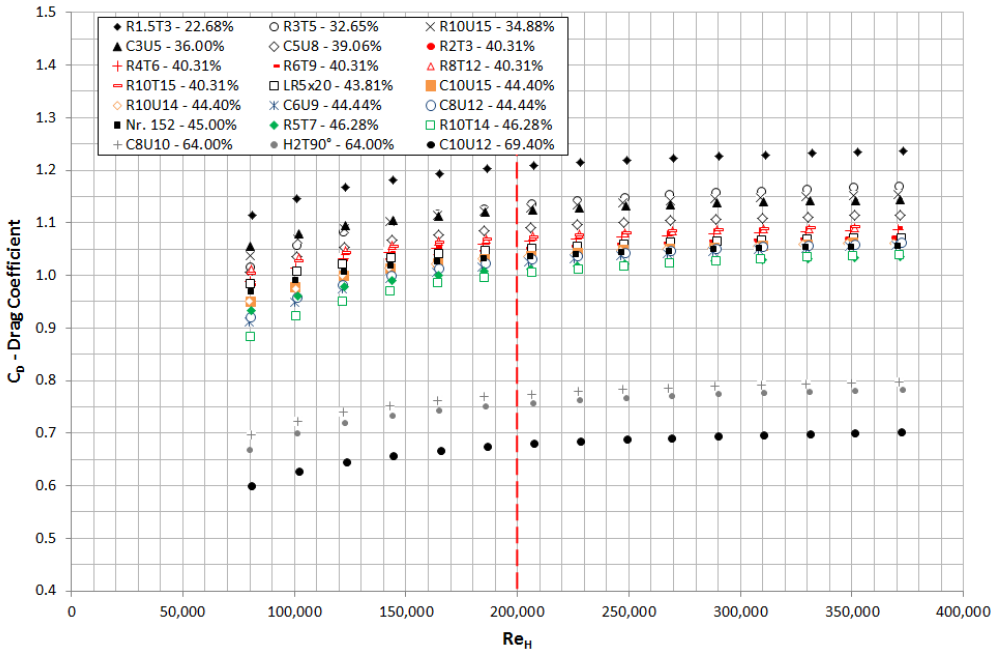

Fig. 6.36 C_D vs. Re_H (unconfined flow).

As regards the confined flow, the loss coefficient data are independent of Reynolds number when Re_L is equal to 3000 and highlight the classical effects of Reynolds that are encountered when an air flow is forced to pass in an indefinite porous medium. Vice versa for the unconfined flow case the influence of Reynolds number on drag coefficient is observed up to values of Re_H=200,000 that are reasonable in accordance with the typical value obtained for fluid flow around a two-dimensional vertical porous plate.

6.6.5.3 Dimension and thickness effect

The geometric dimensions of the holes, expressed in terms of hydraulic diameter (D_h) and thickness (t), cover relevant role in the entire phenomenon. In fact in function of the values assumed by the t/D_h ratio, have been highlighted in Chapter 5 three different wake flow regimes (fully separated, intermediate and fully reattached).

Concerning the confined flow, the influence of diameter and thickness of the holes was analysed in the t/D_h ratio range of $0.1 \div 1.5$. Instead, regarding the unconfined flow the reference interval was from 0.1 to 0.5. So, the comparison between the two cases can be carried out in the t/D_h common range of $0.1 \div 0.5$. In Fig. 6.37 and Fig. 6.27 the effects played by t/D_h ratio on the loss coefficient (K) and drag coefficient (C_D) are reported.

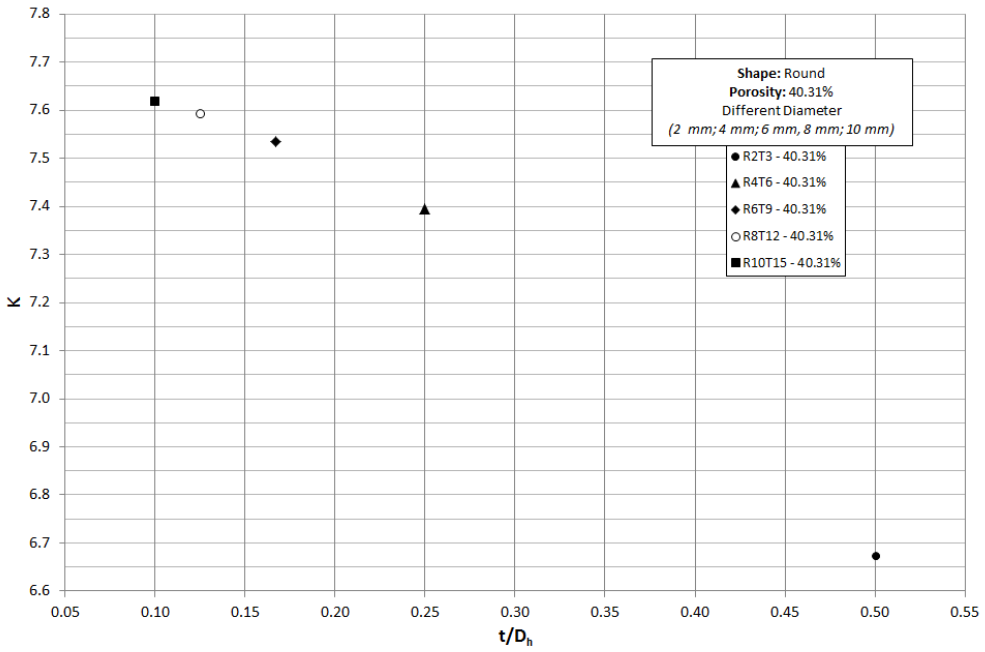

Fig. 6.37 K vs. t/D_h ratio (confined flow).

In case of confined flow increasing the t/D_h ratio of the holes from 0.1 to 0.5, the loss coefficient decreases with a non-linear behaviour. Passing to the effect of diameter on drag coefficient for the case of unconfined flow, it is well reported in Fig. 6.27. The drag coefficient also decreases in correspondence with high values of the t/D_h ratio but with a linear behaviour. With the aim of operating some

comparisons between the two different typologies of tests, Fig. 6.38 includes both Fig. 6.37 and Fig. 6.27 in a common scale. The diagram shows, with respect to the three wake flow regimes, the patterns F vs. t/D_h for confined and unconfined test.

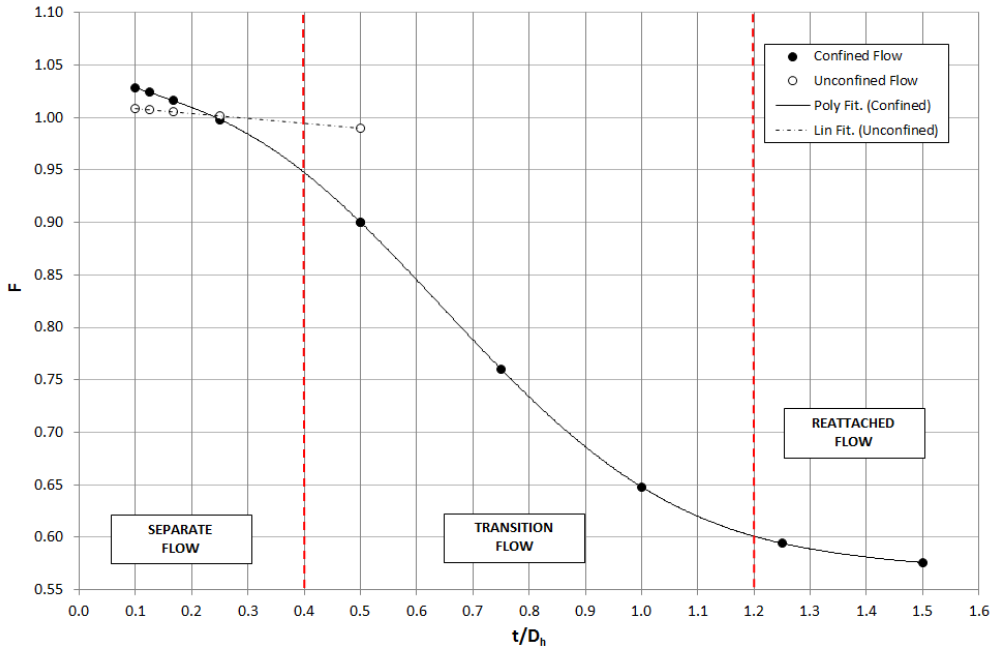

Fig. 6.38 F vs. t/D_h ratio.

Further analysis of the data lead to note that the decrease of the F function respect to the maximum value is about 12.4 % in the case of confined flow and 1.91 % in the case of unconfined stream. From this point of view it is possible to see that the additional effects of diameter and thickness that are emphasized in the case of confined flow become less visible in unconfined condition. This aspect is surely imputable to the condition of the flow around a body. In fact as well explained by Plate (1971) and Lee and Kim (2001), at the top of a barrier a separation of flow occurs and downstream of the barrier a big zone of depression is present. These aerodynamic effects, not present in confined case, lead to hide and to minimize the effects of diameter and thickness of the holes. Therefore, though less pronounced than in the case of confined flow, the t/D_h ratio does not lose its importance but retains a marginal role for this type of porous objects.

6.6.5.4 Shape effect

The shape effect has been evaluated in case of confined flow on four samples of grid and in case of unconfined flow on two samples of windbreak. The only shapes available for this kind of test were round and square. In both cases the effects of the shape of the holes are negligible, because the discrepancies between the data for round and square shapes are irrelevant and they are comparable with the measurement errors.

6.7 Validation of the proposed scaling criterion

Consider the case of windbreaks of a generic porous structure where it is necessary to study more in details the relative behaviour with respect to the fluid flow through some tests in wind tunnel. Thanks to the deep analysis performed in Chapter 5 on confined porous materials, represented by perforated plates, it has been possible to highlight which are the key parameters that control the phenomenon. These are porosity level (ε), Reynolds number (Re) and the ratio between thickness and hydraulic diameter of the holes (t/D_h). By using these parameters it has been possible to define a sort of scaling criterion that is necessary to respect when some wind tunnel tests on porous elements are required (§5.7). However this criterion is derived only in case of confined flow through a porous medium which can be seen as a sort of uniform flow that invests an indefinite porous screen. Generally, the typical structures of civil engineering equipped with porous media are not subject to this flow condition. Consequently, they are not made of an indefinite porous material but are characterised by their fundamental geometric dimensions (Fig. 6.39).

(a) Permeable façade (b) Porous advertising tower

(c) Shading façade (d) Windbreak barriers

Fig. 6.39 Examples of porous structures in civil engineering.

Therefore, the scaling criterion cannot be applied directly but has to be further adapted in order to include also the aspect due to the external dimensions of the structure. The modification consists in joining the criterion found with the classical geometric scaling process. In particular, the simple geometric scale will be applied for the predominant dimensions of the structure and the scaling criterion found will be respected only in the porous kernel. This assumption turns out to be valid because it has been verified implicitly in (§6.6.4) during the analysis of the feasibility of the geometric scaling hypothesis. More in detail the scaling criterion found was

respected in the porous core of the barrier and the geometric scaling hypothesis was applied for the predominant dimensions (in this case the *height*). In order to check the goodness of this assumption the windbreaks were geometrically scaled using five different scale factors. As explained in §6.6.4, the five barriers presented all the same drag and moment coefficients and consequently the same aerodynamic resistance. Therefore to perform some wind tunnel tests in a geometrical scale or in another one results to be totally indifferent, so confirming the initial assumptions and validating the entire scaling procedure.

Hereupon it is useful to reformulate the scaling criterion found, in a more general form, in the light of the new insights obtained from the comparison between the case of confined flow and the case of the unconfined one (see §6.6.5). In the following, one can find a schematic procedure that can be used when it is necessary to operate a correct scaling process for porous structures in wind tunnel.

6.7.1 Scaling procedure

At this point it is fundamental to extend the scaling method found to more complex structures as the case of roads, bridges or footbridges equipped with porous windbreaks. With the aim of making clearer the procedure of scaling in Fig. 6.40 are reported, in graphical way, all the crucial steps that must be followed.

(a) I Step: Prototype

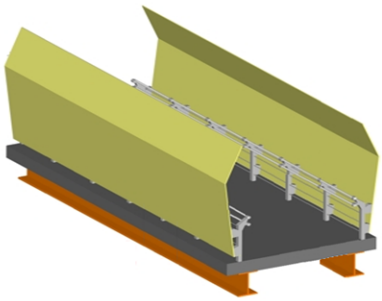

(b) II Step: Section model

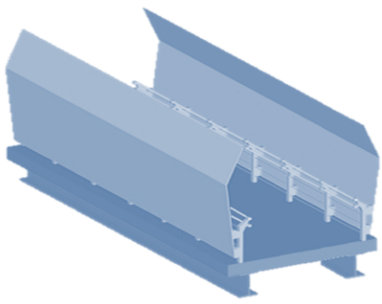

(c) III Step: Scale overall dimensions

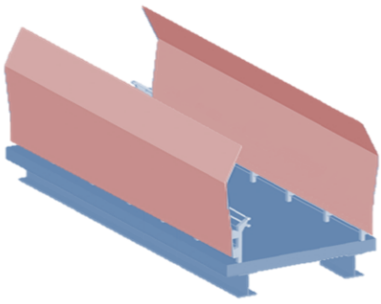

(d) IV Step: Use criteria in porous core

Fig. 6.40 Steps of scaling process.

Let us imagine to have to carry out some wind tunnel tests for the stable-cabled footbridge reported in Fig. 6.40a. The tests in wind tunnel require to schematize the prototype in a characteristic section model (Fig. 6.40b). The stylized section model

has to be transformed in WT model by appropriate geometric scaling. Geometrical scale is set (for example scale model equal to 1:20) and adopted for the entire WT model (Fig. 6.40c). Finally the scaling criterion found is respected only in the porous core of the structure, i.e. the windbreaks (Fig. 6.40d). The scaling criterion can be correctly applied on the porous part of the structure respecting some key parameters, that are listed here below.

6.7.1.1 Porosity, shape and arrangement of holes

The porosity results the dimensionless parameter that holds the most weight in the whole phenomenon in both cases of confined and unconfined flow. Thus, it is necessary to maintain the same porosity level passing from model to prototype as expressed by the formula:

$$\begin{gathered}\left(\varepsilon\right)^{(p)} = \left(\varepsilon\right)^{(m)} \\ \varepsilon_p = \varepsilon_m\end{gathered} \tag{6.12}$$

The role of the shape of the holes is negligible because both loss (K) and drag (C_D) coefficient remain constant for different shape and position of holes. This aspect is a fundamental part of the phenomenon since it proves the completely independence of the problem on the shape and position of holes. It also emphasizes that the porous level, that has to be kept unchanged from prototype to model, can be reached with any shape and arrangement of the holes.

6.7.1.2 t/D_h ratio

The t/D_h ratio is the parameter that controls the flow behaviour inside the holes. In fact it is able to define and to delimit the various types of flow regime that can develop inside the holes. Thus, when passing from prototype to model in order not to change the wake flow regime, it is important to conserve the same t/D_h ratio:

$$\begin{gathered}\left(\frac{t}{D_h}\right)^{(p)} = \left(\frac{t}{D_h}\right)^{(m)} \\ \frac{t_p}{(D_h)_p} = \frac{t_m}{(D_h)_m}\end{gathered} \tag{6.13}$$

6.7.1.3 Reynolds number effects

In order to correctly reproduce the viscous and inertial effects due to the air flow through the porous structures it would be necessary to maintain the Reynolds similitude ($Re_p = Re_m$). Usually it is quite difficult to respect this strict condition, then it is necessary to resort to incomplete similitude and operate extrapolations, between the prototype and model, only for the zone where the Reynolds effects are not present. Therefore to avoid Reynolds effects and to maintain a sort of Reynolds similitude between the prototype and model, it is necessary to consider the following:

Performing tests at $Re \geq Re_{crit}$

where Re_{crit} is the limit threshold for the Reynolds number that insures perfect independence between motion and Reynolds number.

In this work, as already shown in §6.6.5.2, two different definitions of the Reynolds number are given. The first Reynolds number (Re_L) is related to the macro-porous scale of the material; in fact it is defined in function of the air flow inside the porous core and the geometric characteristics of the pore. The second Reynolds number (Re_H) uses a predominant dimension of the structure (in this case the height of the windbreak) as characteristic length and its takes into account the role played by inertial forces to viscous ones for the overall dimensions of the body.

Considering the case of the typical structures of civil engineering it is more appropriate to work with a definition of Reynolds number based on a characteristic dimension of the structure rather than a Reynolds definition at porous scale. In fact, as highlighted in §6.6.4 and §6.6.5, the principal aerodynamic effects are mainly imputable to the external shape of the structures and not to porous part. In addition, for flow around a bluff body, it is almost impossible to formulate a Reynolds number definition at macro-porous scale due to the inability to determine the wind speed inside the holes. Therefore a more suitable definition of the Reynolds number can be written as follows:

$$Re = \frac{U_\infty \cdot \ell}{\nu} \tag{6.14}$$

where: U_∞ is the undisturbed flow velocity; ℓ is a characteristic dimension of the structure and ν is the kinematic viscosity of the air.

Extending this reasoning to the case of 2D porous windbreak subjected to the same fluid flow configuration explained in this chapter, and considering the critical value found for Reynolds number ($Re_{crit} = 200,000$), the prescription for Reynolds can be modified as:

Performing tests at $Re_H \geq 200,000$

This prescription should be evaluated carefully for each case in exam (porous tower, bridge and windbreaks, permeable façade) by some opportune tests in wind tunnel in order to find the critical value of Reynolds number that insures perfect independence between motion and Reynolds number. In this manner the influence of Reynolds number effects can be evaluated separately on the system under analysis through focused tests with the aim to pinpoint the dependence of motion from Reynolds number.

Chapter 7

WT tests on van and windbreak

7.1 Introduction

In Chapter 6 special attention has been paid to the study of flow field around an unconfined porous medium. This flow configuration well represents the flow condition which a two dimensional windbreak is subject to. In that series of experiments it has been possible to evaluate the behaviour of the screen respect to the air flow and to quantify the aerodynamic forces acting on the screen in correspondence of different porosity levels.

The principal aim of this section is the evaluation of the flow field downstream the barrier, in order to estimate the aerodynamic forces acting on an object positioned in the wake of the windbreak. Usually the windbreaks are positioned on important infrastructures like highways, bridges, viaducts, etc., in order to reduce the wind action on the users. The major problem for these structures is related to the risk of vehicle overturning, that causes a lot of accidents and fatalities every year. Considering that the vehicles more susceptible to roll-over problems during high cross-winds are vans, lorries and trucks (as said in Chapter 2), it has been decided to use a Luton van as reference vehicle to quantify the aerodynamic load downstream the barrier.

The main idea is to realize a new experimental set-up able to recreate the flow conditions which a small van, located downstream a porous windbreak, is subject to. In order to do that it is necessary to know the pressure field around the Luton van and consequently the aerodynamic forces induced by the flow through a permeable barrier. The fences used in these experimental tests, are the same as in Chapter 6, and consist of rectangular perforated plates with different levels of porosity, dimension, thickness and shape of holes.

7.2 Experimental set-up

The experimental set-up recreates at geometric scale 1:20 a prototype of Luton van positioned 3 m downstream of a 4 m high windbreak. These two reference distances have been defined on the basis of the Italian code for the construction of roads (*Norme funzionali e geometriche per la costruzione delle strade - Infrastructure and Transport Ministry Decree n. 6792 of November 2001*). This particular van was

chosen since it was similar to those which typically blow over during periods of high cross-winds.

The preparation of this set-up has been a very sensitive issue because of the various constructive particulars that are involved. In fact, it was necessary to plan a particular van model that was able to measure pressures (on its surface) and aerodynamic actions (forces and moments) with a good level of accuracy. This type of set-up has the function to recreate a 2D flow condition and to contain and support the windbreaks and the van during all testing phases. A more schematic view of the set-up that has been built in CRIACIV wind tunnel is well represented in Fig. 7.1.

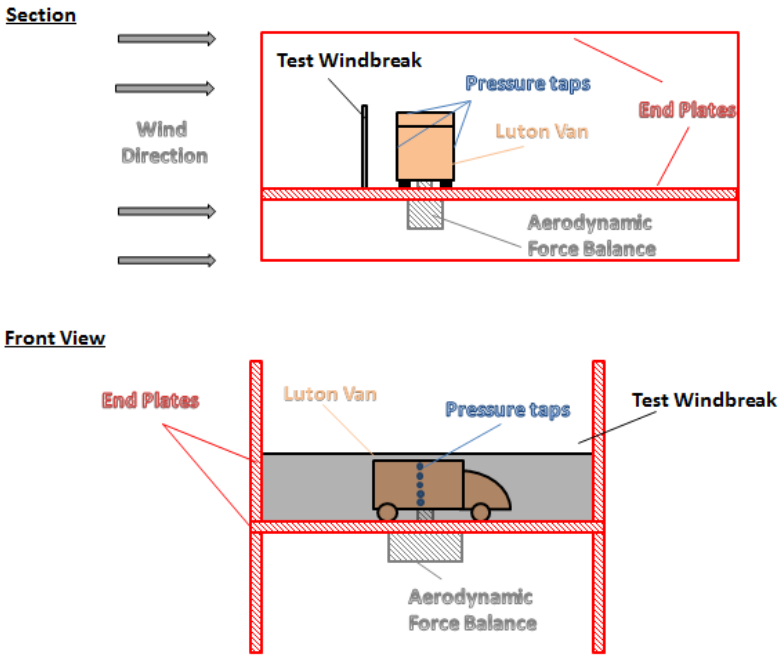

Fig. 7.1 Experimental set-up scheme; section and front view.

The air flow is channelled inside the end plates and passes above and through the windbreak samples. Downstream of the barrier is located an instrumented model of Luton van which is able to capture with high resolution the pressure and the aerodynamic loads induced by the air flow through the windbreak. The model of van is stationary and the dynamic effects due to the vehicle motion are not considered.

The experimental set-up consists of three different parts, the H-shaped end plates, the windbreak sample and the model of the Luton van. The wooden end plates designed for the windbreak tests (see Chapter 6) are able to recreate a good testing approaching flow in terms of mean wind speed profiles, of boundary layer and turbulence levels. Consequently it was decided to employ the same type of end plates but with some convenient changes. The vertical panels in plywood and the inclined wood props were not changed. In the horizontal end plate four holes were made, at a distance of 15 cm from the barrier, whose goal was to connect the model of the van to an instrumented force balance by four threaded rods (Fig. 7.2).

Fig. 7.2 Particular of the connection between the model of van and balance.

To keep fixed the windbreaks in a correct position during all tests the same stainless steel frame employed for the previous tests was used. In this case not being interested in the aerodynamic forces and moments on the barrier, measured in the previous tests, the frame was fixed rigidly to the floor of the wind tunnel, in order only to support the windbreak samples (Fig. 7.3).

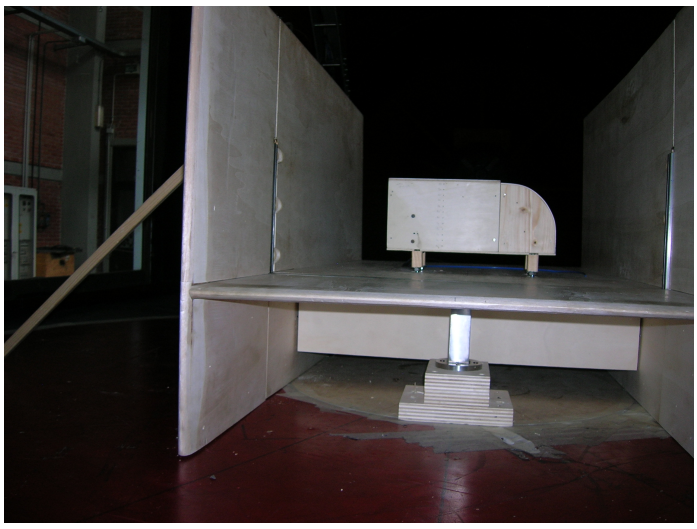

Fig. 7.3 Particular of the windbreak support.

With the purpose to expose to the flow only the porous windbreaks and not other parts of the metallic support, the external elements of the frame were properly hidden and covered inside the end plates by means of suitable slots (Fig. 7.3).

Regarding the Luton van a hollow stylized model in plywood, at the geometric scale 1:20 was designed and realized (Fig. 7.4). The WT model has been obtained taking inspiration from a typical Luton van available in Italian market (Iveco Daily

35C). In fact, the model recreates in scale a prototype 5.95 m long, 2.20 m wide and 2.60 m tall on a chassis which raises it approximately 1 m off the ground.

(a) Prototype (b) WT Model

Fig. 7.4 Luton van (Iveco Daily 35C).

The van model has been opportunely built to accommodate inside a piezoelectric transducer for the measurement of pressures and to be rigidly connected to an aerodynamic balance. The model was equipped with 31 pressure taps located in the central section of the body: 12 on the front side, 7 on the roof and 12 on the rear side of the van. The pressure taps were obtained through a micro perforation of the walls of van and the subsequent junction with small flexible Teflon tubes (Fig. 7.5).

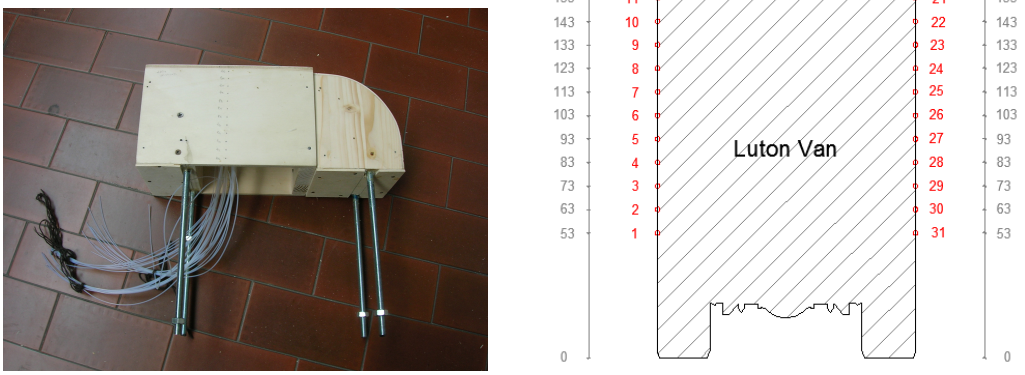

(a) Model (b) Position of pressure taps

Fig. 7.5 Pressure instrumentation of the Luton van model.

In order to ensure a stable connection between the van and the force balance the four threaded rods shown in Fig. 7.2 were blocked in correspondence of the tyres of the van by means of epoxy resin. The reproduction of the distance between the chassis and the ground (horizontal plywood panel) was insured by means of four

wooden stylized wheels. In addition the model was further lifted up of 2 mm to avoid any possible problem of friction between the model and the wooden horizontal end plate.

At this point the whole set-up has been fixed to the wind tunnel ground using six L-shaped brackets and screws in order to create a system with high stiffness. Below the H-shaped end plates a high-frequency force balance (HFB) was placed and suitably covered with appropriate boxes (Fig. 7.6). The latter had a double function: isolating the measuring equipment from possible air flows in order to guarantee an uncontaminated environment of measurement and minimizing the blockage ratio of the set-up (solid blockage ratio equal to 4 %).

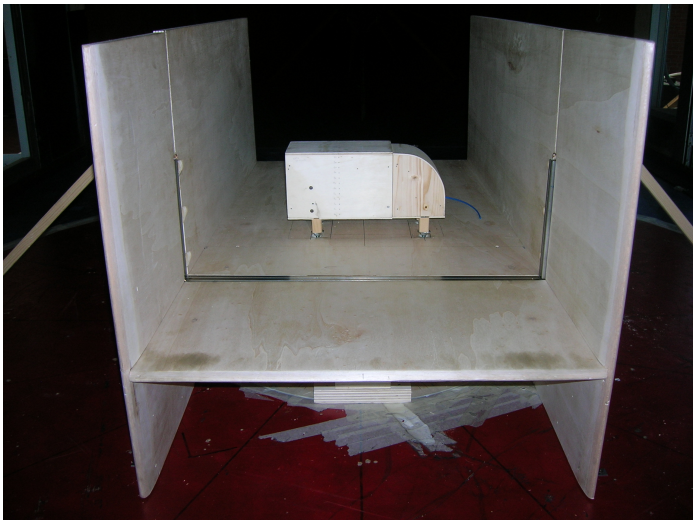

Fig. 7.6 View of the experimental set-up.

7.2.1 Instruments of measure

Before moving on the experimentation stage, it is useful to describe briefly the type of measuring equipments that have been used, in order to characterize scrupulously the levels of accuracy of measurement.

7.2.1.1 Pressure system unit (*DTC Initium*)

The pressure system that has been used consists of 31 pressure taps linked to a piezoelectric transducer (ESP). Considering the availability of a new pressure measurement equipment at CRIACIV and its high precision it was decided to use the DTC Initium system instead of the PSI 8400 unit used in §5.2.1. The DTC Initium provides a powerful economical data acquisition system for PSI DTC series of miniature ESP pressure scanners. This advanced system represents the ambition of the *Pressure Systems, Inc.* to eliminate in-situ calibration from electronic pressure scanning technology. It integrates an advanced analog circuit design with PSI innovative Digital Temperature Compensation (DTC) technology to maintain optimal accuracy without requiring on line span calibration of the pressure scanners. This progressive technology relies on a unique mounting technique to the silicon piezoresistive

pressure sensors within the DTC scanners that facilitates accurate measurement of bridge resistance for use in real-time correction of thermal errors using personalized compensation algorithms stored in an EEPROM embedded within each scanner. The result is an electronic pressure scanning system that provides state-of-the-art accuracy over the entire scanner operating temperature after only an initial re-zero. The DTC Initium directly connects any combination of up to eight 32 or 64 port DTC Series ESP scanners to provide up to 512 channels of simultaneous pressure measurements. In fact each of the eight available channels on DTC unit is able to measure simultaneously 64 pressure taps. In Fig. 7.7 is reported a picture of DTC Initium system and two ESP scanners with 32 ports.

Fig. 7.7 DTC Initium unit and ESP scanners.

Static pressures can be measured with a sampling frequency up to 1200 Hz for each PSI channel. The number of acquisition ports used are inversely proportional to the sampling frequency. For example, using 16, 32 and 64 pressure ports the maximum values of sampling frequency than can be reached for each port are respectively 1200 Hz, 650 Hz and 325 Hz. Table 7.1 reports the main technical specifications of the DTC Initium unit.

Specifications	**Values**
Number of ESP supported	8
Static Accuracy ($\geq$ 5 psid)	$\pm$ 0.05 %FS
Static Accuracy ($\geq$ 10 psid)	$\pm$ 0.10 %FS
Thermal Error ($\geq$ 5 psid)	$\pm$ 0.002 °C %FS
Thermal Error ($\geq$ 10 psid)	$\pm$ 0.001 °C %FS
A/D resolution	8 bit
Measurement resolution	$\pm$ 0.003 %FS
Operating temp. range	0 $\div$ 70 °C

Table 7.1 Characteristics of DTC Initium unit.

The pressures acting on the model's surface must be transmitted to the sensor without distortions. The pressure taps are linked to an ESP transducer through small highly flexible plastic tubes, manufactured in Teflon. In order to transmit the pressures without undergoing distortions, each transmission pipe is equipped with

a damper, which is obtained through a reduction of the pipe cross-section. This reduction consists of the insertion of cylindrical elements, made of brass or Teflon or other materials, whose outer diameter is smaller than the inner diameter of the pipe. The system constituted by tubes and dampers is properly calibrated so that its response frequency does not influence the measurements. The Fig. 7.8 shows the typical outline of a Teflon pipe equipped with a damper.

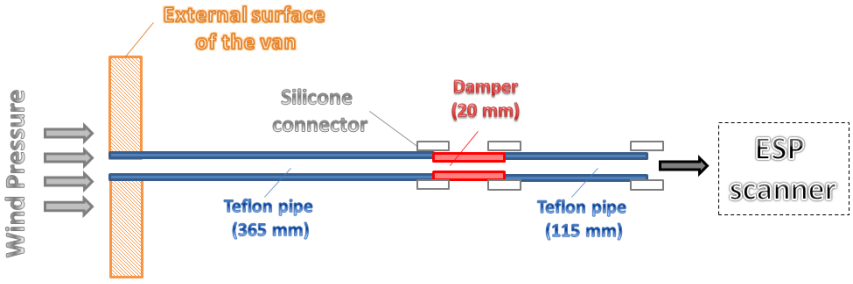

Fig. 7.8 Outline of the connection between pressure tap and ESP scanner.

Thanks to its small dimensions (13 x 21.5 x 69 mm for the sensor in use) the PSI scanner is located inside the model of the van. Using this innovative solution for the pressure measurements it is possible to reach a high level of accuracy in the range of ± 0.1 mm of water (≈ 1.0 Pa) as compared to ± 0.25 mm (≈ 2.5 Pa) offered by PSI 8400 unit.

7.2.1.2 Aerodynamic force system (*HFB*)

The aerodynamic forces and moments induced by the air motion on the Luton van were measured by means of a high frequency aerodynamic force balance (HFB). The HFB in use is the same balance that was adopted on windbreaks tests in Chapter 6 and more precisely the model FT-Delta SI-615-15 manufactured by ATI Industrial Automation. Please refer to §6.2.1.1 for the technical specifications of the instrument.

7.2.1.3 Velocity system (*Pitot tubes and hot-wire*)

The wind speed was measured by means of two Pitot-Pradtl tubes and a hot-wire anemometer. The Pitot tubes were used in the course of the measurements with the purpose of recording the wind speed during the tests. The hot-wire anemometer was employed to measure the turbulence intensity and the boundary layer thickness inside the wooden end plates. Please refer to §5.2.1.3 for the technical details of these devices.

7.2.2 Characteristics of the porous windbreaks

The windbreaks positioned upstream of the van are the same models that were used in the tests described in Chapter 6. In fact, due to their geometrical dimension (0.20 m x 0.60 m) they were able to represent at a scale 1:20 different porous fences.

The barriers had a porosity level from 22.68 % to 69.40 % obtained with different dimensions, thickness and shapes of the holes. To investigate the complete range of porosity ($\varepsilon = 0 \div 100$), two configurations were analysed: one including a completely solid barrier ($\varepsilon = 0$ %) and the opposite case without barrier ($\varepsilon = 100$ %).

Table 7.2 briefly reports the main characteristics of the windbreaks that were used in these experimental tests.

Model	**Porosity %** (ε)	**Thickness [mm]**	D_h**[mm]**	**Shape**
Full	00.00			
R1.5T3	22.68	1.5	1.5	Round
R3T5	32.65	1.0	3.0	Round
R10U15	34.88	1.5	10.0	Round
C3U5	36.00	1.0	3.0	Square
C5U8	39.06	1.0	5.0	Square
R2T3	40.31	1.0	2.0	Round
R4T6	40.31	1.0	4.0	Round
R6T9	40.31	1.0	6.0	Round
R8T12	40.31	1.0	8.0	Round
R10T15	40.31	1.0	10.0	Round
LR5x20	43.81	1.0	8.5	Oblong
C10U15	44.40	1.0	10.0	Square
R10U14	44.40	1.0	10.0	Round
C6U9	44.44	1.0	7.0	Square
C8U12	44.44	1.0	8.0	Square
Nr.152	45.00	1.0	6.0	Cross
R5T7	46.28	1.0	5.0	Round
R10T14	46.28	1.0	10.0	Round
C8U10	64.00	1.0	8.0	Square
H2T90	64.00	1.0	2.0	Hexagonal
C10U12	69.40	1.5	10.0	Square
Empty	100.00			

Table 7.2 Windbreak features.

The solid barrier (*Full*) represents the maximum case of shelter effect that can be reached and gives also an idea of the wake downstream of a solid object. The empty case represents the opposite condition where the van is subject to maximum wind action and then to null shelter effect. For this particular set-up, tests have been completed on 23 windbreak samples at different wind velocities and with air flowing normal to the fence without any angle of inclination (Fig. 7.9). With the aim to evaluate the effects of the porosity, sixteen samples of windbreak were tested in CRIACIV BLWT and differed each other for porosity level, diameter, thickness and shapes of holes. To study the role of the shape two additional samples with different shape of the holes (*round and square*) but same hydraulic diameter, thickness and porosity were analysed. The influence of the t/D_h ratio was studied on five additional samples having the above mentioned ratio in the range ($0.1 \div 0.5$).

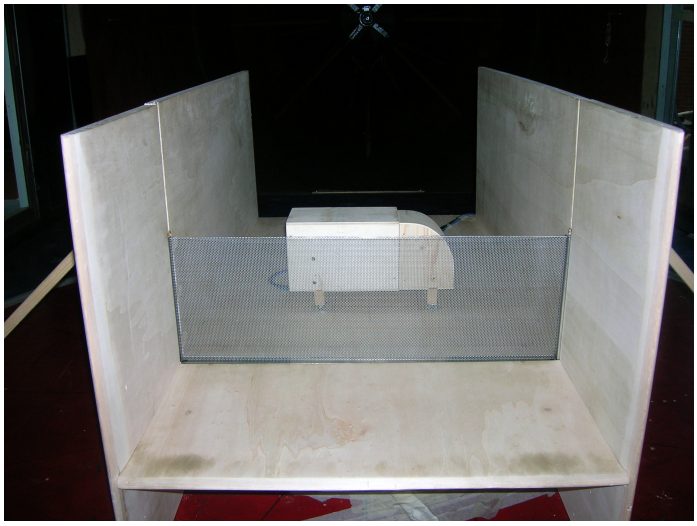

Fig. 7.9 Windbreak sample (model H2T90, $\varepsilon = 64.00\%$) and Luton van.

7.3 Study of the flow inside the end-plates

The study of flow inside the end plates was discussed in §6.3. Therein in correspondence of the windbreak section, the related vertical and horizontal mean wind speed profiles, the intensity of turbulence and the estimation of the boundary layer thickness on the walls of the end plates were reported. Since the wooden end plates have never been moved or modified from the test chamber of the wind tunnel, during the introduction of the model of the Luton van, the characterization of the flow inside the end-plates reported in §6.3 can be considered applicable also to the presents tests.

7.4 Experimental measurements

Using the new set-up it is possible to have a general idea of the flow characteristics that develops downstream of a porous windbreak. The aim of the tests was to measure the pressure pattern around a model of the van positioned downstream the barrier and the corresponding aerodynamic forces and moments. As for the case of windbreaks, also here the tests were conducted with wind flowing in both directions through the barrier samples in order to account for some possible asymmetries in the windbreak structure. Each of the 23 samples were tested in correspondence of eight different wind speed values. The HFB balance recorded data for 66 seconds at a sampling frequency of 2000 Hz, while the DTC Initium unit acquired pressure signals for 60 seconds with a sampling frequency of 650 Hz. The flow velocity was monitored by two Pitot tubes that acquired data for 66 seconds at sampling frequency of 2000 Hz. None of the samples tested exhibited any signs of dirt accumulation or structural failure before or after the experimental tests.

In function of the reference measuring instruments the Table 7.3 reports the principal parameters that were measured during the tests.

Quantity	Unit	Instrument
V_{mean}	$[m/s]$	Pitot BLWT
V_{std}	$[m/s]$	Pitot BLWT
u_{mean}	$[m/s]$	Pitot Up-wind
u_{std}	$[m/s]$	Pitot Up-wind
$F_{(x,y,z),mean}$	$[N]$	HFB
$F_{(x,y,z),std}$	$[N]$	HFB
$T_{(x,y,z),mean}$	$[Nm]$	HFB
$T_{(x,y,z),std}$	$[Nm]$	HFB
$Pressure_{mean}$	$[mm_{H_2O}]$	Pressure taps PSI
$Pressure_{std}$	$[mm_{H_2O}]$	Pressure taps PSI

Table 7.3 Quantities measured in wind tunnel.

The wind speed was measured by means of two Pitot tubes located in two fixed points on the testing chamber. The first Pitot tube was positioned in an external zone respect to the set-up and had the aim to measure the reference air flow in wind tunnel in terms of mean wind speed $[V_{mean}]$ and standard deviation $[V_{std}]$. The second Pitot tube was collocated upstream of the end-plates (placed at a distance of 70 cm), and was able to record the mean and standard deviation of the undisturbed wind speed approaching the set-up $[u_{mean}; u_{std}]$. Converting the six digital signals given by the aerodynamic balance (HBF) with the use of calibration matrix (K), it was possible to obtain the mean and the relative standard deviation of the aerodynamic forces $F_{(x,y,z),mean}; F_{(x,y,z),std}]$ and torques $[T_{(x,y,z),mean}; T_{(x,y,z),std}]$. The pressure pattern around the body of the van was measured by the use of 31 pressure taps, positioned on the windward side, on the roof of the van and on the leeward side, and for each pressure tap it was possible to get mean and standard deviation of the pressure signal $[Pressure_{mean}; Pressure_{std}]$. Fig. 7.10 reports two characteristic pictures of the measurement phase; in particular a photograph of DTC Initium unit and a view of the PC monitor during the recording process are shown.

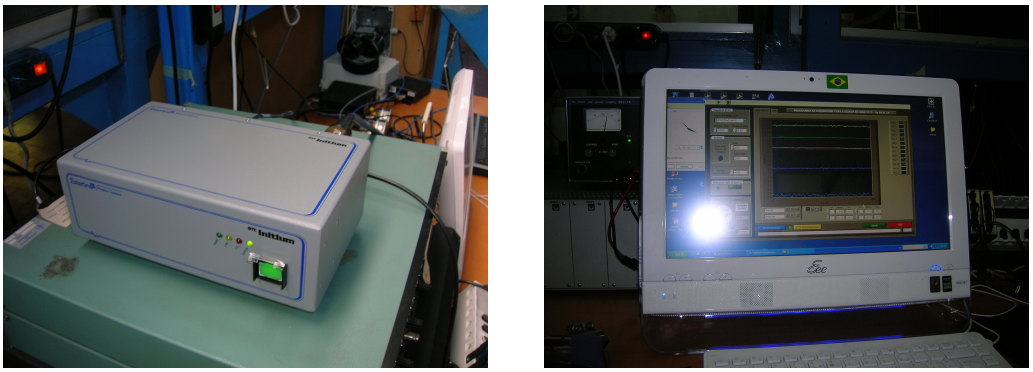

(a) DTC Initium unit (b) Signal acquisition on PC

Fig. 7.10 Particular of measurement phase.

For each typology of barrier sample, three fundamental graphs have been created. The first one reports the pressure pattern around the van expressed by means of pressure coefficients. The second graph presents the relationship between the aerodynamic loads and the reference wind speed. The third one shows the Reynolds number influence on the aerodynamic drag and moment coefficients.

7.5 Experimental results

The analysis of the experimental data is divided in two parts, the first one is related to the elaboration of the pressure data acquired by the DTC Initium unit and the second refers to the aerodynamic forces and moments measured through the HFB system.

7.5.1 Pressure data

When dealing with fluid dynamics measurements, in order to isolate every possible dependence between the measured quantities, it is common practice to recover to the use of dimensionless coefficients. In this case the measured quantities are the pressures on the surface of a rigid van model, and the related non-dimensional parameter is the pressure coefficient. This is usually expressed as follows:

$$C_p = \frac{p - p_\infty}{\frac{1}{2} \cdot \rho \cdot u_\infty^2} \tag{7.1}$$

where: p is the pressure value measured in correspondence of each pressure tap; ρ is density of the air; p_∞ and u_∞ are respectively the undisturbed pressure and the wind speed. The undisturbed velocity (u_∞) is represented by the wind speed measured upstream of the barrier by means of the Pitot tube.

As a consequence, in the flow field around a body there are points having positive pressure coefficients up to one, and negative pressure coefficients including coefficients less than minus one. Therefore, pressure coefficients equal to zero show that the pressure is the same as the free stream pressure; values of C_p equal to 1 indicate that the pressure is stagnation pressure and the point is a stagnation point; and in the regions where the flow velocity is greater than u_∞, the pressure coefficients are negative.

In order to have an immediate graphical visualization of the pressure coefficient trend around the body of the van, the C_p data are superimposed on the van outline. The positive and negative values of C_p are identified respectively by the red colour and by the blue one. For each one of the 23 samples of barrier an opportune graph similar to Fig. 7.11 has been built for each of the eight testing wind speed values. Here two graphs are presented that report the mean pressure coefficient distribution around the van for two extreme cases of shelter effect, the case with solid fence (Fig. 7.11a) and the case without the barrier (Fig. 7.11b). The C_p data reported in these graphs are calculated in correspondence of the maximum testing wind speed.

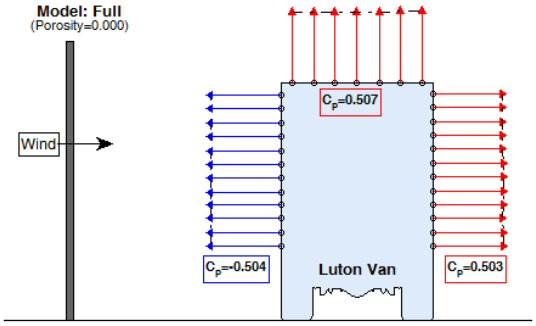

(a) Solid barrier, $\varepsilon = 0.00$ %

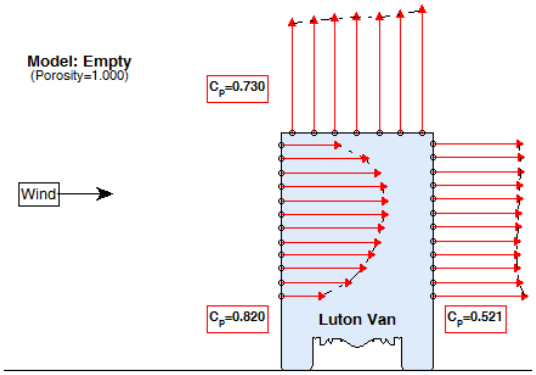

(b) No barrier, $\varepsilon = 100.00$ %

Fig. 7.11 C_p distribution around the Luton van in the two extreme cases of solid barrier and no barrier.

In case of solid windbreak, the face of the van directly exposed to the wind offers constant negative values of C_p with an average equal to -0.504, while in the case without the screen the trend is non-linear with a mean positive C_p of 0.820. From this graph it is possible to give immediately a first idea of the effect played by the barrier. In fact, if a solid barrier is present, a recirculation zone characterized by a strong depression develops on the windward face of the van. This zone is imputable to the flow separation that occurs at the top of the barrier similarly to a bluff-body flow. Otherwise the van is directly subject to the positive pressure exercised by the wind action without any modification of the approaching air flow.

Using the pressures measured upwind and downwind of the van it is possible to have an indication of the drag force that the air flow induces on the model of the van. In fact the drag force (D^p), excluding the friction drag contribution, can be easily obtained from the pressure data by integration:

$$\begin{aligned} D^p &= \int p_{front} dA - \int p_{rear} dA \\ D^p &= \int (p_{front} - p_{rear}) dA \end{aligned} \tag{7.2}$$

where: p_{front} and p_{rear} are respectively the pressure pattern on the windward and leeward face of the van and dA is the infinitesimal area of integration. The difference p_{front} - p_{rear} represents the net pressure (p_n) that contributes to create the drag force on the model of Luton van. Fig. 7.12 reports the pattern of the net pressure for one sample tested, in correspondence of eight different wind speed values. The distributions of pressure present, with respect to the height of the van (expressed by the z-coordinate), a non-linear behaviour with a common maximum value for z equal to 80 mm.

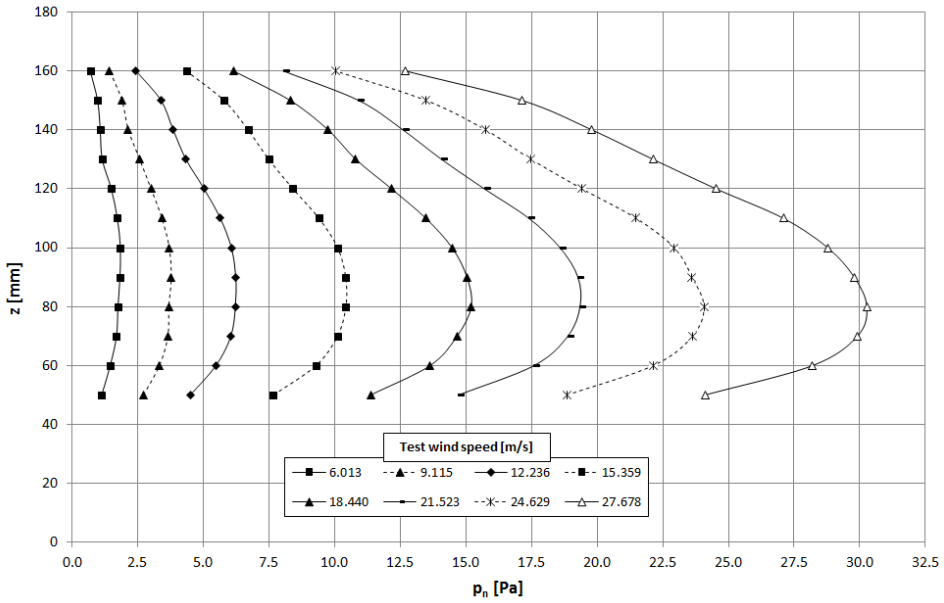

Fig. 7.12 Net pressure for the barrier R1.5T3 (ε=22.68 %, D_h=1.5 mm and t=1.5 mm).

The pressure integration in equation (7.2) has a two-fold purpose: to make the data comparable with drag forces measured with the HFB and to understand what is the error made if the drag force is evaluated using the pressure data. Consequently, for each sample of windbreak tested it has been possible to define a drag coefficient (C_D^p) of the van defined through the pressure data as:

$$C_D^p = \frac{D^p}{\frac{1}{2} \cdot \rho \cdot u_\infty^2 \cdot A} \tag{7.3}$$

where: D^p is the drag force calculated by integration of the pressure data; u_∞ is the undisturbed wind speed and A is the front area of the van directly invested by the wind.

7.5.2 Aerodynamic data

As regards the data obtained from the aerodynamic balance, as already seen in the case of tests on the wind barriers (*Chapter 6*), it is necessary to combine the various components of forces and torques in order to obtain global forces and moments acting

on the model. Since the reference system of the HFB was identical to the one used for tests on barriers, the same method of vectorial composition (explained in §6.5) was applied. Fig. 7.13 reports a schematic view of all the aerodynamic components of forces and moments which the van is subject to (*Drag, Lift, Z-Torque and Moment*).

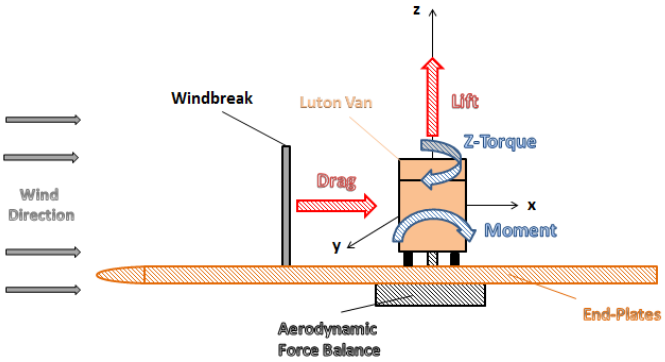

Fig. 7.13 Forces and moments acting on the Luton van model.

The actions that have been considered in the elaboration are the drag and the moment around the y-axis. The lift force and z-torque have been omitted from the process because they had a small weight with respect to the others and were comparable with the errors made by instrument of measure. Consequently, this aspect highlights that the set-up is able to recreate almost perfectly a 2D flow model.

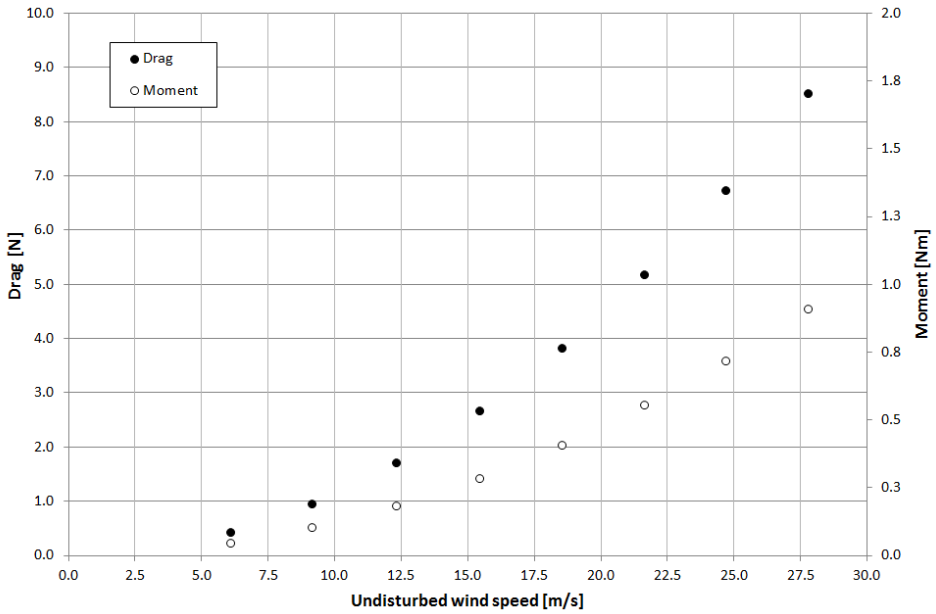

Fig. 7.14 Measured drag force and moment on the van vs. undisturbed wind speed for the barrier H2T90 (ε=64.00 %, D_h=2 mm and t=1 mm).

Fig. 7.14 reports the drag force and the moment induced on Luton van by the presence of the fence H2T90 for different values of undisturbed wind speed (u_∞).

As expected the drag force and moment show a quadratic relationship with respect to the undisturbed wind speed. Knowing the principal aerodynamic actions on the van it is possible to express dimensionless relationship of force and moment through the respective dimensionless coefficients of drag ($C_{D,van}$) and moment ($C_{M,van}$), as follows:

$$C_{D,van} = \frac{D}{\frac{1}{2} \cdot \rho \cdot u_{\infty}^2 \cdot A} \tag{7.4}$$

$$C_{M,van} = \frac{M}{\frac{1}{2} \cdot \rho \cdot u_{\infty}^2 \cdot A \cdot H_{van}} \tag{7.5}$$

where: D and M are respectively the drag and the moment measured by the high frequency force balance (HFB) on the van; A is the area of the van exposed to the wind and H_{van} is the height of the van.

The fundamental parameter which provides a dimensionless representation of the velocity is the Reynolds number. In order to operate direct comparison with the windbreaks data (*Chapter 6*) also for these series of tests the reference Reynolds number is based on the height of the barrier, and it is defined as:

$$Re_H = \frac{u_{\infty} \cdot H}{\nu} \tag{7.6}$$

where: H is the height of the barrier, fixed equal to 0.2 m, and ν is the kinematic viscosity of the air.

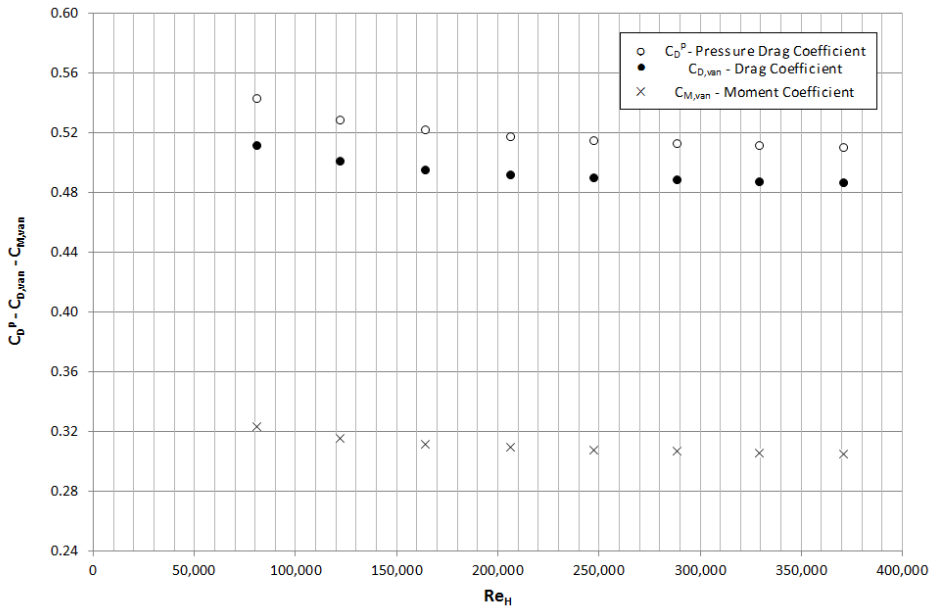

Fig. 7.15 C_D^p, $C_{D,van}$ and $C_{M,van}$ vs. Re_H for barrier H2T90 (ε=64.00 %, D_h=2 mm and t=1 mm).

Fig. 7.15 reports the relationship between drag and moment coefficients ($C_{D,van}$ and $C_{M,van}$) versus the Reynolds number (Re_H). The graph reports also the drag

coefficient obtained from the pressure data (C_D^p) and defined by the equation (7.3). Fig. 7.15 confirms the presence of viscous effects in a confined region of motion defined for Re_H in the range 80,000 ÷ 200,000. Exceeded the critical value of 200,000, the values of the aerodynamic coefficients do not depend on Reynolds number. The drag coefficient obtained by pressure measure (C_D^p) appears to be overestimated compared to the drag coefficient measured by the HFB. More in detail it is larger by about 6 % for $Re_H < 200{,}000$ and by 3 % for $Re_H \geq 200{,}000$. For all windbreak samples tested the C_D^p coefficients are always larger than the drag coefficients measured by HFB. This effect is mostly attributable to the 3D effects that develop around the model of the van which cannot be considered with the number and the position of the pressure taps that are installed on the model. In addition to the three-dimensional aspects of the model must be considered also the effects due to friction drag which cannot be accounted with the pressure taps.

Another important dimensionless parameter that is useful to define is the ratio b/H of the point of application of the drag force (b) to the height of the van (H_{van}). Knowing the moment (M) and the drag force (D) on the van, the point of application can be simply obtained [$b = M/D$]. Fig. 7.16 reports the drag coefficient of the van and the ratio b/H versus the Reynolds number for the windbreak sample H2T90. The graph confirms that there exists a dependency of $C_{D,van}$ on the Reynolds number in the range $80{,}000 < Re_H < 200{,}000$.

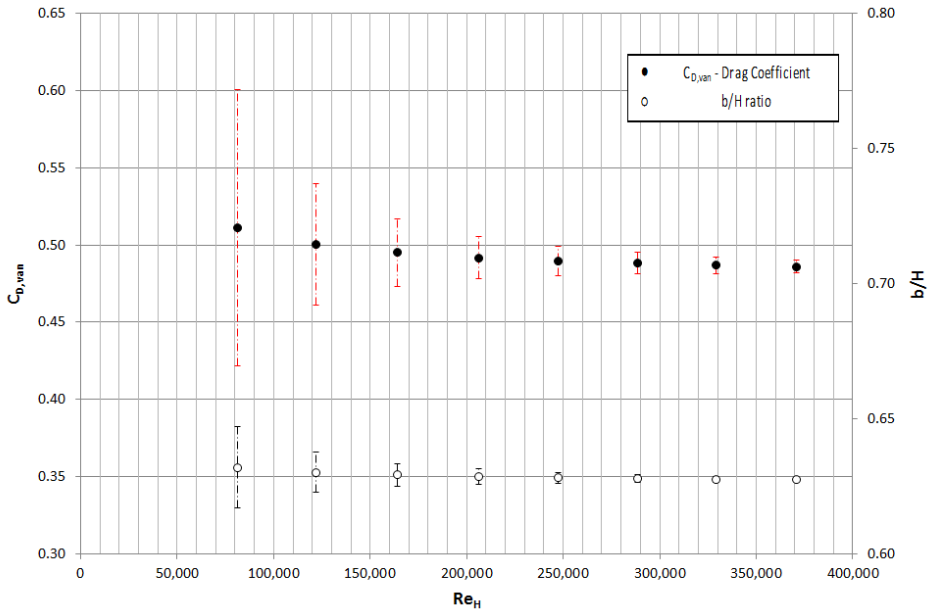

Fig. 7.16 $C_{D,van}$ and b/H ratio for the barrier H2T90 (ε=64.00 %, D_h=2 mm and t=1 mm).

Due to the uncertainty of the measurements in Fig. 7.16 are reported the errors bars in correspondence of each variable plotted. More in detail, the error bars have been determined introducing the full scale error of the HFB in correspondence of each component of force and moment. The red bars represent the errors made by the aerodynamic balance during the measure of the drag force and the black bars describe

the errors in the estimation of the b/H ratio. The first points of measurement are affected by an error of approximately 15 % and for the last ones it is less than 1%. This behaviour is imputable to low values of force and moment that are recorded by HFB at low wind speed.

The trend of the b/H ratio highlights that the point of application of the drag force, then the aerodynamic centre of the van, is situated at the 62.5 % of the height of the van.

7.6 Analysis of the data

In this part the more salient results of this set of measurements will be reported and commented. The principal parameters that are used to characterize the behaviour of the wake of the windbreak are the pressure coefficient on the van surface (C_p), the aerodynamic coefficients of the van ($C_{D,van}$ and $C_{M,van}$) and the b/H ratio. The drag coefficient (C_D^p) coming from the pressure data in this analysis will not be used because it is only an overestimation of drag measured by HFB and consequently it is appropriate the use of the $C_{D,van}$ coefficient only.

The discussion of the results, as done in Chapters 5 and 6, will be distinguished on the basis of various factors that are capable of influencing the reference dimensionless parameters. In particular, the effects of porosity level and Reynolds number, diameter, thickness and shape of the holes will be carefully analysed.

7.6.1 Effect of porosity level and Reynolds number

Being the porosity level the key parameter of the whole process two different approaches will be followed, a qualitative and more intuitive one, and a purely theoretical one. The first method consists in an accurate graphical evaluation of the pressure patterns around the van that were obtained for different porosity levels. The mean pressure coefficients on the surface of the van (calculated in correspondence to the maximum testing wind speed) are collected to recreate a sort of video. Fig. 7.17 shows all the frames obtained for the tests carried out on the 23 windbreak samples.

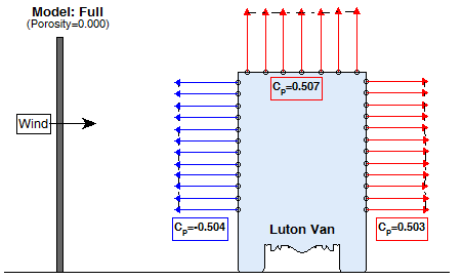

(a) Solid barrier, $\varepsilon = 0.00$ %

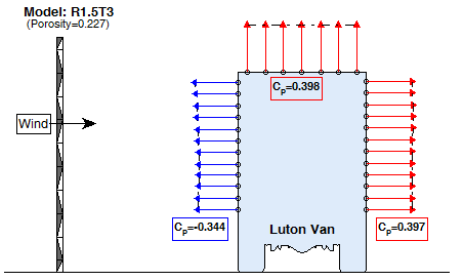

(b) R1.5T3, $\varepsilon = 22.68$ %

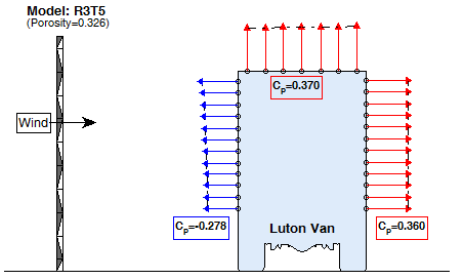

(c) R3T5, $\varepsilon = 32.65$ %

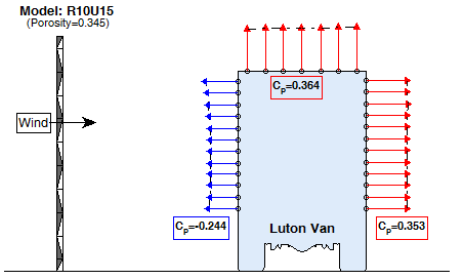

(d) R10U15, $\varepsilon = 34.88$ %

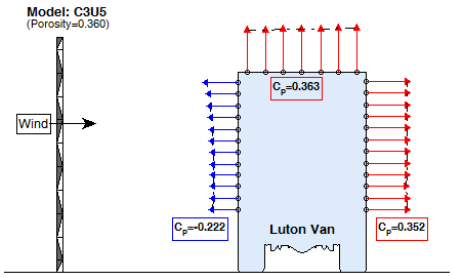

(e) C3U5, $\varepsilon = 36.00$ %

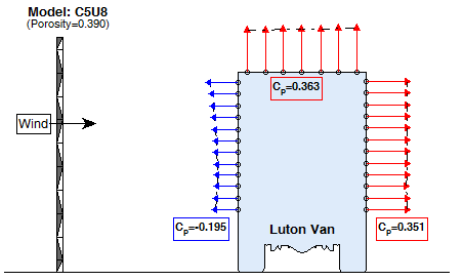

(f) C5U8, $\varepsilon = 39.06$ %

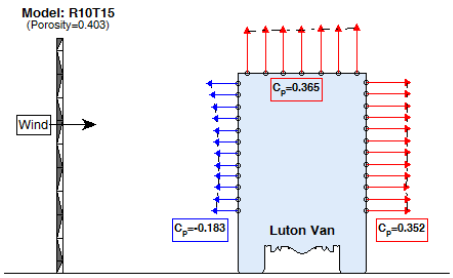

(g) R10T15, $\varepsilon = 40.31$ %

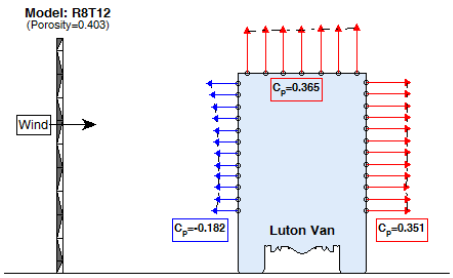

(h) R8T12, $\varepsilon = 40.31$ %

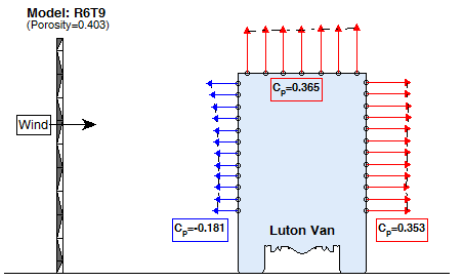

(i) R6T9, $\varepsilon = 40.31$ %

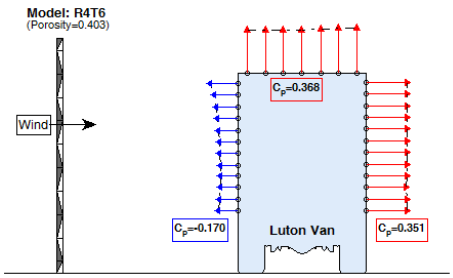

(j) R4T6, $\varepsilon = 40.31$ %

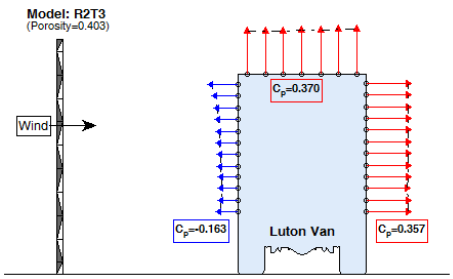

(k) R2T3, $\varepsilon = 40.31$ %

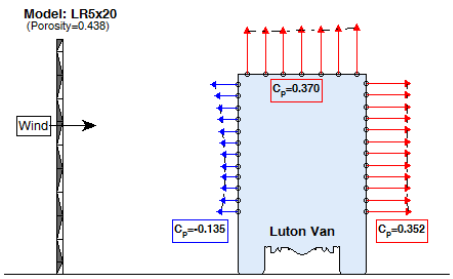

(l) LR5x20, $\varepsilon = 43.81$ %

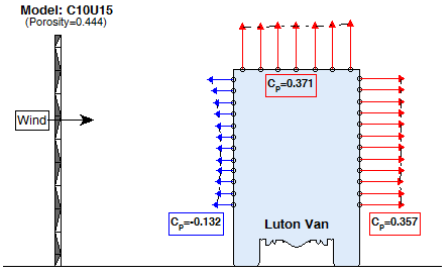

(m) C10U15, $\varepsilon = 44.40$ %

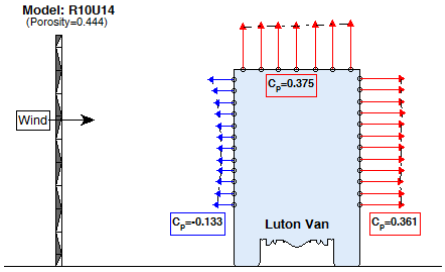

(n) R10U14, $\varepsilon = 44.40$ %

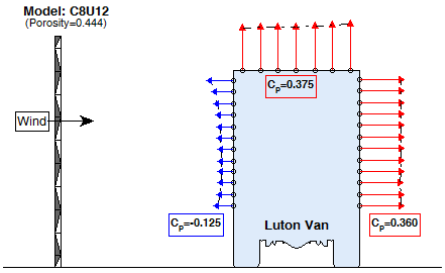

(o) C8U12, $\varepsilon = 44.44$ %

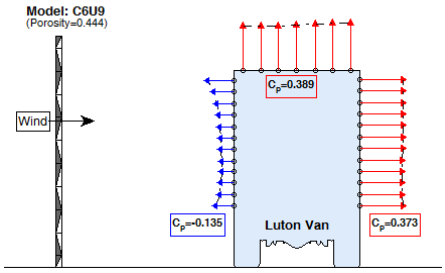

(p) C6U9, $\varepsilon = 44.44$ %

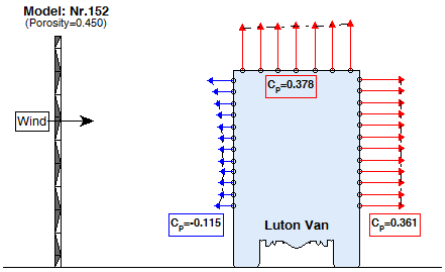

(q) Nr.152, $\varepsilon = 45.00$ %

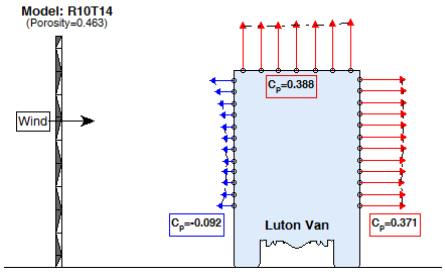

(r) R10T14, $\varepsilon = 46.28$ %

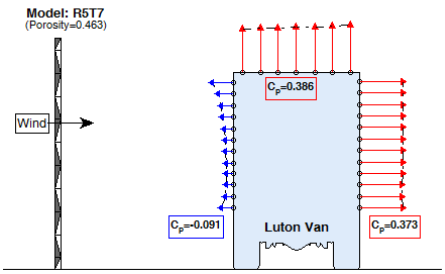

(s) R5T7, $\varepsilon = 46.28$ %

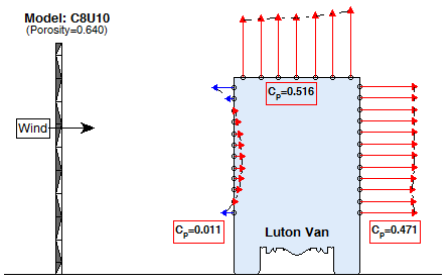

(t) C8U10, $\varepsilon = 64.00$ %

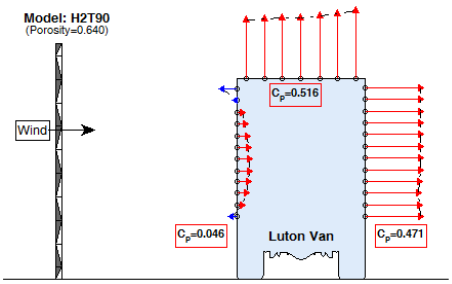

(u) H2T90, $\varepsilon = 64.00$ %

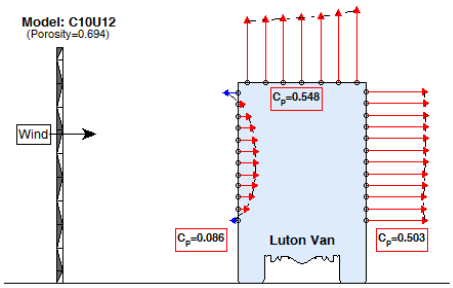

(v) C10U12, $\varepsilon = 69.40$ %

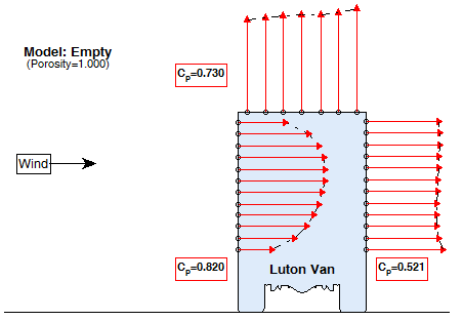

(w) No barrier, $\varepsilon = 100.00$ %

Fig. 7.17 Mean C_p distribution and porosity level (ε).

Fig. 7.17 reports for the 23 samples of barrier the effects of porosity level on the mean distribution of C_p around the Luton van. Considering the pictures from Fig. 7.17b to Fig. 7.17v it can be stated that the C_p patterns in the leeward side of the van are not strongly affected by the porosity that remains almost regular for the entire range of porosity analysed. This aspect is attributable to flow separation that occurs at the top of the barrier, creating large area with high vorticity, called by Plate (1971) *eddy zone*, where the van is contained. By contrast, increasing the porosity of the windbreak, the C_p values registered in the upward face of the van show behaviours totally dissimilar in correspondence of the various levels of porosity. In fact, the C_p data pass from negative to positive values, with different patterns ranging from constant to non-linear. As regards the roof of the van, with the exception of the solid barrier and the condition without the fence, the pressure coefficients remain almost the same in terms of trend (linear) and mean values. Thus, it is emphasized that the pressure component that mainly controls the variation of drag force is the frontal pressure pattern. Concerning the role of the porosity of the barrier it is possible to state that the barrier tends to create a wide sheltered area downstream that is characterized by a strong decrease of pressure. This pressure decrement can become a real depression for ε in the range $0 \div 46.28$ % and a sharp reduction of wind pressure for porosity between the 64.00 % and the 69.40 %. The flow field downstream of the porous barrier is mainly regulated by the interaction of two different phenomena. The first one, governed by the porosity level, is due to air moving through the porous windbreak, and the second one, responsible of the depression zone downstream of the barrier, is imputable to a flow separation that occurs in the upper part of the fence, similarly to a bluff-body flow. The interaction between these two aspects can be easily visualized observing the C_p patterns. In fact, in case of solid windbreak ($\varepsilon = 0$) the huge depression downstream of the screen is entirely attributable to the flow separation. Increasing the level of porosity, it can be noticed that the suction on the windward side begins to reduce due to the presence of flow through the barrier. For further increase of the porosity level, the suction zone disappears and the flow through the porous medium becomes the relevant characteristic.

In order to quantify the problem in purely theoretical terms it is necessary to recover to the second approach, where an analytical treatment of the data occurs.

Fig. 7.18 reports for all the windbreak samples the relationship between the drag coefficient of the van ($C_{D,van}$) and the Reynolds number (Re_H). At first sight it is possible to notice that there is a strong dependence on porosity level because the drag coefficients vary with porosity in the range $0.03 \div 1.25$.

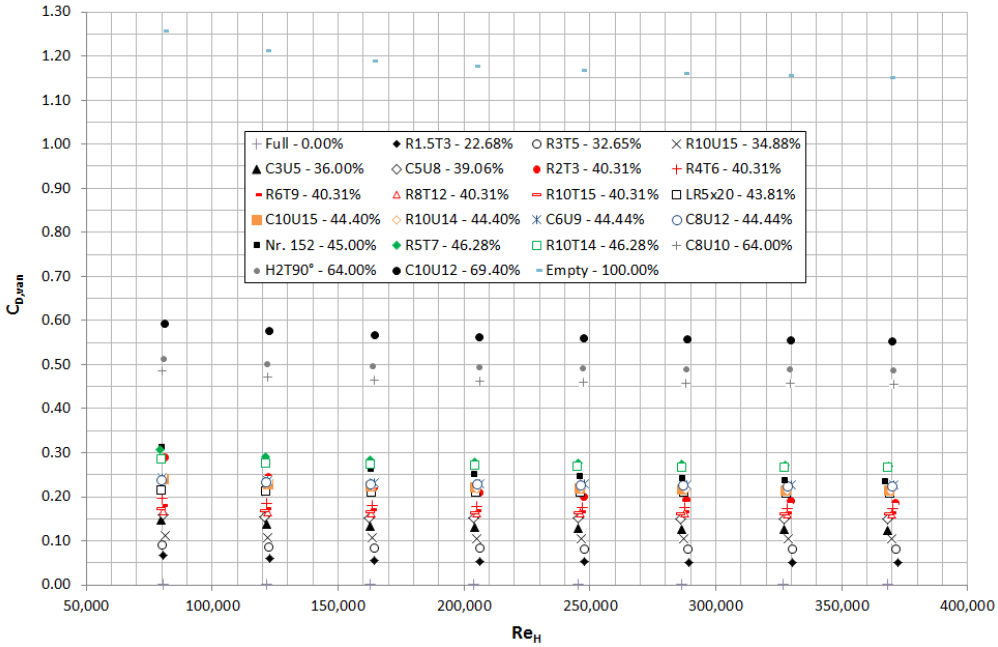

Fig. 7.18 $C_{D,van}$ vs. Re_H for all the windbreak samples tested.

As expected the maximum values of the drag coefficient are found for high values of porosity level and vice versa. Consequently barriers with low porosity offer a higher flow resistance and hence a lower aerodynamic load induced on the van. Also in this case to evaluate the dependency of drag and moment coefficients on porosity level it is possible to employ a typical procedure that is used in porous media analyses [Pinker and Herbert (1967); Brundrett (1993); Valli *et al.* (2009)]. The procedure consists in separating each aerodynamic coefficient through two functions, one depending only on porosity (ε) and the other one depending only on Reynolds number (Re_H). Here the procedure of decomposition is applied only to drag coefficient, but it can be also applied to moment coefficient and to b/H ratio in the same way, following the formula:

$$C_{D,van}(\varepsilon, Re_H) = G''(\varepsilon) \cdot F''(Re_H) \tag{7.7}$$

where:
$G''(\varepsilon)$ is a function of porosity level;
$F''(Re_H)$ is a function of Reynolds number.

Considering only the $C_{D,van}$ mean values that are independent from Reynolds number (in this case the average of last two points of each $C_{D,van}$ - Re_{van} diagram,

reported in Fig. 7.18) for each kind of windbreak samples, it was possible to obtain the analytic expression of $G''(\varepsilon)$ by a simple fitting of the data.

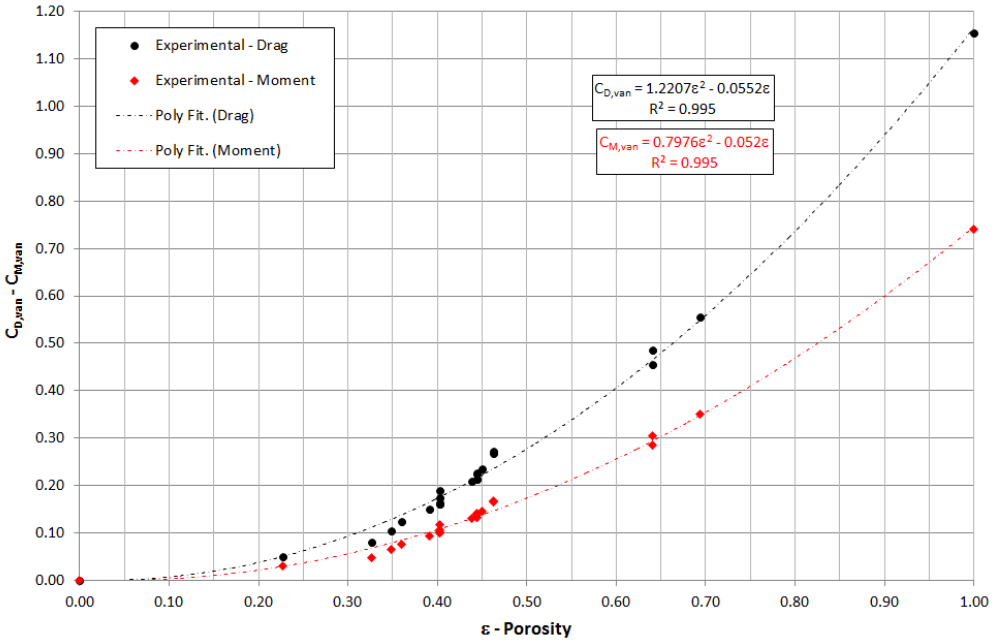

Fig. 7.19 $G''(\varepsilon)$ fitting function.

Fitting the black points of Fig. 7.19, the $G''(\varepsilon)$ function has been calculated and the best fitting is well represented by a polynomial function in the form:

$$G''(\varepsilon) = 1.2207\varepsilon^2 + 0.0552\varepsilon \tag{7.8}$$

$$\textbf{with: } R^2 = 0.995$$

Fig. 7.19 expresses in a more immediate way the dependence on porosity of the aerodynamic coefficients of the van. The $G''(\varepsilon)$ estimated is compatible with the physical limits of the problem, as $G''(\varepsilon) \to 0$ when $\varepsilon \to 0$, in the case of solid windbreak. In fact, in this condition the van is not directly subject to any wind actions. Vice versa $G''(\varepsilon) \to 1.15$ as $\varepsilon \to 1$ and represents the condition which the van would be subject to, when no shielding is adopted. In fact, a similar value ($C_{D,van}$ =1.1) is found in literature by Sterling *et al.* (2010) as a reference value for side drag force coefficient of Luton van.

The effects of Reynolds number and the relative zone of dependence or independence can be evaluated by equation (7.7), solving for $F''(Re_H)$:

$$F''(Re_H) = \frac{C_{D,van}(\varepsilon, Re_H)}{G''(\varepsilon)} \tag{7.9}$$

Using the equation above for all the data reported in Fig. 7.18, it is possible to remove the dependency of porosity and evaluate more accurately the Reynolds number

effects. From Fig. 7.19 it can be observed that the Reynolds effects are delimited by a critical threshold of the Reynolds number around 200,000. For values of Re_H higher than 200,000 it is possible to observe that the experimental data are totally independent of the Reynolds number. This value confirms what was found for the tests on windbreaks in §6.6.1. In fact, both in case of tests on barriers and tests on objects placed downstream of a windbreak, the respective aerodynamic coefficients result independent on Reynolds number for the same threshold value (Re_H = 200,000).

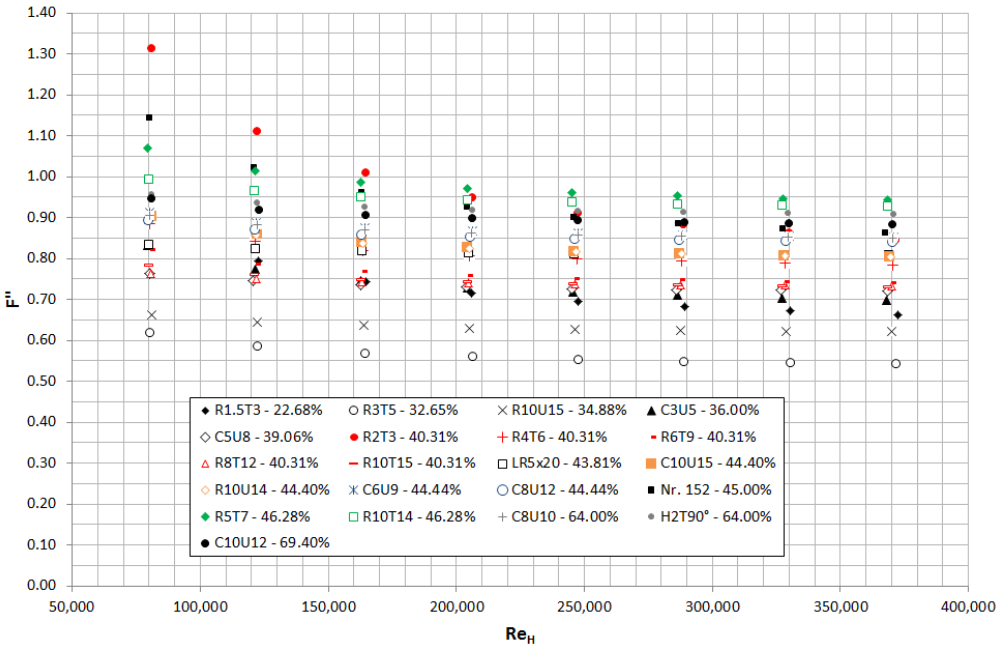

Fig. 7.20 F" function vs. Re_H for all the porous windbreaks tested.

The F" functions still do not collapse on a single curve, so that in addition to the effects of porosity there are also other parameters that play a significant role, such as the hydraulic diameters, shapes and thickness of the holes.

In order to understand what happens to the aerodynamic centre of the van when the porosity level of the windbreak changes, it is necessary to consider the point of application of the drag force and the related dimensionless parameter b/H ratio. This effect is shown in Fig. 7.21 which reports the mean value of the ratio b/H, calculated where the data in Fig. 7.16 are independent of Re_H, for different porosity levels of the barrier. To have an immediate comparison between the aerodynamic centre of the van (*indicated with black dots*) and the relative centre of gravity, a red dotted line has been superimposed on the graph. The b/H ratio is included in the range $0.563 \div 0.641$ and shows a growth (*by approximately 13%*) for increasing values of porosity, up to a sort of asymptote in correspondence with the case of van without barrier (Fig. 7.17w). This growth is mainly imputable to the different shapes of the pressure distribution that are encountered, on the windward side of the van, for different porosity level of the barrier. The point of application of the drag force is always lower than the centre of gravity of the van with the exception

of the case *No barrier* where the b/H ratio turns out to be almost coincident with the centre of gravity. Then it is possible to observe that the aerodynamic centre of the van is strongly affected by the porosity level of the barrier positioned upstream of the van and it could be well described by a polynomial fitting curve.

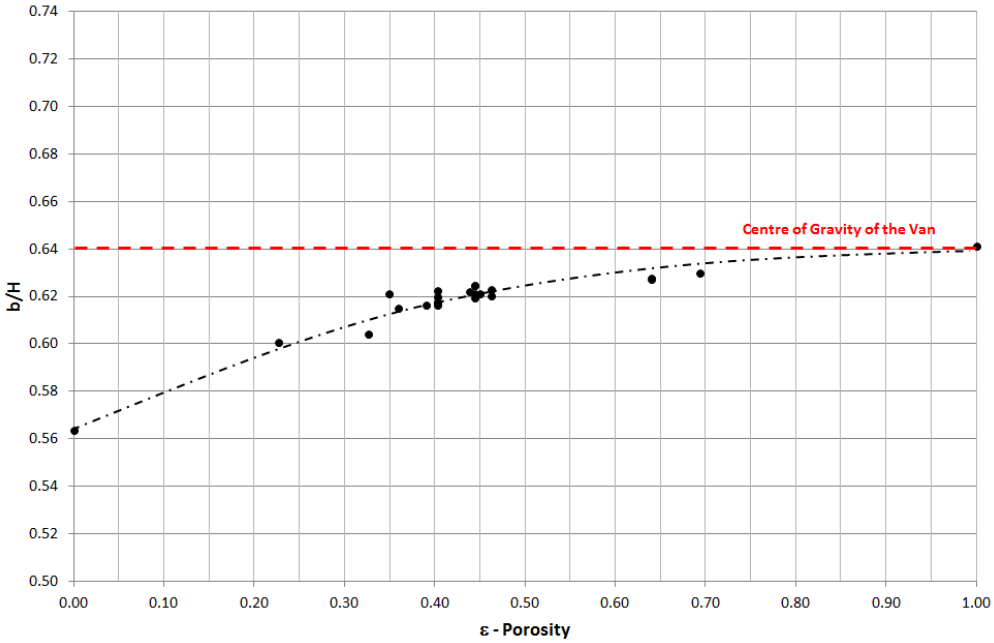

Fig. 7.21 b/H ratio on the van vs. porosity of the windbreaks tested.

From this graph it is possible to visualize which are the beneficial effects due to presence of the barrier. The first effect, as already said, is directly linked to a sharp reduction of the pressure distribution on the windward side of the van. A second effect is the modification of the aerodynamic centre of the van due to the presence of the porous barrier. In fact, decreasing the porosity level, not only the drag force on the van but also the point of application of drag itself decrease. Then, there is an increment of the global vehicle safety measured especially in terms of overturning moment reduction.

In order to emphasize the role played by diameter, thickness and shape of the holes, the drag coefficient of the van ($C_{D,van}$) was chosen as reference parameter.

7.6.2 Diameter and thickness effects

With the purpose to study more in detail the effect of thickness and hydraulic diameter of holes on the aerodynamic characteristics of the van, expressed by the van drag coefficient, some additional investigations have been carried out on five windbreak samples. In order to have homogeneous samples and to avoid the effect played by porosity and shape of holes, the tests were conducted at the same level of porosity ($\varepsilon = 40.31$ %) with the same shape (round), but with different values of the t/D_h ratio. The typology of barriers used for the tests and their main features are summarized in Table 7.4.

Model	Porosity % (ε)	t [mm]	D_h[mm]	t/D_h	Shape
R2T3	40.31	1.0	2.0	0.500	Round
R4T6	40.31	1.0	4.0	0.250	Round
R6T8	40.31	1.0	6.0	0.167	Round
R8T12	40.31	1.0	8.0	0.125	Round
R10T15	40.31	1.0	10.0	0.100	Round

Table 7.4 Barrier samples employed for diameter and thickness tests.

Fig. 7.22 shows the drag coefficient of the van, measured for all the five fences analysed, in function of the Reynolds number.

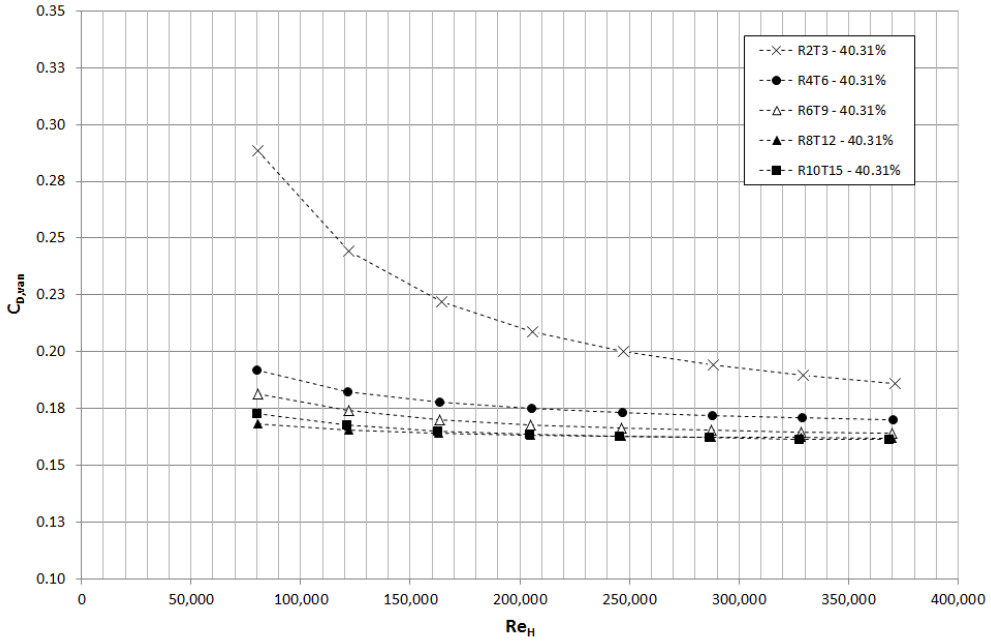

Fig. 7.22 $C_{D,van}$ vs. Re_H for the t/D_h tests.

The figure points out that the drag coefficient of the van is higher for the barriers having the smallest values of the diameter of holes and thus higher values of the t/D_h ratio. In fact, it is clearly evident that the maximum value for $C_{D,van}$ is found for the sample with $D_h = 2$ mm and $t = 1$ mm, that is $t/D_h = 0.5$. The sample R2T3 shows also a more pronounced dependence on the Reynolds number especially for Re_H values lower than 200,000. From Fig. 7.22 it is quite difficult to say which are the effects for the other kinds of barrier because the data are close and overlapped. Consequently, to have more readable data, two additional diagrams were realized. They report only the mean values of $C_{D,van}$, obtained where there is no dependence on the Reynolds (average of last two points in Fig. 7.22), in function of the diameter of the holes (Fig. 7.23) and the t/D_h ratio (Fig. 7.24).

Considering Fig. 7.23 it can be stated that increasing the hole diameter, the drag coefficient decreases of about 13 %, but in order to have a deeper comprehension it

is necessary to pass to the t/D_h domain (Fig. 7.24).

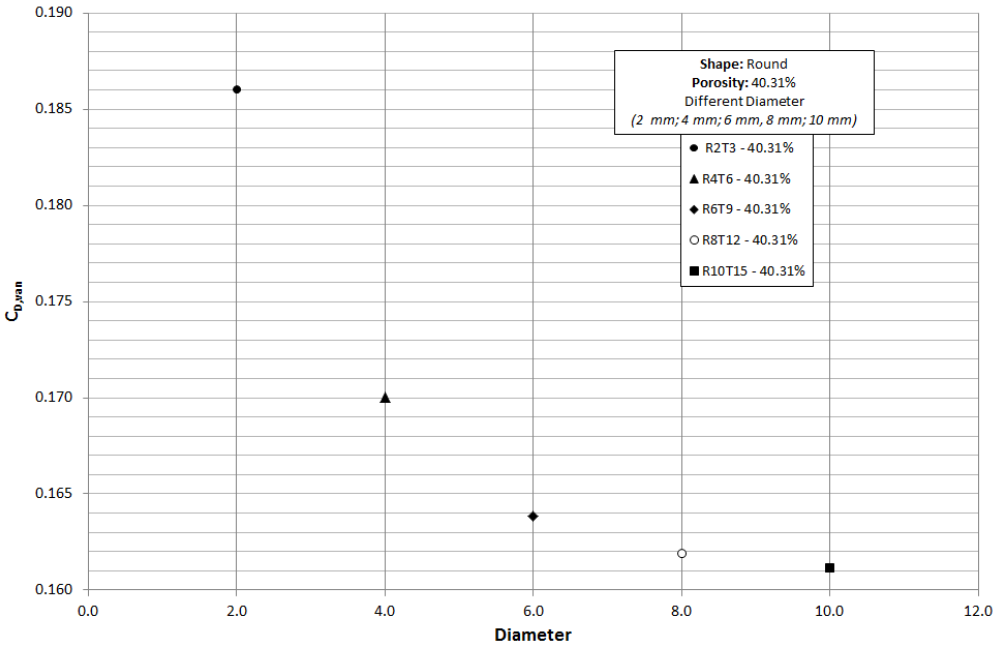

Fig. 7.23 $C_{D,van}$ vs. Diameter.

The t/D_h domain explains very well what happens to the drag coefficient of the van. In fact, there exists a linear relationship between $C_{D,van}$ and t/D_h ratio which leads to have the maximum values of $C_{D,van}$ for higher values of the t/D_h.

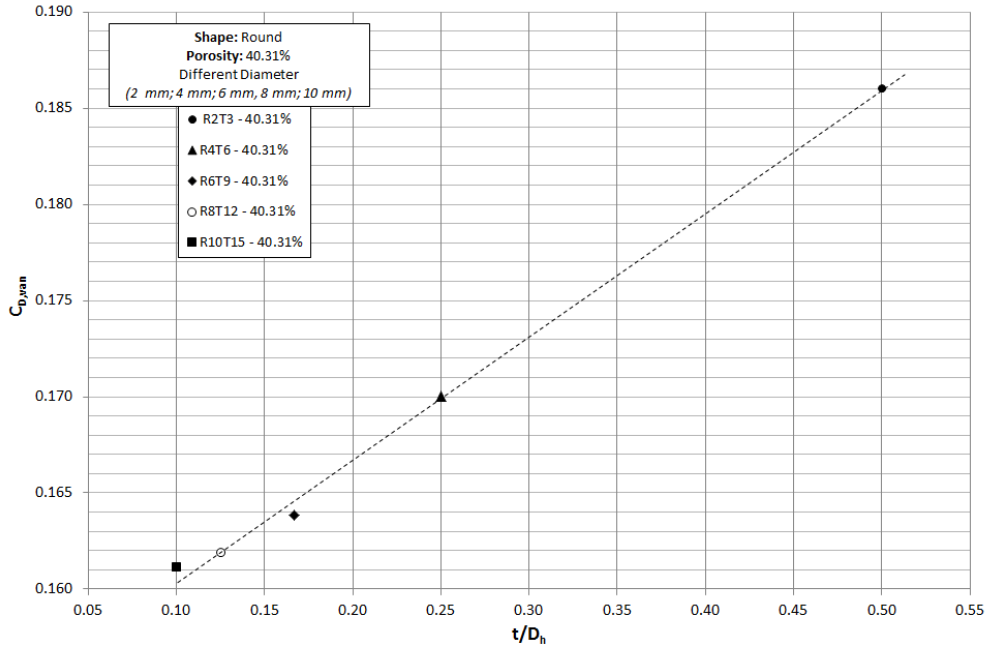

Fig. 7.24 $C_{D,van}$ vs. t/D_h ratio.

This problem can be explained reminding the three different flow regimes of the barrier wake explained in §5.6.5 and the pattern of C_p reported in Fig. 7.17. In correspondence of low values of t/D_h ratio the wake is characterized by a fully separated flow regime ($t/D_h \lesssim 0.4$) which implies a maximum flow resistance offered by the barrier and consequently minimal $C_{D,van}$ values for the van. Increasing the t/D_h ratio the wake begins to tend to the fully reattached flow regime ($t/D_h \gtrsim 1.2$), characterized by low values of drag coefficient of the barrier and thus major flow resistance of the van that is well demonstrated by the growth of $C_{D,van}$ in Fig. 7.24. This hypothesis is confirmed by Fig. 7.17(g, h, i, l, m) where increasing the t/D_h ratio the pressure coefficient patterns around the upwind face of the van decrease.

Therefore with the purpose to simplify the problem and give a visual idea of the phenomenon it is possible to state that if the ratio t/D_h increases, the mass flow through the barrier also increases and consequently the related aerodynamic drag on the van. These aspects are further supported by the results obtained in Chapter 6 during the t/D_h tests on porous windbreaks. In fact, the C_D data reported in §6.6.2 showed a trend exactly opposite to what was found in Fig. 7.24 with a drag coefficient that decreased almost linearly with the increasing of t/D_h ratio.

7.6.3 Shape effect

In order to investigate whether the shape of the holes is a key parameter to characterize the wake of the barrier, specific tests were carried out. Two different types of barrier were tested, differing only for the shape of the holes, but with the same porosity level ($\varepsilon = 44.40$ %), same hydraulic diameter and thickness. The following table briefly reports the main features of the samples used for this test (Table 7.5).

Model	**Porosity % (ε)**	t **[mm]**	D_h**[mm]**	**Shape**
R10U14	44.40	1.0	10.0	Round
C10U15	44.40	1.0	10.0	Square

Table 7.5 Barrier samples for shape tests.

Fig. 7.25 puts in relation the drag and moment coefficient of the van obtained for two different shapes of the holes versus the characteristic Reynolds number. In the picture are reported with square markers the data measured downstream of a barrier having square holes and with circular markers the data related to the barrier with round holes. The diagram is further divided in two bands of colour where the red indicated the moment coefficient of the van ($C_{M,van}$) and the black the drag coefficient of the van ($C_{D,van}$).

From the graph it is possible to affirm that the dependence on hole shape is negligible since the discrepancies between the results for round and square shapes are irrelevant and are comparable with the measurement errors. Then it can be argued that placing a van in the wake of two porous barriers having the same porosity, diameter and thickness of the holes but only different for the shape of the holes, there is no difference in terms of aerodynamic load on the van.

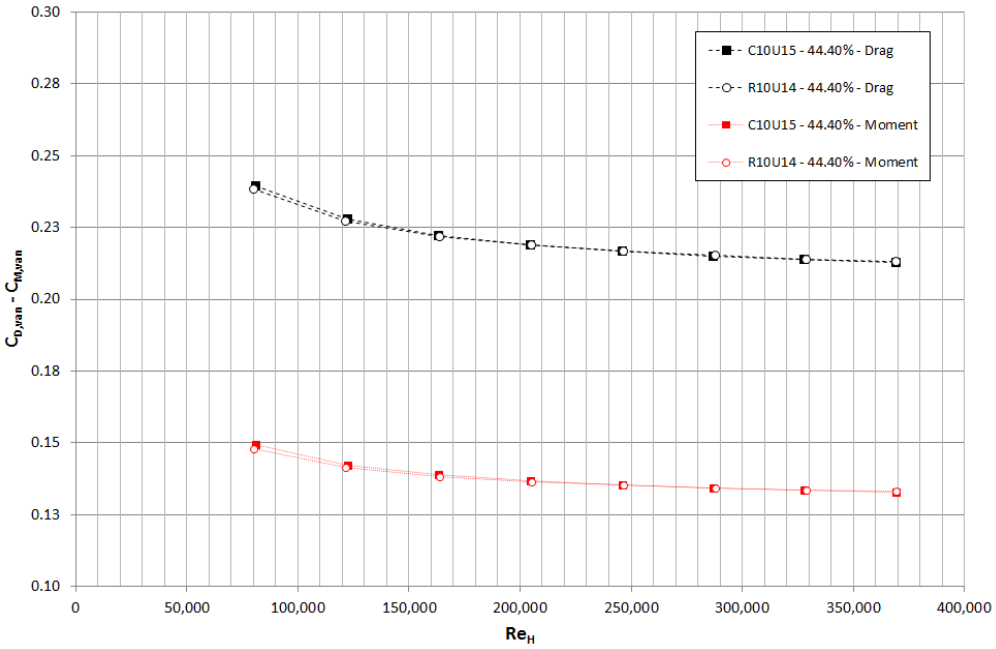

Fig. 7.25 $C_{D,van}$ vs. Re_H for shape tests.

Consequently the shape tests confirm what was already noticed in Chapters 5 and 6 and suggested by ESDU81039 (1985) and Idelchik (1994).

7.7 Concluding remarks

Wind tunnel tests were carried out in order to quantify the aerodynamic loads on a stationary high-sided commercial vehicle positioned downstream of several typologies of porous wind screens.

The vehicle was schematized by a wooden WT model of Iveco Daily 35C at scale 1:20, suitably instrumented with pressure taps, and linked to a high-frequency force balance. The windbreaks were represented by 23 rectangular perforated plates with different porosity levels, hydraulic diameter, thickness and shape of the holes.

Aerodynamic loads on the van were quantified by dimensionless parameters as the pressure coefficient, the drag and moment coefficients and the b/H ratio. All the dimensionless quantities were influenced by the characteristics of the barrier (porosity, diameter and thickness but not by the shape of the holes) and by the Reynolds number. The Reynolds effects were present only in a confined viscous region of motion identified by Re_H values lower than 200,000.

The windbreak operates a sharp reduction of the wind action on the windward side of the van by the interaction of two distinct phenomena. On the one hand, the porosity level modifies the mass flow through the screen and on the other hand the flow separation creates a large suction area downstream of the barrier. In addition to these macro aspects a marginal role, completely opposite to what was found in Chapter 6, is played by the diameter and thickness of the holes. In fact, the drag coefficient increases almost linearly with the increasing of the t/D_h.

Chapter 8

Vehicle overturning risk analysis

8.1 Introduction

In this chapter the risk analysis will be carried out against the phenomenon of vehicle overturning in order to quantify the probability of overturning or of the closure of a given road infrastructure due to high cross-wind. More in particular the analysis will be performed using the various contributions coming from Chapters 2, 5, 6, 7 and following the risk management framework and the research conceptual map reported in Chapter 1.

In this work the entire risk chain explained by Pliefke *et al.* (2007) is covered, as all the crucial points of the Risk Management framework (risk identification, risk assessment and risk treatment) are analysed. The risk identification phase is composed by the definition of the system and the individuation of the relative hazard. In this case the system is well represented by a van positioned on a windy road infrastructure (like a road, a bridge, a viaduct) and the hazard is the wind action. The risk assessment part consists of two sub-procedures, the risk analysis and the risk evaluation module, whose tasks are to be seen in quantifying the risk and comparing it to other competing risks. For this kind of problem two principal sources of risk are present, the first one is well represented by aerodynamic effects on the bridge deck and the second is related to the aerodynamic effects around the van. In this study the attention is focused only on the overturning problem of the van, then the aerodynamic effects on the structure due to wind are not taken into account. Consequently, choosing only one type of risk, the risk evaluation module is omitted. So for this reason, the risk assessment step is only composed by the risk analysis, in which the probability of failure will be estimated in terms of closing hours of the infrastructure. The risk treatment is performed considering that the resultant probability of failure is too high and cannot be accepted; then several risk mitigation measures (represented by 23 different windbreaks) are adopted in order to reduce the probability of failure.

The method of analysis proposed will be applied to a hypothetical case study in order to quantify the probability of overturning corresponding to different levels of sheltering. Finally, knowing the probability of failure due to the vehicle overturning phenomenon it is possible to have a measure of risk in terms of the average number of hours per year in which the road infrastructure has to be closed.

In order to understand more deeply the risk procedure adopted the treatment will be divided into three macro-parts: Hazard, Vulnerability and Risk in accordance to the scheme reported in Fig. 8.1.

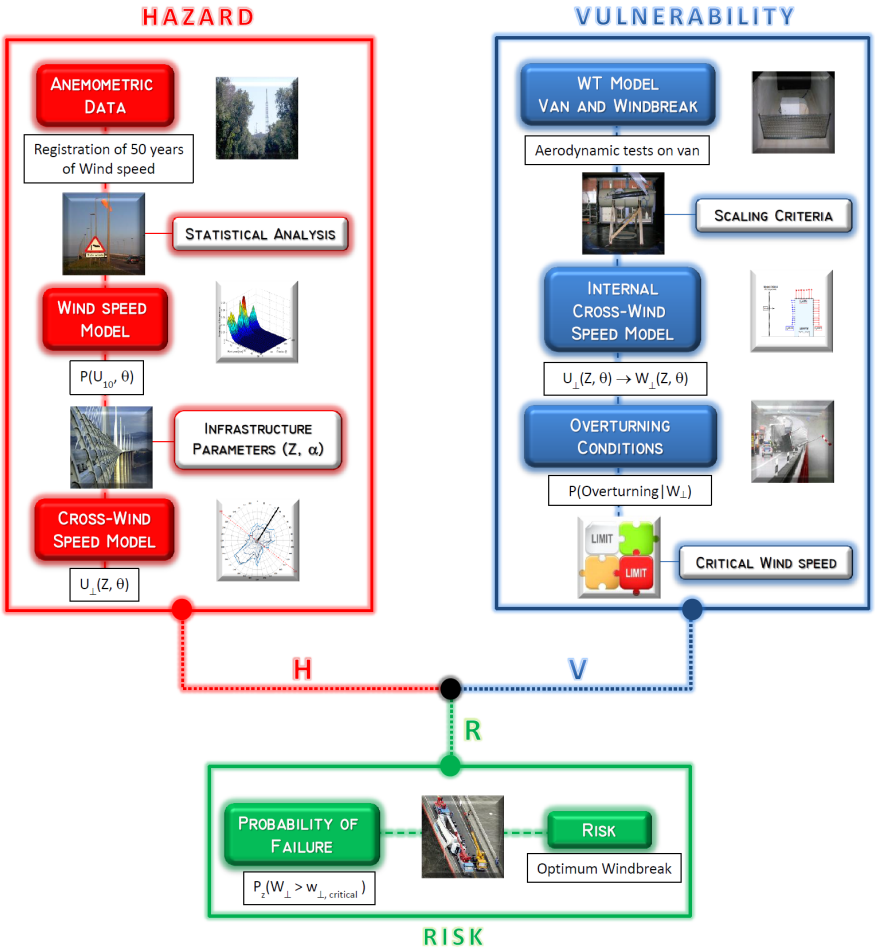

Fig. 8.1 Risk procedure scheme.

The risk procedure is initialized through the definition of the probability of failure ($P_{Failure}$) defined as the probability of exceedance of a fixed threshold. In this case having to deal with cross-wind speed data as hazard and considering that also the overturning conditions are well expressed in function of a critical threshold of cross-wind speed, the probability of failure or of overturning vehicles can be written as:

$$\begin{aligned} P_{Failure} &= P(W_{\perp} > w_{\perp,crit}) \\ P_{Failure} &= 1 - P(W_{\perp} \leq w_{\perp,crit}) \end{aligned} \tag{8.1}$$

where: $W_{\perp}$ is the cross-wind speed acting on the van and $w_{\perp,crit}$ is the critical threshold of cross-wind speed at which the overturning of the vehicle occurs.

In other terms it is possible to have overturning phenomena when the cross-wind speed exceeds the critical overturning cross-wind speed ($w_{\perp,crit}$). $w_{\perp,crit}$ is a function of the typology of mean of transportation and the relative velocity of the vehicle.

8.2 Hazard

The hazard, as indicated by the red box in Fig. 8.1, is well represented by the historical records of mean wind speed. For this work the hazard data consist of 50 years of anemometric measures of intensity and direction of wind speed, that were kindly provided by the monitoring climatological network of Italian Air Force (*Centro Nazionale di Meteorologia e Climatologia Aeronautica - CNMCA*).

8.2.1 Reference anemometric data

The available data refer to the meteorological station of Monte Argentario, located in the south part of Tuscany (Italy), for the period from 1st January 1961 to 31st December 2010. The anemometer is collocated on a steel mast positioned at a distance of 10 meters of height from the ground (Fig. 8.2a).

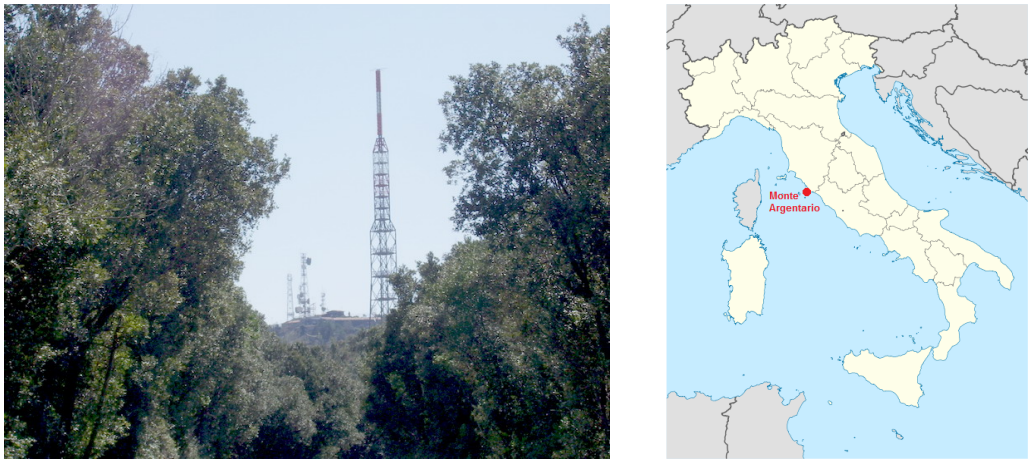

(a) Anemometric station (b) Location

Fig. 8.2 Monte Argentario station.

The records consist of measures of wind and the data are composed by eight daily acquisitions of mean wind speed over 10 minutes and direction for 36 directional sectors, acquired every 3 hours. The total number of available data is 143672 but only 143097 are useful for the statistical elaborations due to measurement errors that occurred during the measurements.

The wind data are included in the range $0 \div 48.36$ m/s for the mean wind speed values and from 10° to 360° for the direction (where: 360°=North; 90°=East; 180°=South; 270°=West). The wind calms are identified as those wind data values where both the mean wind speed and the wind direction are equal to zero.

Fig. 8.3 reports the frequency distribution of wind speed in the entire range of analysed data. The presence of two different distributions that overlap is highlighted, one for the wind calms (represented by red bar) and the other one for non-zero wind speeds (represented by blue bars). The wind calms for the meteorological station of Monte Argentario represent 9.85 % of the data and are mainly concentrated in the summer months.

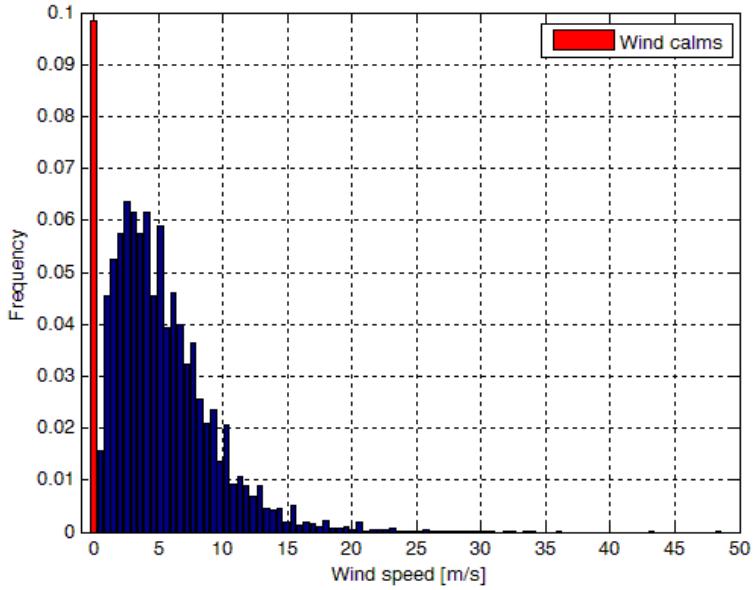

Fig. 8.3 Frequency distribution of wind speeds.

Fig. 8.4 reports the wind rose of the anemometric data, and gives a general vision of the direction of the predominant winds. The winds are well distributed around all the sectors but principally they blow from North-East and South-West. The directions between 200° ÷ 240° (South-West) are the predominant directions of winds, considering that about 25 % of registered winds come from this area.

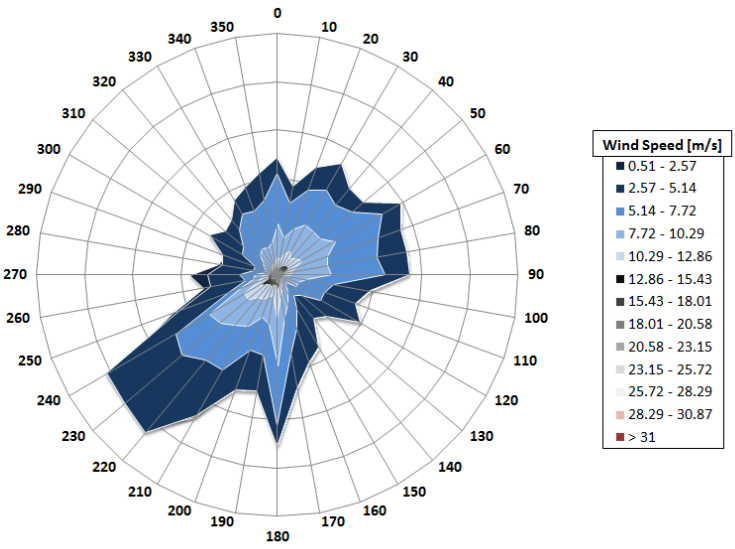

Fig. 8.4 Wind rose.

8.2.2 Probability distribution of wind speed

The Weibull distribution has been widely used in describing wind-speed data [Weibull (1951); Takle and Brown (1977) and Carta *et al.* (2009)]; indeed it is commonly accepted to model the mean wind speed distribution in the entire range of wind velocity (high, moderate and low) and in correspondence of different atmospheric stability conditions (stable, neutral and unstable) (Deaves and Lines, 1997). Nevertheless, some sites have wind characteristics that cannot be taken into account with the use of only one probability distribution function. In fact, for particular wind regimes it is more appropriate to resort to models of mixture distributions (McLachlan and Peel, 1998) which are capable to model several aspects of the distribution (high frequencies of null winds, bimodal shapes, etc.) with greater accuracy.

In the existing literature of the statistical analysis of wind data the use of goodness of fit is not very common practice and too often is neglected and avoided. The principal tests to evaluate the goodness of fit of a given distribution are: the Chi-square test, the Kolmogorov-Smirnov test and the Anderson-Darling test. The authors usually limit themselves to show overlapping representations of the histogram of the sample of wind speeds and the fitted probability density function in order to give a visual comparison of the goodness of fit. For this work several probability distribution functions were tested and for each distribution the goodness of fit was evaluated, only with the Kolmogorov-Smirnov test. This is used to decide if a sample comes from a hypothesized continuous distribution and it is based on the cumulative distribution function (*CDF*). Considering that the probability of failure, in equation (8.1), is expressed as a function of the CDF, the Kolmogorov-Smirnov test is the most appropriate measure to evaluate the goodness of fit.

The probability distribution that best respects the Kolmogorov-Smirnov test is a non-negative three-parameter Burr XII distribution (Burr, 1942). The Burr XII distribution is mainly used in reliability analysis as a more flexible alternative to Weibull distribution [Wingo (1983); Wang *et al.* (1996) and Zimmer *et al.* (1998)] and its three-parameter form is a generalisation of the log-logistic distribution (Shao, 2000). The three-parameter Burr XII distribution is defined by the following CDF:

$$\begin{aligned} &F_{BXII}(u) = 1 - \left[1 + \left(\frac{u}{b}\right)^{a}\right]^{-k}, u \geq 0 \\ &F_{BXII}(u) = 0, \quad otherwise \end{aligned} \tag{8.2}$$

and by the probability density function:

$$\begin{aligned} &f_{BXII}(u) = \frac{ak}{b}\left(\frac{u}{b}\right)^{a-1}\left[1 + \left(\frac{u}{b}\right)^{a}\right]^{-(k+1)}, u \geq 0 \\ &f_{BXII}(u) = 0, \quad otherwise \end{aligned} \tag{8.3}$$

where: u is the variable, that in this case is the mean wind speed; b is the scale parameter, having the same units as u, and a and k are continuous shape parameters of the Burr type XII distribution ($a, b, k > 0$). If this distribution is used to fit wind speed data, the probability of observing periods of zero wind speed is not properly accounted, in fact $F_{BXII}(0; a, b, k) = 0$. The problem of properly including

wind calms into the distribution has been reduced (but not eliminated) through the definition of a hybrid probability density function (Takle and Brown, 1977). The method used simply removes those measurements identified as *calms*, and fits the CDF distribution to the non-zero wind speeds. The zero wind speeds are then reintroduced to give the proper mean and variance and renormalize the distribution. Applying the hybrid model to the Burr type XII distribution, the equation (8.2) can be rewritten as:

$$\begin{aligned} &F_{BXII}^{Hyb}(u) = F_0 + (1 - F_0)F_{BXII}(u), \quad u \geq 0 \\ &F_{BXII}^{Hyb}(u) = 0, \quad otherwise \end{aligned} \tag{8.4}$$

and the relation (8.3) becomes:

$$f_{BXII}^{Hyb}(u) = F_0\delta(u) + (1 - F_0)f_{BXII}(u), \quad \forall u \in \mathbb{R} \tag{8.5}$$

where: F_0 is the probability of observing zero wind speed (wind calms); $\delta(u)$ is the Dirac delta function; $F_{BXII}(u)$ and $f_{BXII}(u)$ are respectively the Burr cumulative distribution function and the probability density function. This hybrid distribution has been analysed and employed in various studies [Takle and Brown (1977); Auwera *et al.* (1980); Tuller and Brett (1984); Merzouk (2000); Solari *et al.* (2003)].

Finite maximum likelihood estimators for the three-parameter Burr XII distribution do not always exist due to the possibility to have non-degenerated limiting distributions (Shao, 2004). Currently the first and the most used methodology for the estimation of parameters consists in applying the equation (8.2) to the empirical CDF coming from the data and obtaining a, b, k by a non-linear least squares method. Usually this approach leads to an overestimation of the parameters which must be further refined by means of appropriate non-linear optimization algorithms (*Generalized Reduced Gradient, Gradient Projection, etc.*). In this work two different statistical analyses are preformed: the first one considers the totality of the data without taking into account the wind direction (omnidirectional probability) and the second one is carried out with respect to the 36 sectors of provenance of wind (directional probability). After a first check that the omnidirectional data satisfied the test of Kolmogorov-Smirnov, the parameters (a, b, k) of the Burr distribution were estimated in order to meet the goodness of fit according to Kolmogorov test. In order to clarify the discussion, this aspect and the relative procedure for the parameter estimation will be explained with a brief example during the omnidirectional analysis.

8.2.2.1 Omnidirectional analysis

In order to highlight the usefulness of the hybrid model respect to the classical one a brief comparison is reported and commented. The available data of mean wind speed are listed in Table 8.1 in order to give an idea of the anemometric sample available. The table classifies the data in function of the possible values of the wind speed and direction. The records that will be considered in the statistical analysis are the wind calms (identified by speed and direction equal to zero) and the valid data of wind (speed > 0 and direction in the range $10° \div 360°$).

Direction	Wind Speed Data			Total
	< 0	0	> 0	
< 0	168	1	308	309
0	0	14095	82	14177
≤ 360	3	5	129002	129010
> 360	0	0	8	176
Total	171	14101	129400	**143672**

Table 8.1 Monte Argentario wind data sample

The hybrid model in the equations (8.4) and (8.5) will be applied to the wind data without the wind calms (129002 data), while the classical approach will be used for the totality of the valid data including the calms (143097 data). The other data reported in the table (575 values) will be neglected because affected by errors.

The first step of statistical analysis consists in the determination of the empirical cumulative probability function $[P^*(U \leq u)]$ and of the related probability of exceedance $[P(U > u)=1 - P^*(U \leq u)]$ from the wind data sample.

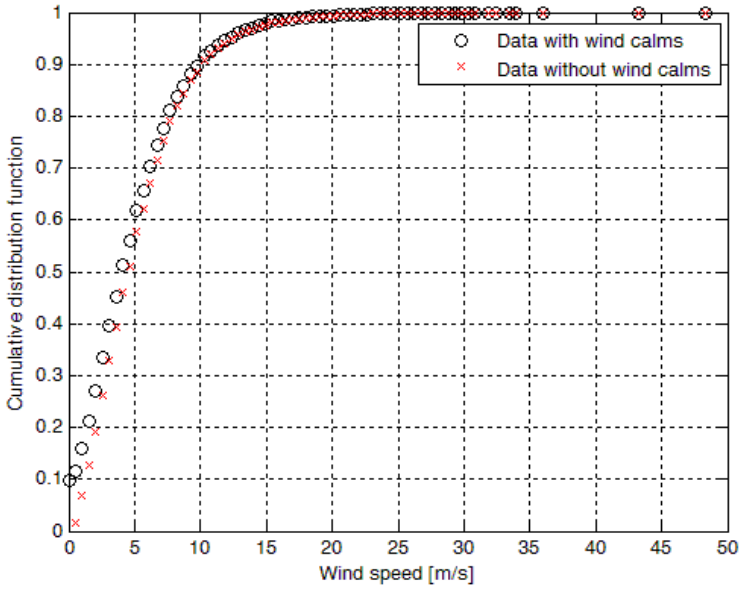

Fig. 8.5 Comparison between cumulative distribution functions for the classical approach (black circles) and for the hybrid one (red symbols).

Observing the sample of anemometric wind data U_1, U_2, ..., U_n, arranged in ascending order, the empirical cumulative distribution function $F_e(u)$ is defined as:

$$F_e(u) = \frac{\#[i : U_i \leq u]}{n} \tag{8.6}$$

The value of $F_e(u)$ represents the percentage of the data of the sample that are less than or equal to u (where the notation # is the number of elements of the set reported in square brackets) and then the F_e function is the cumulative distribution function of the random variable $[P^*(U \leq u)]$. This step is carried out for the hybrid and classical approach. Fig. 8.5 shows the empirical cumulative distribution functions for both cases.

At this point, knowing the empirical CDF, it is possible to estimate the parameters for the theoretical CDF (Burr type XII distribution) using the following procedure. The parameter estimation procedure consists of two parts that are linked. In the first phase, the empirical CDF functions are fitted with a non-linear least squares method (*Trust-Region algorithm*) using a function with the form (8.2) and the parameters are obtained. This phase has the aim to obtain a rough estimation of the parameters (a, b, k) of the equation (8.2) in order to trigger the process of optimization in the second phase.

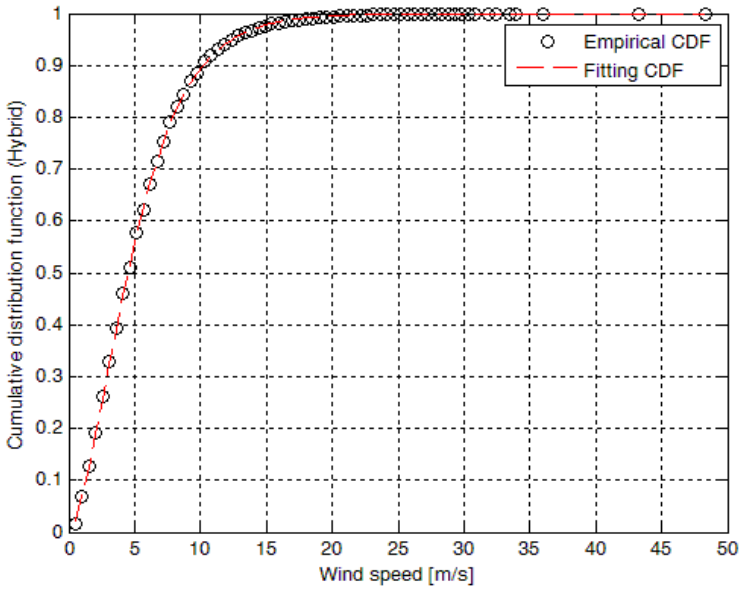

Fig. 8.6 Empirical and fitting CDF for the classical model.

Fig. 8.6 reports the empirical CDF with circle points overlapped with the fitting of CDF of Burr XII distribution (red dotted line) for the classical model. The parameters obtained by non-linear least squares analysis are reported in Table 8.2.

Parameters	**Classical**	**Hybrid**
a	1.190	1.579
b	1800.00	20.250
k	1056.00	7.869

Table 8.2 Estimation of the Burr XII parameters (first phase).

In Fig. 8.7 is reported a comparison between the empirical CDF and Burr type XII CDF obtained for classical and hybrid model. The graph highlights that the hybrid model seems to work better than the classical approach. In fact, there is almost perfect correspondence between the empirical data and the theoretical model. Asterisk symbols (hybrid model) are distributed with a well-defined linear pattern while the circles (classical approach) are more dispersed following a non-linear trend. This aspect is further emphasized from the large discrepancy that is encountered between the classic model and the ideal line for low values of the empirical CDF.

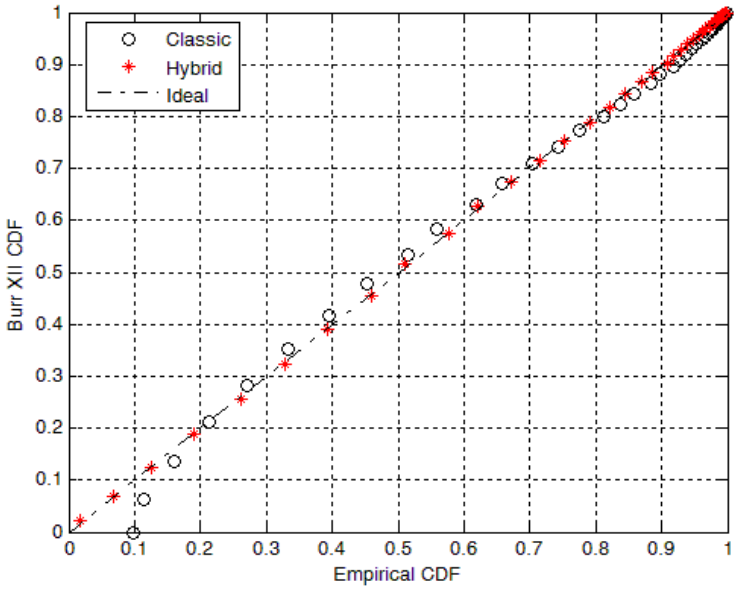

Fig. 8.7 CDF comparison between classical model and hybrid model.

The second phase consists in an algorithm of optimization, written in Matlab environment, where the Burr parameters (a, b, k) are modified in order to satisfy the Kolmogorov-Smirnov test (KS).

The goodness of fit is performed as a standard statistical test of hypotheses; in this case the null and the alternative hypotheses are:

- $\mathbf{H_0}$: the data follow the specified Burr type XII distribution;
- $\mathbf{H_1}$: the data do not follow the specified Burr type XII distribution.

The Kolmogorov-Smirnov statistic (D) is based on the largest difference between the theoretical and the empirical cumulative distribution function:

$$D := \max_{0<u<+\infty} |F_e(u) - F_{BXII}(u)| \tag{8.7}$$

where: $F_e(u)$ is the empirical cumulative distribution function and $F_{BXII}(u)$ is the theoretical Burr type XII cumulative distribution function.

The hypothesis regarding the form of the distribution is rejected at the chosen significance level (α) if the test statistic (D) is greater than the critical value (d_α) obtained from the Kolmogorov table. If the sample is large ($n > 50$) (Miller, 1956), the threshold value for the test can be estimated from the following formula:

$$d_\alpha = \sqrt{\frac{\ln\left(\frac{2}{\alpha}\right)}{2n}} \tag{8.8}$$

where: α is the significance chosen level (a value of α=0.05 is typically used for most applications) and n is the dimension of the sample. In case of hybrid model $n = 129002$ and $\alpha = 0.05$, the critical value of the tests is $d_{0.05} = 0.00378$.

In the light of this the basic equation for the optimization algorithm becomes:

$$\max_{0<u<+\infty} |F_e(u) - 1 + \left[1 + \left(\frac{u}{b}\right)^a\right]^{-k}| < d_{0.05} \tag{8.9}$$

The computation is performed using a derivative-free optimization method on the unconstrained multi-variable function reported in equation (8.9). The optimization process is initialized using as starting points for a, b, k the values obtained in the first phase (reported in Table 8.2), and continues until the parameters that satisfy the relation (8.9) are not found. Clearly this method makes sense if the specified distribution (obtained with the first estimation of the parameters) already satisfies the KS test or it is very close to the satisfaction threshold. In fact using this optimization phase it is possible to search the best estimation of the parameters of the distribution that fulfil the KS test.

Table 8.3 reports the parameters (a, b, k) obtained by the optimization process both for classical and hybrid model, the value of the Kolmogorov-Smirnov statistic (D) and the threshold value (d_α) for the sample at significance level of 0.05.

Parameters	**Classical**	**Hybrid**
a	1.2561	1.5846
b	826.7845	20.5484
k	582.0277	8.0686
D	0.09853	0.00316
d_α	0.00359	0.00378

Table 8.3 Estimation of the Burr XII parameters (second phase).

As expected due to the presence of the wind calms the classical approach does not respect the KS test, in fact $D > d_\alpha$. By contrast, in the hybrid model the KS test is fully satisfied and for the next analyses only the hybrid model will be employed. Fig. 8.8 reports the omnidirectional cumulative distribution function and the probability of exceedance calculated with the hybrid model. Both the graphs show the high accuracy of the fitting of the theoretical with respect to the empirical data.

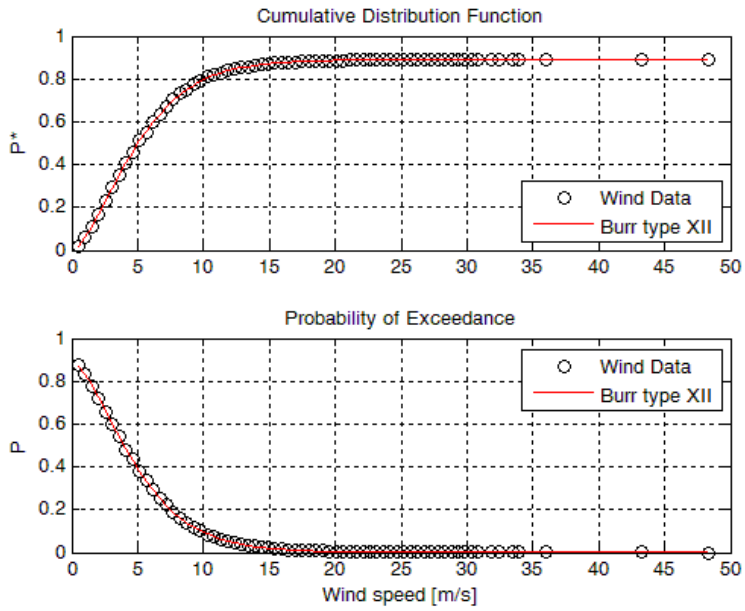

Fig. 8.8 $P^*(U \leq u)$ and $P(U > u)$ obtained with the hybrid model.

Fig. 8.9 shows the comparison between the Burr type XII probability density function and the histogram of the wind data sample. The Burr distribution follows very well the sample but in order to quantify the goodness of fit a Chi-square test would be necessary. The test in this work is not performed because the risk analysis will be carried out in the next paragraphs using only the CDF distribution, whose reliability has been evaluated with the KS test.

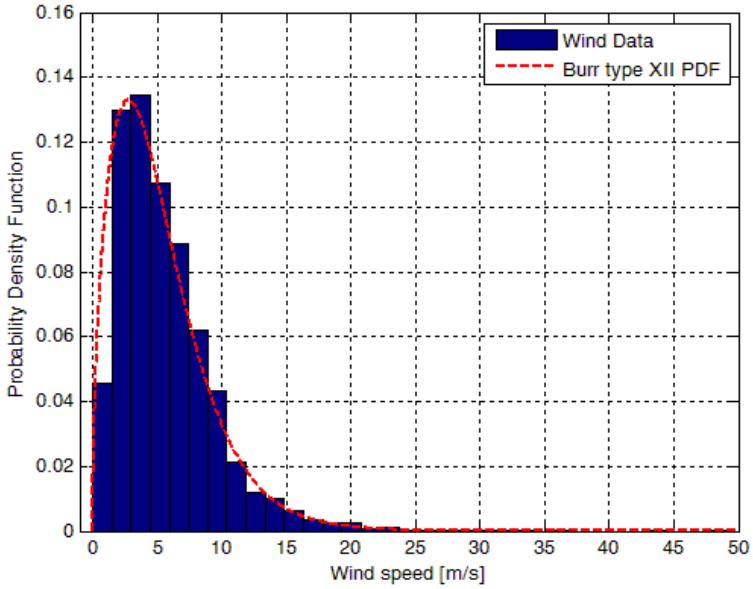

Fig. 8.9 $f_{BXII}^{Hyb}(u)$ distribution for the hybrid model.

8.2.2.2 Directional analysis

In this section the statistical analysis of the sample of wind data is extended for each wind direction. Considering the goodness of the hybrid method on the omnidirectional data the analysis is carried out applying only this approach and neglecting the classical method. The directional analysis is conducted separately for each sector of wind, then the resulting distributions are expressed in terms of conditional probability because they are obtained for fixed ranges of directions ($\theta_i^- < \theta < \theta_i^+$). For this analysis the Burr type XII distribution reported in equation (8.2) may be modified as:

$$P^*(U \leq u | \theta_i^- < \theta < \theta_i^+) = 1 - \left[1 + \left(\frac{u}{b_i}\right)^{a_i}\right]^{-k_i} \tag{8.10}$$

$$P(U > u | \theta_i^- < \theta < \theta_i^+) = 1 - P^*(U \leq u | \theta_i^- < \theta < \theta_i^+) \tag{8.11}$$

where: a_i, b_i, k_i represent the parameters of the Burr distribution calculated for each i-th sector of wind and i are the 36 sectors. Equation (8.11), as already said, is a conditional probability and in order to remove the conditional dependency on the range $\theta_i^- < \theta < \theta_i^+$, it is necessary to define the joint probability function using the total probability theorem:

$$P(U > u, \theta_i^- < \theta < \theta_i^+) = P(U > u | \theta_i^- < \theta < \theta_i^+) \cdot P(\theta_i^- < \theta < \theta_i^+) \tag{8.12}$$

where: the term $P(U > u, \theta_i^- < \theta < \theta_i^+)$ is the joint probability function and the part $P(\theta_i^- < \theta < \theta_i^+)$ is the probability to observe wind from the i-th sector.

The procedure used for the estimation of the Burr distribution parameters is the same as the one adopted for the omnidirectional case.

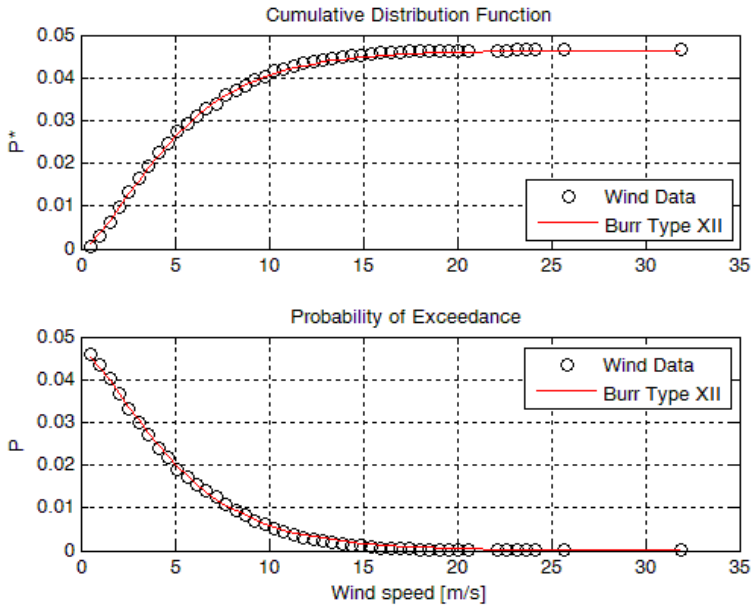

Fig. 8.10 $P^*(U \leq u, \theta_i^- < \theta < \theta_i^+)$ and $P(U > u, \theta_i^- < \theta < \theta_i^+)$ for the sector $i = 24$.

Table 8.4 reports, for each i-th sector, the angle range ($\theta_i^- - \theta_i^+$), the parameters of Burr distribution (a, b, k), the value of Kolmogorov statistic (D), the critical value of the KS test ($\mathrm{d}_{0.05}$) and the sectorial probability $\mathrm{P}(\theta_i^- < \theta < \theta_i^+)$.

$\theta_i^- - \theta_i^+$	**a**	**b**	**k**	**D**	$\mathbf{d}_{0.05}$	$\mathbf{P}(\theta_i^- < \theta < \theta_i^+)$
5° - 15°	1.5513	180.6777	200.6204	0.01690	0.02445	0.0240
15° - 25°	1.6166	31.1550	14.4354	0.01116	0.02172	0.0304
25° - 35°	1.5941	40.5377	19.9256	0.00850	0.02045	0.0343
35° - 45°	1.6792	16.0099	5.0809	0.01239	0.02131	0.0316
45° - 55°	1.6926	20.7692	7.4396	0.01478	0.02107	0.0323
55° - 65°	1.6541	25.9185	10.7508	0.01354	0.01905	0.0395
65° - 75°	1.7001	37.5028	23.2511	0.01107	0.02064	0.0337
75° - 85°	1.7136	67.1085	68.0235	0.00980	0.02104	0.0324
85° - 95°	1.6707	110.9381	139.2163	0.01591	0.02063	0.0337
95° - 105°	1.6120	15.1234	5.9342	0.00771	0.02548	0.0221
105° - 115°	1.6413	11.8259	4.5889	0.00926	0.02689	0.0198
115° - 125°	1.7663	8.9953	3.3552	0.00790	0.02631	0.0207
125° - 135°	1.9446	5.1080	1.6065	0.00821	0.03152	0.0144
135° - 145°	1.8302	5.2354	1.5472	0.00816	0.03331	0.0129
145° - 155°	1.9078	5.4703	1.6028	0.00936	0.02791	0.0184
155° - 165°	1.7281	9.6832	2.9847	0.00702	0.02534	0.0223
165° - 175°	1.6684	16.8119	6.1013	0.00627	0.02239	0.0286
175° - 185°	1.6565	53.6826	31.7107	0.01087	0.01715	0.0487
185° - 195°	1.5433	40.6084	19.2008	0.00813	0.02177	0.0303
195° - 205°	1.5587	16.9454	5.9271	0.00864	0.02135	0.0314
205° - 215°	1.5399	12.7509	4.1701	0.01260	0.01807	0.0439
215° - 225°	1.5919	9.3381	3.0817	0.01655	0.01683	0.0506
225° - 235°	1.4738	53.4864	28.6422	0.01450	0.01670	0.0514
235° - 245°	1.4812	17.3578	5.6260	0.01586	0.01658	0.0522
245° - 255°	1.3970	12.5126	3.6620	0.02210	0.02280	0.0276
255° - 265°	1.2728	28.4438	8.5340	0.02767	0.02791	0.0184
265° - 275°	1.4017	10.8719	3.4282	0.01972	0.02704	0.0196
275° - 285°	1.6123	6.8531	2.4637	0.01077	0.03315	0.0130
285° - 295°	1.6871	7.4548	2.8980	0.01038	0.03380	0.0126
295° - 305°	1.7391	9.7826	3.9386	0.00867	0.02895	0.0171
305° - 315°	1.6986	20.6492	10.6222	0.01004	0.03067	0.0152
315° - 325°	1.6460	135.8196	182.7782	0.01655	0.02811	0.0181
325° - 335°	1.6586	143.5462	210.6267	0.01945	0.02578	0.0216
335° - 345°	1.7113	24.3876	12.7864	0.01629	0.02542	0.0222
345° - 355°	1.6857	28.0670	15.4862	0.01750	0.02409	0.0247
355° - 5°	1.7804	23.5813	11.1848	0.01832	0.02177	0.0302

Table 8.4 Characteristic parameters for the directional analysis.

For all of the 36 sectors the parameters satisfy the KS test because all values of

the Kolmogorov statistic are under the critical threshold and this demonstrates the good adaptation of the specified theoretical distribution to the empirical data. As shown in Fig. 8.11 and Fig. 8.12 the parameters of the Burr distribution are different from the omnidirectional values and strongly depend on the wind direction.

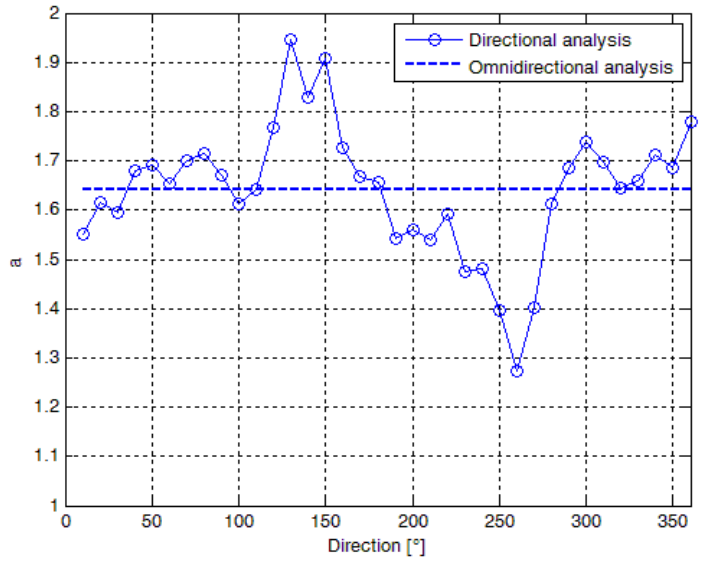

Fig. 8.11 Trend of Burr parameter a for each wind direction.

The shape parameter a presents larger deviations from omnidirectional case for values of θ of 130° and 260°, while the parameters b and k have the same pattern for different values of the angle θ only with a small shift.

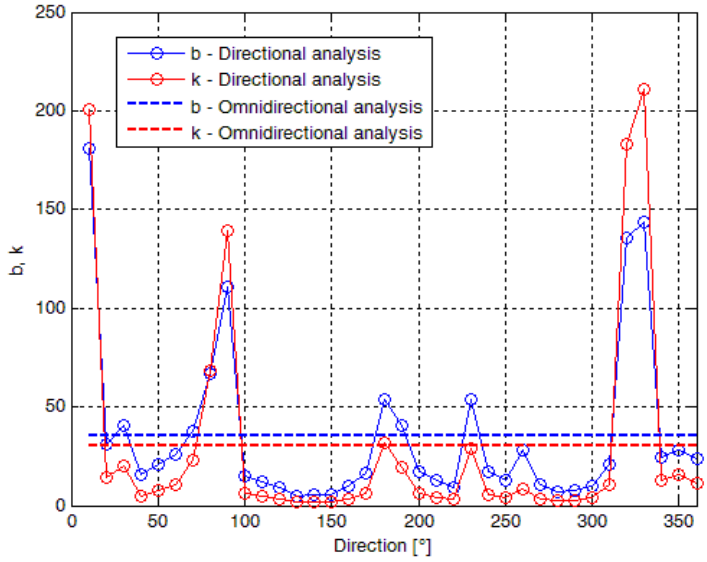

Fig. 8.12 Trends of Burr parameters b, k for each wind direction.

With the aim to have a schematic 3D view of the joint probability of exceedance and the joint probability density function for the 36 different wind directions, two three dimensional pictures are reported below (Fig. 8.13 and Fig. 8.14):

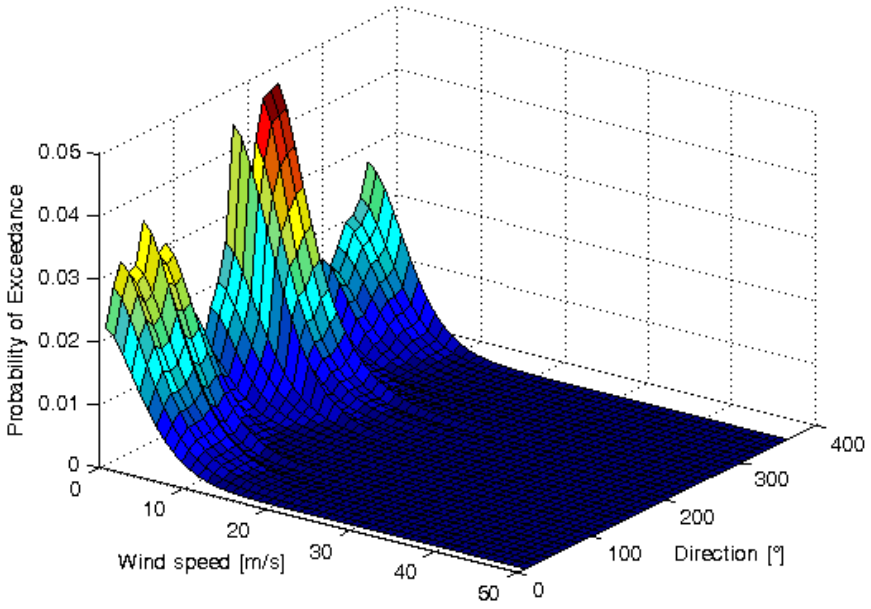

Fig. 8.13 Burr joint probability of exceedance.

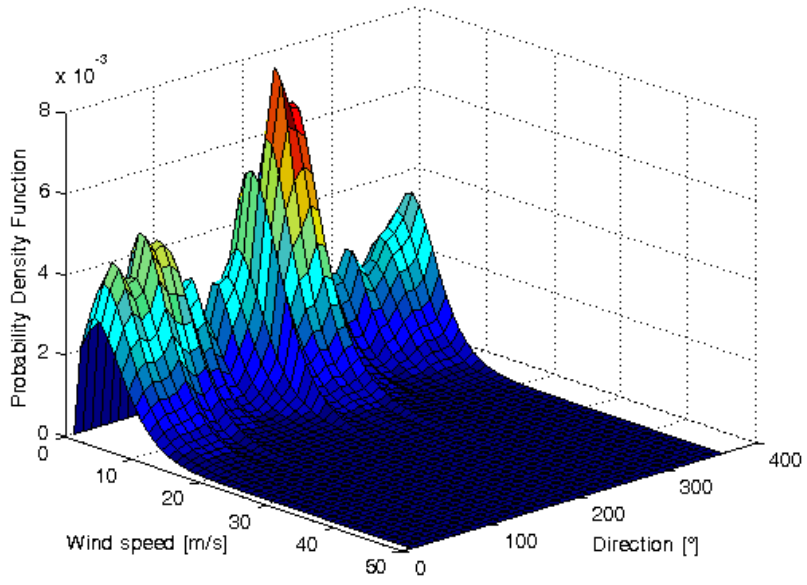

Fig. 8.14 Burr joint probability density function.

Both functions are calculated for the Burr type XII distribution with the parameters estimated in Table 8.4; at first sight the 3D surfaces show the presence of two

peaks of probability for the directions of predominant winds (θ=220° and θ=240°).

8.2.3 Cross-wind speed model

An analytical model was defined in the previous sections by the Burr type XII probability distribution, for both the mean wind speed (U_{10}), measured at 10 meters of height from the ground, and the direction (θ). After that, in order to obtain a suitable model for the cross-wind speed, it is necessary to define the reference infrastructure for which the risk of vehicles overturning is quantified. To apply the simple risk procedure proposed, a hypothetical case study is defined. In this work the reference infrastructure is represented by a highway road viaduct located in an area subject to strong winds. As already said, the risk analysis does not take into account the wind effects on the structure itself but only the risk of overturning vehicles is examined. The analysis of both aspects will be the starting point for future developments of this research work. For this typology of structure (road viaduct) the fundamental parameters that have to be considered are the height with respect to the ground, which for simplicity will be called *altitude (z)*, and the angle of orientation of the structure (α). In this application example these two parameters are fixed respectively to: z=40 m and α =55°.

8.2.3.1 Infrastructure parameters: altitude effect

Fig. 8.15 reports in a schematic manner the effects of the altitude (z) on the mean wind speed profile $U(z)$. In fact, as widely known, in the lower layers of the atmosphere the air masses in movement are influenced by the underlying soil. Therefore the wind speed increases progressively with the height due to the effect of air friction with the ground surface following a wind speed profile.

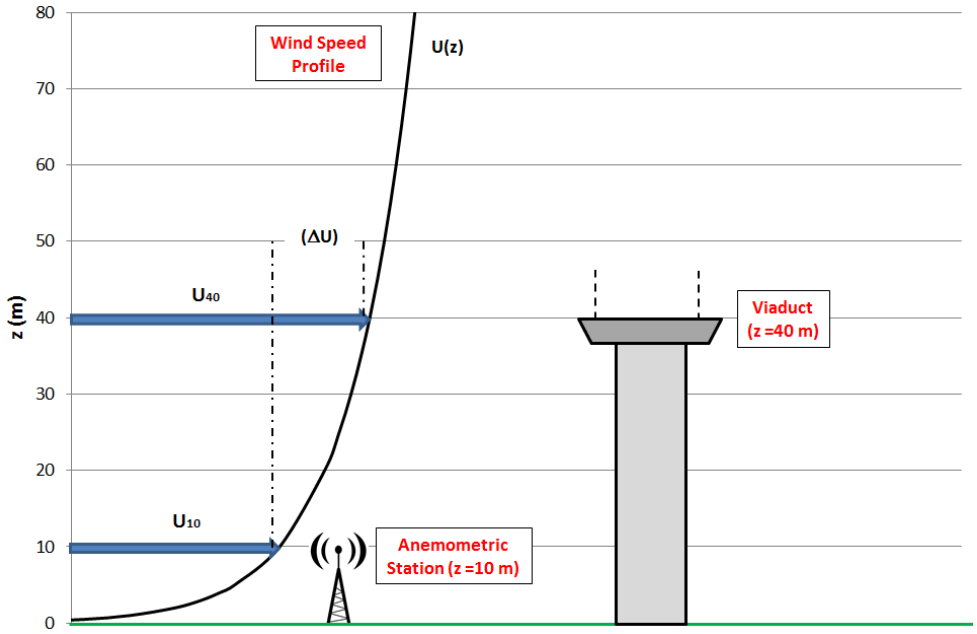

Fig. 8.15 Effects of altitude on the wind speed.

The main idea is to extrapolate the results of the statistical analysis on the data obtained from the anemometric station (located 10 meters above the ground) to different heights. For this case study, referring to Fig. 8.15, it is necessary to know the wind speed (U_{40}) at the viaduct level (z=40 m). Consequently, becomes fundamental to quantify the increment of wind speed (ΔU) for a given difference in height respect to the anemometer position (U_{10}).

Usually the effect of the altitude can be taken into account using a classical logarithmic wind speed profile and following the instructions reported in Eurocode-1 (1991). The mean wind speed $v_m(z)$ at a given altitude (z) above the ground depends on the soil roughness, the orography and the basic wind speed; the Eurocode-1 (1991) recommends the use of the relationship:

$$v_m(z) = c_r(z) \cdot c_o(z) \cdot v_b \tag{8.13}$$

where: $c_r(z)$ is the roughness coefficient, $c_o(z)$ is the orography coefficient and v_b is the basic wind speed. The roughness coefficient, $c_r(z)$, considers the growth of the wind speed with the altitude and the effect played by the roughness of soil, and it is obtained as:

$$\begin{aligned} c_r(z) &= k_r \cdot \ln\left(\frac{z}{z_0}\right), \quad z_{min} \le z \le 200\,m \\ c_r(z) &= c_r(z_{min}), \qquad\qquad z \le z_{min} \end{aligned} \tag{8.14}$$

where: z_0 is the roughness length, z_{min} is the minimum height and they strictly depend on the terrain category. Recommended values are given in Table 8.5.

	Terrain category	z_0 **[m]**	z_{min} **[m]**
0	Sea or coastal area exposed to the open sea.	0.003	1
I	Lakes or a flat and horizontal area with negligible vegetation and without obstacles.	0.01	1
II	Area with low vegetation such as grass and isolated obstacles (trees, buildings) with separations of at least 20 obstacle heights.	0.05	2
III	Area with regular cover of vegetation or buildings or with isolated obstacles with separations of maximum 20 obstacle height (such as villages, suburban terrain, permanent forest).	0.3	5
IV	Area in which at least of 15 % of the surface is covered with buildings and their average height exceeds 15 m.	1.0	10

Table 8.5 Terrain categories and terrain parameters (Eurocode-1, 1991).

The terrain factor (k_r) depends on roughness length (z_0), following the formula:

$$k_r = 0.19 \cdot \left(\frac{z_0}{0.05}\right)^{0.07} \tag{8.15}$$

The orography factor, $c_o(z)$, is strategic where orography becomes relevant (hills, cliffs etc.). In fact, it is necessary to consider the orography factor where the orographic effect increases wind velocities by more than 5 %. The effects of orography may be neglected when the average slope of the upwind terrain is less than 3°. The procedure that can be used for determining $c_o(z)$ is given in the Annex A.3 of the Eurocode-1 (1991). Finally the basic wind speed v_b is a function of the directional and seasonal factors and the characteristic 10 minutes mean wind velocity.

The logarithmic wind speed profile, reported in equation (8.13), is generally valid for high wind speeds where the mechanical turbulence is dominant and the airflow may therefore be assumed to be neutrally stratified (Simiu and Miyata, 2006). Vice versa at low wind speed the effects induced by thermal stratifications of the atmosphere become comparable with the mechanical turbulence. Consequently, the shape of the wind speed profile is not well-known and it is approximately assumed constant. In this application example the above aspect is not taken into account. In fact, the logarithmic profile will be considered valid for the entire range of wind speed and will be applied on the anemometric data. In order to simplify the analysis it is also assumed that the basic wind speed (v_b) after the Eurocode-1 (1991) corresponds exactly to the mean wind speed obtained by historical wind measures (U_{10}). Under these assumptions the equation (8.13) can be modified as:

$$U_z = c_r(z) \cdot c_o(z) \cdot U_{10} \tag{8.16}$$

where: U_{10} is the mean wind speed obtained from the anemometric data.

Supposing to realize the viaduct in an area with low vegetation (as in the neighbourhood of the Monte Argentario station) the structure falls into the category II of terrain in accordance to the Eurocode-1 (1991). For this category Table 8.5 fixes the terrain parameters equal to z_0=0.05 m and z_{min}=2 m. Considering that the viaduct is positioned at z =40 m from the ground, it is then possible to obtain all the coefficients of the equation (8.13). The terrain factor (k_r), as already indicated in equation (8.15), depends on roughness length (z_0) and for category II is equal to k_r=0.19. The roughness coefficient $c_r(z)$ is given by (8.14):

$$c_r(z) = 0.19 \cdot \ln\left(\frac{40}{0.05}\right) = 1.27$$

The orography factor, $c_o(z)$, is fixed equal to 1 and the orographic effects are not taken into account. The choice of setting the orography coefficient as unitary was dictated by the fact that the anemometric data of Monte Argentario, considering the intrinsic characteristics of the station, are surely affected by some orographic effects. In the light of these considerations the increase of mean wind speed at the height of the viaduct can be evaluated from the anemometric data respecting the following equation:

$$U_{40} = 1.27 \cdot U_{10} \tag{8.17}$$

The increment of wind speed (ΔU), indicated in Fig. 8.15, is equal to 27 % of the mean wind speed measured at 10 m.

8.2.3.2 Infrastructure parameters: orientation effect

As already seen in the literature review in Chapter 2 the overturning critical wind speed is expressed in function of the orthogonal component of wind speed respect to the longitudinal axis of the vehicle (cross-wind speed) [Carr *et al.* (1993) and Kwon *et al.* (2011)] and also the experimental tests in Chapter 7 are performed in this flow condition. Consequently it is fundamental to define the cross-wind speed component, $U_{\perp}(z,\theta)$, from the anemometric data incorporating also factors like the altitude (z) and the orientation of a given road infrastructure.

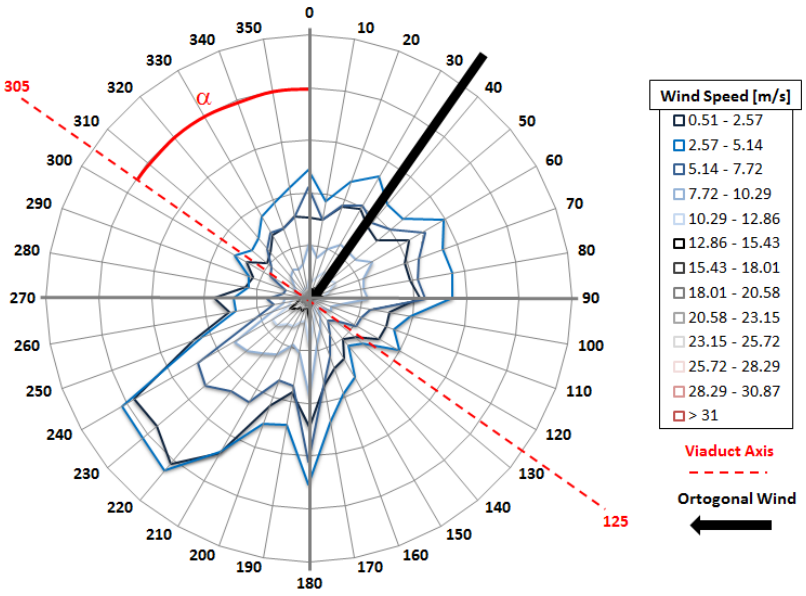

Fig. 8.16 Reference system for the orientation.

Fig. 8.16 reports the wind rose (Monte Argentario station) with superimposed the cross-wind direction (bold black arrow) and a hypothetical infrastructure axis (dashed red line). The effect of orientation and then the cross-wind speed can be considered using the following relationship:

$$U_{\perp}(z,\theta) = U_z \cdot |sin(\theta + \alpha)| \tag{8.18}$$

where: α is the angle of orientation of the infrastructure respect to the reference system for the wind direction, θ is the wind direction and U_z is the mean wind speed at a given altitude z. Equation (8.18) provides for each wind direction (θ) the orthogonal component of wind velocity (along the direction indicated by the bold black arrow) for different altitudes. In the case study the viaduct is positioned at an altitude of 40 m and presents an angle of orientation α =55° measured counter-clockwise with respect to the north of the wind rose. Hence, the equation (8.18) can be rewritten as:

$$U_{\perp}(40,\theta) = U_{40} \cdot |sin(\theta + 55°)| \tag{8.19}$$

8.3 Vulnerability

The vulnerability of the system is well described by the blue boxes reported in the following diagram (Fig. 8.17) and can be further expressed analytically as: $p(Overt.|U_{\perp}, \theta)$. This term represents the conditional probability that the vehicle overturning occurs, given the cross-wind speed ($U_{\perp}$) and the wind direction (θ).

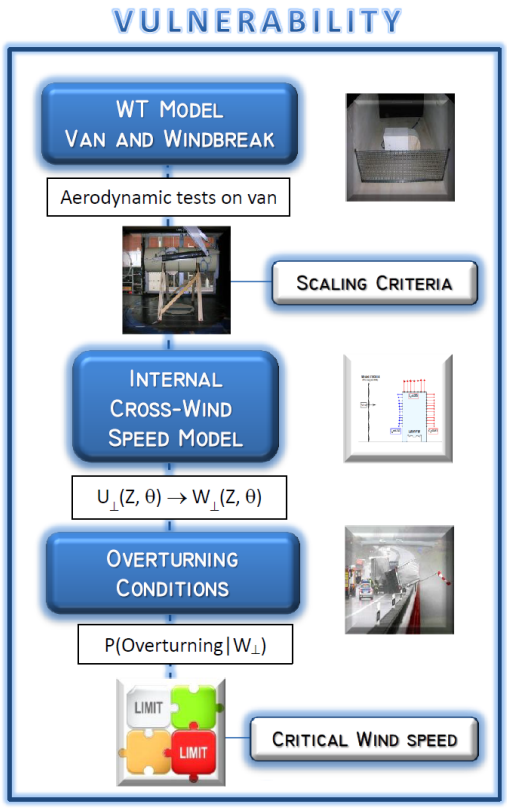

Fig. 8.17 Vulnerability steps.

The entire vulnerability phase is based on the results provided in output by the wind tunnel tests on a model of van and windbreaks. In fact, using these aerodynamic data it is possible to quantify the internal cross-wind speed obtained for a given value of the external cross-wind velocity for different typologies of shelter. Finally in the overturning conditions for a given mean of transportation and in function of its velocity, the critical overturning wind speeds are reported. In order to perform the vulnerability analysis, in the following all the individual steps reported in the block diagram in Fig. 8.17 are explained and applied to the case study.

8.3.1 Internal cross-wind speed

For a given model of high-sided vehicle positioned downstream of a porous barrier, the internal cross-wind speed can be obtained from experimental tests in wind tunnel, using the scaling procedure exposed in Chapter 6. The purpose of this kind of test

is to obtain correlation between the external cross-wind speed ($U_\perp$) and the internal cross-wind speed ($W_\perp$) in function of the typology of the barrier used (Fig. 8.18).

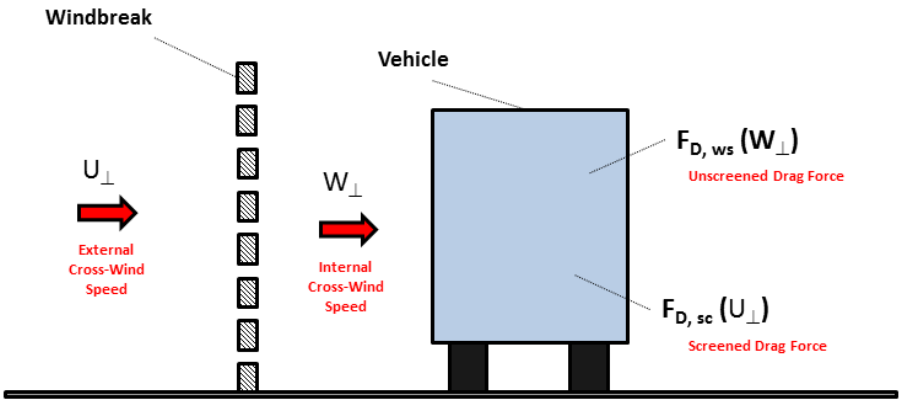

Fig. 8.18 Schematic view of the experimental tests in wind tunnel.

With the experimental tests it is possible to measure only the wind actions on the model of vehicle expressed in terms of forces and torques in function of different values of the external wind speed. Consequently, the internal velocity is obtained as derived quantity because it is not directly measured but estimated under some particular assumptions as an apparent mean wind speed. The best way to obtain very accurate data of internal cross-wind speed is to support the force measurements with PIV flow visualizations with the aim to have a deeper comprehension of the velocity field. In spite of it, Allori and Nuti (2008) have demonstrated that the two different typologies of tests lead to the same results. In fact, there is almost perfect correspondence between the internal mean wind speed obtained with PIV technique and force measurements (apparent wind speed). Then, these tests result interchangeable to quantify the mean wind speed downstream of the barrier. The procedure adopted to estimate the apparent mean internal cross-wind speed is applied to drag force only. The experimental campaign includes tests aiming to study the aerodynamics of the van with or without the presence of barrier. In case of unscreened condition, where the subscript (*ws - without screen*) indicates the absence of the windbreak, the drag force can be defined as follows:

$$F_{D,ws}(U_\perp, C_{D,ws}) = \frac{1}{2} \cdot \rho \cdot U_\perp^2 \cdot A \cdot C_{D,ws} \tag{8.20}$$

where: ρ is the air density, $U_\perp$ is the external cross-wind speed, A is the area of the vehicle facing to the wind and $C_{D,ws}$ is the drag coefficient of the vehicle obtained in absence of the porous windbreak.

Solving the equation (8.20) for $C_{D,ws}$ it is possible to obtain the drag coefficient of the van for the unscreened case as:

$$C_{D,ws} = \frac{F_{D,ws}}{\frac{1}{2} \cdot \rho \cdot U_\perp^2 \cdot A} \tag{8.21}$$

In the same way the drag force for the screened condition, where the subscript (*sc - screened*) indicates the presence of the barrier, can be written as:

$$F_{D,sc}(U_\perp, C_{D,sc}) = \frac{1}{2} \cdot \rho \cdot U_\perp^2 \cdot A \cdot C_{D,sc} \tag{8.22}$$

where: $C_{D,sc}$ is the drag coefficient of the vehicle obtained in the presence of the porous windbreak.

If the following assumptions are introduced and verified during the tests:

- the effects of Reynolds number on the drag coefficient of the vehicle are not present or negligible;
- the pressure field around the vehicle does not strongly vary depending on the type of barrier.

the drag force measured for screened condition can be re-written in function of an apparent internal wind speed ($W_\perp$) and the unscreened drag coefficient ($C_{D,ws}$) as:

$$F_{D,sc}(W_\perp, C_{D,ws}) = \frac{1}{2} \cdot \rho \cdot W_\perp^2 \cdot A \cdot C_{D,ws} \tag{8.23}$$

Under these hypotheses the two drag forces in equation (8.22) and (8.23) are equal:

$$\begin{gathered} F_{D,sc}(U_\perp, C_{D,sc}) = F_{D,sc}(W_\perp, C_{D,ws}) \\ \frac{1}{2} \cdot \rho \cdot U_\perp^2 \cdot A \cdot C_{D,sc} = \frac{1}{2} \cdot \rho \cdot W_\perp^2 \cdot A \cdot C_{D,ws} \\ U_\perp^2 \cdot C_{D,sc} = W_\perp^2 \cdot C_{D,ws} \end{gathered} \tag{8.24}$$

then, the internal cross-wind speed can be obtained by a simple inversion of the last formula in equation (8.24) as:

$$\begin{aligned} W_\perp^2 &= U_\perp^2 \cdot \frac{C_{D,sc}}{C_{D,ws}} \\ W_\perp &= U_\perp \sqrt{\frac{C_{D,sc}}{C_{D,ws}}} \end{aligned} \tag{8.25}$$

It is fundamental to remember that the internal mean cross-wind speed is an apparent velocity obtained under particular assumptions. Furthermore, this apparent speed provides a measure of the reduction of the external cross-wind velocity due to the presence of the fence and it also gives an idea of the protection factor, expressed through the ratio of the drag coefficients. As expected, in case of full barrier the $C_{D,sc}$ is almost zero and the $W_\perp$ tends to zero. Vice versa if the barrier is not present, the $C_{D,sc}$ is equal to $C_{D,ws}$, then the internal wind speed corresponds to the external one ($W_\perp = U_\perp$). In this way, knowing the drag coefficient of the vehicle in screened condition, for different barriers, and in the unscreened case, it is possible to obtain a measure of the degree of protection of the shelter and quantify the internal cross-wind speed.

Extending this reasoning to the wind tunnel experimental tests performed in Chapter 7 on a model of Luton van, positioned downstream of a porous barrier, it is possible to quantify the shelter effect offered by different models of analysed barrier. Table 8.6 reports for each model of wind fence, the porosity level (ε), the drag coefficient measured on the van model ($C_{D,sc}$) and the ratio of screened and unscreened drag coefficients ($C_{D,sc}/C_{D,ws}$). Applying the simple formula in (8.25) and using the data collected in Table 8.6 it is easy to quantify the apparent internal cross-wind speed which the van is subject to, for different porosity levels of the windbreak.

Model	**Porosity %** (ε)	$C_{D,sc}$	$C_{D,sc}/C_{D,ws}$
Solid	00.00	0.0006	0.0005
R1.5T3	22.68	0.0511	0.0441
R3T5	32.65	0.0812	0.0701
R10U15	34.88	0.1047	0.0903
C3U5	36.00	0.1259	0.1087
C5U8	39.06	0.1503	0.1297
R2T3	40.31	0.1936	0.1671
R4T6	40.31	0.1745	0.1506
R6T9	40.31	0.1646	0.1420
R8T12	40.31	0.1623	0.1401
R10T15	40.31	0.1621	0.1399
LR5x20	43.81	0.2095	0.1808
C10U15	44.40	0.2146	0.1852
R10U14	44.40	0.2148	0.1854
C6U9	44.44	0.2276	0.1964
C8U12	44.44	0.2238	0.1931
Nr.152	45.00	0.2393	0.2065
R5T7	46.28	0.2728	0.2354
R10T14	46.28	0.2676	0.2309
C8U10	64.00	0.4571	0.3945
H2T90	64.00	0.4877	0.4209
C10U12	69.40	0.5570	0.4807
No-barrier	100.00	1.1587	1.0000

Table 8.6 Shelter effect for different windbreaks.

From the Table 8.6 can be noticed that the ratio $C_{D,sc}/C_{D,ws}$ increases at the increasing of porosity level. More in detail, $C_{D,sc}/C_{D,ws}$ is equal to 1 when no barrier is installed and tends to zero when a solid windbreak is employed. In case of solid barrier the ratio is not properly equal to zero ($C_{D,sc}/C_{D,ws} = 0.0005$) due to negligible experimental errors that are encountered during the measurements of the drag force.

In order to protect the users of the viaduct from the external wind action, especially for the most exposed types of vehicle such as the Luton van, it is fundamental to correctly choose the typology of barrier that has to be employed. The best way

to take this decision is to create a general model of the viaduct, windbreak and Luton van in the wind tunnel and to perform some measuring of the aerodynamic forces. In this case there are not available data on the above experimental set-up, but it is assumed that the data obtained for the model of van and windbreaks exposed in Chapter 7 can be reasonably extended also to this case study. Clearly this assumption is affected by errors because the aerodynamic behaviour of the deck-barrier system is not considered, but it is quite reliable if only the wind effects on the users are taken into account. For this application example is assumed to place on the viaduct two 4 m high porous windbreaks, with the same characteristics of the tested barriers and respecting the scaling procedure explained in Chapter 6. In order to include in internal cross-wind speed also the contributions of anemometric data and infrastructure parameters ($z = 40$ m and $\alpha = 55°$), the equation (8.25) can be modified as:

$$W_{\perp}(40,\theta) = U_{\perp}(40,\theta)\sqrt{\frac{C_{D,sc}}{C_{D,ws}}} \tag{8.26}$$

Using the equation (8.26) for all of the 23 porous windbreaks it is possible to pass from external to internal cross-wind speed on the viaduct and operate a comparison between the different barriers.

8.3.2 Overturning conditions

The study presented by Carr *et al.* (1993) reports for several typologies of large commercial vehicles (Luton van, draw bar trailer, articulated lorry, petrol tanker, tipper truck, bus, etc.) the overturning critical mean cross-wind speed in function of the vehicle velocity.

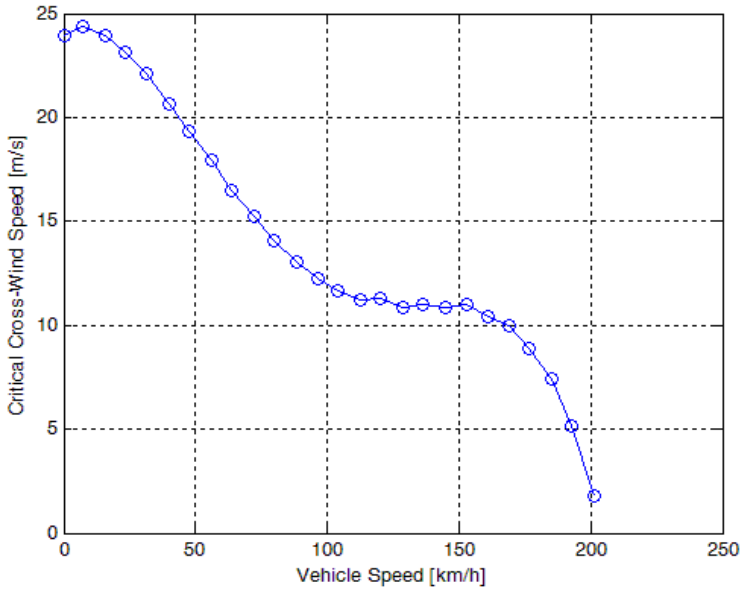

Fig. 8.19 Overturning critical cross-wind speed vs. vehicle velocity for a Luton van.

The limit curves reported by Carr *et al.* (1993) are obtained combining the aerodynamic effects of the high-sided vehicles, evaluated by wind tunnel test, with the mechanical model of the vehicle dynamics (tyres, suspension, etc.). As an example Fig. 8.19 reports the critical limit curve for overturning instability of the Luton van, that is the reference vehicle for this work. This kind of van is vulnerable to overturning instability due to its poor aerodynamic behaviour, and because it is authorised to circulate at high speed. Indeed the speed limits for Luton van are the same as for the classical cars. In fact observing the limit curve in Fig. 8.19 it can be noticed the non-negligible decrement of the critical cross-wind speed passing from 90 km/h (speed limit for Italian extra-urban roads) to 130 km/h (speed limit for Italian highways). In correspondence to these two speed limits the critical cross-wind speed changes from 12.8 m/s to 10.8 m/s, thereby increasing the risk of roll-over. This reasoning can be simply extended also to other typologies of road vehicles, considering their relative limit curves exposed in Chapter 2.

Thanks to the limit curves and fixing the vehicle velocity it is possible to define the probability of overturning as follows:

$$\begin{aligned} P(\text{Overturning}|W_\perp) &= 0 \qquad W_\perp \leq w_{\perp,crit} \\ P(\text{Overturning}|W_\perp) &= 1 \qquad W_\perp > w_{\perp,crit} \end{aligned} \tag{8.27}$$

The overturning phenomenon is a deterministic event that occurs if the internal cross-wind speed ($W_\perp$) exceeds the overturning threshold ($w_{\perp,crit}$) and does not occur if $W_\perp$ is less or equal than $w_{\perp,crit}$. Fig. 8.20 highlights this concept for a Luton van moving at 130 km/h on a road infrastructure.

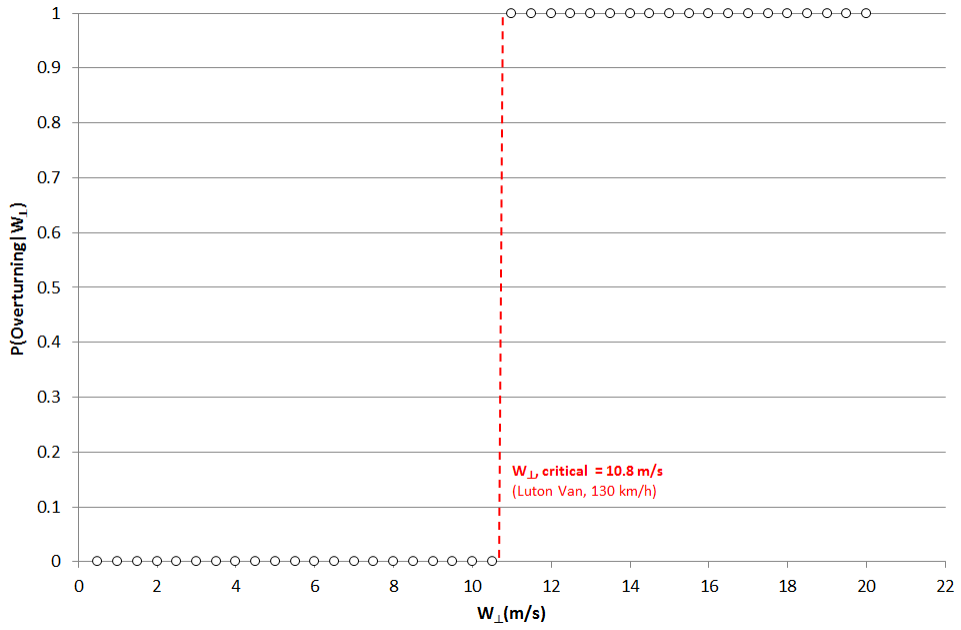

Fig. 8.20 $P(\text{Overturning}|W_\perp)$ for a Luton van moving at 130 km/h.

Using this deterministic model of vulnerability it is possible to define the overturning safety as:

$$W_{\perp} \leq w_{\perp,crit} \tag{8.28}$$

then, in this particular case study the inequality (8.28) becomes:

$$W_{\perp}(40,\theta) \leq w_{\perp,crit} \tag{8.29}$$

that has to be satisfied in order to avoid the problem of Luton van overturning.

8.4 Probability of failure and risk

The probability of failure ($P_{Failure}$) corresponds to the overturning of the vehicles and it is defined as the probability to have an internal cross-wind speed at the level of the viaduct higher than a certain limit threshold for the cross-wind speed ($w_{\perp,crit}$). In terms of average value of hours per year in which the analysed infrastructure has to be closed to traffic in order to avoid overturning problems, the corresponding risk can be estimated by the following relation:

$$\begin{aligned} Risk &= P_{Failure} \cdot h_{year} \\ Risk &= P(W_{\perp} > w_{\perp,crit}) \cdot h_{year} \end{aligned} \tag{8.30}$$

where: $h_{year} = 8760$, that is the number of hours in a year.

The analytic expression that allows to pass from the reference anemometric wind data to the internal cross-wind speed for the analysed viaduct, for all the different typologies of barriers, is composed of two deterministic models. In fact both the equations (8.18) and (8.25) do not contain any random element with the exception of the single wind speed component. Thus the only element with a stochastic character in the whole risk analysis is represented by the anemometric wind data of Monte Argentario. The anemometric data are firstly converted into external cross-wind speeds at the reference altitude (z) and orientation (α) of the viaduct ($U_{\perp}(40,\theta)$) using the formula (8.19) and then changed into internal cross-wind speed ($W_{\perp}(40,\theta)$) using the deterministic model (8.26).

Fig. 8.21 reports the joint Burr probability of exceedance of the external cross-wind speed. It has the aim to show the role played by the infrastructure parameters on the wind speed data. As expected the cross-wind speed component presents maximum values for the directions of wind that are closer to the perpendicular to the longitudinal axis of the viaduct. In addition it is also remarkable the effect played by the altitude, in fact the velocities are higher than those reported in Fig. 8.13, of about 30 %, due to the wind speed profile factor.

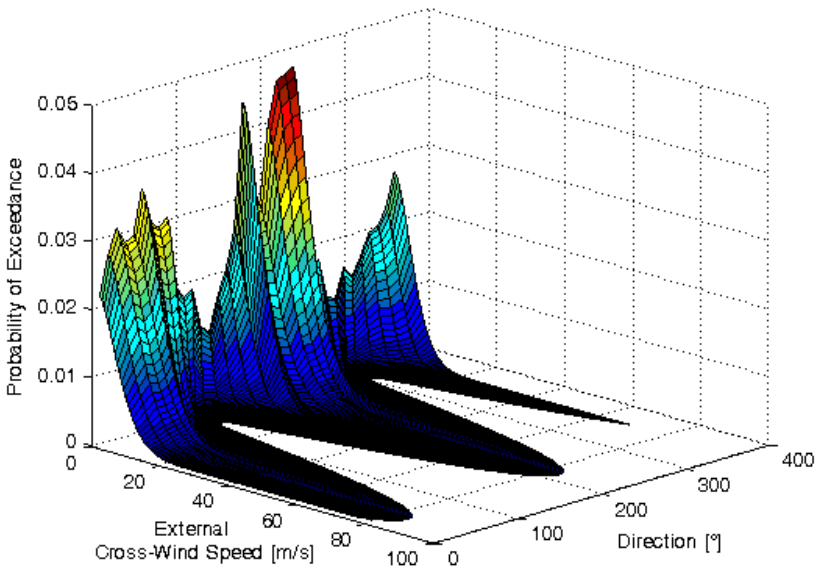

Fig. 8.21 Burr joint probability of exceedance $P(U_{\perp}(40) > u_{\perp}, \theta_i^- < \theta < \theta_i^+)$.

Fig. 8.22 reports the marginal probability of exceedance of the external cross-wind speeds at the reference altitude and for the given orientation of the viaduct. This distribution does not consider the dependency on wind direction (θ), as the probability is obtained as the sum of each individual sectoral contribution.

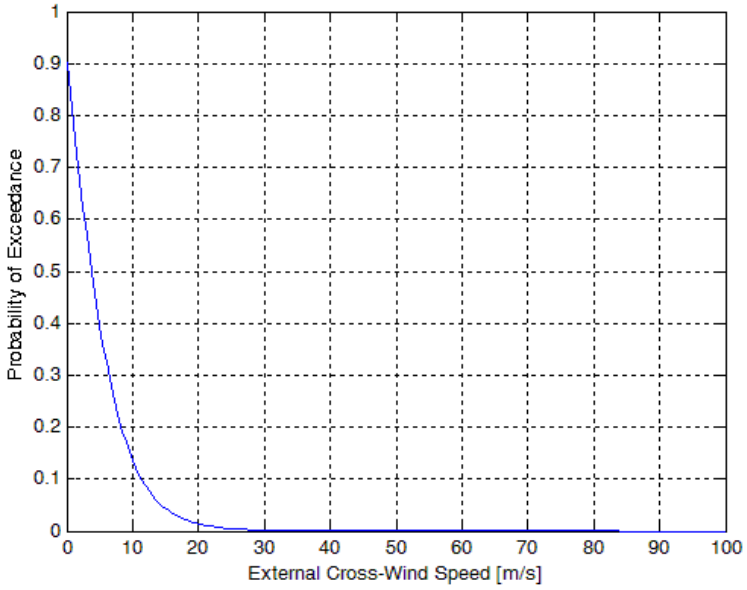

Fig. 8.22 Burr marginal probability of exceedance $P(U_{\perp}(40) > u_{\perp})$.

The probability reported in Fig. 8.21 and Fig. 8.22 represents also the probability of exceedance of internal cross-wind speed for the case in which any windbreak is not installed on the viaduct deck; indeed, only in this condition the external cross-wind speed is equal to the internal one.

At this point knowing the probabilistic model of external cross-wind speed, using the deterministic model (8.26) and the experimental data reported in Table 8.6, it is possible to quantify the internal cross-wind speed for 23 different windbreaks and operate the risk treatment in accordance with the general risk framework proposed by Pliefke *et al.* (2007). Fig. 8.23 reports the effect played by a particular model of porous windbreak on the Burr joint probability function.

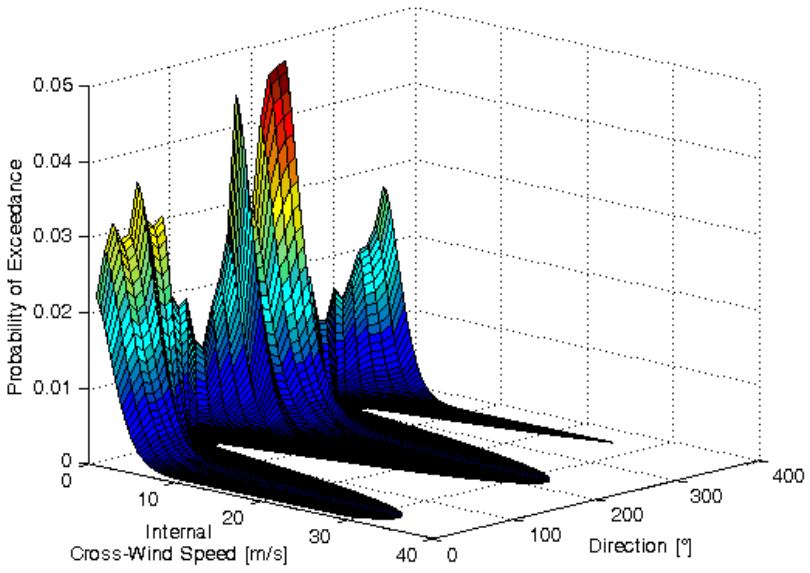

Fig. 8.23 Burr joint probability of exceedance $P(W_{\perp}(40) > w_{\perp}, \theta_i^- < \theta < \theta_i^+)$, for the barrier R4T6 ($\varepsilon = 40.31$ %).

Fig. 8.23 exhibits an aspect quite similar to Fig. 8.22 but with a strong reduction of the internal cross-wind speed. In particular, the barrier R4T6 ($\varepsilon = 40.31$ %) operates a decrease of wind velocity of about 55 %. Then, using the limit levels and the relative curve for the overturning stability of the Luton van (Fig. 8.19) it is possible to quantify the probability of failure given in the equation (8.30).

Fig. 8.24 shows in a graphical way the definition of probability of failure given in (8.1). In fact the graph reports for unscreened condition the 3D surface of the Burr joint probability distribution function for the internal cross-wind speed superimposed with the critical value of cross-wind speed. The critical value of wind velocity for overturning of Luton van is represented by a 3D red limit plane (achieved fixing a vehicle speed equal to 130 km/h). The value of the probability of exceedance, obtained from the solid interpenetration between the surface of distribution and the red plane, represents the relative probability of failure in correspondence of each wind direction.

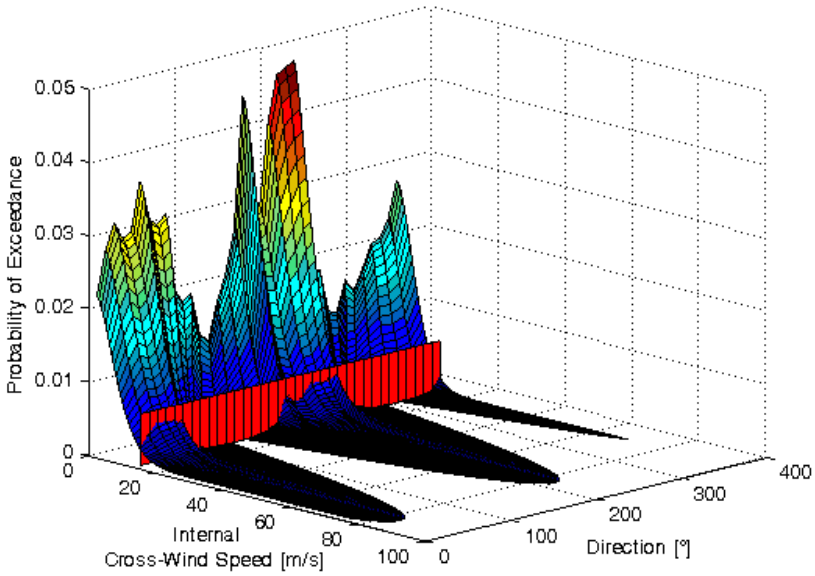

Fig. 8.24 Burr joint probability of exceedance $P(W_{\perp}(40) > w_{\perp}, \theta_i^- < \theta < \theta_i^+)$ for unscreened condition and limit plane ($w_{\perp,crit}$).

Fig. 8.25 reports the marginal probability of exceedance, obtained by adding the individual contributions of probability for all wind sectors, in correspondence of different typologies of barrier.

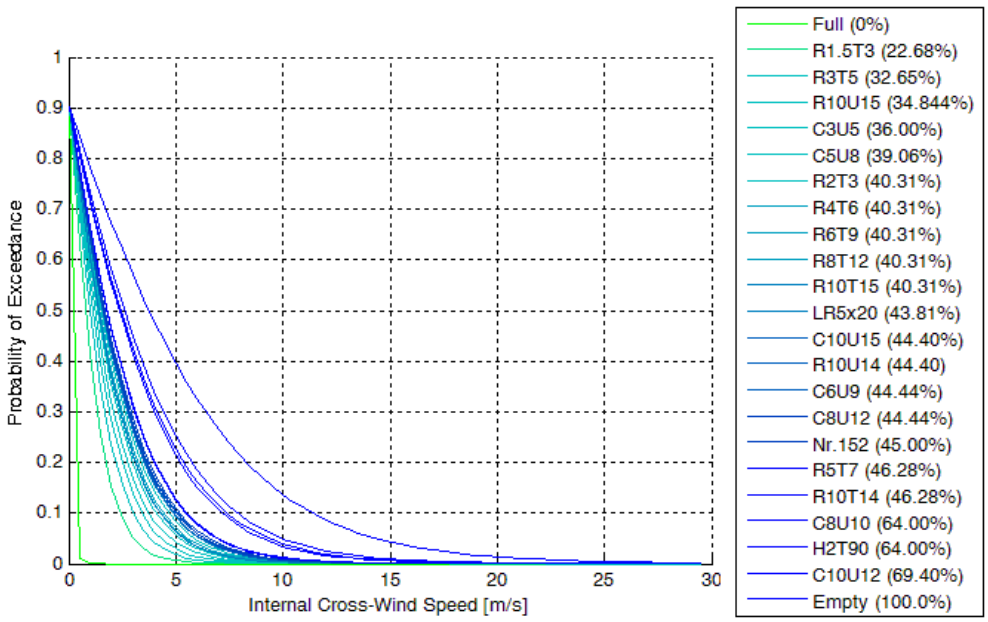

Fig. 8.25 Marginal probability of exceedance $P(W_{\perp}(40) > w_{\perp})$ for different shelter conditions.

The types of barriers are represented by means of the scale of colours that go from green (*full screened condition*) to blue (*unscreened condition*) in order to highlight the effects of porosity level on the probability distribution. As expected, increasing the porosity, the internal cross-wind speed also increases.

Fig. 8.26 reports in probabilistic terms the limit curve for the overturning of the Luton van (Fig. 8.19) for different levels of shelter. In fact, on the y-axis the critical cross-wind speed is replaced by the related probability of overturning (calculated using the wind data of Monte Argentario station and applyed to the system viaduct-barrier). Also in this case the role played by the different typologies of barrier is represented with different colour tonalities.

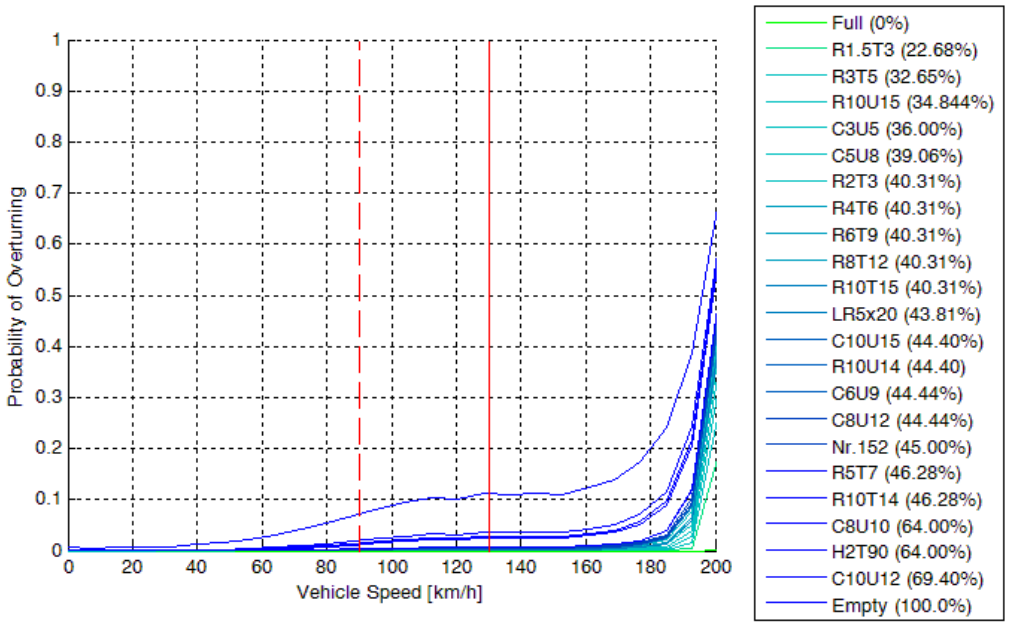

Fig. 8.26 Probability of overturning vs. Luton van speed.

The diagram puts in relationship the probability of vehicle overturning with the driving velocity of Luton van with superimposed the common speed limits for the Italian roads: 90 km/h on the extra-urban roads (broken red line) and 130 km/h on the highways (continuous red line).

The risk quantification is calculated referring to the marginal probability of exceedance (probability of failure) and it represents the number of hours in a year in which the viaduct has to be closed to traffic, in order to avoid the Luton van overturning. A further hypothesis that has to be introduced is related to the vehicle speed, because the probability of failure is a function of it. Indeed it is assumed that the Luton van crosses the viaduct at the maximum allowable velocity to circulate on a given road infrastructure, according to the Italian Road Code (*Infrastructure and Transport Ministry Decree n. 285 of April 1992 and subsequent modifications and additions*). At this point it is possible to build graphs that report the risk, quantified applying the equation (8.30), for the different shelter conditions.

This particular risk analysis allows to cover also the point of *risk treatment* explained by Pliefke *et al.* (2007), because the risk of overturning is mitigated by the introduction of porous windbreak suitably selected.

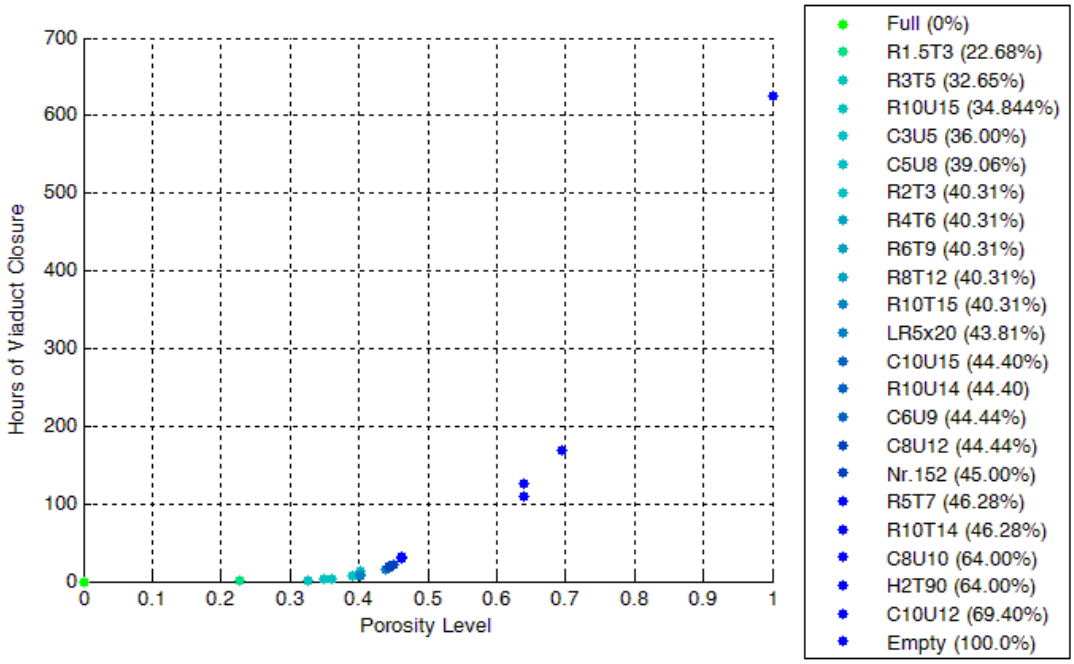

Fig. 8.27 Hours of viaduct closure vs. porosity level for Luton moving at 90 km/h.

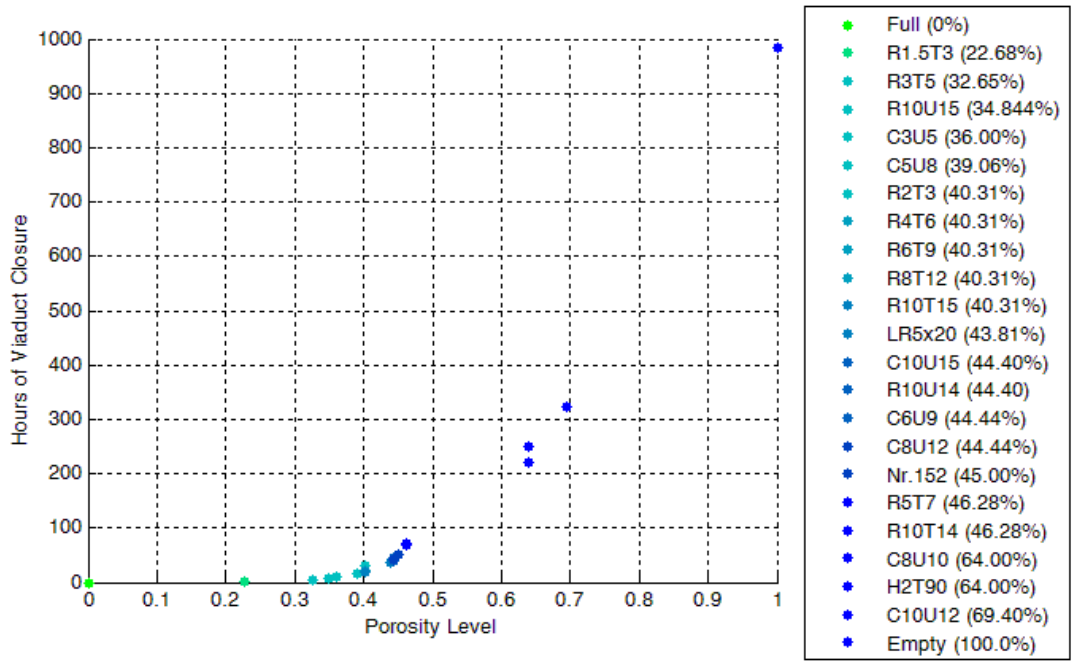

Fig. 8.28 Hours of viaduct closure vs. porosity level for Luton moving at 130 km/h.

In order to avoid the roll-over of Luton van crossing the viaduct at 90 km/h or 130 km/h, Fig. 8.27 and Fig. 8.28 show the average number of hours in a year where the viaduct is expected to be closed due to high cross-winds. Fig. 8.28 stresses also the necessity to adopt a risk mitigation measure since the viaduct in exam will be closed for about 1000 hours in a year (40 days in a year). As a matter of fact Juricko (2008) reports in its study that a closure of a given road infrastructure for 220 hours in a year is non-economic and leads to large negative consequences in terms of human and social impacts. Moreover this number of hours should be further reduced if the road infrastructure is strategic and of primary importance. For similar reasons the paper by Smith and Barker (1998) fixed at 40 the maximum number of hours of closure in a year for several typologies of road infrastructures.

Table 8.7 collects the number of annual closing hours for the reference viaduct obtained for the two different driving velocities of the Luton van (90 km/h and 130 km/h).

Model	**Porosity %**	**90 km/h**	**130 km/h**
Full	00.00	0	0
R1.5T3	22.68	0	1
R3T5	32.65	1	3
R10U15	34.88	2	6
C3U5	36.00	4	10
C5U8	39.06	7	16
R2T3	40.31	13	30
R4T6	40.31	10	23
R6T9	40.31	8	20
R8T12	40.31	8	19
R10T15	40.31	8	19
LR5x20	43.81	16	37
C10U15	44.40	17	39
R10U14	44.40	17	39
C6U9	44.44	20	46
C8U12	44.44	19	44
Nr.152	45.00	22	52
R5T7	46.28	31	71
R10T14	46.28	30	68
C8U10	64.00	109	221
H2T90	64.00	126	251
C10U12	69.40	168	323
Empty	100.00	625	983

Table 8.7 Hours of viaduct closure for different speeds of Luton van.

Combining these literature references and the data reported in Table 8.7 it is possible to define a limit threshold for porosity level of the wind barriers in order to protect the viaduct users. For example, fixing at 130 km/h the reference velocity of the Luton van and at 40 hours the maximum number of hours per year of closure

of the viaduct (Smith and Barker, 1998), the maximum porosity level of the barrier which must be considered is equal to 44.40 % (Fig. 8.29).

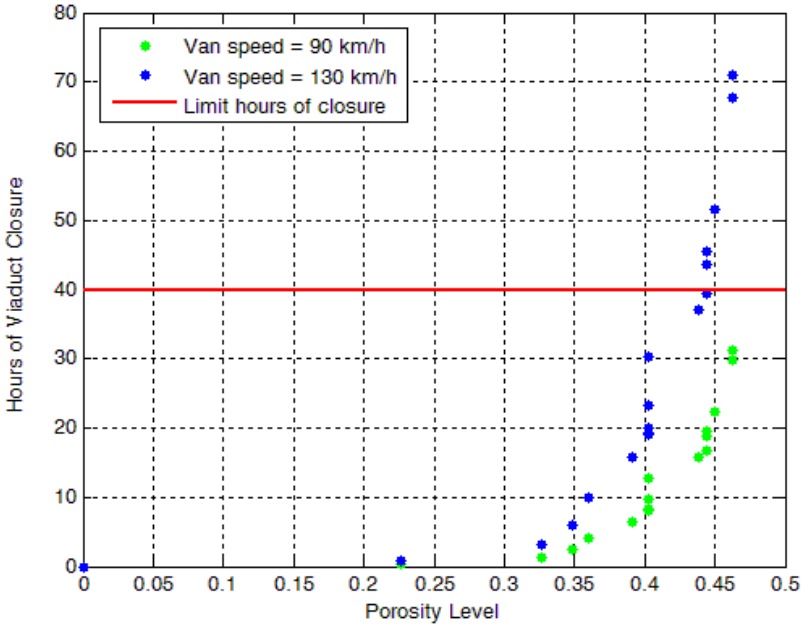

Fig. 8.29 Limit number of hours of closure of the viaduct.

Under this limit condition the suitable windbreaks are those with porosity in the range from 0 % to 44.40 %. The choice of a lower limit for the porosity level, not considered in this work, is problematic because it is function of many variables, such as the structural aspects of infrastructure and the cost-benefit factor. In fact, it should be noticed that viaducts or bridges equipped with barriers having a lower level of porosity are surely more comfortable for the users but they present a worse aerodynamic response. Introducing a solid barrier on a viaduct it would be possible to have zero hours of closure but it would cause a higher wind load on the whole infrastructure able to compromise structural behaviour of the viaducts [Ricciardelli *et al.* (2002); Kleinhanss *et al.* (2007)]. Indeed, Ricciardelli (2003) reports that the addition of the new jersey barriers on a cable-stayed bridge deck (WT model of Sunshine Skyway bridge) brings substantial modification to both mean and RMS pressure distributions around the bridge deck. More in particular the introduction of traffic barriers leads to almost double the fluctuating pressure coefficients in the leeward portion of the deck, which explains the larger dynamic torsional response of the deck with barriers, with respect to the deck without them. Even more significant are the changes observed on the pressure distributions for the oscillatory structure. In fact the vulnerability to aero elastic phenomena like vortex shedding lock-in and flutter is significantly enhanced. Flutter and lock-in are extremely dependent on the cross-section of the bridge deck and they are highly influenced by appendages and vertical plates (windbreaks, traffic barriers) positioned along the deck surface. For this reasons, Trein and Shirato (2011) have investigated the influence of several

unsteady pressure patterns around bridge decks on the flutter derivatives in order to identify the pressure distribution that minimize the flutter instability.

If the reference infrastructure is a principal road, positioned at ground level, the structural aerodynamic effects are mainly translated in terms of global static loads acting on the barrier and are more easily linked to costs. In fact imagining to realize barriers with high porosity level the costs for the realization of the structures of foundation are definitely lower than in the case with null or low porosity because the wind loads on the barrier are surely of minor entity.

In addition to structural problem it is necessary to consider also environmental and architectural impacts that are strictly linked to the presence of the barrier. Very often the pleasure of crossing a viaduct or a long span bridge relates to the beauty of the landscape that is possible to admire which would be absolutely denied if windbreak barriers are employed.

The inclusion of all these additional aspects can be seen as a starting point for future developments of this research. In this way it would be possible to operate a risk mitigation including several strategic factors like user safety, structural aspects and environmental and architectural impacts.

Chapter 9

General conclusions and outlook

This doctoral work deals with the strategies of mitigation of high cross-winds on road infrastructures in order to minimize the risk of overturning for large commercial vehicles (trucks, lorries, vans) through the introduction of porous wind fences. This aspect is nowadays recognized as a key issue in the design of several road infrastructures due to the high number of accidents and fatalities that happen on European routes every year.

The contribution of this thesis is double fold. Firstly, it aims to define a comprehensive scaling criterion that can be used when wind tunnel tests on porous structures are required. Secondly, it aims to provide a procedure to quantify the risk associated with the overturning issue of large vehicles for different levels of sheltering.

The existing literature is a bit evasive and elusive about the correct scaling of porous structure in wind tunnel tests, or at least there is not a general similitude criterion. In particular, the geometric scaling of porous elements is difficult or almost impossible to realize. This depends on the difficulty in representing at the wind-tunnel scale those entities that are already small at full scale, such as the little openings of the porous structures. The scaling procedure is the missing tool that allows to perform extrapolations between a wind tunnel model and the prototype. Several porous samples were experimentally studied in the CRIACIV wind tunnel in two different flow conditions (confined and unconfined) in order to get data able to define a rule of scale. The scaling criterion consists in applying the classical geometric scaling process for the general dimensions of the structure and satisfying particular requirements only for those elements that can be schematized as a porous medium. The basic prescriptions that have to be respected in the porous core, passing from the prototype to wind tunnel model, concern the porosity level, the shape and arrangement of the holes, the ratio of thickness to hydraulic diameter, and the Reynolds number.

The second contribution is the development of a simple vehicle overturning risk procedure that is able to cover the entire risk chain (risk identification, risk assessment and risk treatment) explained by Pliefke *et al.* (2007). In fact, after the identification of the hazard (cross-wind action) and the relative vulnerability of the system (vehicle on a windy viaduct) the risk is quantified and treated to be minimized. In the hazard part an alternative to the Weibull probability distribution

for the modelling of historical anemometric wind data is proposed (Burr type XII probability function). In the vulnerability part of the work, thanks to the wind tunnel tests, conceived on the basis of the previously mentioned rule of scale, the cross-wind action on a model of commercial vehicle (Luton van) has been determined in correspondence of several conditions of sheltering. In order to establish if the overturning phenomenon may occur, a critical threshold for the overturning cross-wind speed, in function of the speed of the vehicle, is determined after a literature review. In the risk analysis, using the results of the hazard and vulnerability steps, the probability of failure, i.e. of vehicle overturning, for different conditions of sheltering is quantified. In this way it is possible to choose a barrier, with a given level of porosity, rather than another, depending on the level of risk that may be accepted and the speed limit for the vehicle in the given road infrastructure. This simple risk procedure could be of greater help for practitioners, especially during the stages of design or intervention on an existing road infrastructure when the effects of high cross-winds have to be mitigated.

Clearly the outlined risk procedure is able to provide only the maximum porosity of barriers that can be chosen to guarantee user safety towards the overturning phenomenon. Nevertheless, also the choice of a lower limit, not considered in this thesis, is an important issue which depends on many variables, such as the structural aspects of the infrastructure, the cost-benefit factor and the environmental and architectural impacts. The inclusion in the risk analysis of all these additional aspects pave the way for future developments of the present research work.

Bibliography

Alhajraf, S. (2004). Computational fluid dynamic modeling of drifting particles at porous fences. *Environmental Modelling and Software*, **19**, 163–170.

Allori, D. and Nuti, M. (2008). *Risposta srutturale ed analisi del comfort delle passerelle pedonali: Sperimentazione in galleria del vento.* Master's thesis, University of Florence - Faculty of Engineering.

Annand, W. J. D. (1953). The resistance to air flow of wire gauzes. *Journal of Royal Aeronautical Society*, **57**, 141–146.

Antohe, B. V. and Lage, J. L. (1997). A general two-equation macroscopic turbulence model for incompressible flow in porous media. *Journal of Heat and Mass Transfer*, **40**(13), 3013–3024.

AS/NZS-4360 (1999). Risk management.

Augusti, G., Borri, C., and Niemann, H. (2001). Is Aeolian risk as significant as other environmental risks? *Journal of Reliability Engineering and System Safety*, **74**, 227–237.

Auwera, L., Meyer, F., and Malet, L. (1980). The use of the Weibull three-parameter model for estimating mean wind power densities. *Journal of Climate and Applied Meteorology*, **19**, 819–825.

Baines, W. D. and Peterson, E. (1951). An Investigation of Flow Through Screens. *Transactions of the American Society of Mechanical Engineers*, **73**, 467–480.

Baker, C. (1991a). Ground vehicles in high cross winds part I: Steady aerodynamic forces. *Journal of Fluids and Structures*, **5**(1), 69–90.

Baker, C. (1991b). Ground vehicles in high cross winds part III: The interaction of aerodynamic forces and the vehicle system. *Journal of Fluids and Structures*, **5**(2), 221–241.

Baker, C. and Reynolds, S. (1992). Wind-induced accidents of road vehicles. *Journal of Accident Analysis and Prevention*, **24**(6), 559–575.

Baker, C., Wood, C., and Gawthorpe, R. (1985). Strong winds in complicated hilly terrain - field measurements and wind-tunnel study. *Journal of Wind Engineering and Industrial Aerodynamics*, **18**(1), 1–26.

Basak, P. (1977). Non-Darcy Flow and Its Implications to Seepage Problems. *Journal of the Irrigation and Drainage Division*, **103**, 459–473.

Bear, J. (1972). *Dynamics of Fluids in Porous Media*. Elsevier, New York.

Bejan, A. (1995). *Entropy Generation Minimization*. CRC Press, Boca Raton.

Bejan, A., Dincer, I., Lorente, S., Miguel, A. F., and Reis., A. (2004.). *Porous and Complex Flow Structures in Modern Technologies*. Springer-Verlag, New York.

Bitzel, F. (1962). Die Einwirkung von Seitenwindkrafter auf den Strassenverkehr. *Zeitschrift für Verkehrssicherheit*.

Bofah, K. and Alhinai, K. (1986). Field tests of porous fences in the regime of sand laden wind. *Journal of Wind Engineering and Industrial Aerodynamics*, **23**, 309–319.

Boldes, U., Colman, J., Maranon, J., and Leo, D. (2001). Field study of the flow behind single and double row herbaceous windbreaks. *Journal of Wind Engineering and Industrial Aerodynamics*, **89**, 665–687.

Borges, A. R. and Viegas, D. (1988). Shelter effects on a row of coal piles to prevent wind erosion. *Journal of Wind Engineering and Industrial Aerodynamics*, **29**, 145–154.

Borri, C. and Briganti, D. (2006). *L'ingegneria del vento: un'antica, modernissima scienza*. Firenze University Press, Florence.

Brandle, J. and Finch, S. (1991). How Windbreaks Work. Technical report, University of Nebraska Cooperative Extension.

Brundrett, E. (1993). Prediction of pressure-drop for incompressible-flow through screens. *Journal of Fluids Engineering*, **115**, 239–242.

Buccolieri, R., Gromke, C., Sabatino, S. D., and Ruck, B. (2009). Aerodynamic effects of trees on pollutant concentration in street canyons. *Journal of Science of the Total Environment*, **407**(19), 5247–5256.

Burr, I. W. (1942). Cumulative frequency functions. *Annals of Mathematical Statistics*, **13**, 215–232.

Carr, G. W., Ing, E., and Rose, M. (1993). Cross wind stability of vehicles on bridges. *Safety and the Automobile, AUTOTECH93*, **1**, 16–19.

Carta, J., Ramirez, P., and Velsquez, S. (2009). A review of wind speed probability distributions used in wind energy analysis. Case studied in the Canary Islands. *Journal of Renewable and Sustainable Energy Reviews*, **13**, 933–955.

Castro, I. (1971). Wake characteristics of two-dimensional perforated plates normal to an air stream. *Journal of Fluid Mechanics*, **46**, 599–609.

Chen, X. and Kareem, A. (2003). Aeroelastic Analysis of Bridges: Effects of Turbulence and Aerodynamic Nonlinearities. *Journal of Mechanical Engineering*, **129**, 885 – 895.

Chepil, W. S. (1945). Dynamics of wind erosion. Nature of movement of soil by wind. *Journal of Soil Science*, **60**, 305–320.

Chhabra, R. P. (1993). *Bubbles, drops, and particles in non-Newtonian fluids.* CRC Press, Boca Raton.

Clarke, C. and Caroline, P. (2000). Facing the Challenge of Natural Disasters in Latin America and the Caribbean: An IDB Action Plan. Technical report, Inter-American Development Bank.

Coleman, S. and Baker, C. (1990). High sided road vehicles in cross winds. *Journal of Wind Engineering and Industrial Aerodynamics*, **36**(Part 2), 1383–1392.

Collins, R. (1961). *Flow of Fluids Through Porous Materials.* Van Nostrand, New York.

Comiti, J., Sabiri, N., and Montillet, A. (2000). Experimental characterization of flow regimes in various porous media. Limit of Darcy or creeping flow regime for Newtonian and purely viscous non-Newtonian fluids. *Journal of Chemical Engineering Science*, **55**, 3057–3061.

Cook, N. J. (1990). *The designers guide to wind loading of building structures. Part 2. Static structures.* Butterworths, London.

Cooper, R. (1978). Tests on $1/5^{th}$ scale model APT-P in the MIRA wind tunnel. Technical report, British Rail Research. TMAERO 28.

Cooper, R. (1979). The effects of cross winds in trains. *Aerodynamic of Transportation*, **1**, 127–136.

Cooper, R. (1982). Wind tunnel tests on a $1/25^{th}$ scale ATP-P model. Technical report, British Rail Research. TMAERO 43.

Copley, J. (1987). The three-dimensional flow around railway trains. *Journal of Wind Engineering and Industrial Aerodynamics*, **26**(1), 21–52.

Cornell, W. G. (1958). Losses in flow normal of plane screens. *Transactions of the American Society of Mechanical Engineers*, **80**, 791–799.

Davenport, A. G. (1972). An approach to human comfort criteria for environmental wind conditions. In *Colloqium on Building Climatology.*

Deaves, D. and Lines, I. (1997). On the fitting of low mean windspeed data to the Weibull distribution. *Journal of Wind Engineering and Industrial Aerodynamics*, **66**, 169–178.

Dierickx, W., Cornelis, W. M., and Gabriels, D. (2003). Wind Tunnel Study on Rough and Smooth Surface Turbulent Approach Flow and on Inclined Windscreens. *Journal of Biosystems Engineering*, **86**(2), 151–166.

Dong, Z., Qian, G., Luo, W., and Wang, H. (2006). Threshold velocity for wind erosion: the effects of porous fences. *Journal Environmental Geology*, **51**, 471–475.

Dong, Z., Luo, W., Qian, G., and Wang, H. (2007). A wind tunnel simulation of the mean velocity fields behind upright porous fences. *Journal of Agricultural and Forest Meteorology*, **146**(1-2), 82–93.

DuBois, D. (1916). A formula to estimate the approximate surface area if height and weight be known. *Archives of Internal Medicine*, **17**, 863–871.

Dullien, F. (1992). *Porous Media: Fluid Transport and Pore Structure*. Academic Press, Massachusetts.

Dybbs, A. and Edwards, R. (1984). *A new look at porous media fluid mechanics Darcy to turbulent, Fundamentals of Transport Phenomena in Porous Media Flow*. Martinus Nishoff, Dordrecht.

Emmelmann, H. (1987). Driving stablity in side winds. *Aerodynamic of Road Vehicles*, **1**, 214–235.

ESDU81039 (1985). Flow of liquids. Pressure losses across orifice plates, perforated plates and thick orifice plates in ducts. Technical report, ESDU.

Eurocode-1 (1991). Eurocode 1 - Actions on structures - Part 1-4: General actions - Wind actions. Technical report, European Union.

European-C14 (2001). Impact of wind and storm on city life and built environment. In *European Cost Action C14*. European Cost Action C14.

Evans, C. L. (1949). *Principles of Human Physiology*. Lea and Febiger, Philadelphia.

Fang, F. and Wang, D. (1997). On the flow around a vertical porous fence. *Journal of Wind Engineering and Industrial Aerodynamics*, **67-68**, 415–424.

Fatnassi, H., Boulard, T., and Bouirden, L. (2003). Simulation of climatic conditions in full-scale greenhouse fitted with insect-proof screens. *Journal of Agricultural and Forest Meteorology*, **118**(1-2), 97–111.

FORCE-Technology (2002). Wind tunnel tests with Cour de Justice des Communautees Europèennes. Technical report, DMI 2002152.

Gan, G. and Riffat, S. B. (1997). Pressure loss characteristics of orifice and perforated plates. *Journal of Experimental Thermal and Fluid Science*, **14**(2), 160–165.

Gandemer, J. (1975). Wind environment around buildings: aerodynamic concept. In *Fourth International Colloqium on Wind Effects on Buildings and Structures, Heathrow*.

Gandemer, J. (1978). Aerodynamic studies on built-up areas made by C. S. T. B. at Nantes, France. *Journal of Wind Engineering and Industrial Aerodynamics*, **3**, 227–240.

Ganoulis, J., Brunn, P., Durst, F., Holweg, J., and Wunderlich, A. (1989). Laser measurements and computations of viscous flows through cylinders. *Journal of Hydraulic Engineering*, **115**, 1123–1140.

Gatzen, C., Pucik, T., and Ryva, D. (2011). Two cold-season derechoes in Europe. *Journal of Atmospheric Research*, **100**, 740–748.

Geyer, S. (2008). *Scaling principles for bridge deck furniture and effect on aerodynamic performance of section models.* Master's thesis, University of Florence - Faculty of Engineering.

Gold, E. (1935). The effect of wind, temperature, humidity and sunshine on the loss of heat of a body at temperature 98°F. *Quarterly Journal of the Royal Meteorological Society*, **61**, 316–346.

Grootenhuis, P. (1954). A correlation of the resistance to air of wire gauzes. *Proceedings of the Institution of Mechanical Engineers*, **168**, 837–846.

Groth, J. and Johansson, A. V. (1988). Turbulence reduction by screens. *Journal of Fluid Mechanics*, **197**, 139–155.

Guan, D., Zhang, Y., and Zhu, T. (2003). A wind-tunnel study of windbreak drag. *Journal of Agricultural and Forest Meteorology*, **118**(1-2), 75–84.

Hagen, L. and Skidmore, E. (1971). Turbulent velocity fluctuations and vertical flow as affected by windbreak porosity. *Transactions of the American Society of Agricultural Engineers*, **14**, 634–637.

Hall, M. and Hiatt, J. P. (1996). Measurements of pore scale flows within and exiting ceramic foams. *Journal of Experiments in Fluid*, **20**, 433–440.

Heisler, G. M. and Dewalle, D. R. (1988). Effects of windbreak structure on wind flow. *Journal of Agriculture, Ecosystems and Environment*, **22-23**, 41–69.

Hill, R. and Koch, D. (2002). The transition from steady to weakly turbulent flow in a close-packed ordered array of spheres. *Journal of Fluid Mechanics*, **465**, 59–97.

Hoerner, S. (1965). *Fluid-Dynamic Drag.* Hoerner Fluid Dynamics, New York.

Honda, A., Ito, M., and Kimura, H. (1992). Aerodynamic instability of pre-stressed concrete cable-stayed bridge with noise barrier. *Journal of Wind Engineering and Industrial Aerodynamics*, **41/44**, 1169–1180.

Hunt, J. C. R., Poulton, E., and Mumfort, J. (1976). The effects of wind on people; new criteria based on wind tunnel experiments. *Journal of Building and Environment*, **11**, 15–28.

Hunt, J. R. and Poulton, E. (1972). Some effects of wind on people. In *Proceedings of Conference on External Flows at Bristol University.*

Idelchik, I. (1994). *Handbook of Hydraulic Resistance.* CRC Press, Boca Raton.

ISO31000 (2009). Risk management, principles and guidelines.

ISO73 (2009). Risk management and vocabulary.

Isyumov, N. and Davenport, A. (1978). Evaluation of the effects of tall buildings on pedestrian level wind environment. In *ASCE Annual Convention*.

Isyumov, N. and Davenport, A. G. (1975). The ground level wind environment in built-up areas. In *Fourth International Colloqium on Wind Effects on Buildings and Structures, Heathrow*.

Iversen, J. (1981). Comparison of wind tunnel modeling and fullscale snow fence drifts. *Journal of Wind Engineering and Industrial Aerodynamics*, **8**, 231–249.

Jacobs, A. (1985). The normal force coefficient on a thin closed fence. *Boundary Layer Meteorology*, **32**, 329–335.

Jolls, K. and Hanratty, T. (1966). Transition to turbulence for flow through a dumped bed of spheres. *Journal of Chemical Engineering Science*, **21**, 1185–1190.

Jones, N., Scalan, R., Sarkar, P., and Singh, L. (1995). The effect of section model details on aeroelastic parameters. *Journal of Wind Engineering and Industrial Aerodynamics*, **54**, 43–45.

Judd, M., Raupach, M., and Finnigan, J. (1996). A wind tunnel study of turbulent flow around single and multiple windbreaks part I: velocity fields. *Boundary Layer Meteorology*, **80**, 127–165.

Juricko, Z. (2008). Maslenicki most dobit ce burobrane. *Jutarnji list, 29.01.2008*.

Kaiser, H. (1959). Die Strömung an Windschutzstreifen. *Berichte des Deutschen Wetterdienstes*, **5**, 1–36.

Karabelas, A., Wegner, T., and Hanratty, T. (1973). Flow pattern in close packed cubic array of spheres near the critical Reynolds number. *Journal of Chemical Engineering Science*, **28**, 673–682.

Kleinhanss, K., Romberg, M., Saul, R., and Schmidt-Hurtienne, B. (2007). Die zweite Strelasundquerung mit der Schrägseilbrücke über den Ziegelgraben. *Bauingenieur*, **82**, 159–169.

Koch, D. and Ladd, A. (1997). Moderate Reynolds number flows through periodic and random arrays of aligned cylinders. *Journal of Fluid Mechanics*, **349**, 31–66.

Koss, H. H. (2006). On differences and similarities of applied wind comfort criteria. *Journal of Wind Engineering and Industrial Aerodynamics*, **94**(11), 781–797.

Kuwahara, F., Yamane, T., and Nakayama, A. (2006). Large eddy simulation of turbulent flow in porous media. *International Communications in Heat and Mass Transfer*, **33**(4), 411–418.

Kwon, S., Kim, D., Lee, S., and Song, H. (2011). Design criteria of wind barriers for traffic. Part 1: wind barrier performance. *Journal of Wind and Structures*, **14**, 55–70.

Latifi, M., Midoux, N., Storck, A., and Gence, J. (1989). The use of microelectrodes in the study of flow regimes in a packed bed reactor with single phase liquid flow. *Journal of Chemical Engineering Science*, **44**, 2501–2508.

Laws, E. M. and Livesey, J. L. (1978). Flow Through Screens. *Annual Review of Fluid Mechanics*, **10**, 247–266.

Lawson, T. and Penwarden, A. (1975). The effects of wind on people in the vicinity of buildings. In *Fourth Internationl Colloqium on Wind Effects on Buildings and Structures, Heathrow.*

Lee, S. and Kim, H. (1998). Velocity field measurements of flow around a triangular prism behind a porous fence. *Journal of Wind Engineering and Industrial Aerodynamics*, **77-78**, 521–530.

Lee, S. and Kim, H. (2001). Hole diameter effect on flow characteristics of wake behind porous fences having the same porosity. *Journal of Fluid Dynamics Research*, **28**, 449–464.

Lee, S., Park, K., and Park, C. (2002). Wind tunnel observations about the shelter effect of porous fences on the sand particle movements. *Jorunal of Atmospheric Environment*, **36**, 1453–1463.

Lee, S. J. and Kim, H. (1999). Laboratory measurements of velocity and turbulence field behind porous fences. *Journal of Wind Engineering and Industrial Aerodynamics*, **80**, 311–326.

Lesage, F., Midoux, N., and Latifi, M. (2004). New local measurements of hydrodynamics in porous media. *Journal of Experiments in Fluid*, **37**, 257–262.

Lin, Y., Jin, J., Zou, B., Cong, Z., Wen, X., Tu, X., and Ye, J. (1984). Effect of fence techniques in leveling sand accumulation around sandbreaks. *Desert Resources*, **4**, 16–25.

Liu, R., David, S., and Ting, K. (2007). Turbulent flow downstream of a perforated plate: sharp-edged orifice versus finite-thickness holes. *Journal of Fluids Engineering*, **129**, 1164–1171.

Loewe, F. (1972). The land of storms. *Weather*, **27**, 110–121.

Lowrance, W. (1976). *Of Acceptable Risk: Science and the Determination of Safety.* William Kaufmann, Waltham, Massachusetts.

Mair, W. and Stewart, A. (1985). The flow past yawed slender bodies, with and without ground effects. *Journal of Wind Engineering and Industrial Aerodynamics*, **18**(3), 301–328.

Masuoka, T. and Takatsu, Y. (2002). Turbulence characteristics in porous media. In D. B. Ingham and I. Pop, editors, *Transport Phenomena in Porous Media II*, pages 231–256. Pergamon, Oxford.

Matschke, G. and Heine, C. (2002). Full scale tests on side wind effects on trains. Evaluation of aerodynamic coefficients and efficiency of wind breaking devices. *Notes on Numerical Fluid Mechanics and Multidisciplinary Design*, **79**(10), 27–38.

McLachlan, G. and Peel, D. (1998). *Finite mixture models*. John Wiley and Sons, New York.

Melbourne, W. and Joubert, P. (1971). Problems of wind flow at the base of tall buildings. In *Third International Colloqium on Wind Effects on Buildings and Structures, Tokyo*.

Melbourne, W. H. (1978). Criteria for environmental wind conditions. *Journal of Wind Engineering and Industrial Aerodynamics*, **3**, 241–249.

Merzouk, N. (2000). Wind energy potential of Algeria. *Journal of Renewable Energy*, **21**, 553–562.

Mickley, H., Smith, K., and Korchak, E. (1965). Fluid flow in packed beds. *Journal of Chemical Engineering Science*, **20**, 237–246.

Miguel, A. F. (1998). Airflow through porous screens: From theory to practical considerations. *Journal of Energy and Buildings*, **28**(1), 63–69.

Miguel, A. F., van de Braak, N. J., and Bot, G. P. A. (1997). Analysis of the Airflow Characteristics of Greenhouse Screening Materials. *Journal of Agricultural Engineering Research*, **67**(2), 105–112.

Miller, D., Rosenborg, N., and Bragley, W. (1975). Wind reduction by a highly permeable tree shelter belt. *Journal of Agricultural and Forest Meteorology*, **14**, 321–333.

Miller, L. (1956). Table of Percentage Points of Kolmogorov Statistics. *Journal of the American Statistical Association*, **51**, 111–121.

Montemagno, C. and Gray, W. (1995). Photoluminescent volumetric imaging: a technique for the exploration of multiphase flow and transport in porous media. *Journal of Geophysical Research Letters*, **22**, 425–428.

Munich Re (2001). Natural Disasters. Annual Review of Natural Disasters 2000. Technical report, Munich Reinsurance Group.

Munson, B. (1988). Very low Reynolds-number flow through screens. *Journal of Fluids Engineering*, **110**, 462–463.

Munson, B., Young, D., and Okiishi, T. (2002). *Fundamentals of Fluid Mechanics*. John Wiley and Sons, New York.

Nageli, W. (1941). Untersuchungen über die Windverhältnisse im Bereich yon Windschutzstreifen. *Mitteilungen der Schweizerische Anstalt fur forstliches Versuchswesen*, **23**, 221–276.

Nield, D. and Bejan, A. (1995). *Convection in Porous Media*. Springer-Verlag, New York.

Niven, R. (2002). Physical insights into the Ergun and Wen and Yu equations for fluid flow in packed and fluidized beds. *Journal of Chemical Engineering Science*, **57**, 527–534.

Packwood, A. (2000). Flow through porous fences in thick boundary layers: comparisons between laboratory and numerical experiments. *Journal of Wind Engineering and Industrial Aerodynamics*, **88**, 75–90.

Papesch, J. (1992). Wind tunnel test to optimize barrier spacing and porosity to reduce wind damage in horticultural shelter systems. *Journal of Wind Engineering and Industrial Aerodynamics*, **44**, 2631–2642.

Park, C. and Lee, S. (2003). Experimental study on surface pressure and flow structure around a triangular prism located behind a porous fence. *Journal of Wind Engineering and Industrial Aerodynamics*, **91**, 165–184.

Pattone, E., Shaw, R., Judd, M., and Raupach, M. (1998). Large eddy simulation of windbreak flow. *Boundary Layer Meteorology*, **87**, 275–306.

Pedras, M. H. J. and de Lemos, M. J. S. (2000). On the definition of turbulent kinetic energy for flow in porous media. *International Communications in Heat and Mass Transfer*, **27**(2), 211–220.

Penwarden, A., Grigg, R., and Rayment, R. (1978). Measurements of Wind Drag on People Standing in a Wind Tunnel. *Journal of Building and Environment*, **13**, 75–84.

Penwarden, A. D. (1973). Accettable Wind Speed in Towns. *Journal of Building Science*, **8**, 159–167.

Penwarden, A. D. and Wise, A. (1975). Wind environment around buildings. Technical report, Building Research Establishment Report.

Perera, M. D. (1981). Shelter behind two-dimensional solid and porous fences. *Journal of Wind Engineering and Industrial Aerodynamics*, **8**, 93–104.

Pinker, R. A. and Herbert, M. V. (1967). Pressure-loss associated with compressible flow through square-mesh wire gauzes. *Journal of Mechanical Engineering Science*, **9**, 11–23.

Plate, E. J. (1971). The aerodynamics of shelter belts. *Journal of Agricultural and Forest Meteorology*, **8**, 203–222.

Pliefke, T., Sperbeck, S., Urban, M., Peil, U., and Budelmann, H. (2007). A Standardized Methodology for Managing Disaster Risk An Attempt to Remove Ambiguity. In *5th International Probabilistic Workshop, Ghent, 2007*.

Pugh, L. G. (1971). The influence of wind resistance in running and walking and the mechanical efficiency of work against horizontal or vertical forces. *Journal of Physiology*, **213**, 255–276.

Raine, J. and Stevenson, D. (1977). Wind protection by model fences in a simulated atmospheric boundary layer. *Journal of Wind Engineering and Industrial Aerodynamics*, **2**, 159–180.

Raju, K. R., Garde, R., Singh, S., and Singh, N. (1988). Experimental study on characteristics of flow past porous fences. *Journal of Wind Engineering and Industrial Aerodynamics*, **29**, 155–163.

Ratcliff, M. A. and Peterka, J. A. (1990). Comparison of pedestrian wind acceptability criteria. *Journal of Wind Engineering and Industrial Aerodynamics*, **36**, 791–800.

Reynolds, A. (1969). Flow deflection by gauze screens. *Journal of Mechanical Engineering Science*, **11**, 290–294.

Ricciardelli, F. (2003). On the wind loading mechanism of long-span bridge deck box sections. *Journal of Wind Engineering and Industrial Aerodynamics*, **91**, 1411–1430.

Ricciardelli, F., de Grenet, E. T., and Hangan, H. (2002). Pressure distribution, aerodynamic forces and dynamic response of box bridge sections. *Journal of Wind Engineering and Industrial Aerodynamics*, **90**, 1135–1150.

Richards, P. J. and Robinson, M. (1999). Wind loads on porous structures. *Journal of Wind Engineering and Industrial Aerodynamics*, **83**(1-3), 455–465.

Robinson, C. G. (1987). *The effect of atmospheric turbulence on trains*. Ph.D. thesis, Nottingham University.

Rode, S., Midoux, N., Latifi, M., Storck, A., and Saatdjian, E. (1994). Hydrodynamics of liquid flow in packed beds: an experimental study using electrochemical shear rate sensors. *Journal of Chemical Engineering Science*, **49**, 889–900.

Sabiri, N.-E. and Comiti, J. (1997). Experimental validation of a model allowing pressure gradient determination for non-Newtonian purely viscous fluid-flow through packed beds. *Journal of Chemical Engineering Science*, **52**(20), 3589–3592.

Saleh, S., Thovert, J., and Adler, P. (1993). Flow along porous media by particle image velocimetry. *AIChE Journal*, **39**, 1765–1776.

Scheidegger, A. (1974). *The Physics of Flow through Porous Media*. University of Toronto Press, Toronto.

Schubauer, G., Spangenberg, W., and Klebanoff, P. (1948). Aerodynamic characteristics of damping screens. Technical report.

Schwartz, R., Fryrear, D., Harris, B., Bilbro, J., and Juo, A. S. R. (1995). Mean flow and shear stress distributions as influenced by vegetative windbreak structure. *Journal of Agricultural and Forest Meteorology*, **75**, 1–22.

Sederman, A. J., Johns, M., Bramley, A., Alexander, P., and Gladden, L. (1997). Magnetic resonance imaging of liquid flow and pore structure within packed beds. *Journal of Chemical Engineering Science*, **52**, 2239–2250.

Seginer, I. (1972). Windbreak drag calculated from the horizontal velocity field. *Boundary Layer Meteorology*, **3**, 87–97.

Seguin, D., Montillet, A., and Comiti, J. (1998). Experimental characterization of flow regimes in various porous media: Limit of laminar flow regime. *Journal of Chemical Engineering Science*, **53**, 3897–3909.

Shao, Q. (2000). Estimation for hazardous concentrations based on NOEC toxicity data: an alternative approach. *Journal of The International Environmetrics Society*, **11**, 583–595.

Shao, Q. (2004). Notes on maximum likelihood estimation for the three-parameter Burr XII distribution. *Journal of Computational Statistics and Data Analysis*, **45**, 675–687.

Shibu, S., Chhabra, R., and Eswaran, V. (2001). Power law fluid flow over a bundle of cylinders at intermediate Reynolds numbers. *Journal of Chemical Engineering Science*, **56**, 5545–5554.

Simiu, E. and Miyata, T. (2006). *Design of Buildings and Bridges for Wind*. John Wiley and Sons, New York.

Siple, P. and Passel, C. F. (1945). Measurements of dry atmospheric cooling in subfreezing temperatures. *Proccedings of the American Philosophical Society*, **89**, 177–179.

Skjetne, E. and Auriault, J. (1999). New insights on steady non-linear flow in porous media. *European Journal of Mechanics - B/Fluids*, **18**, 131–145.

Smith, B. and Barker, C. (1998). Design of wind screens to bridges, experience and application on major bridges. In *Proceedings of the International Symposium on Advances in Bridge Aerodynamics, Copenhagen*.

Solari, G., Castino, F., and Rusca, L. (2003). Wind climate micro-zoning: a pilot application to Liguria Region (North Western Italy). *Journal of Wind Engineering and Industrial Aerodynamics*, **91**, 1353–1375.

Stephenson, J. and Stewart, W. (1986). Optical measurements of porosity and fluid motion in packed beds. *Journal of Chemical Engineering Science*, **41**, 2161–2170.

Sterling, M., Quinn, A., Hargreaves, D., Cheli, F., Sabbioni, E., Tomasini, G., Delaunay, D., Baker, C., and Morvan, H. (2010). A comparison of different methods to evaluate the wind induced forces on a high sided lorry. *Journal of Wind Engineering and Industrial Aerodynamics*, **98**(1), 10–20.

Surrey, D., Cooper, K., and Davenport, A. (1988). Aerodynamics of urban transient vehicles. *Canadian Journal of Civil Engineering*, **15**, 37–48.

Takanami, K., Kitahara, T., and Matsushita, A. (1976). Conversion from wind vector into aerodynamics inputs acting as vehicle body on side wind gusts. Technical report, 16th FISITA Congress.

Takeda, K. and Kato, M. (1992). Wind tunnel blockage effects on drag coefficient and wind-induced vibration. *Journal of Wind Engineering and Industrial Aerodynamics*, **41**, 897–908.

Takle, E. and Brown, J. (1977). Note on the Use of Weibull Statistics to Characterize Wind-Speed Data. *Journal of American Meteorological Society*, **17**, 556–559.

Teitel, M., Dvorkin, D., Haim, Y., Tanny, J., and Seginer, I. (2009). Comparison of measured and simulated flow through screens: Effects of screen inclination and porosity. *Journal of Biosystems Engineering*, **104**(3), 404–416.

Trein, C. and Shirato, H. (2011). Coupled flutter stability from the unsteady pressure characteristics point of view. *Journal of Wind Engineering and Industrial Aerodynamics*, **99**(2-3), 114–122.

Tuller, S. and Brett, A. (1984). The characteristics of wind velocity that favour the fitting of a weibull distribution in wind speed analysis. *Journal of Climate and Applied Meteorology*, **23**, 124–134.

Valli, A., Hyvluoma, J., Jsberg, A., Koponen, A., and Timonen, J. (2009). Pressure Drop for Low Reynolds-Number Flows Through Regular and Random Screens. *Transport in Porous Media*, **80**, 193–208.

van der Merwe, D. and Gauvin, W. (1971). Velocity and turbulence measurements of air flow through a packed bed. *AIChE Journal*, **17**, 519–528.

Vigiak, O., Sterk, G., Warren, A., and Hagen, L. (2003). Spatial modeling of wind speed around windbreaks. *Catena - Interdisciplinary Journal*, **52**, 273–288.

Villermaux, E. and Hopfinger, E. J. (1994). Periodically arranged co-flowing jets. *Journal of Fluid Mechanics*, **263**, 63–92.

Wang, F., Keats, J., and Zimmer, W. (1996). Maximum likelihood estimation of the Burr XII distribution with censored and uncensored data. *Journal of Microelectronics Reliability*, **36**, 359–362.

Ward, J. C. (1964). Turbulent flow in porous media. *Journal of the Hydraulics Division*, **5**, 1–12.

Ward Smith, A. (1971). *Pressure Losses in Ducted Flows*. Butterworths, London.

Wegner, T., Karabelas, A., and Hanratty, T. (1971). Visual studies of flow in a regular array of spheres. *Journal of Chemical Engineering Science*, **26**, 59–63.

Weibull, W. (1951). A Statistical Distribution Function of Wide Applicability. *Journal of Applied Mechanics*, pages 293–297.

Weighardt, K. (1953). On the resistance of screens. *Aeronautical Quarterly*, **4**, 186–192.

White, F. (2001). *Fluid Mechanics*. McGraw-Hill, Boston.

Wilson, J. (1985). Numerical studies of flow through a windbreak. *Journal of Wind Engineering and Industrial Aerodynamics*, **21**, 119–154.

Wilson, J. (1997). A field study of the mean pressure about a windbreak. *Boundary Layer Meteorology*, **85**, 327–358.

Wingo, D. (1983). Maximum likelihood methods for Atting the Burr Type XII distribution parameters to life test data. *Biometrical Journal*, **25**, 77–84.

Wodie, J. and Levy, T. (1991). Non-linear rectification of Darcys law. *Comptes Rendus de l'Acadmie des Sciences*, **312**, 157–161.

Zimmer, W., Keats, J., and Wang, F. (1998). The Burr XII distribution in reliability analysis. *Journal of Quality Technology*, **30**, 386–394.